STABILITY OF EXCITATORY CONNECTIVITY PREDICTS THE PROBABILITY OF CA1 PYRAMIDAL NEURONS TO UNDERGO ACTIVITY-DEPENDENT PLASTICITY

Dissertation der Fakultät für Biologie

der Ludwig-Maximilians-Universität München

Tim Phillip Castello-Waldow

München, Juni 2019

Declaration of academic integrity / Eidesstattliche Erklärung

Hiermit erkläre ich an Eidessatt, Tim Phillip Castello-Waldow, geboren am 03. Mai 1989 in Preetz, dass ich die vorliegende Dissertation mit dem Titel "Stability of excitatory connectivity predicts the probability of CA1 pyramidal neurons to undergo activity-dependent plasticity" selbstständig und ohne unzulässige Hilfe erarbeitet habe. Sämtliche Stellen der Arbeit, die im Wortlaut oder dem Sinn nach anderen Werken entnommen sind, habe ich durch Angabe der Quellen kenntlich gemacht.

Diese Arbeit war in gleicher oder ähnlicher Fassung noch nicht Bestandteil einer Studien- oder Prüfungsleistung.

München, 27.01.2020   Tim Phillip Castello-Waldow

Ort und Datum   Unterschrift (Tim Phillip Castello-

                                                  Waldow)

ZUSAMMENFASSUNG

Im Gehirn eines Säugetieres benötigt das Bilden, Speichern und wieder Abrufen einer Erinnerung die Kommunikation von Neuronen. Diese Kommunikation führt dazu, dass Gruppen von Zellen entstehen, von denen angenommen wird, dass diese die neuronale Repräsentation der Erinnerung ausmachen. Neuronen interagieren hauptsächlich über elektrische und chemische Verbindungen miteinander. Diese Verbindungen werden Synapsen genannt. Sie tragen eine einzigartige molekulare und strukturelle Signatur, welche ihnen den direkten Informationstransfer ermöglicht. Abhängig von der Hirnregion, können Synapsen ein Leben lang halten oder unterlaufen ständigen Veränderungen. Umwelteinflüsse hingegen verursachen robuste Umgestaltungen der synaptischen Verbindungen, unabhängig von der Hirnregion. Die Stabilisierung und Fortdauer der veränderten Verbindung führt letztendlich zur Bildung einer neuen Erinnerung, die, wovon man ausgeht, in der verbundenen Gruppe von Neuronen gespeichert wird.

In dieser Studie untersuche ich, wie sich neuronale Aktivität, ausgelöst durch eine angereicherte Umgebung, auf die strukturelle, synaptische Plastizität im dorsalen Hippocampus auswirkt. Des Weiteren analysieren wir, ob und wie die Veränderung der synaptischen Plastizität Einfluss auf das Formen und wieder Abrufen einer Hippocampus-abhängigen Erinnerung hat. Um zu verstehen, wie neuronale Aktivität speziell die Synapsen von aktiven Neuronen verändert, werden während der angereicherten Umgebung aktive Neuronen mit einem fluoreszierenden Label markiert. Dies ermöglicht es uns die synaptischen Veränderungen von zukünftig aktiven Neuronen prospektiv, als auch retrospektiv zu betrachten.

Wir haben herausgefunden, dass die Stabilität von strukturellen synaptischen Verbindungen schon vor der neuronalen Aktivität Einfluss auf die Wahrscheinlichkeit hatte, ob eine Zelle Teil der neuronalen Repräsentation der angereicherten Umgebung wird. Neuronen mit stabileren Verbindungen wurden eher aktiv und hatten eine höhere Wahrscheinlichkeit, verglichen mit Zellen mit weniger stabilen Verbindungen. Nach dieser starken neuronalen Aktivität konnten wir eine Stabilisierung des gesamten Netzwerks, auch von primär inaktiven Neuronen beobachten. Außerdem konnten wir zeigen, dass synaptische Plastizität im Hippocampus direkt mit der Bildung einer Hippocampus-abhängigen Erinnerung korrelierte. Mäuse, die eine höhere Dichte an Synapsen im Hippocampus hatten, lernten die

Hippocampus-abhänge Aufgabe schlechter, als Mäuse mit geringerer Dichte. Passend dazu zeigten Mäuse mit einer höheren synaptischen Plastizität ein verbessertes Lernen.

Diese Arbeit wird unser weiteres Verständnis vom Formen und Abrufen von Erinnerungen und wie diese von neuronaler Aktivität induzierten Plastizität beeinflusst werden verbessern.

ABSTRACT

The formation, storage, and recall of memory require communication between neurons inside the mammalian brain. This communication gives rise to cellular ensembles that are believed to be the neuronal representation of that memory. Neurons mainly interact with each other through electrical or chemical connections, called synapses. These synapses feature unique molecular and structural characteristics which enable direct information transfer. Depending on the area of the brain, synapses can last throughout the lifespan of an animal or undergo frequent changes. Environmental influences, however, seem to induce robust remodeling of the synaptic connections independent of the brain region. The stabilization and persistence of the change of connectivity eventually lead to the formation of a new memory, which is believed to be stored in the neuronal ensemble linked by this connection.

Here I examine the influence of neuronal activity, which is induced by exposure to an enriched environment (EE) onto the structural synaptic plasticity of the dorsal hippocampus. Furthermore, I investigate if and how the change of synaptic plasticity modulates hippocampal-dependent memory formation and retrieval. To understand how neuronal activity modifies the connectivity specifically of active neurons, I labeled neurons activated during the EE with a fluorescent marker. This technique enabled tracking spine dynamics of prospective and retrospective active neurons compared to inactive neurons.

We found that the stability of structural synaptic connectivity prior to the neuronal activity predicted the probability to become part of the neuronal representation of the EE. Neurons featuring more stable connectivity were more likely to become active and part of the ensemble compared to neurons with less stable connectivity. After the potent neuronal activation due to the exposure to the EE, I observed a network stabilization of neurons that did not show direct neuronal activity during the EE. In addition, hippocampal synaptic plasticity was directly correlated with hippocampal-dependent memory formation and recall. Mice exhibiting higher spine densities learned the hippocampal-dependent fear conditioning worse compared to mice with lower spine densities. In conjunction, mice representing a higher synaptic turnover also showed improved hippocampal learning.

This study will help the further understanding how the formation and retrieval of memories are influenced by neuronal activity-induced synaptic plasticity.

Table of Contents

CHAPTER 1 – INTRODUCTION

T he ability of the nervous system to adapt to a changing environment and to permanently solve newly arising questions, the ability to think about and to learn new tasks and the ability to store information and to recall these memories is a huge evolutionary advantage and the reason why the brain is one of the most essential existing organs. Nevertheless, recent research is just beginning to understand how this organ works and how it achieves its different functions.

Even though it is already known that synaptic plasticity, both at the molecular (Monné, 1948; Flexner JB, 1963; Costa-Mattioli et al., 2005) and the network level (Bliss and Lomo, 1973; Martin et al., 2000), is essential for learning and memory surprisingly little is known how neuronal microcircuits of active neurons change during a specific task.

> *"Activity-dependent synaptic plasticity is induced at appropriate synapses during memory formation, and is both necessary and sufficient for the information storage underlying the type of memory mediated by the brain area in which that plasticity is observed."*
> (Martin et al., 2000)

Although it is already known that the hippocampus plays a crucial role in episodic learning and memory (Scoville & Milner, 1957; Morris et al., 1986; Tsien et al., 1996), we are only starting to understand the importance of connections between neurons and different brain regions. Since the brain is such a complex organ, it is challenging to examine the key components necessary for learning and memory. Additionally, the environment plays a vital role in learning and memory. Environmental influences like enrichment (Kempermann et al., 1997; Bouet et al., 2011) or stress (Joëls et al., 2004; Conrad, 2010) are critical effectors to the ability of learning and memory. To fully uncover the mechanisms that are involved in learning and memory, we need to study the bases of neuronal networks further. Detailed investigations about neuronal protein composition, timing, and location of protein translation, connectomics, hormone combination, and environmental influences will broaden our understanding of how our brains function.

1.1 Learning and Memory

One of the main features of the brain are learning and memory. From the beginning and during the whole life of an individual, sensory stimuli shape the brain. These modifications affect both the connectivity and the molecular level leading to learning and formation of memories.

Neuroscientists and psychologists have classified and arranged three principal distinctions in this taxonomy. The first two are based on the duration of memory. Working memory refers to the maintenance of information for brief periods (milliseconds to seconds) (D.O. Hebb, 1949; Miller et al., 1960; Miyake, A. & Shah, P., 1999), whereas long-term memory refers to the acquisition of information over more extended periods (minutes to years) (Miller, 1956; Baddeley, 1966). This difference in time is caused by different underlying mechanisms such as protein synthesis that has been shown to be required for long-term memory (Milner et al., 1998; Nader et al., 2000, 2000; Scharf et al., 2002) and stabilization of structural connectivity (Xu et al., 2009; Yang et al., 2009). Long-term memory can be further divided into declarative or explicit and non-declarative or implicit memory (**Fig. 1.1.1**).
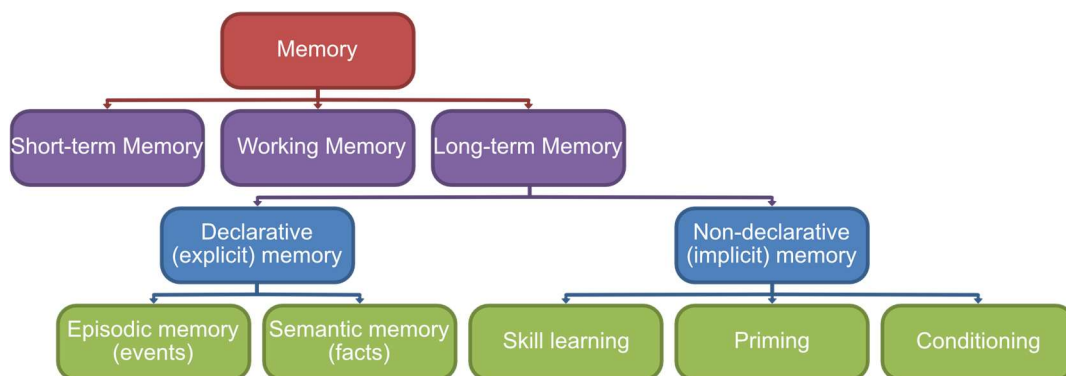
Fig. 1.1.1: Taxonomy of memory systems. The two major distinctions are based on memory duration (working- and long-term memory). Long-term memory can be divided based on different types of memory. Modified from (Squire and Zola-Morgan, 1991).

Declarative memory refers to the remembering of events and facts that are learned consciously (explicit memory) (Tulvig & Donaldson, 1972; Eichenbaum, 2000; Eichenbaum, 2001), whereas non-declarative memory refers to memories expressed through performance and learned unconsciously (implicit memory) (Schacter, 1987). It can be subdivided into priming, skill learning (Jones and Roberts, 1968), and conditioning. Conditioning refers to the formation of associations between a conditioned and unconditioned stimulus (Pavlovian conditioning) (Pavlov, 1927).

The molecular and cellular mechanisms underlying learning and memory had been extensively studied during the last two decades. However, current cutting edge research aims to further dissect the network contributions of storing and recalling memories.

1.2 The Hippocampal Formation

The hippocampus is among the most studied brain regions in humans and rodents. This introduction will focus on the rodent hippocampus. In the rodent brain, the dorsal hippocampus is located between the neocortex and the diencephalon and curves ventrally toward the temporal lobe forming the intermediate hippocampus and edging in the ventral hippocampus (Fanselow and Dong, 2010). It integrates multimodal sensory information from the entorhinal cortex (EC) and moreover has extensive connectivity to subcortical and frontal cortical structures. The hippocampal formation can be subdivided into the Subiculum, CA1, CA2, CA3, and the dentate gyrus (DG), which are distinct subregions displaying differences in cell morphology, composition, connectivity and computation (**Fig. 1.2.1**).
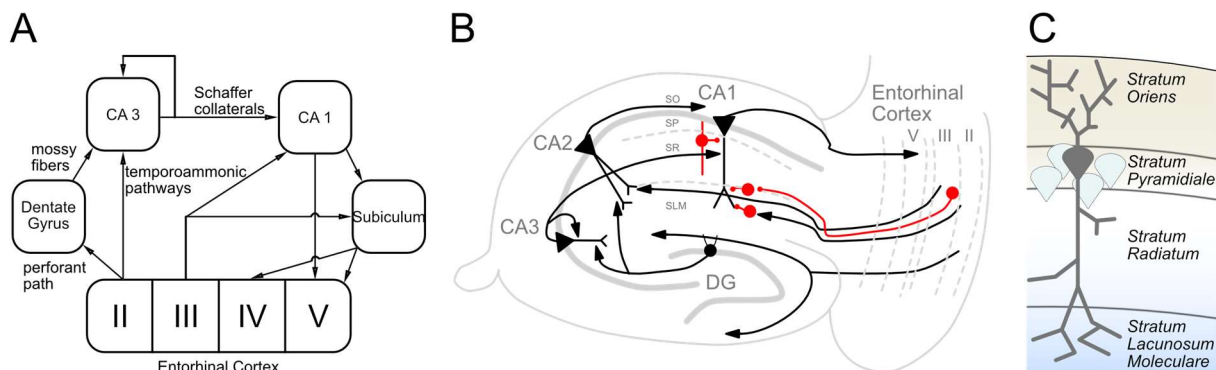
Fig. 1.2.1: The connectivity of the hippocampal formation. (**A**) Simplified schematic of the hippocampal excitatory connectivity. Modified from (Martin and Clark, 2007). The main excitatory inputs come from the EC layer II and III neurons. They send their axons via the perforant path or through the temporoammonic pathways to the DG and CA3 and CA1. The in the DG processed information is further transmitted through the mossy fibers to the CA3. The CA3 sends its Schaffer collaterals to the CA1 but also shows strong recurrent connections to itself. CA1, as the primary output unit of the hippocampus, excites either the Subiculum or the EC layer V directly. (**B**) Simplified schematic of the anatomic hippocampal connectivity. Modified from (Zemla R & Basu J, 2017). The main excitatory inputs come from the EC layer II and III neurons. They send their axons to the DG, CA3, CA2, and CA1. The in the DG processed information is further transmitted to the CA3 and with weaker connectivity to CA2. They send their axons to the CA1. CA1, as the main output unit of the hippocampus then excites EC layer V. A small subset of the inhibitory network is shown in red. Long range inhibitory neurons from EC layer III sent their axons to other inhibitory neurons in the *stratum lacunosum moleculare* (SLM) to induce disinhibition. Other inhibitory neurons receive excitatory input von the EC or the Schaffer collaterals to feed-forward inhibit the CA1 pyramidal neurons. (**C**) Detailed overview of CA1 region. Basal dendrites span into the *stratum oriens* (SO). The somata of the principle excitatory neurons are located in the *stratum pyramidiale* (SP). The main apical trunk

dendrites extend into the *stratum radiatum* (SR), while the most distal apical tuft dendrites range over the *stratum lacunosum moleculare* (SLM).

The hippocampus got famous after its bilateral surgical removal in the patient Henry Molaison who, after the successful surgery, was incapable of forming new episodic memories (Scoville & Milner, 1957). This finding gave rise to the theory that the hippocampus might be involved in memory acquisition and long-term consolidation by passing information to cortical areas – a process that got known as systems consolidation (McClelland et al., 1995; Dudai and Morris, 2000). Evidence was brought by animal experiments supporting the finding of the importance of the hippocampus for episodic and declarative memory, such as recognition memory (Tulving and Markowitsch, 1998; Clayton et al., 2001; Morris, 2001; Engelmann et al., 2011). While the hippocampus became more extensively studied it moved into the focus of forming spatial representations of the environment while being involved in the ability of place coding and learning (O'Keefe and Dostrovsky, 1971; Olton DS et al., 1979; Morris et al., 1982; Sutherland et al., 1983).

Now there is strong evidence that the hippocampal formation is involved and crucial for forming long-term memories about people, places, objects, and events and for recalling these memories. It has been shown that the formation and recall of episodic memory require the interaction between the EC and the dorsal hippocampus (Buzsáki and Moser, 2013). Hereby the hippocampus receives inputs through the perforant path from the entorhinal cortex to the DG or directly to the CA1, CA2, and CA3 through the temporoammonic pathways (Suh et al., 2011) (**Fig. 1.2.1 A-B**). When the information reaches the DG, it is forwarded through the tri-synaptic pathway further to the CA1 which is the central output region of the hippocampus which sends its afferents to the deep layer V of the EC (**Fig. 1.2.1 A-B**). Recent studies revealed long-range interaction between the hippocampus and the prefrontal cortex that showed importance on working memory (Spellman et al., 2015) and memory retrieval (Ciocchi et al., 2015; Rajasethupathy et al., 2015). However, during the formation of episodic memory, the hippocampus converges temporal, spatial, and sensory information from the long-range but also local circuitries leading to the creation of ensembles that represent space, time, and context. These ensembles are defined as neuronal sub-population being co-active during behavior and are believed to reflect a functional micro-circuit which represents the experienced event. Even though these ensembles incorporate a particular event for some time, it has been shown

that the neuronal representations are plastic and change with time (Rubin et al., 2015; Attardo et al., 2018). One of the most prominent ensemble formations happens during spatial representation by so-called place cells. These place cells are CA1 pyramidal neurons that fire only at defined spatial locations of a specific environment (O'Keefe and Dostrovsky, 1971; Park et al., 2011) eventually forming what is called a cognitive map. The emergence of hippocampal place maps was believed to be influenced by the medial entorhinal cortex (MEC) grid cells (Fyhn et al., 2004; Hafting et al., 2005), which convey spatial information to hippocampal place cells. However, lesioning the EC showed minor effects onto place fields (Brun et al., 2008), which leaves the question of the emergence of spatially tuned ensembles still room for speculations and further research.

Similar ensembles can be found during contextual information processing. These context-specific ensembles were shown to represent behaviorally relevant knowledge about the experienced context (Liu et al., 2012b; Denny et al., 2014). Channelrhodopsin (ChR2) expression under the neuronal activity controlled cFos promoter labeled co-active neurons and enabled to manipulate behavior, learning, and recall (Liu et al., 2012b; Ramirez et al., 2013). Neuronal ensembles that were shown to be functional and behavioral relevant for one specific context were called Engram cells. Even though these neuronal engrams were shown to be present in the DG and the CA3 proving evidence of a functional engram in CA1 failed (Ramirez et al., 2013). How contextual representations emerge is still part of current research. The subgranular zone (SGZ) in the DG is one of the few places in the mammalian brain with neurogenesis throughout lifetime (Tavazoie et al., 2008). Recent data suggest that newborn hyperexcitable granule cells might play a vital role in the engram formation (Danielson et al., 2016).

Non-negligible is the contribution of inhibitory neurons onto the hippocampal circuit function. Parvalbumin+ (PV+) interneurons mainly target the axon-initial segment (Axo-axonic) and proximal basal dendrites in the *stratum oriens* of pyramidal neurons (Basket PV) (Pelkey et al., 2017) (**Fig. 1.2.1 C**). While Somatostatin (SOM+) interneurons target either basal dendrites and the proximal apical dendrites (Bistratified) or the distal basal dendrites and the apical tuft in the SLM (O-LM), both classes receive substantial input from either the CA3 or the EC to provide feed-forward and feedback inhibition (**Fig. 1.2.1 C**), but they also receive inhibitory input from themselves leading to disinhibition of the pyramidal neurons

(Pelkey et al., 2017). The presence of inhibitory neurons contributes massively to the computational power of the hippocampus.

After the internal computation of the hippocampus, the central output regions are the CA1 and the subiculum. They send their axons mainly to the EC. This connection has been shown to be crucial for the production of grid fields showing that CA1 inactivation disrupted the hexagonal firing pattern of the grid cells (Bonnevie et al., 2013). However, the ventral CA1 also targets the amygdala, the prefrontal cortex, and the nucleus accumbens (Bannerman et al., 2014).

The central role of the hippocampus, receiving multimodal inputs and sending its afferents into varies areas of the brain, and the sparse nature of neuronal ensembles representing space, context, and episodic memory, makes the hippocampus to one of the most interesting and studied brain regions of human and rodents.

1.3 Dendritic Spines and Their Structural Dynamics

Dendritic spines were first described in 1893 by Santiago Ramón y Cajal (Ramon y Cajal, 1893). Cajal already postulated that the dendritic protrusions, which are now known as spines, were points of contact between neurons. However, it took more than 50 years, and the invention of electron microscopy before a synapse could be visualized on a dendritic spine (Gray, 1959). Due to missing techniques, spines were believed to be static protrusions. However, filling cultured neurons with a fluorescent dye revealed that spines were dynamic (Ziv & Smith, 1996; Fischer et al., 1998). In the same period of time, it became possible to genetically label neurons using fluorescent protein expression (Chalfie et al., 1994; Chen et al., 2000). However, due to the limitations of light microscopy, all studies were restricted to cultured neurons and slice preparations. Luckily, the two-photon microscope, that allowed for *in vivo* imaging was also developed during the same period (Denk et al., 1990; Denk et al., 1994; Engert and Bonhoeffer, 1999; Maletic-Savatic et al., 1999; Grutzendler et al., 2002; Holtmaat et al., 2005). These initial studies revealed the stability of spines but also changes in shape, size as well as *de novo* formation and elimination. Spine dynamics were shown to respond to the animal's experience and changes in the environment (Lendvai et al., 2000; Trachtenberg et al., 2002).

Even though spines only represent the post-synaptic part of a synapse the majority of adult spines contains the excitatory synaptic scaffold protein PSD-95 which make the spine more likely to be a fully functional synapse (Harris et al., 1992; Arellano et al., 2007). There is evidence that spines without PSD-95 account for the majority of dynamic spines (Holtmaat et al., 2005; Zuo et al., 2005; Cane et al., 2014). Additionally, imaging data of the spine size could be positively correlated to the PSD-95 size, the number of presynaptic vesicles (Harris et al., 1992) and the synaptic strength (Matsuzaki et al., 2001; Asrican et al., 2007). These findings strengthen the rational to use dendritic spines and their size as a proxy for functional synapses. Additionally, spines are often classified by their shape into four main categories (from small to large spines): filopodia, stubby, thin, and mushroom-like spines (Peters and Kaiserman-Abramof, 1970) (**Fig. 1.3.1**). In the cortex and hippocampus, the thin (65%) and mushroom (25%) like spines account for the largest fraction of spines (Peters and Kaiserman-Abramof, 1970). Experts hypothesize that mushroom spines are already at the maximum of their potential size. Thereby it is unlikely that they undergo synaptic strengthening. For that reason, they are often referred to as "memory spines". Thin spines, however, still have the potential to undergo synaptic potentiation and are therefore often referred to as "learning spines" (reviewed in (Bourne and Harris, 2007)).
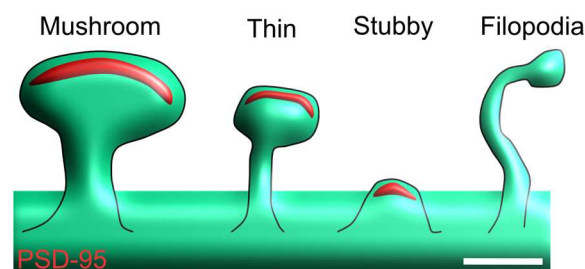
Fig. 1.3.1: The different classes of dendritic spines. From left to right: mushroom-like, thin, stubby, and filopodia. Mushroom, thin and stubby spines contain a PSD-95 (red) and are therefore believed to be functional synapses. Mushroom-like spines are believed to have reached their maximum size and therefore are less likely to undergo synaptic growth. In contrast to the mushroom spine the thin and stubby spines are likely to undergo synaptic potentiation after LTP. Filopodia are immature spines that either become stabilized and thin spines or disappear within two days. Scale bar: 1 µm

In order to identify synaptic structural plasticity, multiple studies applied longitudinal 2-photon imaging of the same dendritic segments over numerous days. This technique allowed following individual spines over that period and assessing the stability and plasticity on the single synapse level (Denk and Svoboda, 1997; Lendvai et al., 2000; Grutzendler et al., 2002; Trachtenberg et al., 2002; Holtmaat et al., 2005). Furthermore, this technique has been applied to many different brain regions, like the hippocampus (Attardo et al., 2015), visual

cortex (Grutzendler et al., 2002; Hofer et al., 2009), barrel cortex (Holtmaat et al., 2006), somatosensory and auditory cortices (Majewska et al., 2006), motor cortex (Xu et al., 2009) and frontal cortices (Zuo et al., 2005). Also, spine dynamics could be manipulated by monocular scotoma (Keck et al., 2008), whisker trimming (Holtmaat et al., 2006), motor learning (Xu et al., 2009; Yang et al., 2009) as well as memory consolidation (Yang et al., 2014).

Spines and their dynamics can be further classified into two distinct kinetic groups: persistent and transient. Persistent spines are either formed and stabilized and remain over months and years (neocortex), or they are formed and disappear. Transient spines, however, are formed, and removed and reformed within days (reviewed in (Berry KP & Nedivi E, 2017)). Whether these transient spines should be considered the same spine after it disappeared and reappeared, or whether it should be called a new spine will be part of the further discussion during this study.

All of the *in vivo* studies had in common that behavioral changes of the mice changed the neuronal activity of the relevant sub-region of that behavior and that in turn the neuronal activity then changed the structural spine dynamics. Indeed activity-dependent synaptic strengthening using long-term potentiation (LTP) was shown to induce growth of filopodia in cultured slices of which some were stabilized and maintained (Engert and Bonhoeffer, 1999; Maletic-Savatic et al., 1999). LTP not only showed the induction of newborn spines through filopodia but also influenced the stabilization of new spines (Lang et al., 2004; Matsuzaki et al., 2004; Nägerl et al., 2004; Hill and Zito, 2013). This stabilization and maturation process seems to be linked to the incorporation of PSD-95 into the spine head. The PSD-95 binds both AMPA and NMDA receptors and thereby is an essential factor to convert a nascent spine into a functional synapse. Knockout of PSD-95 resulted in reduced spine stability and immature synaptic function displayed by a reduced AMPAR to NMDAR ratio (Migaud et al., 1998; Béïque et al., 2006; Ehrlich et al., 2007).

Taken together, spines are important dendritic protrusions that can be a proxy for a functional synapse. To be functional, the spine needs to integrate PSD-95 and AMPA and NMDA receptors. Spines undergo experience-dependent plasticity evoked by sensory stimuli and behavioral changes such as motor learning. In this study, I also aim to identify the influence of sensory stimuli induced neuronal activity onto structural synaptic plasticity in the dorsal hippocampus.

1.4 Two-Photon Excitation Fluorescence Laser-Scanning Microscopy

Traditionally single-photon microscopy has been used to study biological tissue and cells. This required tissue extraction and preparation to gain optical access to the desired region of interest. However, even after the preparation single-photon microscopy was limited to a maximum depth of 100 μm. The reason why conventional light microscopy could not be used for imaging of deeper tissues was the light scattering effect. This effect is particularly influencing shorter and more powerful wavelengths and is reduced for longer wavelengths. Scattering tissue, such as the brain, affects the excitation and immission of photons. The invention of 2-photon excitation fluorescence laser-scanning microscopy (Denk et al., 1990) that uses long, near-infra-red, wavelengths enabled penetration of deeper tissue with less scattering and led to the possibility to study entire tissues without the need for extraction and preparation (Denk et al., 1994). Using this microscopy technique, in combination with fluorescent dyes, which label the cells, permitted imaging up to a depth of 1 mm (Theer et al., 2003).

To excite a fluorophore using 2-photon excitation, two photons need to arrive nearly simultaneously, within 0.5 fs, at the fluorophore to combine their energies. Only this combination of energies can bring the fluorophore to its excited state, which then proceeds the regular fluorescence emission (Denk et al., 1995) (**Fig. 1.4.1A**). To produce sufficient signal using 2-photon excitation, light needs to be concentrated in space and time. The usage of high numerical aperture (NA) objectives leads to the spatial concentration of photons in one focal point. However, to bundle photons in time is more complicated. Powerful lasers that provide 100 fs pulses at a repetition rate of 100 MHz overcome this problem (Spectra-Physics' InSight®DS+™). Advantages of 2-photon microscopy are not only the deeper penetration of light but also the reduced phototoxicity due to the concentration of photons in one single focal point (**Fig 1.4.1.B**). This is especially crucial when it comes to long-term longitudinal *in vivo* imaging (Squirrell et al., 1999).
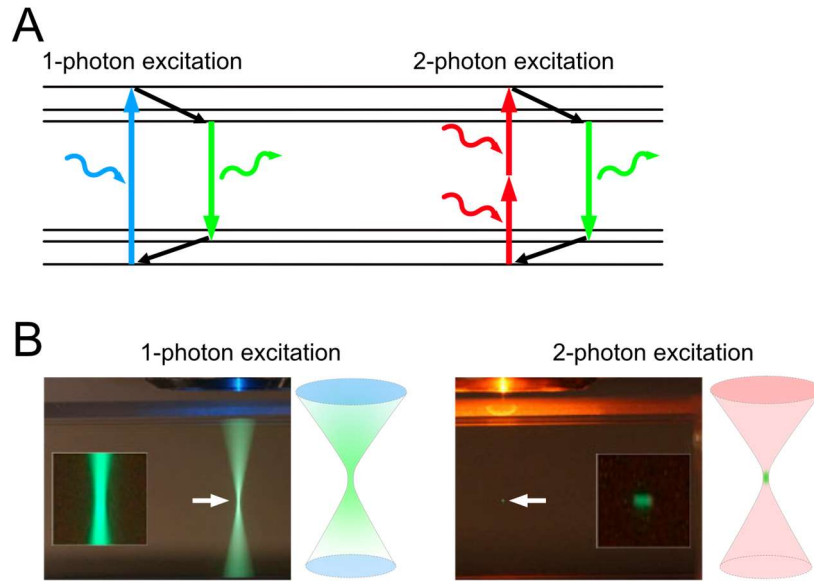
Fig. 1.4.1: The mechanism of 2-photon excitation. (**A**) Jablonsky diagram illustrating 1-photon excitation on the left and 2-photon excitation on the right. 1 photon of high energy blue light is needed to bring the green fluorescent molecule to its excited state before it emits green fluorescence. On the other hand, 2-photons arriving simultaneously (0.5 fs) sum their energy to lift the green fluorescent molecule to its excited state before it emits green fluorescence. (**B**) Differences in the focal point of 1- and 2-photon excitation. Even though the focal plane is the same, a lot of light is out of focus for the 1-photon excitation example, whereas all light is converged into one focal point using 2-photon excitation. White arrows indicate focal points. Photos are taken from Steve Ruzin and Holly Aaron, UC Berkeley.

Another advantage is the already mentioned reduction in scattering. Near-infra-red wavelengths are less scattered during the penetration of the tissue compared to shorter wavelengths. Even though the emission light is equally scattered compared to single-photon microscopy, however, the knowledge that all emitted photons result from one focal point opens the possibility to collect as many photons as possible and assigning them to the focal point of excitation. In contrast, confocal microscopy, using single-photon excitation, needs to "trash" many photons coming from different focal planes using the pinhole. Summarizing, the strength of 2-photon excitation microscopy is the usage within (living) scattering tissue while maintaining resolution and contrast of fluorescent markers.

1.5 Immediate Early Genes to Label Active Neurons Forming the Engram

The idea of an engram, which was defined as an ensemble of neurons that undergo activity-dependent changes after learning, was first described in 1904 by Richard Semon (Semon R, 1904). Initially, scientists used cytochrome-c oxidase activity as a marker for cellular and mitochondrial activity (Wong-Riley, 1989). Later immuno-staining against

immediate early genes (IEG) such as cFos, originally described as a proto-oncogene (Hu et al., 1994), was employed as an indirect marker of cellular activity. cFos expression was first described in 3T3 fibroblasts after platelet-derived growth factor (PDGF) treatment (Greenberg and Ziff, 1984). Later, cFos expression had been shown after activity in neurons activated by the nicotinic acetylcholine receptor or extracellular potassium chloride (Greenberg et al., 1986). The term IEG arises from the fast transcription of the IEG RNA after neuronal activity. *cfos* RNA can be detected already 15 minutes after the event of activity and its protein peaks at 90 minutes after the activity. After cFos, other IEGs had been described (Nedivi et al., 1993). Examples despite cFos were Zif268 (Nedivi et al., 1993), Candidate plasticity gene 15 (Cpg15) (Nedivi et al., 1998), homer1 (Bottai et al., 2002), serum-inducible kinase (SNK) (Pak and Sheng, 2003) and the activity regulated cytoskeletal-associated protein (Arc) (Lyford et al., 1995; Steward et al., 1998) which was simultaneously discovered and described as activity-regulated gene 3.1 (Link et al., 1995).

Later, it became possible to genetically encode the expression of fluorescent markers which were driven by promoters of IEGs. This offered the possibility to correlate a neuronal population which was active during a specific task to its re-activation during recall and to estimate the functional role of this ensemble (Reijmers et al., 2007). Other studies examined neuronal representations in the hippocampus (Deng et al., 2013; Tayler et al., 2013), sensory cortex (Xie et al., 2014) and prefrontal cortex (Zelikowsky et al., 2014). Most of these studies used the Tet-ON/OFF system to define the time point of labeling of active neurons. Here the IEG promoter controls the expression of the tetracycline transactivator (tTA). The gene of interest (e.g. eGFP) however, is controlled by the tetracycline response element (TRE). The animal is fed with Doxycycline (Dox) that binds to the TRE and prevents tTA from binding to the TRE. Only in the absence of Dox, tTA can bind to the TRE and induce the expression of the reporter gene. For this purpose, the feeding is usually changed from Dox-ON to Dox-OFF for 24 hours during which the animal performs a specific task (e.g. FC) and the engram neurons become activated and tagged (**Fig. 1.5.1**). These studies had all in common that they were purely observational and missed the functional proof of the necessity of engram cells for memory. However, Han et al. showed that the overexpression of the cAMP response element-binding protein (CREB) in a subset of neurons in the lateral amygdala (LA) made these neurons more likely to become part of the engram (Han et al., 2007).
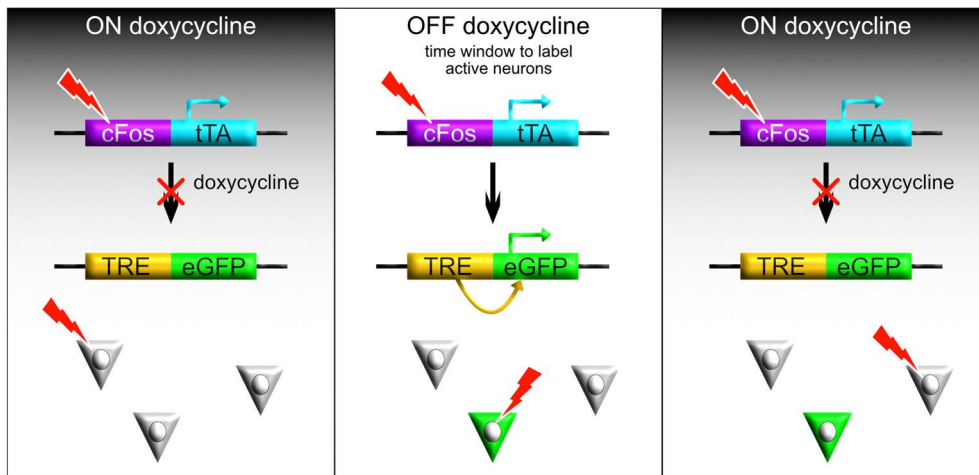
Fig. 1.5.1: The TetON/OFF system to label active neurons. While the animals are fed with doxycycline (Dox), the expression of the cFos dependent tTA does not affect the gene expression of the reporter gene due to blockage of the TRE site by Dox. If the animal is taken OFF Dox, TRE is not blocked by Dox anymore. Now, cFos expressing neurons will also transiently express the reporter gene. After the labeling, the animals are fed with Dox again, which prevents further labeling of other active neurons. Figure adapted from (Deng et al., 2013).

Later they showed that specifically ablating these engram neurons (Han et al., 2009) or inhibiting these neurons (Zhou et al., 2009), but not a random population, led to an interference of the memory. A caveat or advantage of the technique described above was the transient expression of the reporter only in the time window of neuronal activity. Guenthner et al. overcame this issue by permanently labelling active neurons, after their neuronal activity (Guenthner et al., 2013). For this, the promoter of cFos or Arc drives the expression of the Tamoxifen (TAM) dependent Cre-recombinase. Combing it with the expression of a Cre-dependent neuronal marker (e.g. tdTomato) leads to activity-dependent labeling of neurons only in the presence of TAM (**Fig. 1.5.2**).
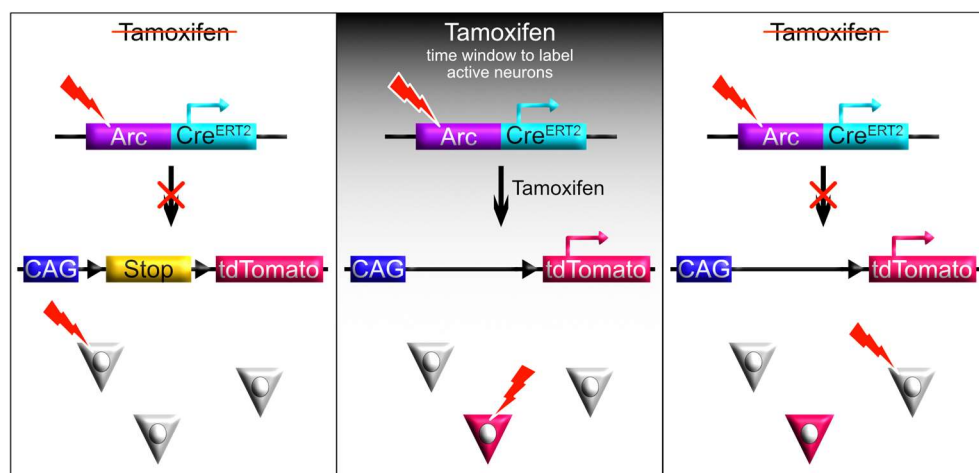
Fig. 1.5.2: Labeling of active neurons using the Arc-driven tamoxifen (TAM) dependent Cre-recombinase. Only neurons which are active in the presence of TAM will permanently express the reporter gene. Neurons active before or after the presence of TAM are not labeled.

This technique could be used to label active neurons in the DG and CA3 during fear conditioning. Subsequent silencing of the engram using optogenetics resulted in an impairment during memory recall (Denny et al., 2014). Another study using the Tet-ON/OFF system could demonstrate the same finding silencing engram neurons in the CA1 (Tanaka et al., 2014). Further proof of the engram was achieved by gain-of-function studies. Here DG granule cells which were active during a contextual fear conditioning were labeled with ChR2. Exposing the mouse to a neutral context and optogenetically activating the engram cells led to freezing to the neutral context as if the animal would remember to be in the conditioned context. Importantly labeling of a random subset of granule cells and activating them during a neutral context did not lead to increased freezing (Liu et al., 2012; Ramirez et al., 2013; Liu et al., 2014).

In summary, it has been possible to label neurons that were active during a specific time and context for a long time. If a neuron was active during a specific time and context it is reasonable acceptance to call it part of the neuronal representation. However, only recently, by manipulating this population, it has been proven that these active cells also participate in the engram. The definition of an engram neuron, therefore, implies its functional involvement in the representation of the memory.

1.6 Optogenetics

Optogenetics has become a powerful technology that is still in the process of development and innovation. The word optogenetics comes from the Greek optos for visible and genetics for genetically encoded. Optogenetic tools are extrinsic proteins expressed in a target organism like cells or animals that can be manipulated using specific wavelengths of light. The most prominent optogenetic tools are Channelrhodopsins (ChR) and its derivatives. ChR is a subfamily of the rhodpisins that works as a light-activated cation channel (Nagel et al., 2002). This family was first discovered in the green algae *Chlamydomonas reinhardtii*, where it functions as photoreceptors to control phototaxis (Sineshchekov et al., 2002). Channelrhodopsin consists of seven transmembrane helices and contains one photoreactive molecule, the all-trans-retinal. The characteristic of this retinal is that it is covalently bound to the protein and that it is light-isomerizable (Nagel et al., 2003). Channelrhodopsin-2 (ChR2), one of the "wild-type" ChR, has its peak absorbance of the all-

trans retinal at 480 nm (Bamann et al., 2008). Illuminating the retinal with blue light (480 nm) leads to a conformational change to 13-cis-retinal. This conformational change induces a change in the shape of the 7 transmembrane helices, which finally leads to the opening of the channel (Nagel et al., 2003). Within milliseconds the 13-cis-retinal relaxes back to the all-trans conformation and thereby closes the channel (**Fig. 1.6.1**).
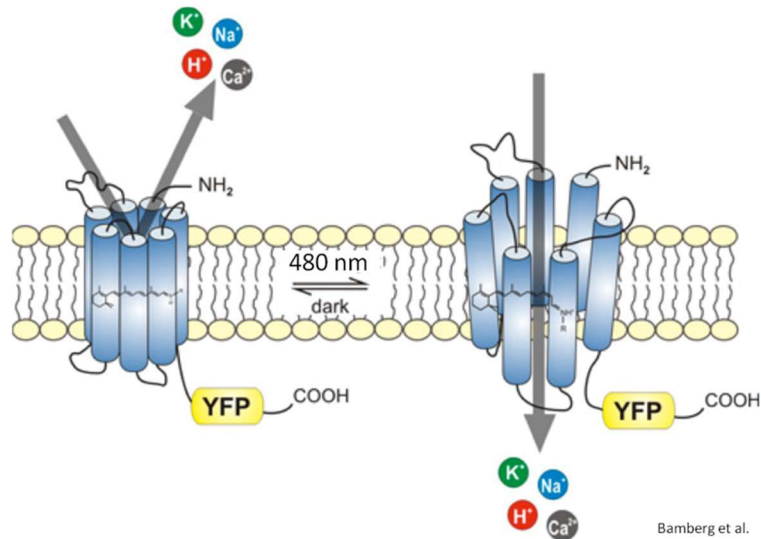
Fig. 1.6.1: Light induced gating mechanism of ChR2. ChR2 contains a covalently bound all-trans-retinal. In this state, the channel is impermeable to any ion. Illuminating the retinal with 480 nm light induces a conformational change to 13-cis-retinal which causes an opening of the channel. It becomes permeable to cations. After a few milliseconds, the retinal relaxes back to the all-trans state, and the channel closes again. Illustration was taken from Ernst Bamberg MPI Biophysics.

Nagel et al. were the first to express ChR2 in oocytes of *X. laevis* and mammalian cells and showed that activation of ChR2 using blue light and the presence of retinal led to induced photo-currents (Nagel et al., 2003). Later Boyden et al. showed that activating ChR2 in cultured neurons induces neuronal spiking (Boyden et al., 2005; Zhang et al., 2006). Nagel and Gottschalk were the first to apply this system *in vivo* in *C. elegans*. They showed that ChR2 could be expressed in muscle cells, and activation led to light-induced contraction of the muscle fibers (Nagel et al., 2005). Nowadays, ChR2 and its further developed variants are applied to multiple different species and in specific parts of the nervous system to influence processes underlying behavior. It has become the most powerful tool for high temporal and spatial resolution manipulation of cellular microcircuits.

CHAPTER 2 – AIM AND MOTIVATION

Over decades of research in neuroscience, experts aimed to link synaptic plasticity, neuronal activity, and their relevance for learning and memory. In fact, it is difficult to treat each of them separately as they all seem to be interconnected. Exposing an animal to a learning paradigm for sure activates neurons responding to this exposure. This neuronal activity, in turn, influences synaptic plasticity by a mechanism like LTP (Bliss and Gardner-Medwin, 1973) or by the formation of new and elimination of old synaptic connections. The induction of synaptic plasticity might then again influence future learning and memory formation. Essentially, the three factors that modulate the brain the most are in a circular relationship with each other and cannot be treated separately.

Artificial induction of neuronal activity by electrical stimulation of hippocampal organotypic slice cultures had been shown to induce robust long-term-potentiation of synapses (Malenka, 1991). This technique, however, was not able to distinguish between individual synapses and thereby could only report a potentiation on the population level but had no information about single synapses. A more recent study took advantage of the development of 2-photon microscopy and the existence of a shielded variant of glutamate. The authors bath-applied this caged glutamate to neurons, and by uncaging of the glutamate in positions close to dendritic shafts using 2-photon laser pulses, they could induce *de novo* spine formation (Kwon and Sabatini, 2011). Both studies clearly indicated that neuronal activity influences synaptic (structural) plasticity. Furthermore, environmental variability and novelty had been shown to influence synaptic plasticity (Juraska et al., 1989; Moser et al., 1994; Rampon et al., 2000; Jung and Herms, 2014) and that this change in synaptic plasticity was beneficial for learning and memory (Kempermann et al., 1997; Bouet et al., 2011). Even though this correlative finding was from different experiments, it was striking that the brain regions changed by the environmental enrichment and involved in the improved learning were identical. In addition, two independent publications showed evidence of learning-induced synaptic remodeling and specific stabilization of spines that were born during the learning task and believed to be essential for the preservation of memory (Xu et al., 2009;

Yang et al., 2009). However, until today, there was no study combining evidence of neuronal activity, synaptic plasticity, and learning.

This thesis aims to try to reveal how neuronal activity which is induced by exposure to an enriched environment influences structural synaptic plasticity in the dorsal CA1 and how the change in synaptic plasticity specifically in activated neurons impacts on hippocampus-dependent learning and memory. I hypothesize that neuronal activity leads to a modification of structural synaptic plasticity exclusively in active neurons after the neuronal activity and that this change in connectivity would finally positively influence hippocampus-dependent learning and memory recall.

CHAPTER 3 – MATERIALS

This list only contains an extract of the most relevant material used for this study.

3.1 Buffers and Media

Table 3.1: Used buffer with composition

BUFFER/MEDIA	COMPOSITION
PHOSPHATE-BUFFERED SALINE (PBS) (10X)	1,37 M NaCl 27 mM KCl 43 mM $Na_2HPO_4*7H_2O$ 14 mM KH_2PO4 in 1l ddH_2O Adjust pH to 7,4 with 1 N NaOH

3.2 Equipment and Consumables

3.2.1 General

Table 3.2.1: General materials and consumables used during this study.

Description	Type	Manufacturer
Agarose	Utra pure^{TM}	Invitrogen
Corn oil	C8267	Sigma
Cover slips	50 mm #1	VWR
Microwave	NN-GD468M	Panasonic
Mounting slide	Superfrost Plus	Thermo Scientific
Multi-well dishes dishes	Nuncla^{TM} Delta Surface	Thermo Scientific
Normal Goat Serum	GTX73249	GeneTex
Objective immersion oil	Imersol^{TM} 518F	Zeiss
Paraformaldehyde	UN2213	Roth
Scale	40SM-200A	Precisa
Shaker	Polymax 1040	Heidolph
Sucrose	S0389	Sigma
Triton X-100	T8787	Sigma
Vortexer	VF2	Janke & Kunkel

3.2.2 Imaging Cannula

Table 3.2.2: Materials and consumables used for the preparation of the imaging cannula.

Description	Type	Manufacturer
Dental drill	Presto II	NSK-Nakanishi Germany
Diamantbohrer FG	Zylinder flach, fein, grob	MF Dental
MICRO compound table KT 70		Proxxon GmbH
MICROMOT drill stand MB 200		Proxxon GmbH
Microscope Cover glass	4 mm round	Engelbrecht Medizintechnik
Präzisions-Nadelfeile	140 mm	Hoffmann Group
Professional drill/grinder IBS/E		Proxxon GmbH
Stainless steel tube	Ø 3 x 0,25mm (Inner Ø 2,5mm),L=500mm	Sawade
UV Curing LED System	365 nm	Thorlabs
UV-Curing Optical Adhesives	NOA81	Thorlabs

3.2.3 Surgery

Table 3.2.3: Materials and consumables used for the different surgeries conducted for this thesis.

Description	Type	Manufacturer
3-D-Gelenkarm		Hoffmann Group
Absorption Triangles	unmounted	Fine Science Tools
Adjustable Precision Applicator Brushes	S379	Parkell
Aufnahme 2SM		Hoffmann Group
Bead Sterilizer		Fine Science Tools
Blunt needles	Different diameters	Dentina
Burrs for Micro Drill	0.5-0.9 mm	Fine Science Tools
C&B Metabond clear powder L		Parkell
C&B Metabond Quick Base B		Parkell
C&B Metabond Universal Catalyst C		Parkell
Dumont Forceps	#3	Fine Science Tools
Fiber optic light source	KL 1500 LCD	Schott
Fine Scissors - ToughCut		Fine Science Tools
Head plates	30x10mm; 8mm diameter hole, titanium	Custom made

Heating blanket	CMA 450 Temperature Controller	Hugo Sachs Elektronik
Hydrofilm transparent roll		Hartmann
Isoflurane Vaporizer	Funnel-Fill	Harvard Apparatus
Kallocryl		Speiko
Kallocryl A/C		Speiko
Lab Active Scavenger		Gropper Medizintechnik
MicroMotor mit Handstück	MM11	DentaTec
Stainless Steel Self-Tapping Bone Screws	Fine Science Tools	Fine Science Tools
Stereotaxic apparatus		Kopf
Trephine	3 mm	MW Dental

3.3 Microscopes

Bruker 2-Photon

Microscope type	Ultima IV
Company	Bruker
Objectives	Plan N 4x/0.10 ∞/-/FN22
	Plan N 10x/0.25 ∞/-/FN22
	LMPlan FLN 20x/0.40 ∞/-/FN26.5
	XLPlan N 25x/1.00 SVMP ∞/0-0.23/FN18
Light sources	Spectraphysics InSight DS+ Dual, X-Cite 120Q, Halogen
Laser lines [nm]	1040, tunable 680 - 1300
Detectors	2 Alkali PMTs, 2 Arsenide phosphide (GaAsP) PMTs
Filter sets	460, 525, 605, 690
Software	PrairieView 5.4.64.116beta

Zeiss LSM 800

Microscope type	Upright confocal microscope with spectral detector array
Company	Zeiss
Objectives	Plan-Apochromat 10x/0.45
	Plan-Apochromat 40x/1.4 Oil DIC
	αPlan-Apochromat 63x/1.46 Oil TIRF
Light sources	Ti:Sapphire laser, HXP 120 V Halogen

Laser lines [nm]   405, 488, 561, 647

Detectors   2 PMT, Spectral detector (GaAsP)

Filter sets   DAPI, Alexa 488, Alexa 594

Contrast methods   DIC

Software   Zen 2.3

Dissecting scope

Microscope type   Compact stereo Microscope

Company   Zeiss

Objectives   5:1 Zoom (0.8-4x)

Light sources   white LED

3.4 Antibodies

Table 3.4: Used antibodies including species and manufacturer.

Antigen/target	Species	Manufacturer
Anti cFos	rabbit	Abcam AB190289
Anti rabbit Alexa 488	goat	Invitrogen A11034
Anti rabbit Alexa 594	goat	Invitrogen A11012

3.5 Mouse Strains

Table 3.5: List of the mouse strains used in this work.

Strain	Characteristic
C57BL/6N	wild-type
Thy1-GFP line M	Enhanced green fluorescent protein (eGFP) expression under the control of a modified Thy1 promoter region (containing the sequences required for neuronal expression but lacking the sequences required for expression in non-neural cells). EGFP expression in a sparse subset of neurons within specific populations; providing a bright, vital Golgi-like stain (Feng G et al., 2000). (Jax/strain/007788)
Gt(ROSA)26Sor$^{tm9(CAG-tdTomato)Hze}$ (Ai9)	The CAG promoter-driven reporter construct is inserted into the Gt(ROSA)26Sor locus containing a loxP-flanked STOP cassette to prevent transcription of the red fluorescent protein variant tdTomato. When bred to mice that express Cre recombinase, the resulting offspring will have the STOP

	cassette deleted in the Cre-expressing tissue(s) - resulting in robust tdTomato fluorescence. These Ai9 mice are useful as a Cre reporter strain - expressing tdTomato fluorescence following Cre-mediated recombination (Madisen et al., 2010). (Jax/strain/007909)
Fos^{tm1.1(cre/ERT2)Luo} (Fos^{CreER})	The *Fos^{CreER}* knock-in/knockout allele was designed to both abolish *Fos* function and express the CreER^{T2} fusion protein from the endogenous *Fos* promoter/enhancer elements. CreERT2 protein activity is inducible; observed following Tamoxifen administration. When *Fos^{CreER}* mice are bred with mice containing *loxP*-flanked sequences, tamoxifen-inducible Cre-mediated recombination will result in deletion of floxed sequences in the *Fos*-expressing cells. Cre recombinase activity is observed in a pattern consistent with endogenous *Fos* expression; active populations of neurons, endothelial cells, oligodendrocytes, and very rarely in other types of glial cells (e.g. astrocytes). Minimal CreERT2 activity in the brain is reported prior to Tamoxifen administration (Guenthner et al., 2013). (Jax/strain/021882)
Arc^{tm1.1(cre/ERT2)Luo} (Arc^{CreER})	The *Arc^{CreER}* knock-in/knockout allele was designed to both abolish activity regulated cytoskeletal-associated protein (*Arc*) gene function and express CreER^{T2} fusion protein from the endogenous *Arc* promoter/enhancer elements. CreER^{T2} protein activity is inducible; observed following tamoxifen administration. When *Arc^{CreER}* mice are bred with mice containing *loxP*-flanked sequences, Tamoxifen-inducible Cre-mediated recombination will result in deletion of floxed sequences in the *Arc*-expressing cells. Cre recombinase activity is observed in active populations of neurons in the brain in a pattern consistent with endogenous *Arc* expression. Some CreER^{T2} activity is observed in the brain prior to tamoxifen exposure (sub-populations of neurons in the brain, including in layer 6 neocortical cells and dentate gyrus granule cells, as well as sparser populations of other cell types) (Guenthner et al., 2013). (Jax/strain/021881)
Neurod6^{tm2(cre/ERT2)Kan} (NEX^{CreER})	The Nex^{CreER} knock-in/knockout allele was designed to express the CreER^{T2} fusion protein from the endogenous Neurod6 (Nex) promoter/enhancer elements. CreERT2 fusion protein activity is inducible; observed following tamoxifen administration. When Nex^{CreER} mice are bred with mice containing *loxP*-flanked sequences, tamoxifen-inducible Cre-mediated recombination will result in deletion of floxed sequences in the Nex-expressing cells. Cre recombinase activity is observed in a dosage dependency; low tamoxifen concentration resulting in sparse and high tamoxifen concentration in dense recombinase activity. Minimal CreERT2 activity in the brain is reported prior to tamoxifen administration (Agarwal et al., 2012).

21

Gt(ROSA)26Sor^{tm27.1(CAG-COP4*H134R/tdTomato)Hze} (Ai27D)	A *loxP*-flanked STOP cassette prevents transcription of the downstream hChR2(H134R)-tdTomato fusion gene. Because this CAG promoter driven reporter construct was targeted for insertion into the *Gt(ROSA)26Sor* locus, hChR2(H134R)-tdTomato expression is determined by which tissue(s) express Cre recombinase. When bred to mice that express Cre recombinase, the resulting offspring will have the STOP cassette deleted in the Cre-expressing tissues; resulting in expression of the hChR2(H134R)-tdTomato fusion protein (Madisen et al., 2012).

3.6 Viruses

Table 3.6: Viruses used for this thesis

Description	Manufacturer
AAV5-hSyn-hChR2(H134R)-eYFP-WPREpA	Addgene
AAV5-EF1a-DIO-hChR2(H134R)-mCherry	In House

3.7 Drugs

Table 3.7: Drugs administered during this study.

Description	Type	Manufacturer
Isoflurane for anesthesia	Isoflurane CP, Flasche 250 ml	Henry Schein VETGmbH
Lidocaine, local anesthetic	Xylocaine Pumpspray	AstraZeneca GmbH
Meloxicam	Metacam 0,5% Injektionslsg	Henry Schein VETGmbH
Ophthalmic ointment	Bepanthen Augen- und Nasensalbe	Bayer AG
Tamoxifen	T5648-5G	Sigma
Vetalgin	Vetalgin 500 mg/ml	MSD Tiergesundheit

CHAPTER 4 – METHODS

4.1 Mouse Holding

All animal procedures conformed to the guidelines of the Max Planck Society and the Animal authority, Regierung Oberbayern (Regierung von Oberbayern – Veterinärwesen). All animal procedure reported were in line with the Tierversuchslizenz - ROB-55.2Vet-2532.Vet_02-16-48. Mice were held on a 12 hour light and 12 hour dark cycle. Experiments were conducted during the 12 hour light period. Standard housing was provided by Techniplast® GM500 for mice green line IVC. A maximum of five mice was housed per cage. After weaning males and females were housed separately and only co-housed for breading purposes. Male mice were only housed with their littermates, while female mice were also mixed. Mice had an area of 501 cm^2, wood chips beading and wood wool as nesting material. Additionally, mice had a wooden tunnel as enrichment. However, after the implantation of the imaging cannula, the tunnel was removed because the head plate of the mice did not fit into the tunnel.

4.2 The Enriched Environment

Rodents that were exposed to an enriched environment (EE) showed changes in their structural synaptic plasticity compared to standard housed animals (Juraska et al., 1989; Moser et al., 1994; Rampon et al., 2000; Jung and Herms, 2014). The main idea of this project was to use the EE to induce structural synaptic plasticity in the dorsal hippocampus of mice. For this, I developed a large and diverse environment that aimed for activating as many sensory inputs as possible at a time. I took two large Type IV rat-cages of 37 cm x 60 cm and connected them by a 20 cm wide x 15 cm long acrylic tunnel resulting in 4440 cm^2. The left cage contained two floors. The ground floor was filled with a thick layer of bedding material giving mice enough depth to dig. It included a small tunnel, a wooden climbing stick, a wooden shelter, a running wheel, a seesaw, cotton pads, hair curler, and bigger

wooden blocks. The upper floor was connected by a wooden ladder to the ground floor and consisted of a wooden board with two holes. It contained a climbing rope which allowed mice to reach the lid grit to continue climbing on the grid (**Fig. 4.2.1B**). The connecting tunnel was filled with hair curlers and wooden toys containing bells. The right cage was also filled with a thick layer of bedding containing additionally a long tube with 4 entries, nesting material, a running wheel, a wooden climbing stick cotton pads, hair curler, a toy to hide food insight which mice could open by poking the lids to the side and a hammock (**Fig. 4.2.1A**). Water was available *ad libitum*. However, food was hidden in the bedding material, in the hiding toy and spread around the area to encourage mice to explore the whole environment extensively. Mice were always housed together with their littermates to increase enrichment; however, if male mice did not have littermates, they needed to be singly housed during the EE.
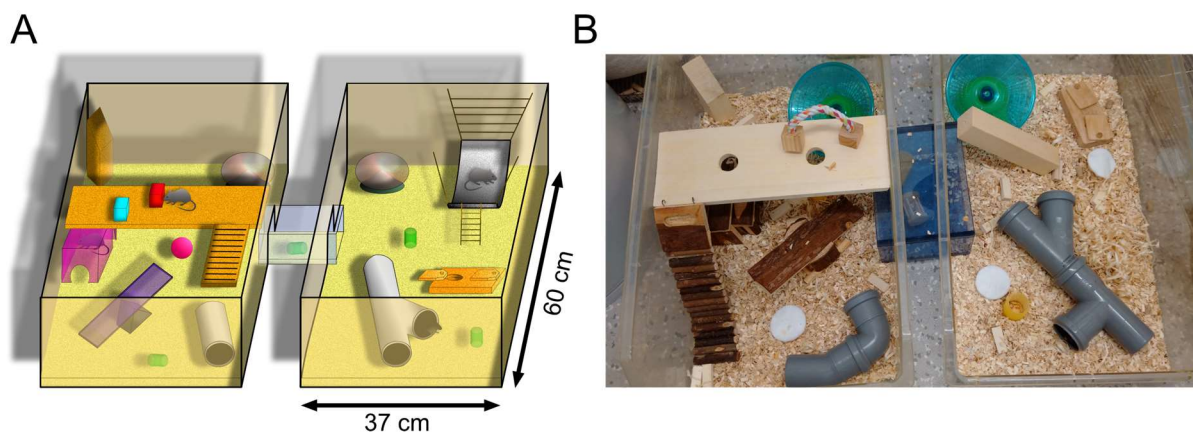

Fig. 4.2.1: The Enriched Environment. (**A**) Schematic of the EE as it was planned. (**B**) EE as it was used for the 16h exposure to label active neurons during the *in vivo* imaging experiment. The environment consisted of two cages (37x60 cm) connected by a tunnel (20x15 cm). It contained two floors, tunnels, climbing sticks, shelter, running wheels, a seesaw, cotton pads, hair curler and wooden blocks, a climbing rope, a food hiding toy, and a hammock. Food was hidden while water was presented *ad libitum*.

4.3 Preparation of the Imaging Cannula

For the preparation of the imaging cannula I cut a 1.6 mm long piece from a 3 mm diameter stainless steel tubing. The walls of the tube were 0.25 mm thick resulting in an inner diameter of 2.5 mm. After having cut the pipe to the correct length, I started with filing rough irregularities using a cylindrical rotating file from a dental drill. I continued filing the edges using a fine file. I put the ring into acetone to clean it from any fatty residuals. Then I dipped one edge of the metal ring into UV-optical curing adhesive and placed the 3 mm ring onto a 4 mm diameter glass coverslip (0.13 mm thick) that I also took from acetone. I glued

the glass and the metal together by shining 365 nm light for one minute and made sure to illuminate the glue from different angles. The next day I filed away the excessive glass using the cylindrical rotating file from the dental drill again (**Fig 4.3.1**).
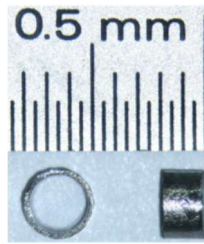

Fig. 4.3.1: The Imaging cannula ready to be implanted over the dorsal hippocampus. The cannula consisted of a metal ring which was 3 mm in diameter and had 0.25 mm walls, which led to an inner diameter and field of view onto the dCA1 of 2.5 mm. The ring was 1.6 mm long to cover the distance from the hippocampus to the top of the skull. A glass coverslip (0.13 mm thick) was glued to the metal ring using UV-optical adhesive. (Image taken from (Ulivi A. et al., 2019))

4.4 Craniotomy and Implantation of an Imaging Cannula over the dCA1

To get visual excess to the dorsal hippocampus I needed to implant an imaging cannula that would bridge the distance between hippocampus and skull and would also seal the brain from the external environment. The procedure for the implantation was as follows: I prepared the stereotactic frame, heated up the heating blanket to 37°C, made sure all instruments were sterile by heating them up to 250°C using a bead sterilizer and covering all surrounding surface with a sterile surgical coverage. I then put the mouse into the anesthesia induction chamber and flooded it with 2.5% Isoflurane in pure O_2. When the animal was in anesthesia, I transferred it to the stereotactic frame covering the nose with the nose cone and provided 1.5% Isoflurane in pure O_2 for the rest of the surgery directly to the mouse' nose. Next, I covered the eyes with eye-ointment. Before starting with the actual operation, I checked whether the anesthesia was deep enough using the toe pinch reflex test. I then administered analgesia as Metacam and Vetalgin according to the animal license referred to above. After I removed the hair from the scalp, I disinfected the skin using a cotton swap and removed the scalp by cutting a triangle shape piece from one ear to the other and frontal until the eyes. After that, I positioned the ear bars to stabilize the skull. Further, I added a drop of Lidocaine, another analgesic, to the skull and removed the periosteum and drilled a small, 0.5 mm diameter hole into the skull of the left hemisphere. Using a screwdriver, I inserted a 0.6 diameter screw into the hole, fixing it by application of

Metabond® using precision applicators. I also covered the whole skull, including the edges of skin with Metabond®. Thereafter, I performed the craniotomy using a 3 mm diameter trephine drill. I was careful not to drill to fast and to deep not to damage the underlying tissue and leaving the dura intact. Next, I carefully removed the dura using Dumont forceps. I then turned on the vacuum in order to slowly ablate the cortical matter using a blunt needle that I lowered into the brain until I reached the *corpus callosum*. Changing the blunt needle size to a smaller gauge enabled me to carefully peel off the fibers until I reached the third layer of the *alveus*, leaving this layer and the hippocampus intact. During the suction procedure and after I arrived at the last layer of the *alveus,* I extensively rinsed the tissue with sterile saline to facilitate the ablation and to remove residual blood. Furthermore, I dipped the imaging cannula into sterile saline before it was placed into the craniotomy to avoid any formation of air bubbles between the brain tissue and the glass bottom of the cannula. I also made sure to put a little bit of pressure onto the tissue to stabilize the preparation. I dried the skull and fixed and sealed the metal ring of the cannula to the skull using Methabond®. Afterward, using a stereotactic arm, I positioned the head plate over the craniotomy and fixed it using dental cement. I made sure that the dental adhesive ran everywhere on the skull to provide as much surface as possible between the head plate, skull, and screw to be as stable as possible. After the cement was hard, I added a thin film over the imaging cannula to avoid any trapping of dirt into the cannula. Finally, I transferred the mice back to their home cage and covered them with nesting material to provide a little bit of heating. For the following two days, mice received one administration of Metacam per day. Additionally, the weight and the surgical wound were checked for potential inflammation.

4.5 Two-Photon *in vivo* Imaging of Dendritic Spines

We started with turning on the PC, laser, software, microscope hardware, heated up the heating blanket to 37°C, turning the fluorescent lamp on, made sure all instruments and objectives were in place. I then put the mouse into the anesthesia induction chamber and flooded it with 2.5% Isoflurane in pure O_2. When the animal was under anesthesia, I quickly removed the film that was covering the imaging cannula by holding onto the head plate and pealing of the film using Dumont forceps. Then, I transferred the

mouse to the heating blanket and to the head plate holder. After the mouse was clipped into the holder, I covered the nose with the nose cone and provided 1.5% Isoflurane in pure O_2 for the rest of the imaging directly to the mouse' nose. Next, I covered the eyes with eye-ointment. Before starting with the actual imaging, I cleaned the imaging cannula from potential residual dirt by filling the cannula with ddH_2O and directly sucking it away using a vacuum. This was repeated 2 to 3 times. I made sure to completely dry the cannula before I put the mouse under the microscope to avoid any trapped water that would hinder the first steps of imaging using air-objectives. I started with using fluorescent light and a 4x objective to align the imaging cannula to the light path after the objective. This was achieved by switching between the focal planes of the top and the bottom of the cannula. If the round cannula was aligned, the two circles of the two focal planes would perfectly overlap. If this was not the case, I had two separate axes to rotate and to tilt the animal and the cannula until I achieved the alignment. I only continued after the cannula was aligned.

After this, I switched to a 10x objective to find and to relocate my ROIs. I continued with a 20x objective to further narrowing down the ROI. Finally, I switched to the last objective, which was a 25x, 1.0 NA water immersion objective. To be able to use it, I again filled the cannula with ddH_2O to build up a water column to the objective. I made sure that the whole front aperture of the objective was covered by water. Using the fluorescent light, I again relocated to the ROI before I switched the microscope to laser-scanning mode. I closed the curtains to avoid damaging the photon multiplier tubes (PMTs), turned off the room lights, and started 2-photon excitation. I continued by focusing onto my dendritic segment of interest by imaging using galvanometric mirror scanning, increasing the digital zoom from 1x to 2x to 5x and then to 10x (**Fig 4.5.1**). Finally, I acquired a z-stack to capture the whole extent of the dendrite of interest. For this, I used a resonant scanner that was able to scan 30 frames per second (30 Hz) to acquire each z-plane four times before the next plane was imaged. The reason why I took 4 individual images was to perform offline averaging due to the occurrence of motion artifacts caused by breathing and/or heartbeat. The four z-planes were offline averaged to overcome these artifacts.
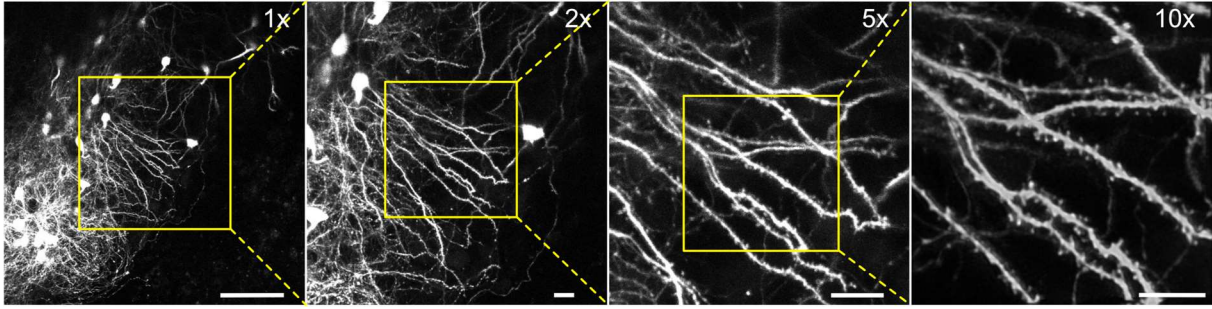
Fig. 4.5.1: Two-Photon *in vivo* imaging of dendritic spines and relocation of a dendritic segment of interest. Images were acquired using 25x 1.0 NA water immersion objective. After the imaging mode was switched to LSM, I used 1x, 2x, 5x, and 10x digital zoom to relocate the ROI. Scale bars: 1x = 100 μm, 2x = 20 μm, 5x = 20 μm, 10x = 10 μm

After all ROIs were imaged, I stopped the anesthesia of the mouse, sucked away the water and added a fresh thin film over the imaging cannula to avoid any trapping of dirt into the cannula. Finally, I transferred the mouse back to their home cage and covered them with nesting material to provide a little bit of heating.

4.6 Image Post-Processing

Using a resonant scanner which was able to scan at 30 Hz, I acquired 4 images per z-plan before moving down to the next plane. I did this to perform offline averaging after all single images were post-processed. My close colleague Ghabiba Weston completely automated the post-processing procedure by coding an interface that communicated with different programs and automatically loaded and saved the images.

After I acquired a z-stack, the result was four similar z-stacks of the same field of view. Each of them was aligned within each stack using the open source software Fiji/ImageJ® and the plugin 'StackReg'. After that, they were loaded into the commercial software AutoquantX3® for 3D blind deconvolution. The four deconvolved z-stacks were then aligned to each other using Fiji/ImageJ® before they were finally averaged to one single z-stack (**Fig.4.6.1**).
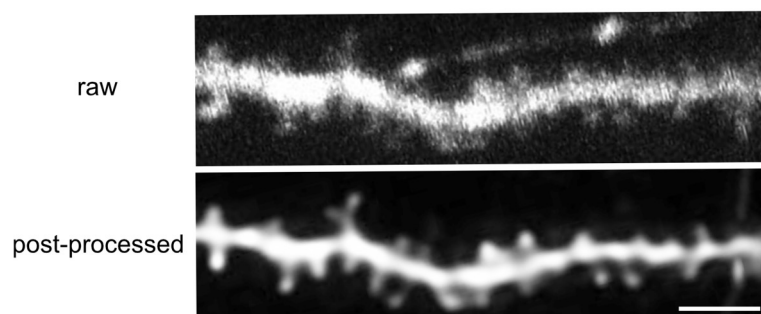
Fig. 4.6.1: Raw and post-processed example dendrite. The top image shows a MIP of one raw image stack that was acquired using the resonant scanner. I acquired four z-stacks per region. Each was aligned within the stack and then deconvolved using AutoquantX3®. Afterward, the four individual image stacks were aligned to each other and finally averaged. This resulted in the lower image. All spines were distinguishable from the shaft and from the background fluorescence. Scale bar, 5 μm.

4.7 Quantification of Dendritic Spines

After I acquired and post-processed all *in vivo* imaging data, I could count the dendritic spines and investigate the dynamics and structural synaptic plasticity of these spines. To do this, I used a custom-written graphical-user-interface (GUI) for MATLAB®, which was called ICount (all credits to Ju Lu – University of California). To start the process, I loaded the 8 image stacks acquired on 8 time points into the program. I identified a suitable dendrite and started tracing it in each of the 8 time points by creating a node-connected line in the center of the dendrite. Tracing and counting were only done in the center image of ICount (**Fig.4.7.1**). By clicking the button time up/down, one could work on the next or previous time point. Once the chosen dendrite was tracked in all 8 time points, I could start to count the spines. Regularly, I counted in the 'Auto Fwd' mode, which let the image to jump automatically to the next time point after having marked the identified spine. I usually started with counting 5 prominent spines that were present in all 8 time points. The reason for this was that these 5 static points could be used as anchor points for a rigid body transformation and an alignment of all 8 time points to a selected reference image. If more stable spines were present in all 8 time points, the better the alignment of the 8 images. When I counted the 8 time points, I were blinded to the actual time point during the experiment to which the image referred to. This was necessary not to be biased while counting. On the other hand, the 8 images were looped, which made it impossible to tell the starting and ending time point. I then counted all spines that were ever present on this dendrite in all of the 8 images. Once I finished counting a dendrite, I re-traced it. I took one spine as the beginning of the dendritic segment as the starting point and traced it until the last spine. This was important to quantify the density of spines per dendritic segment. If a spine was present in a previous time point, then disappeared but reappeared in the next time point I counted it as the same spine. This was helpful to assess recurrent synaptic positions (as discussed in 5.7 and 6.6), however for the analysis of the gain and loss of spines each disappearance was scored as one lost spine, and each appearance was scored as a

gained new spine, also featuring a new spine ID. After having counted all spines on one dendrite and having re-traced it, I continued tracing and counting the dendrites in the image until there were no dendrites left to count. This usually resulted in 1-7 dendrites traced and counted per region.
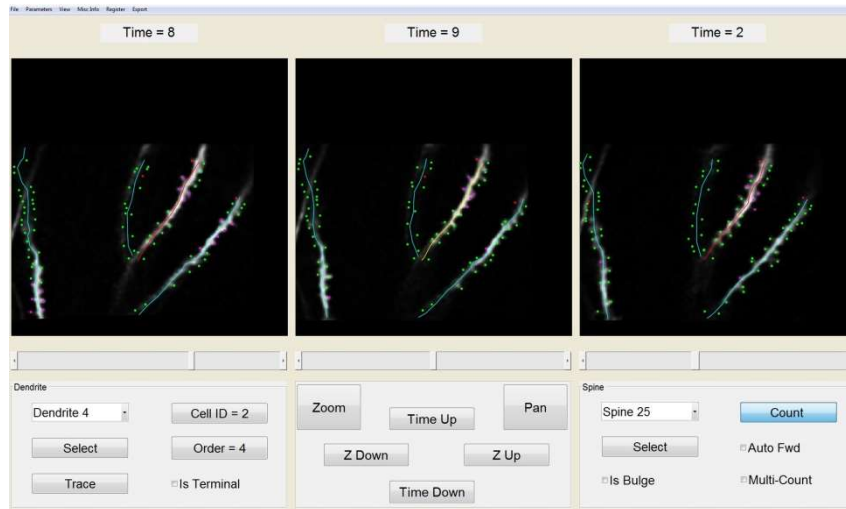

Fig. 4.7.1: Screenshot of the ICount GUI. Counting was only done on the center image while the images left and right served as a help for orientation. Time points were blinded and looped. First, a dendrite was traced, using the 'trace' button, then spines were counted using the 'Auto Fwd' mode.

4.8 Quantification of the size of spines

For quantifying the size of spines, I used the open source software Fiji/ImageJ®. I loaded z-tacks of the region of interest into the program. By scrolling through the z-stack and relocated the spine that I wanted to measure. Which spine to quantify, whether persistent or newborn, dependent on the question I wanted to answer. I focused on the brightest representative plane of the spine and manually drew a region of interest (ROI) around the spine. The shape of that ROI was strongly dependent on the class of spine that I quantified, circular shaped for a mushroom-like spine, rectangular shaped for a thin spine and half circle shaped for a stubby spine. Using the 'measure' tool in Fiji gave me the integrated density of fluorescence, which was a function of the intensity per pixel and the area of the ROI. Both the intensity and the size of the area were important indicators of the size of a spine (**Fig 4.8.1A-left**).
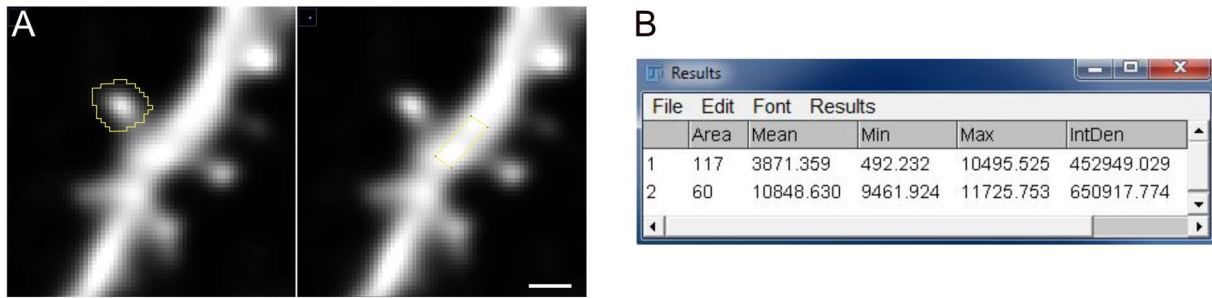
Fig. 4.8.1: Quantification of the size of spines. (**A**) Duplicate of a 2-photon fluorescent image of a dendritic segment to measure the integrated density of fluorescence of the spine and the shaft. The measurement of the shaft served as a normalization for the spine. This example illustrates a measurement of a mushroom-like spine. (**B**) Screenshot of the open source software Fiji/ImageJ®. It shows example measures of the area and the integrated density of fluorescence of the ROI of the spine (1) and shaft (2). After the normalization, the spine had a size of 0.69. Scale bar 1 μm.

Using a different amount of light intensities to image the dendritic segment through time often resulted in an apparent increase or decrease in spine size. However, this change in power was also reflected in the fluorescence intensity of the shaft. For this reason, I performed a second measurement of the integrated density of fluorescence of the shaft of the dendrite just below the spine that I previously measured. I always used a size of 60 pixels for the measurement to be consistent through time. This allowed me to normalize the fluorescence intensity and to counterbalance any effect of fluctuation of light intensity (**Fig 4.8.1A-right**). The example reported a size of 117 pixels for the prominent mushroom-like spine and an integrated density of fluorescence of 452949 a.u. while the shaft measurement had a size of 60 pixels but an integrated density of fluorescence of 650917 a.u. (**Fig 4.8.1B**). This resulted in a final spine size of 0.69.

4.9 Hippocampus-Dependent Trace Fear Conditioning

One learning paradigm that I conducted in combination with the 2-week *in vivo* 2-photon imaging experiment was the hippocampal-dependent trace fear conditioning paradigm. I chose this task for two reasons. First mice learn this task within one short session of approximately 10 minutes and the memory – depending on the specific protocol – can last over multiple weeks (Lugo et al., 2014). The second rational to choose this task was to have a paradigm that involves the hippocampus but also contains hippocampus-independent behavior that would not be related to hippocampal structural synaptic plasticity.

On the day of conditioning, I put mice into the conditioning chamber (19x19 cm) (red box). They had 3 minutes to habituate and to freely explore the chamber. After 3 minutes, I played a 20-second tone (9kH at 80dB), which was followed by a 15-second trace, followed by a 1-second electrical shock (0.75 mA). 105 Seconds later, this sequence was repeated until it reached 3 repetitions including 3 shocks (**Fig. 4.9.1**). To test for the hippocampal-dependent memory, 24 hours later, mice were exposed again to the same context for 3 minutes without presentation of the tone or the shock. 30 minutes later, they were placed in a new environment that they had never seen before (15 cm diameter) (green cylinder). Instead of having a rectangular form, it was round, had bedding material instead of the grid and smelled differently (acetic acid) compared to the conditioning chamber (ethanol). They had 3 minutes to explore the new environment. After, the same tone (9kH at 80dB) that they had learned to associate with the shock was played for 1 minute followed by 1 minute of recovery. This test was done to assess the amygdala and auditory cortex-dependent component of the learning paradigm (Lavond et al., 1993; Weinberger, 2004). During all time (condition and probe trials) mice were automatically tracked and freezing response, as a read-out for fear memory, was recorded and quantified by the commercial software ANY-maze® (**Fig.4.9.1**)
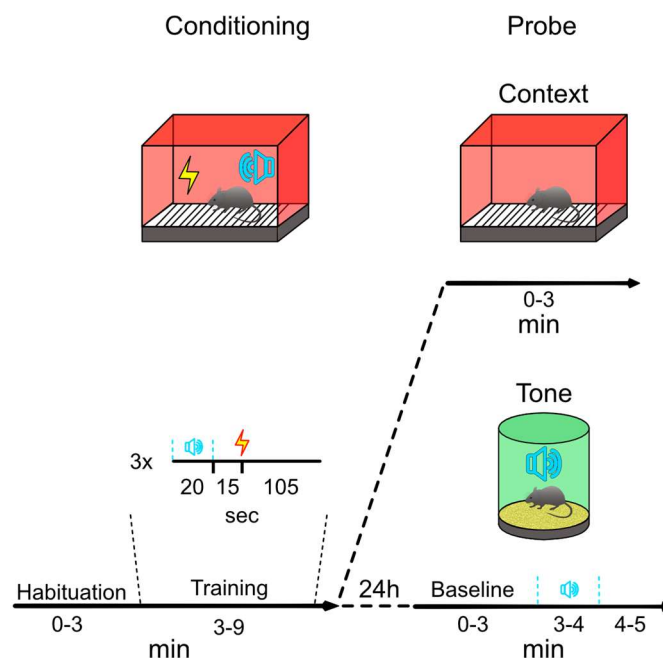

Fig. 4.9.1: Schematic of the hippocampal-dependent trace fear conditioning paradigm. I used that paradigm at the end of the *in vivo* imaging experiment of Arc- and NexCre[ERT2]; Thy1; Ai9 mice. In brief: On the first day mice experienced a trace of a tone, a wait, and shock for 3 times. The next day mice were exposed again to the conditioning chamber without sound or shock. 30 minutes later, they were put into a new environment where the conditioning tone was played for 1 minute.

4.10 Craniotomy for Virus Infusions

We prepared the stereotactic frame, heated up the heating blanket to 37°C, made sure all instruments were sterile by heating them up to 250°C using a bead sterilizer and covering all surrounding surface with a sterile surgical coverage. I then put the mouse into the anesthesia induction chamber and flooded it with 2.5% Isoflurane in pure O_2. When the animal was in anesthesia, I transferred it to the stereotactic frame covering the nose with the nose cone and provided 1.5% Isoflurane in pure O_2 for the rest of the surgery directly to the mouse' nose. Next, I covered the eyes with eye-ointment. Before starting with the actual operation, I checked whether the anesthesia was deep enough using the toe pinch reflex test. I then administered analgesia as Metacam and Vetalgin according to the animal license referred to above. After I removed the hair from the scalp, I disinfected the skin using a cotton swap and made a proximal 2 cm long incision from rostral to frontal into the scalp. After that, I positioned the ear bars to stabilize the skull, added a drop of Lidocaine, another analgesic, to the skull and removed the periosteum. For the infusion of a virus, the skull needed to be perpendicular to the infusion needle. For that reason, the mouse' head was leveled, so that bregma and lambda and also the lateral hemispheres were zeroed to bregma and thereby in one plane which was perpendicular to the infusion needle. After the leveling was achieved, I drilled a 0.5 mm hole at the desired coordinates. Since, here I only report infections of the dorsal hippocampus the coordinates were rostro-caudal: -2.3, lateral 1.5-1.6 and dorsal-ventral -1.3-1.4. Using the stereotactic frame, I then lowered the needle, into the brain and started the infusion of 300 nl at a speed of 100 nl per minute. After the whole volume was injected I lifted the infusion needle for 50 µm giving the liquid space to spread around the injection site. After 5 minutes, I removed the needle from the brain and injected the other hemisphere. After the injection, I closed the wound with a medical suture to increase the curing and to prevent infections. Finally, I transferred the mouse back to its home cage and covered it with nesting material to provide a little bit of heating. For the following two days, mice received one administration of Metacam per day. Additionally, the weight and the surgical wound were checked for potential inflammations.

4.11 Construction of Implantable Optic Fibers

This method was adapted from (Sparta et al., 2011). I first, stripped of the fiber coating from the 400 μm core fiber using a micro-stripper while keeping the fiber attached to the fiber spool. Using a Ruby DualScribe®, I cut 10 mm of the stripped optic fiber. Next, I inserted the ceramic ferrule with the convex side pointing down into a vice. Afterward, I inserted the optic fiber into the ferrule making sure that the ferrule and the fiber formed a flush end at the convex side of the ferrule leaving 2 mm of the fiber outside of the flat end of the ferrule. I added one drop of heat curable epoxy to the flat end of the ferrule and the optic fiber. Further, I cured the epoxy using a heat gun placed ~20 mm away from the epoxy. I used an epoxy that turned black/dark purple when fully cured. I then polished the convex end of the ferrule using pliers to hold the LC®/PC Connector Polishing Disc in place. To polish, I made ~20 rotations on each grade of polishing paper (four grades total). I polished in the order of 30, 6, 1, and 0.2 μm. Finally, I tested the implant by connecting it to the laser via the coupler cord. The polished end of the implant was inserted into the sleeve of the coupler and should have made direct contact with the opposing ferrule. The implant should maintain 70-100% of light output, measured at the tip of the fiber implant using a photometer. A bad implant had less than 70% of light output and a bad focal point near the tip of the fiber optic.

4.12 Permanent Implantation of an Optic Fiber over the dCA1 for Optogenetic Manipulation

We prepared the stereotactic frame, heated up the heating blanket to 37°C, made sure all instruments were sterile by heating them up to 250°C using a bead sterilizer and covering all surrounding surface with a sterile surgical coverage. I then put the mouse into the anesthesia induction chamber and flooded it with 2.5% Isoflurane in pure O_2. When the animal was in anesthesia, I transferred it to the stereotactic frame covering the nose with the nose cone and provided 1.5% Isoflurane in pure O_2 for the rest of the surgery directly to the mouse' nose. Next, I covered the eyes with eye-ointment. Before starting with the actual operation, I checked whether the anesthesia was deep enough using the toe pinch reflex test. I then administered analgesia as Metacam and Vetalgin according to the animal license referred to above. After I removed the hair from the scalp, I disinfected the skin using

a cotton swap and removed the scalp by cutting a triangle shape piece from one ear to the other and frontal until the eyes. After that, I positioned the ear bars to stabilize the skull, added a drop of Lidocaine, another analgesic, to the skull and removed the periosteum. For the implantation of an optic fiber, the skull needed to be perpendicular to the optic fiber that was held in the optic fiber holder. For that reason, the mouse' head was leveled, so that bregma and lambda and also the lateral hemispheres were zeroed to bregma and thereby in one plane which was perpendicular to the optic fiber. After the leveling was achieved, I drilled a small, 0.5 mm diameter hole into the skull of the left frontal hemisphere. I also drilled another small hole of the same diameter into the skull of the left rostral hemisphere. Using a screwdriver, I inserted two 0.6 diameter screws into the holes, fixing them by application of Metabond® using precision applicators. I also covered the whole skull, including the edges of skin with Metabond®. Next, I made a 0.8 mm hole at the desired coordinates. Since, here I only report implantation of optic fibers over the dorsal hippocampus the coordinates were rostro-caudal: -2.3, lateral 1.5-1.6 and dorsal-ventral -1.25-1.3 (**Fig. 4.12.1**). Using the stereotactic frame, I then lowered the optic fiber which was held by the optic fiber-holder down to 1.25 into the brain. The optic fiber was fixed in place using dental cement. I made sure that the dental adhesive ran everywhere on the skull to provide as much surface as possible between optic fiber, skull, and screws to be as stable as possible. After the cement was hard, I loosened the optic fiber older from the fiber. Finally, I transferred the mouse back to its home cage and covered it with nesting material to provide a little bit of heating. For the following two days, mice received one administration of Metacam per day. Additionally, the weight and the surgical wound was checked for potential inflammations.
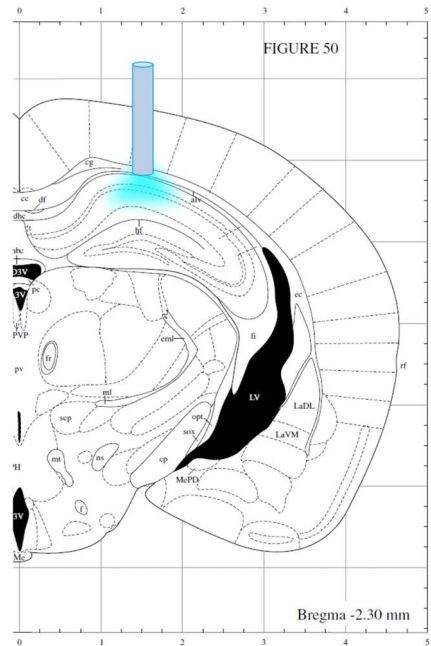
Fig. 4.12.1: Implantation of an optic fiber over the dorsal hippocampus. The coordination for implantation were: rostro-caudal: -2.3, lateral 1.5-1.6 and dorsal-ventral -1.25-1.3. The mouse was held under anesthesia in a stereotactic frame. The skull was opened at the desired position, and the optic fiber was lowered into the brain. It was fixed in place, and the surgical wound was covered with dental cement.

4.13 The Optogenetic Stimulation Set-up

In order to have an optogenetic stimulation set-up that would be highly flexible in the location of use, but also in the application itself, I assembled a fully functional dual color optogenetic stimulation set-up on a moveable cart. The cart contained a PC that served as a driver for the lasers, a Master-8®, a programmable stimulator that enabled to program any stimulation protocol and two different lasers. I equipped the cart with a 460 nm (blue) LuxX™ laser and a 594 nm (orange) COBOLT Mambo™ laser. I aimed to use the 460 nm laser for ChR2(H134R) activation and to use the 594 nm laser for eArch3.0 or eNpHR2.0 activation. Both lasers were built into a LightHUB which combined both lasers into one output path. This output was coupled to an optic fiber that I connected to a fiberoptic rotary joint. This rotary joint enabled simultaneous light delivery to two different brain regions. Theoretically, I could express eArch3.0 or eNpHR2.0 in one brain region and ChR2(H134R) in another brain region, using both lasers and manipulate the two different regions differently. The rotary joint was mounted to a microphone stand, which made the positioning of the optogenetic stimulation extremely flexible (**Fig 4.13.1**).
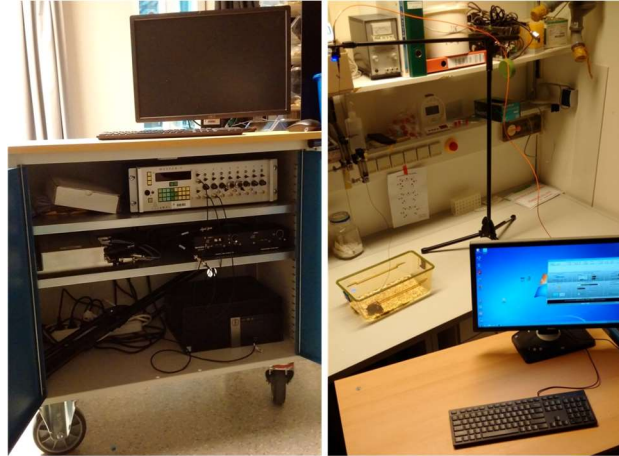
Fig. 4.13.1: The optogenetic stimulation cart. This cart was equipped with a PC that served as a driver for the lasers, a Master-8®, a programmable stimulator, a LightHUB which contained a 460 nm (blue) LuxX™ laser and a 594 nm (orange) COBOLT Mambo™ laser (left). An additional feature was the flexible positioning of the stimulation via the microphone stand (right).

4.14 Quantifying cFos Expression

For quantifying the fluorescence after the cFos immunostaining, I used the open source software Fiji/ImageJ®. I loaded z-tacks of the region of interest into the program. I then split the acquired channels and kept the DAPI and the cFos channel as separate z-stacks. I started the quantification with assigning ROIs to random DAPI+ cells. In a z-stack of 5-10 z-planes, I allocated between 10-25 ROIs per single z-section. I made sure to equally distribute the ROIs across all z-layers. Since I captured the z-stacks with a 5 μm z-resolution, it was likely for a DAPI+ nucleus to appear in more than one z-plane. For that reason, I additionally checked for the largest representation of the DAPI+ nucleus to assign the ROI (**Fig 4.14.1A-left**). I then transferred the ROIs to the cFos channel. This technique ensured that I were choosing my ROIs blindly to the cFos channel without any bias towards brighter or less bright cFos fluorescent neurons. However, this rose the chance to miss the brightest cFos fluorescent neurons independently of investigating the ChR2 stimulated or unstimulated site **(Fig 4.14.1A-right)**.
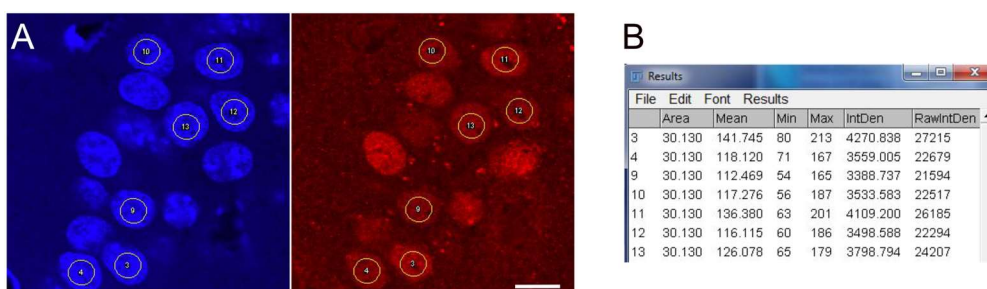
Fig. 4.14.1: Quantification of the cFos fluorescence. (A) Two different single z-planes of a z-stack acquired using confocal microscopy. The left image shows the DAPI channel, and the right image shows the cFos channel. ROIs were chosen over random DAPI+ nuclei to overcome a potential bias during the selection of which cFos signal to measure. ROIs were then transferred to the cFos channel before I measured the fluorescence intensities. **(B)** Screenshot of the open source software Fiji/ImageJ®. It shows example measures of the ROI and mean fluorescence of the ROIs 3 and 4 and 9-11. Scale bar 20 μm.

For all fluorescent intensity measurements (despite the spine size), I measured the mean fluorescence intensity of a constant ROI size **(Fig 4.14.1B)**. The raw mean values were highly dependent on the quality of staining and imaging parameters like the laser power or the gain. For that reason, I normalized all my measurements to the background. To define the background fluorescence, I took one ROI of the same size and shifted it to the edges, outside of the pyramidal layer of the acquired image.

4.15 The Morris Water Maze

The Morris Water Maze (MWM) is a hippocampal-dependent spatial learning paradigm developed by Richard Morris. During the task, the rat or mouse is swimming in a circular arena and has to find a small circular platform that is submerged close below the water surface. Escaping the water serves as the reward for the rodent and ultimately leads to the transfer of the animal back into its home cage where it is usually heated up using an infra-red lamp. Mice learn to locate the platform within 5 to 7 days by using external cues (printed triangle, square, plus and circle) to navigate to the platform. I established this paradigm to combine *in vivo* structural synaptic imaging of the hippocampus together with a hippocampal-dependent spatial learning paradigm.

We trained mice in a 150 cm circular pool which was filled with 21-23°C warm water and contained a 12 cm diameter transparent platform that was submerged 0.5-1 cm below the water surface (**Fig.4.15.1**). The training lasted 5 days, giving them 4 trials per day. Each trial was interleaved with an inter-trial interval (ITI) of 30 minutes during which all the other mice had their first trial before the mouse had its second trial. Each trial started from a different starting position north-west (NW), north-east (NE), south-west (SW) or south-east (SE) and lasted 90 seconds. If the animal was not able to locate the hidden platform within these 90 seconds, it was gently guided to the platform and encouraged to climb on it. The mouse was left sitting on the platform, independent of whether it had found it on its own or after it was guided to it, for 30 seconds. This gave the mouse the chance to orientate itself by using the

external cues and to learn where the platform was located. Then, I picked up the animal and put it back into the home cage. Outside of the home cage, I positioned an infra-red lamp in one corner of the cage. Like this, the mouse could approach the light to get heated up but also to leave the warm area if it became too warm. During all trials I tracked the position of the animal and recorded the time the mouse spent in each quadrant, the distance the animal traveled in each quadrant, the animals speed, the head direction and most importantly the latency in seconds and distance in meter the animal took to reach the platform using the commercial software ANY-maze®. I scripted the software that the tracking automatically stopped, and all results were saved as soon as the animal entered the platform zone. To test for memory recall on day 6, I removed the platform from the pool and gave each mouse one trial of 60 seconds to search for the platform. I assessed the main parameters 'time spent in the target quadrant' and 'distance traveled in the target quadrant' compared to the other three quadrants. Additionally, to get a more detailed insight into the memory, I also quantified the target platform crosses. To understand whether the mouse actively crossed the target platform zone in a higher frequency compared to random zones, I also implemented mock-platform zones in each of the other three quadrants and measured the mock-platform crosses.
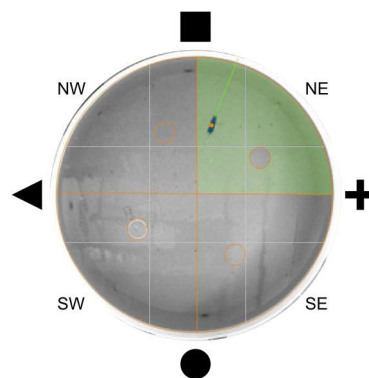

Fig. 4.15.1: The arena of the MWM. The pool had a diameter of 150 cm and contained a submerged, invisible 12 cm diameter platform in quadrant SW which the animal needed to learn to locate. To facilitate orientation, I presented 4 large, different, external cues: printed triangle, square, plus and circle. Mice had 20 trials over 5 days to learn to find the platform. On day 6 the platform was removed to check the memory by quantifying parameters like 'time spent in the target quadrant' and 'distance traveled in the target quadrant'.

4.16 Intracardial Perfusion and Brain Dissection

This method was adapted from (Gage et al., 2012). Mice were deeply anesthetized using a high percentage of Isoflurane and tested for anesthesia using the toe pinch reflex test. I then made an incision through the integument and abdominal wall just beneath the

rib cage and opened the diaphragm. Next, I performed two lateral cuts through the rib cage up to the collarbone. This enabled me to lift the *sternum* up to expose the heart to make a small incision to the posterior end of the left ventricle and to insert an olive-tipped perfusion needle into the ascending aorta. Using a hemostat, I clamped the heart which secured the needle in place and prevented leakage. I then made a small incision to the animal's right atrium to create an outlet for the Paraformaldehyde (PFA) and PBS. Finally, I perfused the animal for 5 minutes with ice-cold Heparin in 1x PBS to prevent blood clotting followed by 5 minutes of ice-cold 4 % PFA in 1x PBS.

Next, I removed the head, made a midline incision along the integument from the neck to the nose to expose the skull. I then cut the skull from both eye sockets, just before I made a second straight cut through the skull following the midline from lambda to bregma until I reached the first cut. I made sure not to damage the brain. This enabled me to lever up both hemispheres of the skull, exposing the brain. Using a spatula I could then carefully removed the brain from the skull. For post-fixation the brain was put into 4 % PFA in 1x PBS for 24 hours at 4°C onto a rotating carousel. After 24 hours the brain was put in 30% sucrose in PBS for 48 hours at 4°C for dehydration. If the brains sunk to the bottom of the tube within 48 hours the brains were further used for slicing, staining, and mounting.

4.17 Plotting and Statistical Analyses

For plotting and statistical analyses I used GraphPad Prism8®. Main tests I used were: non-parametric Mann-Whitney Test, one- and two-way ANOVAs, one-sample Wilcoxon test, Kruskal-Wallis test and Kolmogorov-Smirnov test. If necessary, I corrected for multiple comparisons using: Šidák, Holm-Šidák's and Dunn's. The significance was characterized in 5 intervals (**Table 4.17**).

Table 4.17: Evaluation of significance
Definition of the p-value, interpretation, and the defined value.

p-value	Interpretation	Symbol
$p > 0.05$	not significant	n.s.
$p \leq 0.05$	significant	*
$p \leq 0.01$	very significant	**
$p \leq 0.001$	highly significant	***
$p \leq 0.000$	extreme significant	****

4.18 Protocols

4.18.1 Slice Preparation and Wholemount Antibody Staining

All washing and/or incubation steps are done shaking.

Slicing:

1) Prepare 6% agarose in 1x PBS

2) Put brains into the plastic mounting molds, label molds according to the mouse number

3) Pour warm agarose on top of brains

4) Use curved Dumont forceps to position the brains in the molds, make sure that the olfactory bulb points up (towards the opening of the mold)

5) Let agarose harden while monitoring the position of the brains

6) Put molds on 4°C for ~30min

7) While waiting prepare vibratome

8) Vibratome settings are: fine slice 50 µm, trim 200 µm, frequency should be 66 and amplitude 0.9, speed 21-23

9) Make sure that the mounting platform is leveled

10) Take out mounting platform and fill slicing well with 1x PBS

11) Prepare multi-well plate (6,12 or 24 are suitable) by adding 1x PBS to the first wells

12) Take the solid agarose block out of the mold (use scalpel or razor blades to cut the mold open.

13) Trim excessive agarose away

14) When interested in the dorsal hippocampus, trim frontal lobes away, this saves time on the vibratome

15) Use super glue to mount the agarose embedded brain onto the slicing platform – Cerebellum towards the platform (super glue will harden in contact with PBS)

16) Set slicing window for vibratome

17) Use trim mode until reaching the region of interest

18) Switch to 50 µm slices and collect them using a brush into labeled wells of multi-well plate

19) Stop after having cut the entire region of interest, move cutting blade up, and remove mounting platform from the slicing well

20) Remove the rest of the uncut brain in agarose and excessive super glue using a razor blade

21) Continue with next brain

Antibody Staining:

Day 1

1) Quench brain slices of 15 min in 150 mM Glycine in ddH$_2$0 (1-2 ml per well, depending on the chosen multiwall plate)

2) Exchange solution to 0.2% Triton X-100 in 1x PBS and permeabilize for 1 h

3) Exchange solution to blocking buffer (0.2% Triton X-100 in 5% goat serum in 1x PBS) and block for 30 min

4) Prepare primary antibody (1:1000 – depends on the antibody) in blocking buffer

5) Exchange solutions and add primary antibody

6) Incubate overnight at 4°C

Day 2

7) Wash 3x for 10 min with 1x PBS

8) Prepare secondary antibody (1:1000 – depends on the antibody) in 1x PBS (Attention, fluorescent antibodies are very light sensitive to avoid bleaching, from now on cover multi-well plate with aluminum foil)

9) Exchange solutions and add primary antibody

10) Incubate for 1.5h

11) Wash 3x for 10 min with 1x PBS

12) Prepare DAPI staining (1:1000 of stock solution) in 1x PBS

13) Exchange solutions and add DAPI stain

14) Incubate for 5 min

15) Exchange solutions to 1x PBS

Mounting:

1) Fill a glass pretri dish (12cm diameter) with 1x PBS

2) Using the brush, add all brain slices belonging to one brain into the dish

3) Hold mounting slide with an angle of 15° into the 1x PBS and push one section after the other onto the slide – mount 4-10 sections per slide

4) Add 4-6 drops of hard-set fluorescent mounting medium to the slide

5) Cover using coverslip, avoid air bubbles

6) Put slides into dark and let them harden

7) Image the next day using confocal microscopy

4.18.2 Preparation and Administration of Tamoxifen

Final concentration: 10mg/mL in 50 ml corn oil

Preparation:

1) Dissolve 500 mg of Tamoxifen powder in 5% of the final volume in 100% Ethanol - for 50 ml use 2.5 ml 100% EtOH

2) Vortex

3) Add corn oil to 50 ml final volume

4) Dissolve at 50°C (water bath) – check from time to time

5) Aliquot in 1 ml aliquots and freeze

Administration:

1) Warm frozen Tamoxifen solution to 37°C

2) Inject desired amount of the warm solution IP

Example:

Desired dose: 100 mg/kg   Stock concentration: 10mg : 1mL

100mg : 1kg

100mg : 1000g

0.1mg : 1g

E.g. for a 25g mouse

2.5mg : 25g   2.5mg : **0.25mL**

CHAPTER 5 – RESULTS

5.1 Labeling Active Neurons

To investigate whether neuronal activity induced by environmental enrichment (EE) (Methods 4.2) would lead to a change in structural synaptic plasticity in the dorsal CA1 of the hippocampus I permanently implanted an imaging cannula (Methods 4.3) dorsal to the external capsule and the fibers of the cingulum and corpus callosum (Methods 4.4) (**Fig 5.1.1**). This technique enabled longitudinal optical access to image Thy1-eGFP positive pyramidal neurons and their dendritic arborization using 920 nm 2-photon excitation microscopy.
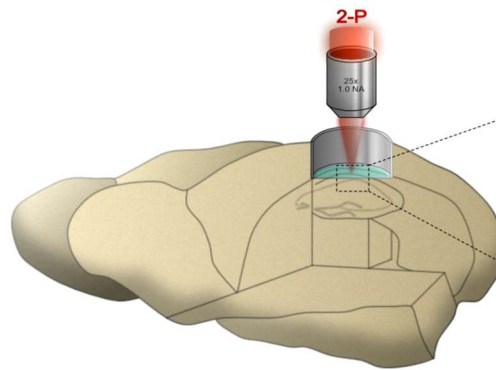
Fig. 5.1.1: Schematic of the implantation site of the imaging cannula over the right dorsal CA1 giving optical access to Thy1-eGFP positive pyramidal neurons using 2-photon microscopy.

Due to optical limitations, I focused my examination on the basal dendrites in the *stratum oriens* and imaged the same dendritic arborization and its synaptic plasticity over a period of 14 days. In order to label cells that became active during the EE, I created a triple transgenic mouse line. I crossed Thy1-eGFP mice with mice where the Immediate-Early Gene (IEG) Arc or cFos drives activity-dependent expression of the Tamoxifen (TAM) dependent Cre-recombinase (Arc-Cre^{ERT2} or FosCre^{ERT2}), which – upon TAM injection - leads to the expression of a red-fluorescent reporter protein (tdTomato) (Ai9), thus effectively reporting neuronal activity during a defined time window. This method resulted in having two populations of neurons within the same brain tissue - eGFP-positive cells (green alone) that

were not active during the EE and eGFP and tdTomato double-positive cells (yellow, as a result from green and red) which were active during the EE (**Fig 5.1.2**).
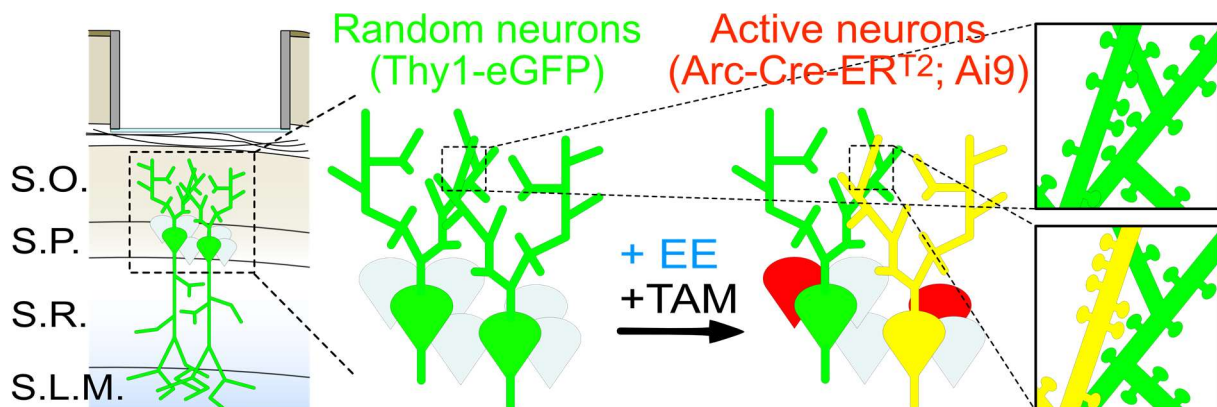

Fig. 5.1.2: Schematic description of the technique. The imaging cannula was implanted over the fibers of the corpus callosum leading to direct and permanent optical access to Thy1-eGFP positive neurons of triple transgenic Thy1-eGFP; Arc/Fos-Cre^ERT2; Ai9 mice – detecting synaptic plasticity before and after neuronal activity induced by EE in inactive, eGFP-positive cells (green alone) and active, double-positive cells (yellow, as a result from green and red) pyramidal neurons. S.O., *Stratum Oriens*, S.P., *Stratum Pyramidale*; S.R., *Stratum Radiatum*; S.L.M., *Stratum Lacunosum-Molecolare*. TAM, single Tamoxifen injection; EE housing in an Enriched Environment. Green, neurons expressing eGFP; red, neurons expressing Arc-driven tdTomato

We first tested whether I could use cFos-driven tdTomato expression in the dorsal CA1 to detect specific activation-driven plasticity elicited by the exploration of an EE. To this aim, I injected intraperitoneally (i.p.) two groups of Fos-CRE^ERT2; Ai9 mice with a single dose of 75 mg/kg, two groups with 150 mg/kg and two groups with 300 mg/kg TAM. Per each treatment, immediately after injection, one group of mice explored an EE for 2h, and one group was housed in their home cages (HC) (**Fig. 5.1.3A**). I sacrificed all animals 10 days after TAM injection and quantified the percentage of pyramidal neurons expressing tdTomato by confocal microscopy (**Fig. 5.1.3B**). Quantifying the confocal images, neither the dose of TAM nor the exploration of the EE seemed to affect how many neurons expressed tdTomato after 10 days (**Fig. 5.1.3C**).
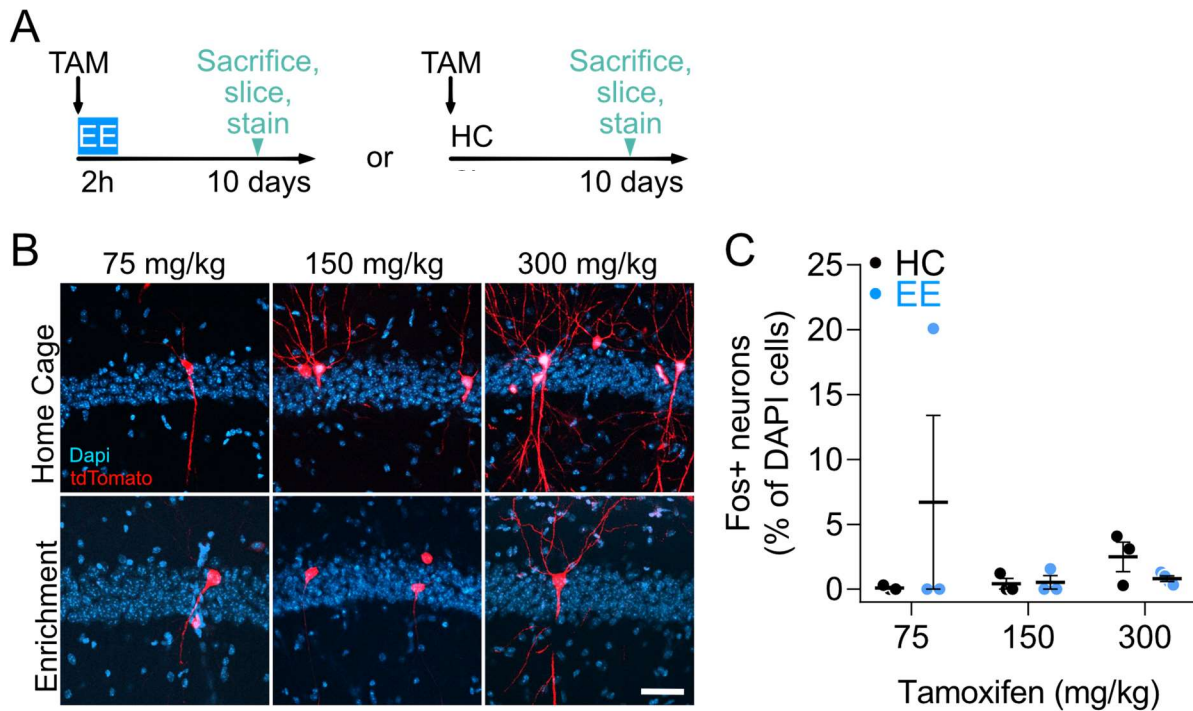
Fig. 5.1.3: (**A**) Experimental scheme illustrating the timeline of the ex-vivo characterization. Mice received either 75, 150 or 300 mg/kg TAM i.p. and either explored an EE for two hours or were put back into their HC. 10 days later mice were sacrificed; brain sections were taken and stained with the nuclear marker DAPI. (**B**) Representative confocal images of the dorsal CA1 of Fos-CRE^{ERT2}; Ai9 mice that either explored an EE or their HC and received different amounts of TAM. Images display 1 z-plane showing cFos-tdTomato positive cells over all DAPI-positive cells. Scale bar 100 µm. (**C**) Quantification of cFos-tdTomato positive cells over all DAPI-positive cells. No concentration or treatment with EE led to an increase in the number of cFos-tdTomato positive neurons. n=3 mice

In parallel, I tested whether I could use Arc instead of cFos-driven tdTomato expression in the dorsal CA1 to detect specific activation-driven plasticity elicited by the exploration of an EE. For this, I examined the same experiment explained above using Arc-CRE^{ERT2}; Ai9 instead of Fos-CRE^{ERT2}; Ai9 mice (**Fig. 5.1.3A**). I also added one group that didn't receive TAM nor was exposed to EE, to control for leakiness of tdTomato expression. I sacrificed all animals 10 days after TAM injection and quantified the percentage of pyramidal neurons expressing tdTomato by confocal microscopy (**Fig. 5.1.4A**). Although any TAM injection led to tdTomato expression, the 75 mg/kg TAM injection yielded a significant (Šidák multiple comparison test corrected 2-way ANOVA, 75mg/kg: p = 0.0044, 150mg/kg: p = 0.2419, 300mg/kg: p = 0.9549) two-fold increase in tdTomato expression after EE in comparison to HC (**Fig. 5.1.4B-C**).
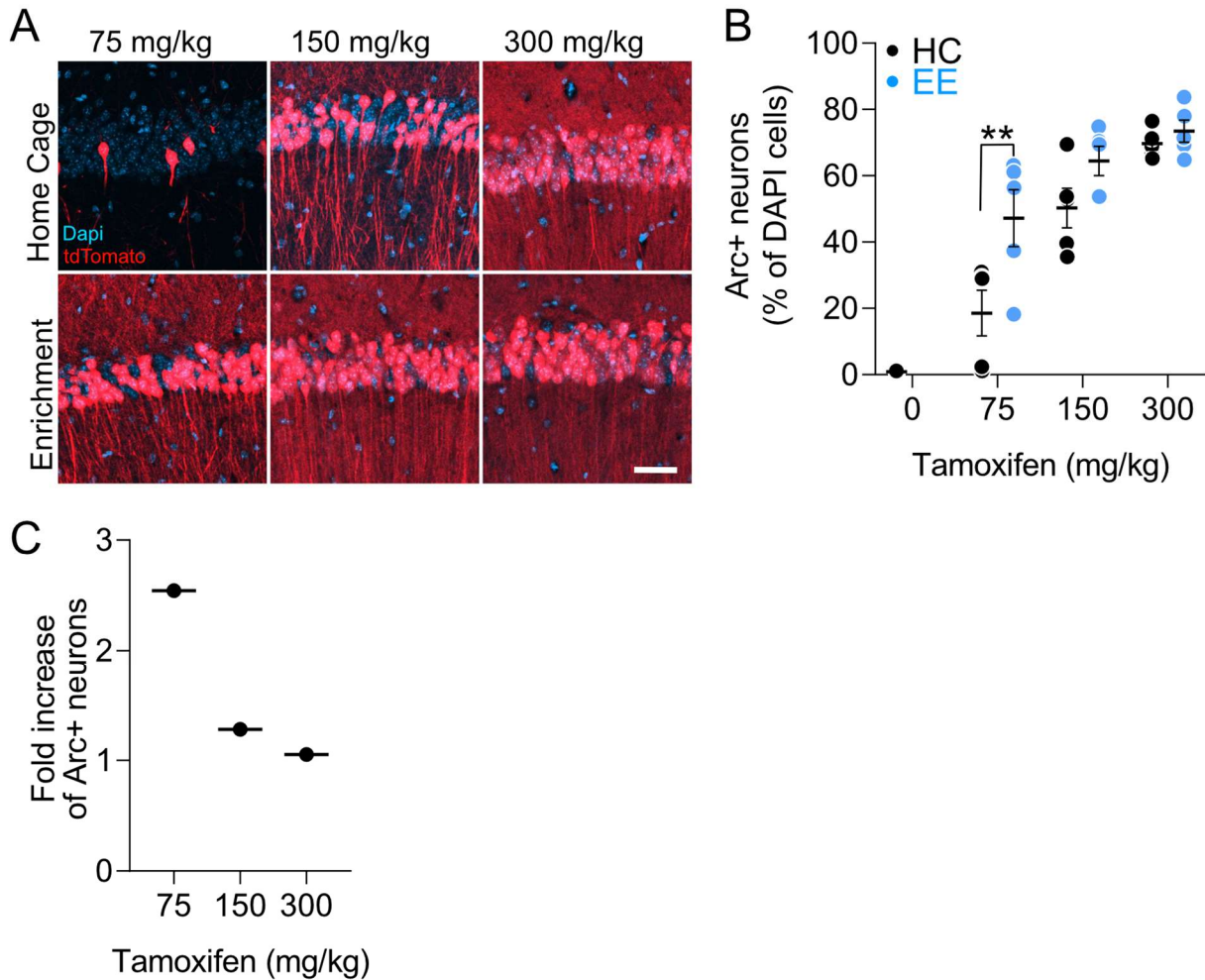
Fig. 5.1.4: Tamoxifen increase tdTomato expression in Arc-CreERT2; Ai9 mice. (**A**) Representative confocal images of the dorsal CA1 of Arc-CRE[ERT2]; Ai9 mice that either explored an EE or their HC and received different amounts of TAM. Images display 1 z-plane showing Arc-tdTomato positive cells over all DAPI-positive cells. Scale bar 100 µm. (**B**) Quantification of Arc-tdTomato positive cells over all DAPI-positive cells. Any concentration of TAM resulted in an increased number of Arc-tdTomato positive cells. The ratio between HC and EE of 75 mg/kg displayed the biggest and significant discrepancy of the three conditions (Šidák multiple comparison test corrected 2-way ANOVA, 75mg/kg: p = 0.0044, 150mg/kg: p = 0.2419, 300mg/kg: p = 0.9549). (**C**) Analyzed fold increase of Arc-tdTomato positive cells between HC and EE. 75 mg/kg revealed the strongest (2.5 fold) increase. n=5 mice

Because of the i.p. TAM injection of 75 mg/kg resulted in the most significant fold increase of Arc-tdTomato positive neurons in animals that explored the EE compared to animals that were exposed to their HC, I decided to use Arc-Cre[ERT2]; Thy1-eGFP; Ai9 mice and to inject 75mg/kg TAM for my further experiments.

5.2 Identifying Spines Belonging to Active Neurons *in vivo*

This thesis aimed to understand whether neuronal activity would influence structural synaptic plasticity. For this, I implanted an imaging cannula dorsal to the CA1 of the hippocampus and imaged dendritic branches and their spines of eGFP-positive pyramidal neurons of Arc-CreERT2; Thy1-eGFP; Ai9 mice. The experiment was designed to capture baseline synaptic plasticity during one week 14 days after the animals underwent the surgery. After this first week during which I imaged on day 1, 2, 4 and 7, I exposed the mice to an EE for 16 hours overnight giving them a single i.p. TAM injection of 75mg/kg to label active neurons with tdTomato. In the morning of day 8 mice were put back into their HC and continued to be imaged using the same imaging intervals as during the first week (day 8, 9, 11, 14). On day 15, all mice underwent a hippocampus-dependent trace fear conditioning. Finally, on the last day of the experiment, on day 16, mice were probed for their memory to the context and tone (**Fig. 5.2.1**).
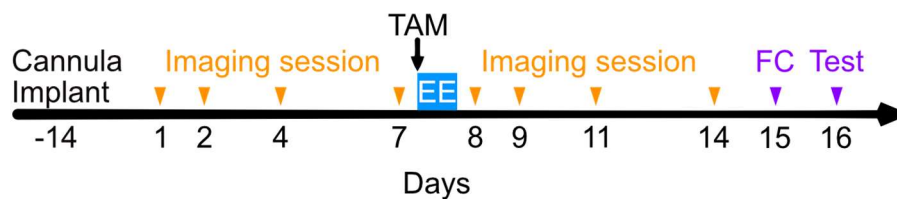

Fig. 5.2.1: Experimental timeline of the *in vivo* imaging experiment. 14 days after the implantation of the imaging cannula mice were imaged for one week to capture baseline synaptic plasticity. After one week, I exposed the mice to an EE for 16 hours overnight giving them a single i.p. TAM injection of 75mg/kg to label active neurons with tdTomato. I continued imaging for another week, keeping the same imaging intervals as during the first week. After the two weeks of imaging, mice also underwent a trace fear conditioning experiment on days 15 and 16.

Since initially, I performed the *ex vivo* characterization experiment (Results 5.1) in parallel to the first *in vivo* imaging experiment I started using both mouse lines - Fos-CRE[ERT2]; Thy1-eGFP; Ai9 and Arc-Cre[ERT2]; Thy1-eGFP; Ai9 - to label active cells during a defined time window. I imaged a random population of dendrites belonging to eGFP positive neurons in groups of both mice. Since the main idea of the project was to identify active neurons which were labeled by cFos- or Arc-tdTomato, I checked for tdTomato baseline expression at day 1 to avoid imaging dendrites coming from neurons that were already positive for tdTomato. I continued imaging the same dendritic branches that I chose on day 1 for the next 14 days. Finally, on the last day of imaging, I verified to see increased tdTomato expression after TAM injection and exposure to the EE. Additionally, this imaging session was used to determine which of the neurons that I kept imaging for 2 weeks became active/tdTomato-positive

during the EE. Using the Arc-Cre^ERT2; Thy1-eGFP; Ai9 animals identified a sparse label of Thy1-eGFP of pyramidal neurons in the *stratum pyramidiale in vivo*. It also showed leakiness of the Arc-Cre^ERT2; Ai9 system resulting in a sparse tdTomato expression during baseline even without the presence of TAM or EE (**Fig. 5.2.2A**). After housing mice for 16 hours in an EE in combination with the activation of the Tamoxifen-dependent, Cre-recombinase yielded a substantial increase in the number of tdTomato-positive neurons. This *in vivo* result strongly resembled the findings from the quantification of the *ex vivo* experiment conducted before (**Fig. 5.1.4A-B**). After the EE I could identify three classes of neurons; neurons that stayed inactive during the EE and therefore only expressed eGFP (arrowhead - eGFP+/tdTomato-), neurons that became active during the EE and started to express tdTomato (arrow - eGFP+/tdTomato+) and neurons that expressed tdTomato from the beginning which could also be followed through time (asterisk – eGFP-/tdTomato+) (**Fig. 5.2.2A**).
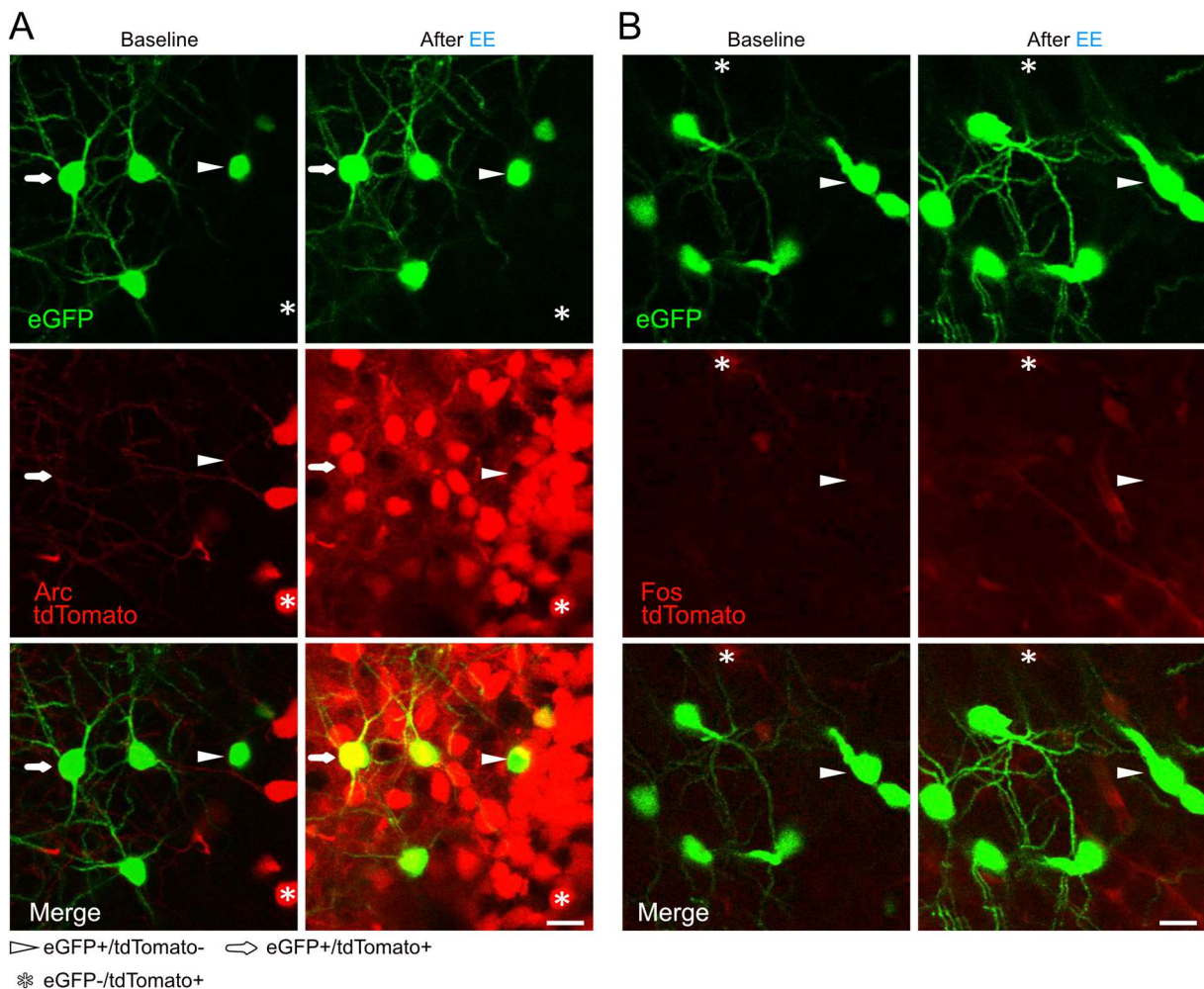

Fig. 5.2.2: Labeling active dCA1 pyramidal neurons using tdTomato *in vivo*. (**A**) Left: Baseline Thy1-eGFP and tdTomato expression prior to exposure to the EE and TAM administration. Note, leakiness of tdTomato expression even without TAM. Right: Substantial increase in the number of tdTomato-positive neurons leading to double positive (eGFP+/tdTomato+) neurons. (**B**) Left: Baseline Thy1-eGFP and tdTomato expression before exposure to the EE and TAM administration. Right: No increase in the number of

tdTomato-positive neurons. Arrowhead - eGFP+/tdTomato- neuron, arrow - eGFP+/tdTomato+ neurons asterisk – eGFP-/tdTomato+ neurons.

Repeating the same experiment using the Fos-CRE^{ERT2}; Thy1-eGFP; Ai9 instead Arc-Cre^{ERT2}; Thy1-eGFP; Ai9 also identified a sparse label of Thy1-eGFP of pyramidal neurons in the *stratum pyramidiale in vivo*. Fos-CRE^{ERT2}; Thy1-eGFP; Ai9 only showed a marginal leakiness of tdTomato expression during baseline compared to Arc-CRE^{ERT2}; Thy1-eGFP; Ai9 mice (**Fig. 5.2.2B**). However, after housing mice for 16 hours in an EE in combination with the activation of the Tamoxifen-dependent, Cre-recombinase did not lead to any expression of tdTomato and thereby not labeling cells active during the EE. This *in vivo* result strongly resembled the findings from the quantification of the *ex vivo* experiment conducted before (**Fig. 5.1.3B-C**). These findings strengthened my decision to use Arc-Cre^{ERT2}; Thy1-eGFP; Ai9 mice and to inject 75mg/kg TAM for my further experiments.

To understand if a dendritic segment belonged to an active or inactive neuron, I needed to be able to trace each dendrite back to its soma. I imaged 227 dendritic sections, of which 3 dendrites could not be traced back to their soma because it was outside the field of view (**Fig. 5.2.3 left**). Overview images were taken as z-stacks using a 25x 1.0 NA objective combined with 1x digital zoom. To capture more detail of the overview, the digital zoom was increased to 2x resolving enough detail to trace dendrites back to their soma (**Fig. 5.2.3 middle**). The digital zoom was further increased to 10x to acquire data which was used to count spines. (**Fig. 5.2.3 right**).
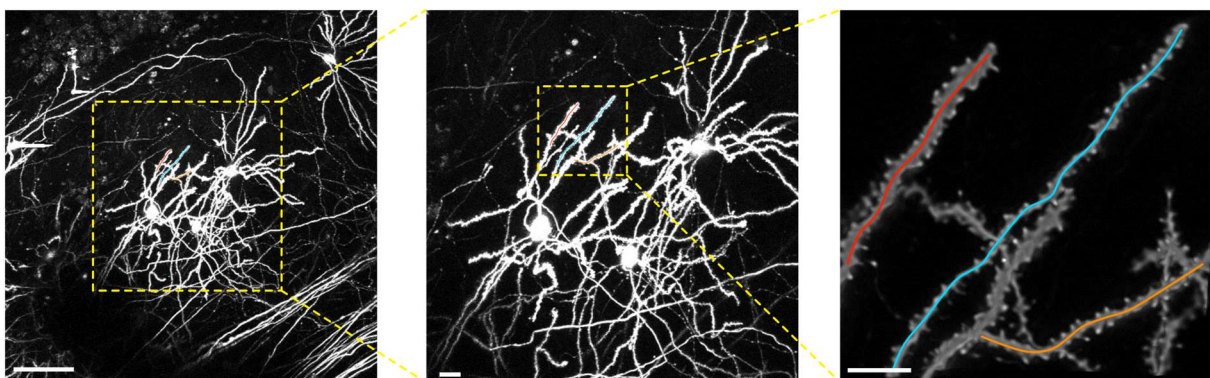

Fig. 5.2.3: Tracing dendritic segments back to their somata. 3 acquired dendritic segments (red, blue, orange) needed to be traced back to their soma to identify whether they belonged to a neuron that was activated during EE or stayed inactive. Left: 1x overview image to relocate the correct area to be imaged the next day of the experiment. Middle: 2x magnification to resolve enough detail to trace dendrites back to the somata. Right: 10x magnification to quantify structural synaptic plasticity by counting dendritic spines. Images show maximum intensity projections of 2-photon microscopy using 920 nm excitation light. Left: 59 z-planes (2 µm per z-step) scale bar: 100 µm. Middle: 59 z-planes (2 µm per z-step) scale bar: 20 µm. Right: 55 z-planes (1 µm per z-step) scale bar: 10 µm.

Using the 10x magnification, I was able to track structural synaptic plasticity over 14 days. I could identify three main classes of spines. The majority (40%) of spines was persistent through time and could be identified on each single imaging day (blue arrowhead). I also found spines that did not exist the previous imaging time point. These spines were called newborn spines (green arrowhead). Additionally, I detected spines that were lost during my experimental timeline (red arrowhead) (**Fig. 5.3.4**). I also identified spines that recurred at the same location as a previous spine got lost (**Fig. 5.3.4** lower example, newborn spine day 9-14). However, I decided to give these spines a new spine ID and call them newborn, because I could not be sure that the spine, even though it was born in the same location, would form the exact synapse as the previous spine would have formed.
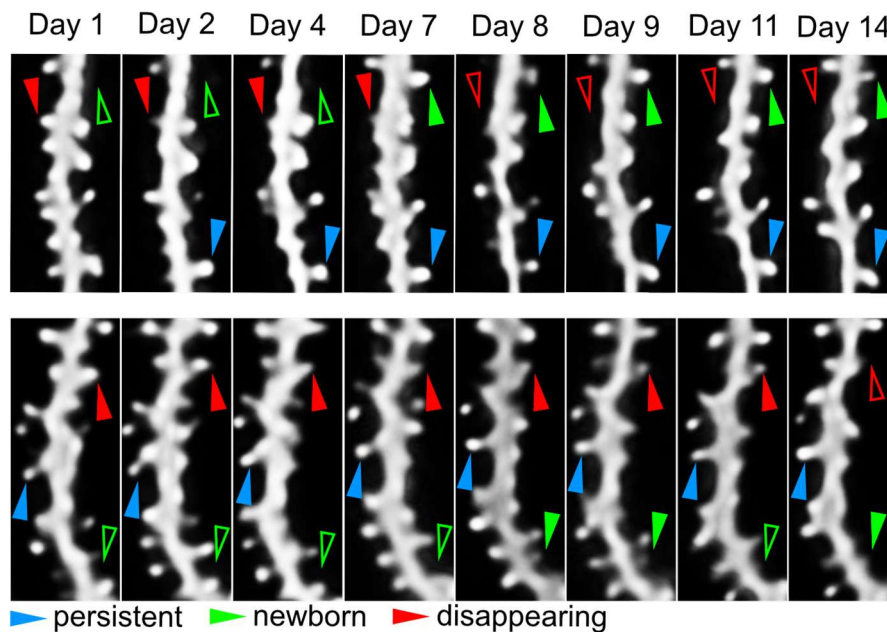

Fig. 5.2.4: Following spine dynamics for 14 days. I could identify three main classes of spines: stable (blue arrowhead), newborn (green arrowhead), and lost spines (red arrowhead). Stable spines were persistent over the whole period of 14 days. Newborn spines were not present the previous time point and only appeared for the first time. Lost spines existed at least the time point before but were missing during the time point of acquisition.

5.3 Synaptic Stability Predicted Neuronal Activity

We imaged 7 Arc-Cre^ERT2; Thy1-eGFP; Ai9 mice of which 3 were males and 4 were females. Out of the 7 mice, I followed 51 neurons within which 19 stayed inactive, 25 became Arc-tdTomato positive, and 7 were either already tdTomato positive from baseline or were outside the field of view so that it was impossible to identify whether they became active during the 16 hours exposure to the EE or not. Out of these 51 neurons, I imaged 227 dendritic segments – 77 were Arc-tdTomato negative, 121 tdTomato positive

and 29 belonged to neurons that already expressed tdTomato from baseline or could not be traced back to their somata (**Table 5.3.1**).

Table 5.3.1: Summary of mice, cells, and dendrites imaged and used for the activity driven tdTomato labeling of neurons and the stochastically random tdTomato labeling of neurons using the Nex- instead of the Arc- promoter.

Genotype	Mice	Sex	Imaged Cells		Imaged Dendrites		Used Cells		Used Dendrites	
Arc	7	3 ♂	44	19 Arc-	198	77 Arc-	33	17 Arc-	135	54 Arc-
		4 ♀		25 Arc+		121 Arc+		16 Arc+		81 Arc+

Due to difficulties of imaging a living and moving (heartbeat, breathing) tissue and post-processing of the images, it occurred that, even though dendrites were imaged throughout time, the image quality was not high enough to resolve spines. Because of this challenge, I further restricted my analysis to use only dendritic segments which I could fully resolve on all imaging time points. This brought my experimental numbers down to 33 neurons, of which 16 became activated and Arc-tdTomato positive after the EE and 135 dendrites within which 81 belonged to the activated neurons (**Tab. 5.3.1**).

The first characteristic that I analyzed was the spine density of Arc-tdTomato negative versus positive neurons. Since I traced the dendrites back to their somata, I was able to track differences in activated and neurons not activated by the EE within the same subjects both prospectively and retrospectively. I decided to quantify my data in two similar ways. Firstly, I took neurons as the independent unit since also my marker of neuronal activity labeled the whole neuron irrespective of which part of the neuron was activated. On the other hand, dendrites are believed to be fully functional and independent computational units hence treating dendrites as the independent unit. I found, when plotting cells, the density of Arc-tdTomato positive neurons was significantly higher compared to Arc-tdTomato negative neurons (Mean densities: Arc-tdTomato+: 1.09 spines/µm, Arc-tdTomato-: 1.00 spines/µm) (Mann-Whitney test, p = 0.0218, n = 17 Arc-tdTomato-, n=16 Arc-tdTomato+) but spine densities were unchanged on all days after EE (one sample Wilcoxon test each day against respective median baseline densities; Arc-tdTomato- D8 p = 0.7467, Arc-tdTomato- D9 p = 0.9265, Arc-tdTomato- D11 p = 0.5477, Arc-tdTomato- D14 p = 0.9632, Arc-tdTomato+ D8 p = 0.7057, Arc-tdTomato+ D9 p = 0.9399, Arc-tdTomato+ D11 p = 0.8603, Arc-tdTomato+ D14 p = 0.3755) (**Fig. 5.3.1A**). When I plotted dendrites, the density of Arc-tdTomato+ dendrites was not different compared to Arc-tdTomato- dendrites (Mean densities: Arc-tdTomato+: 0.9738 spines/µm, Arc-tdTomato-: 0.9556 spines/µm) (Mann-Whitney test, p = 0.3139, n =

54 Arc-tdTomato-, n=81 Arc-tdTomato+) and also spine densities were mainly unchanged on all days after the EE exempt for day 14 Arc-tdTomato+ (one sample Wilcoxon test each day against respective median baseline densities; Arc-tdTomato- D8 p = 0.7520, Arc-tdTomato- D9 p = 0.6569, Arc-tdTomato- D11 p = 0.6142, Arc-tdTomato- D14 p = 0.9864, Arc-tdTomato+ D8 p = 0.7850, Arc-tdTomato+ D9 p = 0.3483, Arc-tdTomato+ D11 p = 0.7931, Arc-tdTomato+ D14 p = 0.0122) (**Fig. 5.3.1B**).
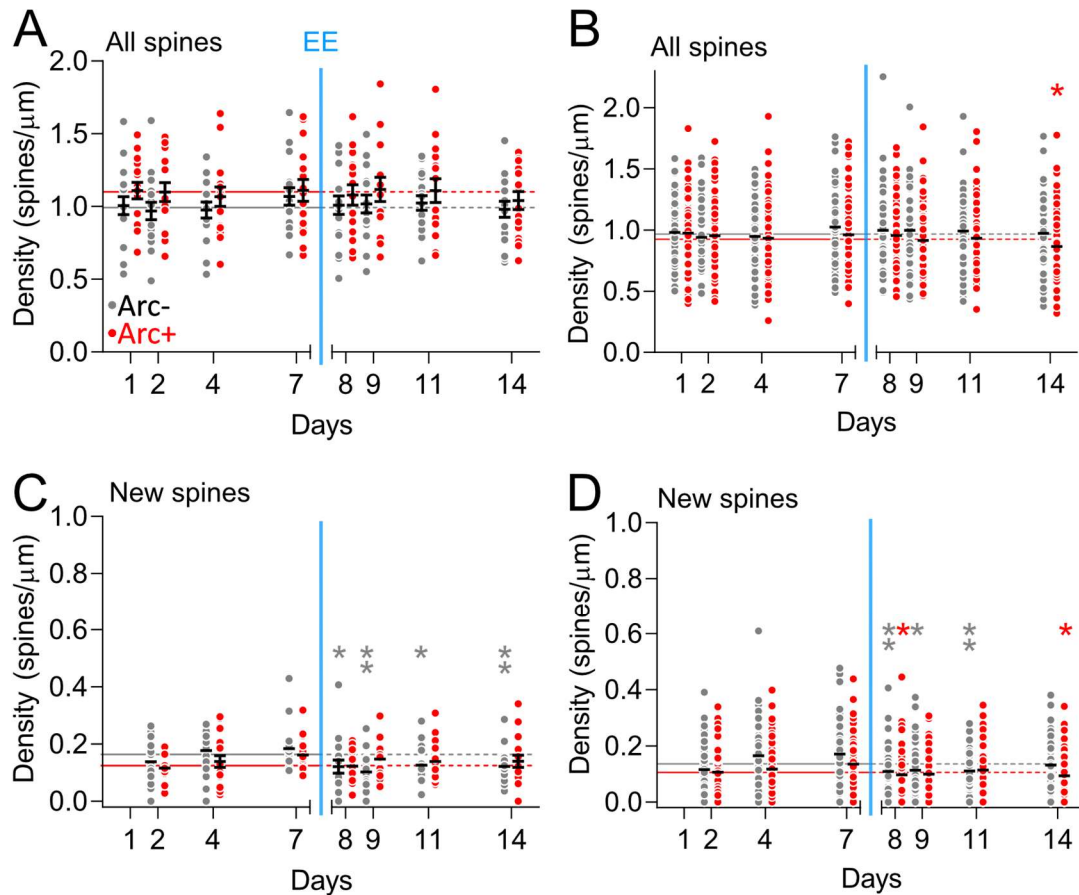
Fig. 5.3.1: Spine densities of all spines and newborn spines plotted as cells (**A** and **C**) and dendrites (**B** and **D**). (**A**) Spine densities of all spines were different between Arc-tdTomato- and Arc-tdTomato+ (Mann-Whitney test, p = 0.0218, n = 17 Arc-tdTomato-, n=16 Arc-tdTomato+). But did not change through time (one sample Wilcoxon test each day against respective median baseline densities; Arc-tdTomato- D8 p = 0.7467, Arc-tdTomato- D9 p = 0.9265, Arc-tdTomato- D11 p = 0.5477, Arc-tdTomato- D14 p = 0.9632, Arc-tdTomato+ D8 p = 0.7057, Arc-tdTomato+ D9 p = 0.9399, Arc-tdTomato+ D11 p = 0.8603, Arc-tdTomato+ D14 p = 0.3755). (**B**) The densities of Arc-tdTomato- and Arc-tdTomato+ dendrites were not different (pairwise Mann-Whitney test, p = 0.3139, n = 54 Arc-tdTomato-, n=81 Arc-tdTomato+). They also did not change substantially through time (one sample Wilcoxon test each day against respective median baseline densities; Arc-tdTomato- D8 p = 0.7520, Arc-tdTomato- D9 p = 0.6569, Arc-tdTomato- D11 p = 0.6142, Arc-tdTomato- D14 p = 0.9864, Arc-tdTomato+ D8 p = 0.7850, Arc-tdTomato+ D9 p = 0.3483, Arc-tdTomato+ D11 p = 0.7931, Arc-tdTomato+ D14 p = 0.0122). (**C**) Spine densities of newborn spines were different between Arc-tdTomato- and Arc-tdTomato+ (pairwise Mann-Whitney test, p = 0.0436, n = 17 Arc-tdTomato-, n=16 Arc-tdTomato+). The density of newborn spines of Arc-tdTomato- neurons was reduced compared to its baseline (one sample Wilcoxon test each day against respective median baseline densities; Arc-tdTomato- D8 p = 0.0202, Arc-tdTomato- D9 p = 0.0021, Arc-tdTomato- D11 p = 0.0305, Arc-tdTomato- D14 p = 0.0093, Arc-tdTomato+ D8 p = 0.9399, Arc-tdTomato+ D9 p = 0.2744, Arc-tdTomato+ D11 p = 0.7820, Arc-tdTomato+ D14 p = 0.8603). (**D**) Spine densities of newborn spines were different between Arc-

tdTomato- and Arc-tdTomato+ (pairwise Mann-Whitney test, p = 0.0052, n = 17 Arc-tdTomato-, n=16 Arc-tdTomato+). The density of newborn spines of Arc-tdTomato- and Arc-tdTomato+ dendrites was reduced compared to their baseline levels (one sample Wilcoxon test each day against respective median baseline densities; Arc-tdTomato- D8 p = 0.0017, Arc-tdTomato- D9 p = 0.0108, Arc-tdTomato- D11 p = 0.0097, Arc-tdTomato- D14 p = 0.4402, Arc-tdTomato+ D8 p = 0.0443, Arc-tdTomato+ D9 p = 0.2043, Arc-tdTomato+ D11 p = 0.5924, Arc-tdTomato+ D14 p = 0.0185). Blue bar indicates time point of 16h EE + 75 mg/kg TAM i.p.. Solid lines medians during baseline, dashed lines median from baseline. * p ≤ 0.05, ** p ≤ 0.01

We also analyzed the spine density of newborn spines, and found, when plotting cells, the density of Arc-tdTomato- neurons was significantly higher compared to Arc-tdTomato+ neurons (Mean densities: Arc-tdTomato+: 0.1387 spines/µm, Arc-tdTomato-: 0.1659 spines/µm) (pairwise Mann-Whitney test, p = 0.0436, n = 17 Arc-tdTomato-, n=16 Arc-tdTomato+). After the EE the density of newborn spines of Arc-tdTomato- neurons was reduced compared to its baseline (one sample Wilcoxon test each day against respective median baseline densities; Arc-tdTomato- D8 p = 0.0202, Arc-tdTomato- D9 p = 0.0021, Arc-tdTomato- D11 p = 0.0305, Arc-tdTomato- D14 p = 0.0093, Arc-tdTomato+ D8 p = 0.9399, Arc-tdTomato+ D9 p = 0.2744, Arc-tdTomato+ D11 p = 0.7820, Arc-tdTomato+ D14 p = 0.8603) (**Fig. 5.3.1C**). When plotting dendrites, the density of Arc-tdTomato- dendrites was significantly higher compared to Arc-tdTomato+ dendrites (Mean densities: Arc-tdTomato+: 0.1196 spines/µm, Arc-tdTomato-: 0.1505 spines/µm) (pairwise Mann-Whitney test, p = 0.0052, n = 54 Arc-tdTomato-, n=81 Arc-tdTomato+). Additionally, after the EE the density of newborn spines of Arc-tdTomato- and Arc-tdTomato+ dendrites was reduced compared to their baseline levels, although Arc-tdTomato- dendrites showed a stronger reduction in newborn spine density compared to Arc-tdTomato+ dendrites (one sample Wilcoxon test each day against respective median baseline densities; Arc-tdTomato- D8 p = 0.0017, Arc-tdTomato- D9 p = 0.0108, Arc-tdTomato- D11 p = 0.0097, Arc-tdTomato- D14 p = 0.4402, Arc-tdTomato+ D8 p = 0.0443, Arc-tdTomato+ D9 p = 0.2043, Arc-tdTomato+ D11 p = 0.5924, Arc-tdTomato+ D14 p = 0.0185) (**Fig. 5.3.1D**).

We were wondering whether the dendritic order contributed to the differences in spine density before the EE. For that reason, I analyzed all dendritic segments and their order of Arc-tdTomato+ and Arc-tdTomato- neurons. The dendritic segment directly emerging from the soma was ranked 1st order, after the first branch point every dendritic segment was graded 2nd order irrespective of size and diameter of the dendritic segment. This grading went on until the 6th order (**Fig. 5.3.2**). I found that I sampled very similar dendritic segments of Arc-tdTomato+ and Arc-tdTomato- neurons (1st: Arc- 5.6%, Arc+ 6.2%; 2nd: Arc- 25.9%,

Arc+ 17.3%; 3rd: Arc- 35.2%, Arc+ 40.5%; 4th: Arc- 29.7%, Arc+ 28.3%; 5th: Arc- 1.9%, Arc+ 4.9%; 6th: Arc- 1.7%, Arc+ 2.8%) (**Fig. 5.3.2).**
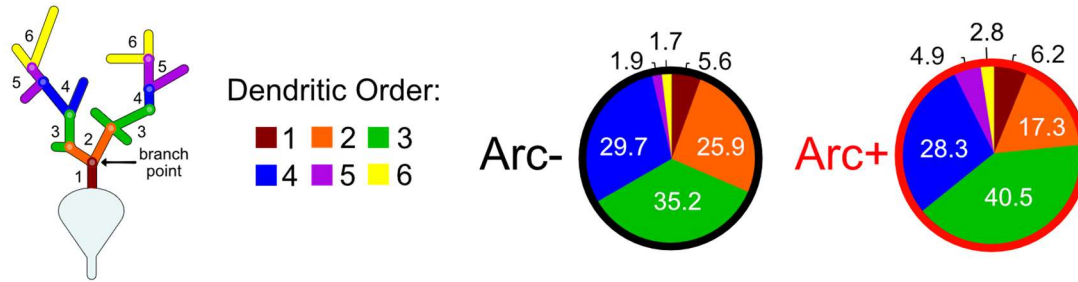

Fig. 5.3.2: Dendritic order of dendritic segments belonging to Arc-tdTomato+ and Arc-tdTomato- neurons. Both groups showed a very similar distribution of dendritic segments. 1st: Arc- 5.6%, Arc+ 6.2%; 2nd: Arc- 25.9%, Arc+ 17.3%; 3rd: Arc- 35.2%, Arc+ 40.5%; 4th: Arc- 29.7%, Arc+ 28.3%; 5th: Arc- 1.9%, Arc+ 4.9%; 6th: Arc- 1.7%, Arc+ 2.8%.

Next, I analyzed the turnover rate of spines per cell or dendrite. The turnover rate was defined as the sum of all spines gained and lost per day divided by the total amount of spines on that day. When I analyzed the turnover per day I found that on day 2 Arc-tdTomato- cells showed a higher turnover rate compared to Arc-tdTomato+ (pairwise Mann-Whitney test, d2 p = 0.0407, d4 p = 0.0591, d7 p = 0.8730, n = 17 Arc-tdTomato-, n=16 Arc-tdTomato+). After the EE I could not observe any significant difference in the turnover rate between Arc-tdTomato- and Arc-tdTomato+ (pairwise Mann-Whitney test, d8 p = 0.9292, d9 p = 0.3265, d11 p > 0.9999, d14 p = 0.3265, n = 17 Arc-tdTomato-, n=16 Arc-tdTomato+) (**Fig. 5.3.3A**). To get a more condensed view onto the data, I pooled time points 2-7 and 9-14 in order to identify major differences between the two groups but also to understand if each group would change through time. I found that the lower turnover rate of prospective Arc-tdTomato+ neurons was predictive of whether a neuron would become activated during the EE. Additionally, this data showed a reduction of turnover rate in Arc-tdTomato- neurons after the EE compared to its own baseline (Šidák multiple comparisons corrected Mann-Whitney test, baseline Arc-tdTomato- vs. Arc-tdTomato+ p = 0.0073, after EE Arc-tdTomato- vs. Arc-tdTomato+ p = 0.3399, Arc-tdTomato- baseline vs. after EE p = 0.0005, Arc-tdTomato+ baseline vs. after EE p = 0.8112; n = 51 Arc-tdTomato-, n=48 Arc-tdTomato+) (**Fig. 5.3.3B**). Furthermore, I did the same analysis on the dendrite level resulting in identical data as presented in for the cells (pairwise Mann-Whitney test, d2 p = 0.0075, d4 p = 0.0021, d7 p = 0.1862, n = 54 Arc-tdTomato-, n = 81 Arc-tdTomato+). After the EE I could not observe any significant difference in the turnover rate between Arc-tdTomato- and Arc-tdTomato+ (pairwise Mann-Whitney test, d8 p = 0.8905, d9 p = 0.8290, d11 p = 0.8430, d14 p = 0.7447,

n = 54 Arc-tdTomato-, n = 81 Arc-tdTomato+). In addition I also pooled the data together

(Šidák multiple comparisons corrected Mann-Whitney test, baseline Arc-tdTomato- vs. Arc-

tdTomato+ p <0.0001, after EE Arc-tdTomato- vs. Arc-tdTomato+ p = 0.6797, Arc-tdTomato-

baseline vs. after EE p = 0.0003, Arc-tdTomato+ baseline vs. after EE p = 0.8977; n = 162
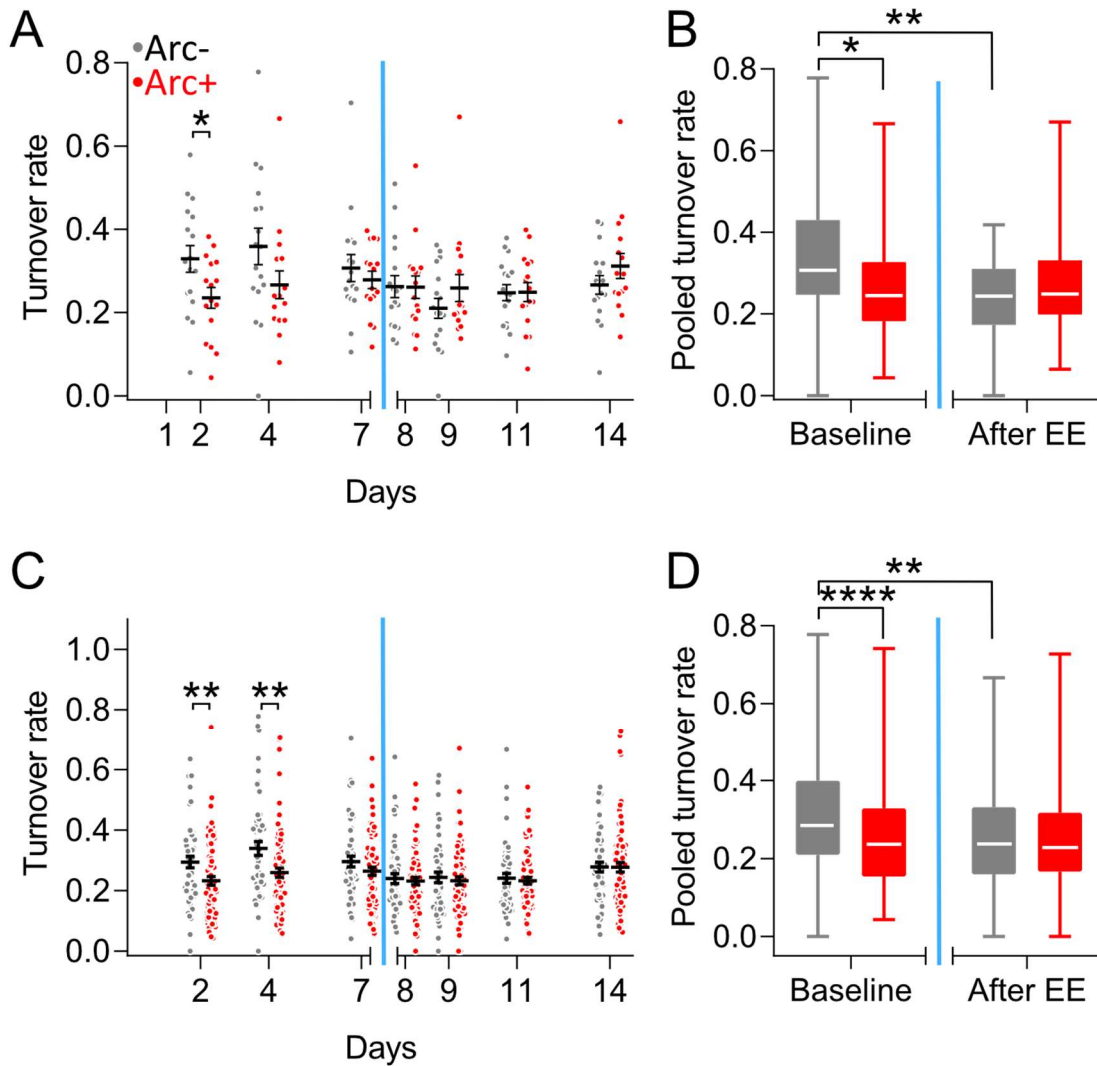
Arc-tdTomato-, n=243 Arc-tdTomato+) (**Fig. 5.3.3C-D**).

Fig. 5.3.3: The baseline turnover rate was predictive whether neurons would become active or inactive during the EE. (**A-B**) Data plotted as cells, (**C-D**) Data plotted as dendrites. (**A**) Pairwise comparison of the turnover rate between Arc-tdTomato- and Arc-tdTomato+ (pairwise Mann-Whitney test, d2 p = 0.0407, d4 p = 0.0591, d7 p = 0.8730, d8 p = 0.9292, d9 p = 0.3265, d11 p > 0.9999, d14 p = 0.3265, n = 17 Arc-tdTomato-, n=16 Arc-tdTomato+). (**B**) Pooled data of day 2-7 and day 9-14 (Šidák multiple comparisons corrected Mann-Whitney test, baseline Arc-tdTomato- vs. Arc-tdTomato+ p = 0.0073, after EE Arc-tdTomato- vs. Arc-tdTomato+ p = 0.3399, Arc-tdTomato- baseline vs. after EE p = 0.0005, Arc-tdTomato+ baseline vs. after EE p = 0.8112; n = 51 Arc-tdTomato-, n=48 Arc-tdTomato+). (**C**) Pairwise comparison of the turnover rate between Arc-tdTomato- and Arc-tdTomato+ (pairwise Mann-Whitney test, d2 p = 0.0075, d4 p = 0.0021, d7 p = 0.1862, d8 p = 0.8905, d9 p = 0.8290, d11 p = 0.8430, d14 p = 0.7447, n = 54 Arc-tdTomato-, n = 81 Arc-tdTomato+). (**D**) Pooled data of day 2-7 and day 9-14 (Šidák multiple comparisons corrected Mann-Whitney test, baseline Arc-tdTomato- vs. Arc-tdTomato+ p <0.0001, after EE Arc-tdTomato- vs. Arc-tdTomato+ p = 0.6797, Arc-tdTomato- baseline vs. after EE p = 0.0003, Arc-tdTomato+ baseline vs. after EE p = 0.8977; n = 162 Arc-tdTomato-, n=243 Arc-tdTomato+). Blue bar indicates time point of 16h EE + 75 mg/kg TAM i.p.. * p ≤ 0.05, ** p ≤ 0.01, *** p ≤ 0.001, **** p < 0.0001

To understand which component of the turnover rate, either the gain or the loss would contribute most to the effect observed in the turnover rate, I split the data into fractional gain and fractional loss. The fractional gain was defined as the number of newborn spines divided by the total amount of spines on that day, whereas the fractional loss was defined as the number of lost spines divided by the total amount of spines on that day. I started with analyzing the fractional gain per day and found no significant difference between Arc-tdTomato- and Arc-tdTomato+ cells (pairwise Mann-Whitney test, d2 p = 0.1202, d4 p = 0.0591, d7 p = 0.2416, d8 p = 0.7971, d9 p = 0.0960, d11 p = 0.6567, d14 p = 0.7282, n = 17 Arc-tdTomato-, n=16 Arc-tdTomato+) (**Fig. 5.3.4A**). To get a more condensed view onto the data, I pooled time points 2-7 and 9-14 in order to identify major differences between the two groups but also to understand if each group would change through time. I found that the reduced fractional gain of prospective Arc-tdTomato+ neurons was predictive of whether a neuron would become activated during the EE. Additionally, this data showed a reduction of fractional gain in Arc-tdTomato- neurons after the EE compared to its own baseline (Šidák multiple comparisons corrected Mann-Whitney test, baseline Arc-tdTomato- vs. Arc-tdTomato+ p = 0.0025, after EE Arc-tdTomato- vs. Arc-tdTomato+ p = 0.1269, Arc-tdTomato- baseline vs. after EE p = 0.0001, Arc-tdTomato+ baseline vs. after EE p = 0.7943; n = 51 Arc-tdTomato-, n=48 Arc-tdTomato+) (**Fig. 5.3.4B**). Furthermore, I did the same analysis on the dendrite level and found that on day 4 Arc-tdTomato- cells showed a higher fractional gain compared to Arc-tdTomato+ (pairwise Mann-Whitney test, d2 p = 0.3816, d4 p = 0.0290, d7 p = 0.1117, n = 54 Arc-tdTomato-, n=81 Arc-tdTomato+). After the EE I did not observe any significant difference in the turnover rate between Arc-tdTomato- and Arc-tdTomato+ (pairwise Mann-Whitney test, d8 p = 0.5563, d9 p = 0.8046, d11 p = 0.6118, d14 p = 0.1211, n = 54 Arc-tdTomato-, n=81 Arc-tdTomato+) (**Fig. 5.3.4C**). Pooling time points 2-7 and 9-14 for the dendrites resulted in a similar, although slightly weaker, finding as for the cells (Šidák multiple comparisons corrected Mann-Whitney test, baseline Arc-tdTomato- vs. Arc-tdTomato+ p = 0.0074, after EE Arc-tdTomato- vs. Arc-tdTomato+ p = 0.4926, Arc-tdTomato- baseline vs. after EE p = 0.0028, Arc-tdTomato+ baseline vs. after EE p = 0.1171; n = 162 Arc-tdTomato-, n=243 Arc-tdTomato+) (**Fig. 5.3.4D**).
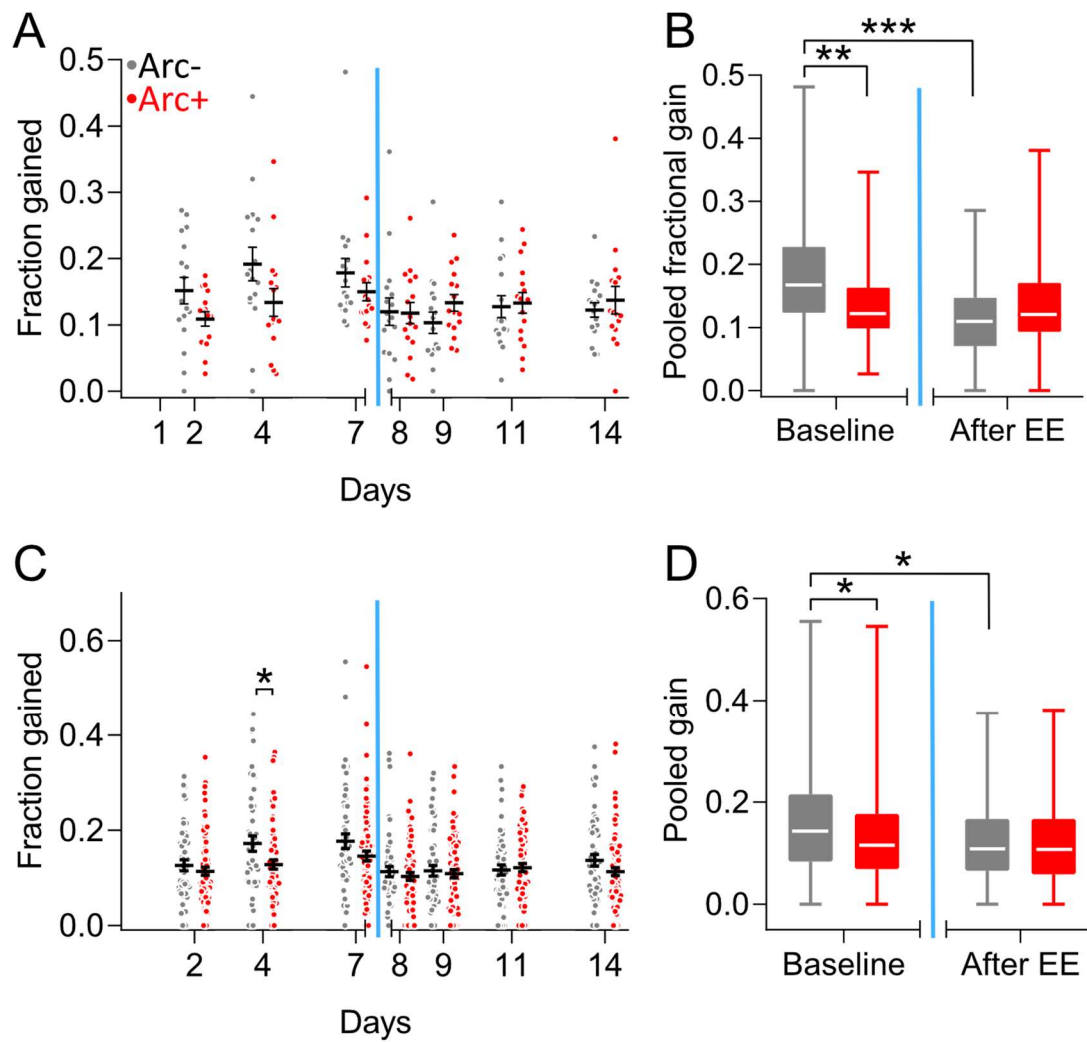
Fig. 5.3.4: The baseline fractional gain was predictive whether neurons would become active or inactive during the EE. (A-B) Data plotted as cells, (**C-D**) Data plotted as dendrites. (**A**) Pairwise comparison of the fractional gain between Arc-tdTomato- and Arc-tdTomato+ (pairwise Mann-Whitney test, d2 p = 0.1202, d4 p = 0.0591, d7 p = 0.2416, d8 p = 0.7971, d9 p = 0.0960, d11 p = 0.6567, d14 p = 0.7282, n = 17 Arc-tdTomato-, n=16 Arc-tdTomato+). (**B**) Pooled data of day 2-7 and day 9-14 (Šidák multiple comparisons corrected Mann-Whitney test, baseline Arc-tdTomato- vs. Arc-tdTomato+ p = 0.0025, after EE Arc-tdTomato- vs. Arc-tdTomato+ p = 0.1269, Arc-tdTomato- baseline vs. after EE p = 0.0001, Arc-tdTomato+ baseline vs. after EE p = 0.7943; n = 51 Arc-tdTomato-, n=48 Arc-tdTomato+). (**C**) Pairwise comparison of the fractional gain between Arc-tdTomato- and Arc-tdTomato+ (pairwise Mann-Whitney test, d2 p = 0.3816, d4 p = 0.0290, d7 p = 0.1117, d8 p = 0.5563, d9 p = 0.8046, d11 p = 0.6118, d14 p = 0.1211, n = 54 Arc-tdTomato-, n = 81 Arc-tdTomato+). (**D**) Pooled data of day 2-7 and day 9-14 (Šidák multiple comparisons corrected Mann-Whitney test, baseline Arc-tdTomato- vs. Arc-tdTomato+ p = 0.0074, after EE Arc-tdTomato- vs. Arc-tdTomato+ p = 0.4926, Arc-tdTomato- baseline vs. after EE p = 0.0028, Arc-tdTomato+ baseline vs. after EE p = 0.1171; n = 162 Arc-tdTomato-, n=243 Arc-tdTomato+). Blue bar indicates time point of 16h EE + 75 mg/kg TAM i.p.. * p ≤ 0.05, ** p ≤ 0.01, *** p ≤ 0.001

After having checked the contribution of the fractional gain to the turnover rate, the next feature was to check the fractional loss. I started with analyzing the fractional loss per day and found no significant difference between Arc-tdTomato- and Arc-tdTomato+ cells (pairwise Mann-Whitney test, d2 p = 0.1118, d4 p = 0.1820, d7 p = 0.8451, d8 p = 0.7625, d9 p = 0.7282, d11 p = 0.8525, d14 p = 0.3090, n = 17 Arc-tdTomato-, n=16 Arc-tdTomato+) (**Fig.**

5.3.5A). Next, I also pooled time points 2-7 and 9-14 in order to identify major differences between the two groups but also to understand if each group would change through time. I found no difference in the fractional loss between Arc-tdTomato- and Arc-tdTomato+ neurons neither before nor after the EE (Šidák multiple comparisons corrected Mann-Whitney test, baseline Arc-tdTomato- vs. Arc-tdTomato+ p = 0.0892, after EE Arc-tdTomato- vs. Arc-tdTomato+ p = 0.4254, Arc-tdTomato- baseline vs. after EE p = 0.0347, Arc-tdTomato+ baseline vs. after EE p = 0.8768; n = 51 Arc-tdTomato-, n=48 Arc-tdTomato+) (**Fig. 5.3.5B**). Furthermore, I did the same analysis on the dendrite level and found that on day 2 and 4 Arc-tdTomato- dendrites showed a higher fractional loss compared to Arc-tdTomato+ (pairwise Mann-Whitney test, d2 p = 0.0057, d4 p = 0.0234, d7 p = 0.5654, n = 54 Arc-tdTomato-, n=81 Arc-tdTomato+). After the EE I did not observe any significant difference in the turnover rate between Arc-tdTomato- and Arc-tdTomato+ (pairwise Mann-Whitney test, d8 p = 0.8799, d9 p = 0.9242, d11 p = 0.2580, d14 p = 0.3236, n = 54 Arc-tdTomato-, n=81 Arc-tdTomato+) (**Fig. 5.3.5C**). Pooling time points 2-7 and 9-14 for the dendrites revealed a significant difference in fractional loss of Arc-tdTomato- and Arc-tdTomato+ dendrites (Šidák multiple comparisons corrected Mann-Whitney test, baseline Arc-tdTomato- vs. Arc-tdTomato+ p = 0.0011, after EE Arc-tdTomato- vs. Arc-tdTomato+ p = 0.9862, Arc-tdTomato- baseline vs. after EE p = 0.0573, Arc-tdTomato+ baseline vs. after EE p = 0.1540; n = 162 Arc-tdTomato-, n=243 Arc-tdTomato+) (**Fig. 5.3.5D**).

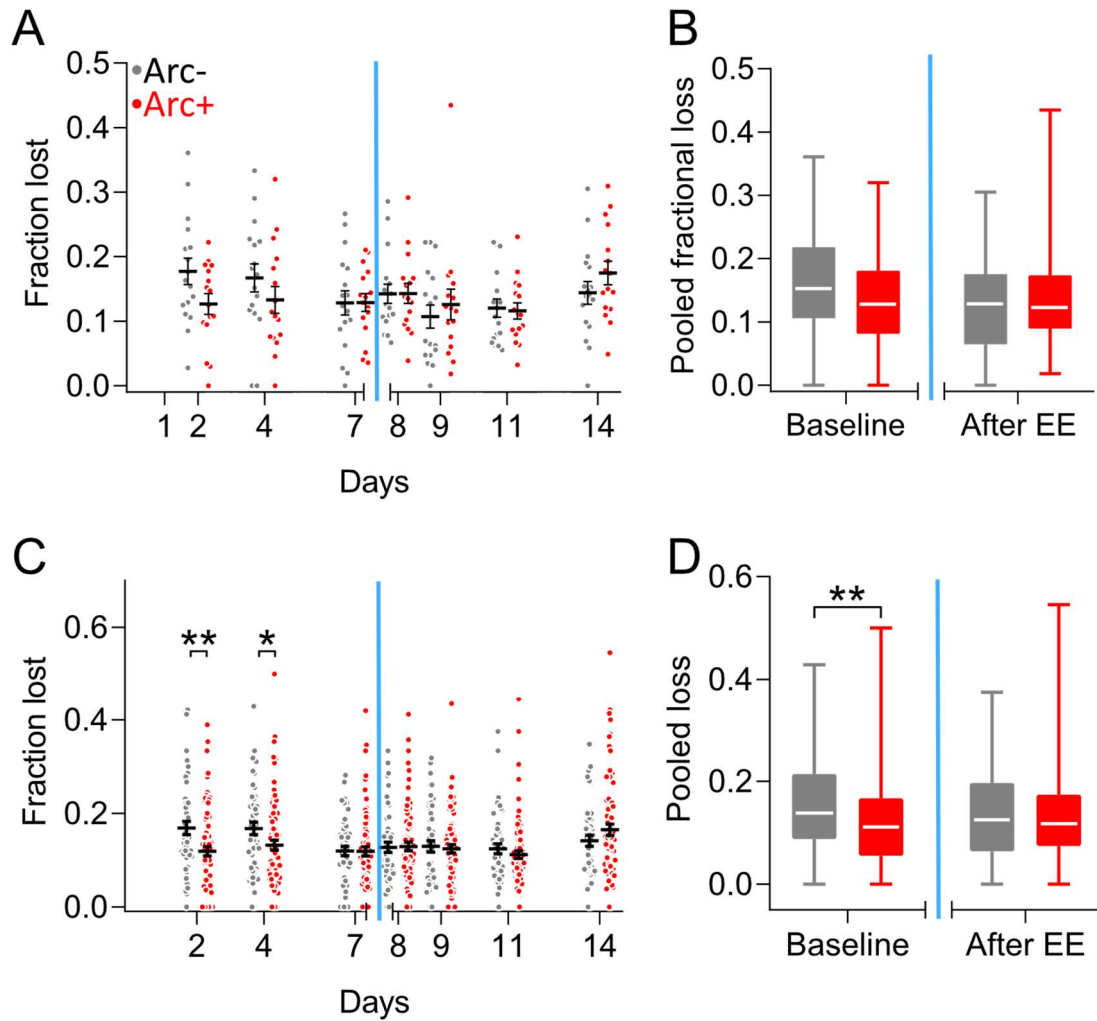**Fig. 5.3.5:** (**A-B**) Data plotted as cells, (**C-D**) Data plotted as dendrites. (**A**) Pairwise comparison of the fractional loss between Arc-tdTomato- and Arc-tdTomato+ (pairwise Mann-Whitney test, d2 p = 0.1118, d4 p = 0.1820, d7 p = 0.8451, d8 p = 0.7625, d9 p = 0.7282, d11 p = 0.8525, d14 p = 0.3090, n = 17 Arc-tdTomato-, n=16 Arc-tdTomato+). (**B**) Pooled data of day 2-7 and day 9-14 (Šidák multiple comparisons corrected Mann-Whitney test, baseline Arc-tdTomato- vs. Arc-tdTomato+ p = 0.0892, after EE Arc-tdTomato- vs. Arc-tdTomato+ p = 0.4254, Arc-tdTomato- baseline vs. after EE p = 0.0347, Arc-tdTomato+ baseline vs. after EE p = 0.8768; n = 51 Arc-tdTomato-, n=48 Arc-tdTomato+). (**C**) Pairwise comparison of the fractional loss between Arc-tdTomato- and Arc-tdTomato+ dendrites (pairwise Mann-Whitney test, d2 p = 0.0057, d4 p = 0.0234, d7 p = 0.5654, d8 p = 0.8799, d9 p = 0.9242, d11 p = 0.2580, d14 p = 0.3236, n = 54 Arc-tdTomato-, n = 81 Arc-tdTomato+). (**D**) Pooled data of day 2-7 and day 9-14 (Šidák multiple comparisons corrected Mann-Whitney test, baseline Arc-tdTomato- vs. Arc-tdTomato+ p = 0.0011, after EE Arc-tdTomato- vs. Arc-tdTomato+ p = 0.9862, Arc-tdTomato- baseline vs. after EE p = 0.0573, Arc-tdTomato+ baseline vs. after EE p = 0.1540; n = 162 Arc-tdTomato-, n=243 Arc-tdTomato+). Blue bar indicates time point of 16h EE + 75 mg/kg TAM i.p.. * p ≤ 0.05, ** p ≤ 0.01

To further test if the stability of connectivity was predictive whether a neuron would become active during the EE, I took the direct measure of the stability of connectivity by quantifying the surviving fraction of spines. The surviving fraction takes a defined amount of spines at any day and checks how many of this specified amount is still present the following day thus providing a direct readout of structural synaptic stability.

We started by measuring the surviving fraction of all spines on day 1 and at day 8 after the EE. This measurement revealed that prospective Arc-tdTomato+ neurons displayed more stable connectivity compared to prospective Arc-tdTomato- neurons. This was shown by having higher surviving fractions on day 2, 4 and 7 (mean day 2: Arc-tdTomato+: 0.8735, Arc-tdTomato-: 0.8228, mean day 4: Arc-tdTomato+: 0.7824, Arc-tdTomato-: 0.7015, mean day 7: Arc-tdTomato+: 0.7083, Arc-tdTomato-: 0.6355). Additionally, this measurement also indicated the effect that neuronal activity induced by EE led to a general increase in network stability. Spines of Arc-tdTomato- neurons underwent an increase in surviving fraction after the EE (mean day 2: 0.8228 vs. mean day 9: 0.8929, mean day 4: 0.7015vs. mean day 11: 0.8048, mean day 2: 0.6355 vs. mean day 14: 0.7290) (**Fig.5.3.6A**). To examine whether the observed difference in the surviving fraction was significant and thereby biologically relevant, I shuffled the identities of Arc-tdTomato- and Arc-tdTomato+ neurons for 10.000 times. I then calculated the 10.000 permutated absolute differences of the surviving fractions per day and asked whether the observed delta from my data would fall in- or outside the obtained distribution of the permutated absolute deltas. Doing this experiment for day 4 resulted in a significant difference between Arc-tdTomato- and Arc-tdTomato+ (**Fig.5.3.6B**). Using this technique to identify significant differences between prospective Arc-tdTomato- and Arc-tdTomato+ before the EE yielded a significant delta for day 2, and 4, but not for day 9, 11, and 14 (Šidák multiple comparisons corrected shuffled test, d2 p = 0.0166, d4 p = 0.0150, d7 p = 0.0369, d9 p = 0.2987, d11 p = 0.5592, d14 p = 0.2017). It also revealed a significant increase in the surviving fraction of spines belonging to Arc-tdTomato- after the EE which was not present for spines from Arc-tdTomato+ neurons (Šidák multiple comparisons corrected shuffled test, Arc-tdTomato- d2 vs. d9 p = 0.0024, d4 vs. d11 p = 0.0021, d7 vs. d14 p = 0.0022, Arc-tdTomato+ d2 vs. d9 p = 0.9967, d4 vs. d11 p = 0.9869, d7 vs. d14 p = 0.7440) (**Fig.5.3.6A).**
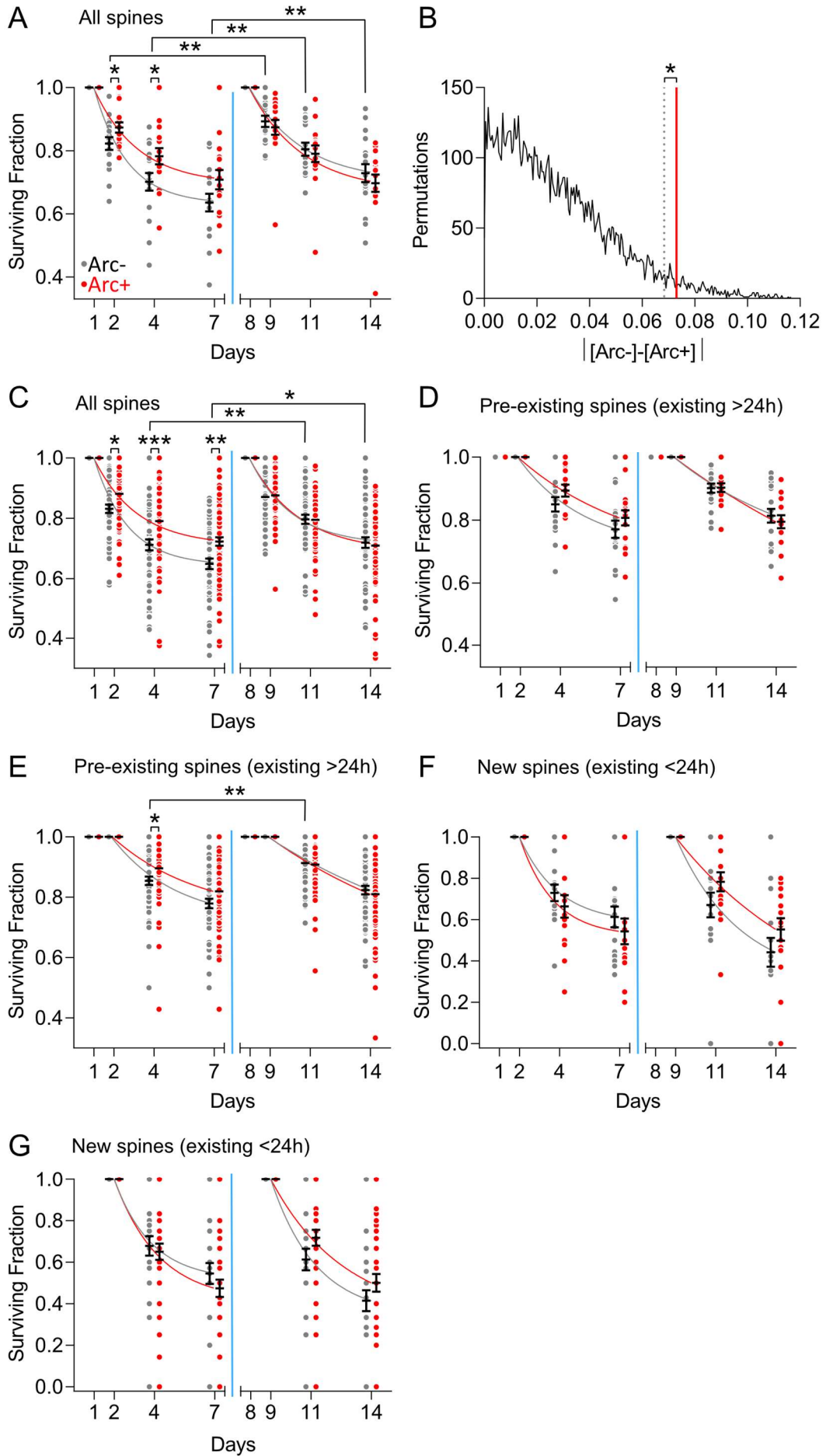
Fig. 5.3.6: Prospective Arc-tdTomato+ neurons display a more stable connectivity. (**A**) Prospective Arc-tdTomato+ neurons displayed a more stable connectivity of all spines compared to prospective Arc-tdTomato- neurons (Šidák multiple comparisons corrected shuffled test, d2 p = 0.0166, d4 p = 0.0150, d7 p = 0.0369, d9 p = 0.2987, d11 p = 0.5592, d14 p = 0.2017). Spines of Arc-tdTomato- neurons underwent an increase in surviving fraction after the EE (Šidák multiple comparisons corrected shuffled shuffled test, Arc-tdTomato- d2 vs. d9 p = 0.0024, d4 vs. d11 p = 0.0021, d7 vs. d14 p = 0.0022, Arc-tdTomato+ d2 vs. d9 p = 0.9967, d4 vs. d11 p = 0.9869, d7 vs. d14 p = 0.7440). (**B**) Shuffled data permutation of day 4 Arc-tdTomato- vs. Arc-tdTomato+ (p-value = 0.0150) Solid red line: actual delta on day 4. Dashed line: 5% boarder of distribution. (**C**) Prospective Arc-tdTomato+ dendrites displayed a more stable connectivity of all spines compared to prospective Arc-tdTomato- dendrites and spines of Arc-tdTomato- dendrites underwent an increase in surviving fraction after the EE (Šidák multiple comparisons corrected Mann-Whitney test, d2 p = 0.0057, d4 p = 0.0004, d7 p = 0.0020, d9 p = 0.9242, d11 p = 0.9652, d14 p = 0.9509, Arc-tdTomato- d2 vs. d9 p = 0.0635, d4 vs. d11 p = 0.0007, d7 vs. d14 p = 0.0135, Arc-tdTomato+ d2 vs. d9 p = 0.4341, d4 vs. d11 p = 0.9913, d7 vs. d14 p = 0.6441). (**D**) Pre-existing spines of Arc-tdTomato+ and Arc-tdTomato- neurons at day 2 and day 9 were not significantly different from each other (Šidák multiple comparisons corrected Mann-Whitney test, d4 p = 0.1115, d7 p = 0.2640, d11 p = 0.5998, d14 p = 0.5509, Arc-tdTomato- d4 vs. d11 p = 0.0440, d7 vs. d14 p = 0.2415, Arc-tdTomato+ d4 vs. d11 p = 0.9038, d7 vs. d14 p = 0.8381). (**E**) Pre-existing spines of dendrites at day 2 and day 9 indicated that prospective Arc-tdTomato+ dendrites displayed a more stable connectivity of pre-existing compared to prospective Arc-tdTomato- dendrites and pre-existing spines of Arc-tdTomato- dendrites underwent an increase in surviving fraction after the EE (Šidák multiple comparisons corrected Mann-Whitney test, d4 p = 0.0091, d7 p = 0.0315, d11 p = 0.5452, d14 p = 0.7194, Arc-tdTomato- d4 vs. d11 p = 0.0017, d7 vs. d14 p = 0.0443, Arc-tdTomato+ d4 vs. d11 p = 0.5342, d7 vs. d14 p = 0.6817). (**F-G**) Newborn spines of neurons and dendrites at day 2 and day 9 did not show that prospective Arc-tdTomato+ cells displayed a more stable connectivity of newborn spines compared to prospective Arc-tdTomato- cells and that newborn spines of Arc-tdTomato- dendrites did not undergo an increase in surviving fraction after the EE. But there was a slight, but not significant, stabilization of newborn spines of Arc-tdTomato+ after the EE (Neuron: Šidák multiple comparisons corrected Mann-Whitney test, d4 p = 0.3448, d7 p = 0.2226, d11 p = 0.1439, d14 p = 0.1343 ; Dendrite: d4 p = 0.6862, d7 p = 0.2213, d11 p = 0.0933, d14 p = 0.1716). Blue bar indicates time point of 16h EE + 75 mg/kg TAM i.p.. Solid lines second order exponential decay fit to data. * p ≤ 0.05, ** p ≤ 0.01, *** p ≤ 0.001

We further analyzed if the observed effect would also be true if I analyzed the numbers as dendrites compared to as neurons. Indeed I found the exact relationship between Arc-tdTomato- and Arc-tdTomato+ dendrites before the EE and I duplicated the finding of the EE stabilizing the surviving fraction of Arc-tdTomato- dendrites after EE (Šidák multiple comparisons corrected Mann-Whitney test, d2 p = 0.0057, d4 p = 0.0004, d7 p = 0.0020, d9 p = 0.9242, d11 p = 0.9652, d14 p = 0.9509, Arc-tdTomato- d2 vs. d9 p = 0.0635, d4 vs. d11 p = 0.0007, d7 vs. d14 p = 0.0135, Arc-tdTomato+ d2 vs. d9 p = 0.4341, d4 vs. d11 p = 0.9913, d7 vs. d14 p = 0.6441) (**Fig.5.3.6C).** Moreover, I were wondering how differently aged spines would contribute to the observed difference of prospective Arc-tdTomato+ neurons and dendrites before the EE and the increased stabilization of Arc-tdTomato- after the EE. For this, I split my analysis in spines that existed for at least 24 hours (pre-existing) and spines that were newborn and existed shorter than 24 hours. Starting with pre-existing spines of neurons at day 2 and day 9 I did not identify any contribution of this class to the previous finding of all spines at day 1 and day 8 (Šidák multiple comparisons corrected Mann-Whitney

test, d4 p = 0.1115, d7 p = 0.2640, d11 p = 0.5998, d14 p = 0.5509, Arc-tdTomato- d4 vs. d11 p = 0.0440, d7 vs. d14 p = 0.2415, Arc-tdTomato+ d4 vs. d11 p = 0.9038, d7 vs. d14 p = 0.8381) (**Fig.5.3.6D**). However, analyzing pre-existing spines of dendrites at day 2 and day 9 indicated a similar finding compared to all spines on day 1 and day 8. Pre-existing spines of prospective Arc-tdTomato+ neurons displayed a slightly more stable connectivity compared to pre-existing spines of prospective Arc-tdTomato- neurons. The effect that neuronal activity induced by EE would lead to an increase of stability of the network could also be verified measuring the surviving fraction of pre-existing spines of dendrites (Šidák multiple comparisons corrected Mann-Whitney test, d4 p = 0.0091, d7 p = 0.0315, d11 p = 0.5452, d14 p = 0.7194, Arc-tdTomato- d4 vs. d11 p = 0.0017, d7 vs. d14 p = 0.0443, Arc-tdTomato+ d4 vs. d11 p = 0.5342, d7 vs. d14 p = 0.6817) (**Fig.5.3.6E**). Finally I analyzed the data from newborn spines (spines existing less than 24 hours) to understand their contribution to the difference in stability of prospective Arc-tdTomato+ compared to prospective Arc-tdTomato- neurons. I didn't find any significant difference between the two surviving fractions of prospective Arc-tdTomato+ and Arc-tdTomato- neurons (Šidák multiple comparisons corrected Mann-Whitney test, d4 p = 0.3448, d7 p = 0.2226) (**Fig.5.3.6F**) or dendrites (Šidák multiple comparisons corrected Mann-Whitney test, d4 p = 0.6862, d7 p = 0.2213) (**Fig.5.3.6G**). However, after the EE, I identified a slight trend, even though not significant, of stabilization of newborn spines of Arc-tdTomato+ compared to Arc-tdTomato-. This small effect was present for cells (Šidák multiple comparisons corrected Mann-Whitney test, d11 p = 0.1439, d14 p = 0.1343) (**Fig.5.3.6F**) and dendrites (Šidák multiple comparisons corrected Mann-Whitney test, d11 p = 0.0933, d14 p = 0.1716) (**Fig.5.3.6G**). On the other hand, EE did not stabilize the network connectivity of inactive Arc-tdTomato- neurons after the EE (Šidák multiple comparisons corrected Mann-Whitney test, Arc-tdTomato- d4 vs. d11 p = 0.5953, d7 vs. d14 p = 0.0872, Arc-tdTomato+ d4 vs. d11 p = 0.0935, d7 vs. d14 p = 0.3753) (**Fig.5.3.6F**) (Šidák multiple comparisons corrected Mann-Whitney test, Arc-tdTomato- d4 vs. d11 p = 0.3966, d7 vs. d14 p = 0.0614, Arc-tdTomato+ d4 vs. d11 p = 0.1926, d7 vs. d14 p = 0.5400) (**Fig.5.3.6G**).

Summarizing the data shown so far, I found that the stability of connectivity of neurons predicted if a neuron would become activated and thereby becoming part of the neuronal representation of the environment. This was demonstrated by the decreased turnover rate, fractional gain, and loss already during baseline of prospective Arc-tdTomato+ neurons

compared to prospective Arc-tdTomato- neurons and most importantly by showing the higher surviving fraction of spines of prospective Arc-tdTomato+ neurons compared to prospective Arc-tdTomato- neurons. Furthermore, I identified that a potent trigger of neuronal activity, here I used an EE, was able to lead to increased stabilization of the network connectivity even of cells that were not directly activated and part of the neuronal representation. Evidence for this was indicated by the decreased turnover rate and fractional gain of Arc-tdTomato- neurons after the EE. Additional proof was brought by the increased surviving fraction of all and pre-existing spines of Arc-tdTomato- neurons after the EE.

5.4 Growth of Newborn Spines Predicted Neuronal Activity

We added another layer of complexity to my data by not only checking the presence or absence of dendritic spines but also by measuring their size (Methods 4.8). This information helped me judging if the increase in surviving fraction of all spines of prospective Arc-tdTomato+ neurons compared to prospective Arc-tdTomato- neurons was due to increased detectability due to a larger spine size.

We found no significant difference in spine size between Arc-tdTomato+ (mean spine size: 0.9554) and Arc-tdTomato- neurons (mean spine size: 0.8585) neither before nor after the EE (Šidák multiple comparisons corrected Mann-Whitney test, baseline Arc-tdTomato- vs. Arc-tdTomato+ p = 0.3303, after EE Arc-tdTomato- vs. Arc-tdTomato+ p = 0.4453, Arc-tdTomato- baseline vs. after EE p = 0.1431, Arc-tdTomato+ baseline vs. after EE p = 0.1921; n = 120 Arc-tdTomato-, n = 120 Arc-tdTomato+) (**Fig. 5.4.1A**). To overcome any sampling differences and to detect any major change in spine size I also normalized each spine size to its original value at the beginning. When I compared each single median per day through time against the median of the 14 days I did not find any differences through time in Arc-tdTomato- Arc-tdTomato+ spines (one sample Wilcoxon test each day; Arc-tdTomato- d2 p = 0.1642, d4 p = 0.8236, d7 p = 0.0803, d8 p = 0.6263, d9 p = 0.6702, d11 p = 0.7611, d14 p = 0.2206, Arc-tdTomato+ d2 p = 0.4522, d4 p = 0.1460, d7 p > 0.9999, d8 p = 0.8078, d9 p = 0.6408, d11 p = 0.6120, d14 p = 0.5291) (**Fig. 5.4.1B**).

Furthermore, I asked if the EE would affect the size of newborn spines (spines that existed for less than 24h prior to the first detection). I did not detect a significant difference in the

pooled raw spine sizes of prospective Arc-tdTomato- (mean spine size: 0.8674) and prospective Arc-tdTomato+ (mean spine size: 0.8494) and Arc-tdTomato- (mean spine size: 0.8748) and Arc-tdTomato+ (mean spine size: 0.7707) after the EE (Šidák multiple comparisons corrected Mann-Whitney test, baseline Arc-tdTomato- vs. Arc-tdTomato+ p = 0.7568, after EE Arc-tdTomato- vs. Arc-tdTomato+ p = 0.3737, Arc-tdTomato- baseline vs. after EE p = 0.7159, Arc-tdTomato+ baseline vs. after EE p = 0.3799; n = 90 Arc-tdTomato-, n = 90 Arc-tdTomato+)(**Fig. 5.4.1C**). Comparing each single median per day through time against the median of the 14 days did also not reveal any differences through time in Arc-tdTomato- Arc-tdTomato+ spines (one sample Wilcoxon test each day; Arc-tdTomato- d2 p = 0.2894, d4 p = 0.8872, d7 p = 0.2449, d9 p = 0.1294, d11 p = 0.9677, d14 p = 0.2286, Arc-tdTomato+ d2 p = 0.9838, d4 p = 0.3387, d7 p = 0.1642, d9 p = 0.8553, d11 p = 0.3387, d14 p = 0.5561) (**Fig. 5.4.1C**). When I normalized the spine size of newborn spines to d2 and d9 after the EE I discovered that spines of Arc-tdTomato+ neurons significantly increased in size in 5 days compared to their baseline (one sample t-test each day against the normalized value 1; Arc-tdTomato+ d4 p = 0.0640, d7 p = 0.0496, d11 p = 0.0590, d14 p = 0.0469) while spines of Arc-tdTomato- did not increase their size significantly (one sample t-test each day against the normalized value 1; Arc-tdTomato- d4 p = 0.6955, d7 p = 0.1428, d11 p = 0.8443, d14 p = 0.1164) (**Fig. 5.4.1D**).
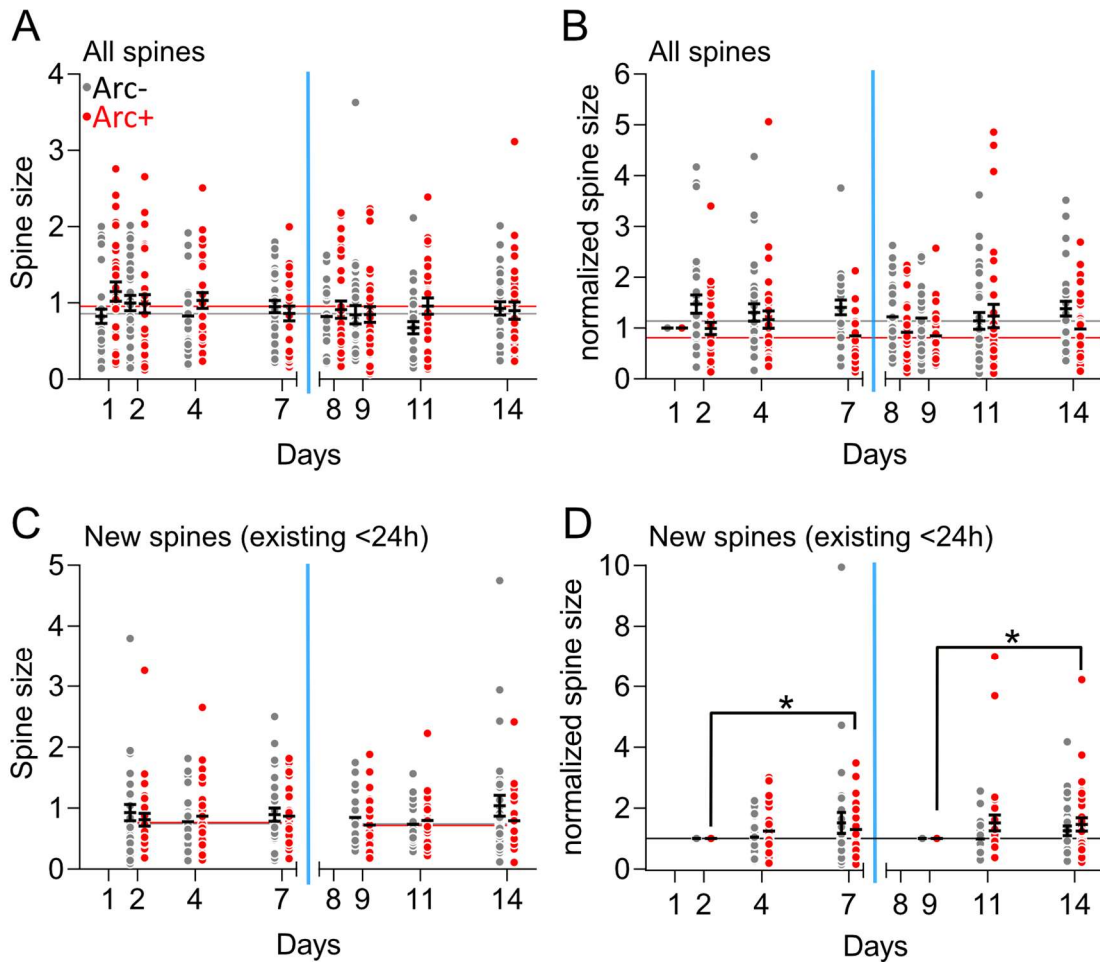
Fig. 5.4.1: (**A**) Raw spine size are stable through time (Šidák multiple comparisons corrected Mann-Whitney test, baseline Arc-tdTomato- vs. Arc-tdTomato+ p = 0.3303, after EE Arc-tdTomato- vs. Arc-tdTomato+ p = 0.4453, Arc-tdTomato- baseline vs. after EE p = 0.1431, Arc-tdTomato+ baseline vs. after EE p = 0.1921; n = 120 Arc-tdTomato-, n = 120 Arc-tdTomato+). (**B**) Normalized spine sizes are stable through time (one sample Wilcoxon test each day; Arc-tdTomato- d2 p = 0.1642, d4 p = 0.8236, d7 p = 0.0803, d8 p = 0.6263, d9 p = 0.6702, d11 p = 0.7611, d14 p = 0.2206, Arc-tdTomato+ d2 p = 0.4522, d4 p = 0.1460, d7 p > 0.9999, d8 p = 0.8078, d9 p = 0.6408, d11 p = 0.6120, d14 p = 0.5291, n=30). (**C**) The size of newborn spines of Arc-tdTomato- and Arc-tdTomato+ is not different and does not change after the EE (Šidák multiple comparisons corrected Mann-Whitney test, baseline Arc-tdTomato- vs. Arc-tdTomato+ p = 0.7568, after EE Arc-tdTomato- vs. Arc-tdTomato+ p = 0.3737, Arc-tdTomato- baseline vs. after EE p = 0.7159, Arc-tdTomato+ baseline vs. after EE p = 0.3799; n = 90 Arc-tdTomato-, n = 90 Arc-tdTomato+). The size of newborn spines is stable through time (one sample Wilcoxon test each day; Arc-tdTomato- d2 p = 0.2894, d4 p = 0.8872, d7 p = 0.2449, d9 p = 0.1294, d11 p = 0.9677, d14 p = 0.2286, Arc-tdTomato+ d2 p = 0.9838, d4 p = 0.3387, d7 p = 0.1642, d9 p = 0.8553, d11 p = 0.3387, d14 p = 0.5561). (**D**) Newborn spines of Arc-tdTomato+ neurons significantly increase their size in 5 days (one sample t-test each day against the normalized value 1; Arc-tdTomato+ d4 p = 0.0640, d7 p = 0.0496, d11 p = 0.0590, d14 p = 0.0469; Arc-tdTomato- d4 p = 0.6955, d7 p = 0.1428, d11 p = 0.8443, d14 p = 0.1164). Blue bar indicates timepoint of 16h EE + 75 mg/kg TAM i.p.. Solid lines medians either over the whole period or epochs. * p ≤ 0.05, ** p ≤ 0.01, *** p ≤ 0.001, **** p < 0.0001

To validate the previous findings that the growth of spines over 5 days could predict whether this spine belonged to an Arc-tdTomato+ or Arc-tdTomato- neuron I pooled the data of baseline and after EE and measured if the spine size would be significantly different from its

normalized value. Indeed I could show that spines born on Arc-tdTomato+ neurons grew significantly larger while spines born on Arc-tdTomato- neurons did not significantly increase in size (one sample Wilcoxon test against 1; Arc-tdTomato- baseline p = 0.5033, Arc-tdTomato- after EE p = 0.7897, Arc-tdTomato+ baseline p = 0.0312, Arc-tdTomato+ after EE p = 0.0343) (**Fig.5.4.2A**).
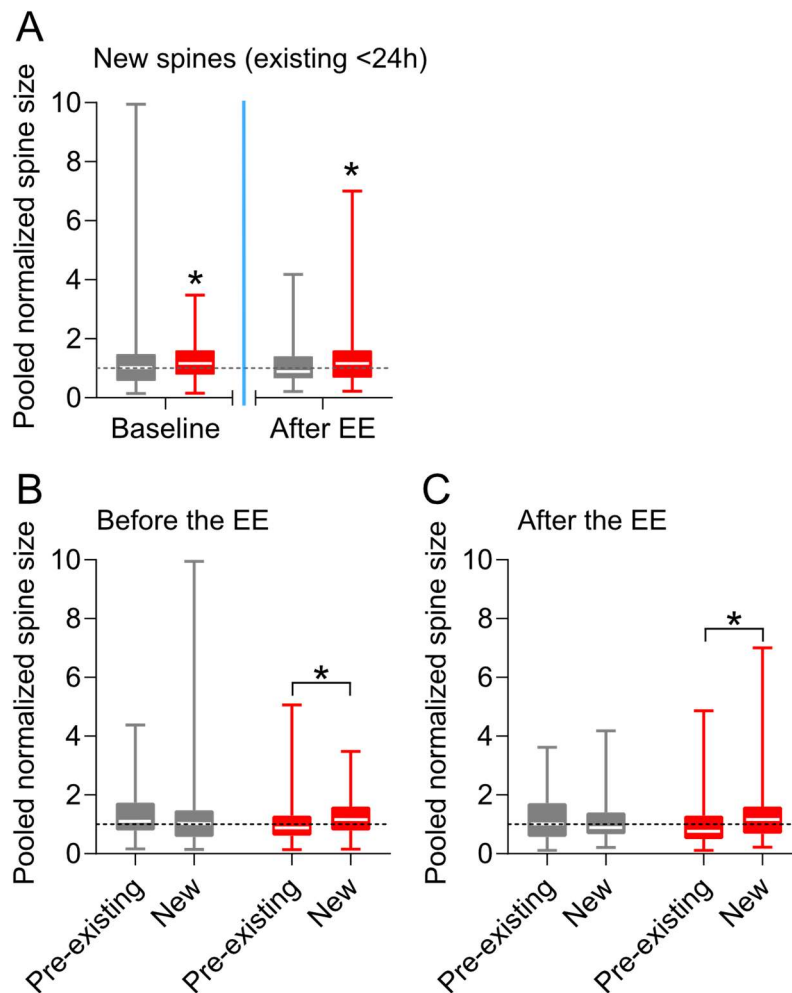

Fig. 5.4.2: The growth in spine size of newborn spines is specific to Arc-tdTomato+ neurons. (**A**) Newborn spines of Arc-tdTomato- do not grow their size but newborn spines of Arc-tdTomato+ do grow. (one sample Wilcoxon test against 1; Arc-tdTomato- baseline p = 0.5033, Arc-tdTomato- after EE p = 0.7897, Arc-tdTomato+ baseline p = 0.0312, Arc-tdTomato+ after EE p = 0.0343). (**B-C**) The growth of newborn spines of Arc-tdTomato= neurons is specific to newborn spines but not to pre-existing spines (Mann-Whitney test, Baseline, Arc-tdTomato- pre-existing vs. newborn p = 0.1547, Arc-tdTomato+ pre-existing vs. newborn p = 0.0391, after EE, Arc-tdTomato- pre-existing vs. newborn p = 0.4816, Arc-tdTomato+ pre-existing vs. newborn p = 0.0144). Blue bar indicates time point of 16h EE + 75 mg/kg TAM i.p.. Dashed line at 1, normalized spine size. * p ≤ 0.05

To understand whether the growth of newborn spines was a general feature of Arc-tdTomato+ neurons and also applied to the pre-existing spines, I directly compared the normalized size of newborn spines to the normalized size of pre-existing spines. Only newborn spines of Arc-tdTomato+ neurons showed the specific growth in size both before

and after the EE, pre-existing spines of Arc-tdTomato+ neurons did not grow in size while spines from Arc-tdTomato- neurons did not grow at all (Mann-Whitney test, Baseline, Arc-tdTomato- pre-existing vs. newborn p = 0.1547, Arc-tdTomato+ pre-existing vs. newborn p = 0.0391, after EE, Arc-tdTomato- pre-existing vs. newborn p = 0.4816, Arc-tdTomato+ pre-existing vs. newborn p = 0.0144)(**Fig.5.4.2B-C**).

This data gives evidence that not only spines of prospective Arc-tdTomato+ neurons have more stable connectivity, but also that newly formed connections but not pre-existing connections independent of whether they are formed before or after the EE are being potentiated specifically in Arc-tdTomato+ neurons.

5.5 Stochastic Labeling of Glutamatergic Neurons

The observed findings that structural synaptic stability predicted if a CA1 pyramidal neuron became active and part of the neuronal representation of an environment and that a potent trigger of hippocampal network activity led to a stabilization of the entire network including the neurons that were inactive during the time point of activity-dependent labeling are built on a couple of assumptions. To prove that my findings were activity related, I needed to rule out that any side-effects from longitudinal 2-photon imaging, i.p. TAM injection and expression of the marker protein tdTomato would not have influenced synaptic stability.

For this reason, I aimed for a system that would be regulated by TAM injection, result in tdTomato expression in a subset of neurons, but would be ultimately activity independent. To implement all these conditions in one experiment, I decided to use Nex-Cre^{ERT2}; Thy1-eGFP; Ai9 mice, which I specifically crossed for this experiment. Nex-Cre^{ERT2}-mice express the TAM dependent Cre-recombinase under the endogenous promoter/enhancer elements of Neurod6 (Nex). This is a developmental marker of glutamatergic neurons, which is still highly expressed in the hippocampus during adulthood. TAM administration leads to a dosage-dependent activation of Cre, which in turn results in dosage dependent tdTomato expression - low TAM concentration resulting in sparse and high TAM concentration in dense recombinase activity and tdTomato label. By using this technique, I was able to label a subset of CA1 pyramidal neurons with tdTomato by stochastic means by merely manipulating the administered TAM concentration. This method resulted in having two

populations of neurons within the same brain tissue - eGFP-positive cells (green alone) and tdTomato double-positive cells (yellow, as a result of green and red). However, the only difference between these two populations was the stochastic probability of the Cre^{ERT2} to become active.

We first tested whether neuronal activity induced by EE would not lead to a significant increase in the number of Nex-tdTomato+ neurons. To this aim, I injected i.p. two groups of in Nex-Cre^{ERT2}; Ai9 mice; with a single dose of 75 mg/kg, to match it to the concentration I previously used for the activity-dependent labeling. Immediately after the injection, one group of mice explored an EE for 2h, and one group was housed in their home cages (HC) (**Fig. 5.5.1A**). I sacrificed all animals 10 days after TAM injection and quantified the percentage of pyramidal neurons expressing tdTomato by confocal microscopy (**Fig. 5.5.1B**). Quantifying the confocal images, verified that the expression of Nex-tdTomato was neuronal activity-independent leading to the same amount of tdTomato+ neurons of HC and EE mice. This was in contrast to what was observed earlier using activity-dependent labeling if Arc-Cre^{ERT2}; Ai9 mice. (**Fig. 5.1.3C**).
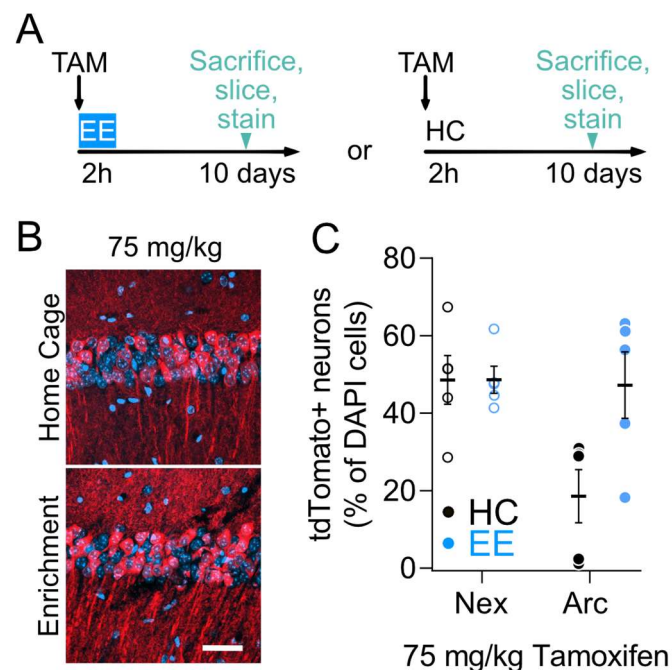

Fig. 5.5.1: (A) Experimental scheme illustrating the timeline of the *ex vivo* characterization of Nex-Cre^{ERT2}; Ai9-mice. Mice received 75 mg/kg TAM i.p. and either explored an EE for two hours or were put back into their HC. 10 days later mice were sacrificed, brain sections were taken and stained with the nuclear marker DAPI. **(B)** Representative confocal images of the dorsal CA1 of Nex-Cre^{ERT2}; Ai9-mice that either explored an EE or their HC. Images display 1 z-plane showing Nex-tdTomato positive cells over all DAPI-positive cells. Scale bar 100 μm. **(C)** Quantification of Nex -tdTomato positive cells over all DAPI-positive cells. The EE did not have

any effect on the number of Nex-tdTomato+ neurons. Empty circles Nex-mice, solid circles Arc-mice; n=5 mice

Having found, that the Nex-Cre^{ERT2}; Thy1-eGFP; Ai9 could be a powerful tool to test for the potential side-effects from longitudinal 2-photon imaging, i.p. TAM injection and expression of the marker protein tdTomato I moved on into the *in vivo* imaging experiment.

For this, I implanted an imaging cannula dorsal to the CA1 of the hippocampus and imaged dendritic branches and their spines of eGFP-positive pyramidal neurons of Nex-Cre^{ERT2}; Thy1-eGFP; Ai9 mice. After one week during which I imaged on day 1, 2, 4 and 7, I injected the mice with a single dosage of 75mg/kg TAM to label a stochastic population of excitatory neurons with tdTomato. On day 8 mice were continued to be imaged using the same imaging intervals as during the first week (day 8, 9, 11, 14). On day 15, all mice underwent a hippocampus-dependent trace fear conditioning. Finally, on the last day of the experiment, on day 16, mice were probed for their memory to the context and tone (**Fig. 5.5.2**).
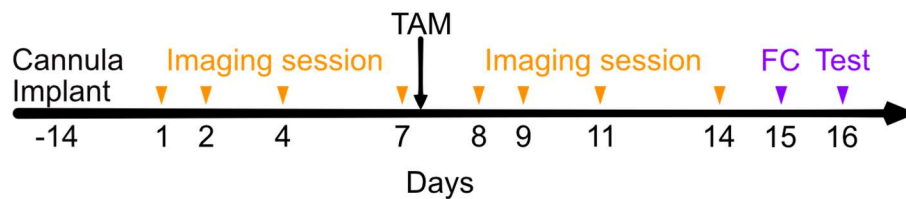
Fig. 5.5.2: Experimental timeline of the *in vivo* imaging experiment. 14 days after the implantation of the imaging cannula mice were imaged for one week to capture baseline synaptic plasticity. After one week, I gave them a single i.p. TAM injection of 75mg/kg to label random neurons with tdTomato. I continued imaging for another week, keeping the same imaging intervals as during the first week. After the two weeks of imaging, mice also underwent a trace fear conditioning experiment on days 15 and 16.

We imaged a random population of dendrites belonging to eGFP positive neurons. Because the main idea of this experiment was to control for TAM-dependent tdTomato expression, at day 1, I checked for tdTomato baseline expression to avoid imaging dendrites coming from neurons that were already positive for tdTomato. I continued imaging the same dendritic branches that I chose on day 1 for the next 14 days. Finally, on the last day of imaging, I verified to see increased tdTomato expression after TAM injection. Additionally, this imaging session was used to determine which of the neurons that I kept imaging for 2 weeks became tdTomato positive after TAM injection. The Nex-Cre^{ERT2}; Thy1-eGFP; Ai9 animals revealed a sparse label of Thy1-eGFP of pyramidal neurons in the *stratum pyramidiale in vivo*. It also showed leakiness of the Nex-Cre^{ERT2}; Ai9 system resulting in a sparse tdTomato expression during baseline even without the presence of TAM (**Fig. 5.5.3**). The activation of the

Tamoxifen-dependent, Cre-recombinase yielded a substantial increase in the number of tdTomato-positive neurons. This *in vivo* result strongly resembled the findings from the quantification of the *ex vivo* experiment conducted before (**Fig. 5.5.1B-C**). In the end, I could identify three classes of neurons; neurons that stayed only eGFP positive (arrowhead - eGFP+/tdTomato-), neurons that started to express tdTomato (arrow - eGFP+/tdTomato+) and neurons that expressed tdTomato from the beginning which could also be followed through time (asterisk – eGFP-/tdTomato+) (**Fig. 5.5.3**).
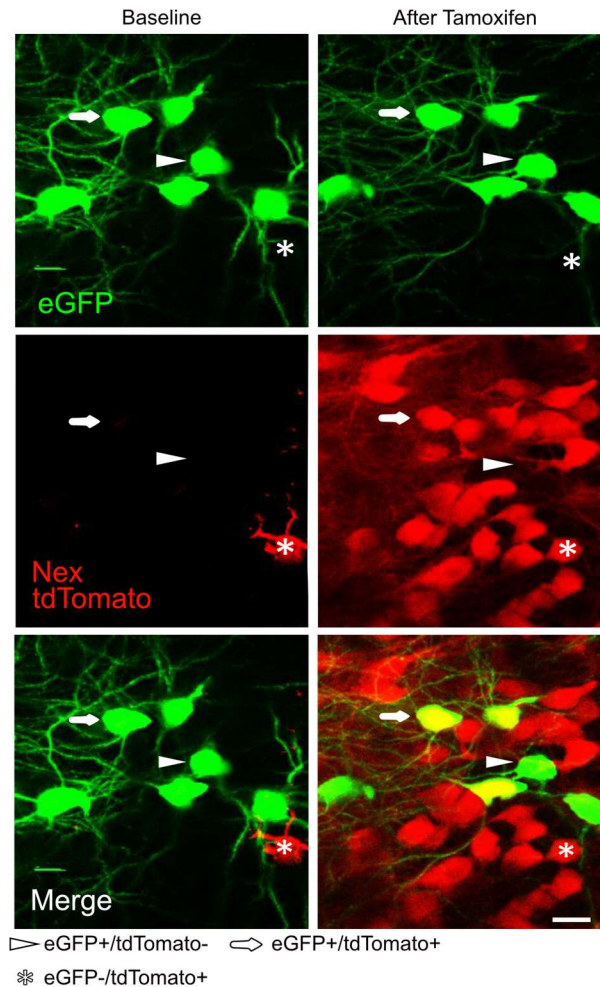
Fig. 5.5.3: Labeling dCA1 pyramidal neurons using tdTomato *in vivo*. Left: Baseline Thy1-eGFP and tdTomato expression prior to TAM administration. Note, leakiness of tdTomato expression even without TAM. Right: Substantial increase in the number of tdTomato-positive neurons. Also leading to double positive (eGFP+/tdTomato+) neurons. Arrowhead - eGFP+/tdTomato- neuron, arrow - eGFP+/tdTomato+ neurons asterisk – eGFP-/tdTomato+ neurons.

Since this data resembled the labeling using Arc-Cre[ERT2]; Thy1-eGFP; Ai9 in combination with neuronal activation and activity-dependent labeling after exposure to 16 hours of EE, I was confident that the imaging experiment of Nex-Cre[ERT2]; Thy1-eGFP; Ai9 would help me to rule

out any side-effects from longitudinal 2-photon imaging, i.p. TAM injection and expression of the marker protein tdTomato would not influence synaptic stability.

5.6 No Effect of tdTomato Expression onto Structural Synaptic Plasticity

We imaged 6 Nex-Cre[ERT2]; Thy1-eGFP; Ai9 mice of which 1 was a male and 5 were females. Out of the 6 mice, I followed 23 neurons within which 10 stayed eGFP+, 11 became Nex-tdTomato+, and 2 were either already tdTomato positive from baseline or were outside the field of view so that it was impossible to identify whether they became tdTomato+ or not. Out of these 23 neurons, I imaged 108 dendritic segments – 61 were Nex-tdTomato-, 44 tdTomato+ and 3 belonged to neurons that already expressed tdTomato from baseline or could not be traced back to their somata (**Table 5.6.1**).

Table 5.6.1: Summary of mice, cells, and dendrites imaged and used for the activity driven tdTomato labeling of neurons and the stochastically random tdTomato labeling of neurons using the Nex- instead of the Arc-promoter.

Genotype	Mice	Sex	Imaged Cells		Imaged Dendrites		Used Cells		Used Dendrites	
Nex	6	1 ♂	21	10 Nex-	105	61 Nex-	15	9 Nex-	67	42 Nex-
		5 ♀		11 Nex+		44 Nex+		6 Nex+		25 Nex+

Also, for this experiment, I needed to exclude several dendritic segments. This brought my experimental numbers down to 15 neurons, of which 6 became Nex-tdTomato positive and 57 dendrites within which 25 belonged to the Nex-tdTomato+ neurons (**Tab. 5.3.1**).

The first characteristic that I analyzed was the spine density of Nex-tdTomato negative versus positive neurons. Also here, I decided to quantify my data as neurons and dendrites. I found, when plotting cells, the density of Nex-tdTomato positive neurons was significantly lower compared to Nex-tdTomato negative neurons (Mean densities: Nex-tdTomato+: 0.8573 spines/µm, Nex-tdTomato-: 1.041 spines/µm) (Mann-Whitney test, $p < 0.0001$, n = 9 Nex-tdTomato-, n = 6 Nex-tdTomato+) but spine densities were unchanged on all days after TAM injection (one sample Wilcoxon test each day against respective median baseline densities; Nex-tdTomato- D8 $p = 0.8203$, D9 $p > 0.9999$, D11 $p = 0.9102$, D14 $p = 0.7344$, Nex-tdTomato+ D8 $p = 0.5625$, D9 $p = 0.3125$, D11 $p = 0.2188$, D14 $p = 0.5625$) (**Fig. 5.6.1A**). When plotting dendrites, the density of Nex-tdTomato+ dendrites was still different compared to Nex-tdTomato- dendrites (Mean densities: Nex-tdTomato+: 0.8376 spines/µm,

Nex-tdTomato-: 1.018 spines/µm) (pairwise Mann-Whitney test, p < 0.0001, n = 42 Nex-tdTomato-, n = 25 Nex-tdTomato+) and also spine densities were unchanged on all days after the TAM injection (one sample Wilcoxon test each day against respective median baseline densities; Nex-tdTomato- D8 p = 0.1668, D9 p = 0.3785, D11 p = 0.2124, D14 p = 0.2136, Nex-tdTomato+ D8 p = 0.2635, D9 p = 0.3388, D11 p = 0.4418, D14 p = 0.9789) (**Fig. 5.6.1B**).
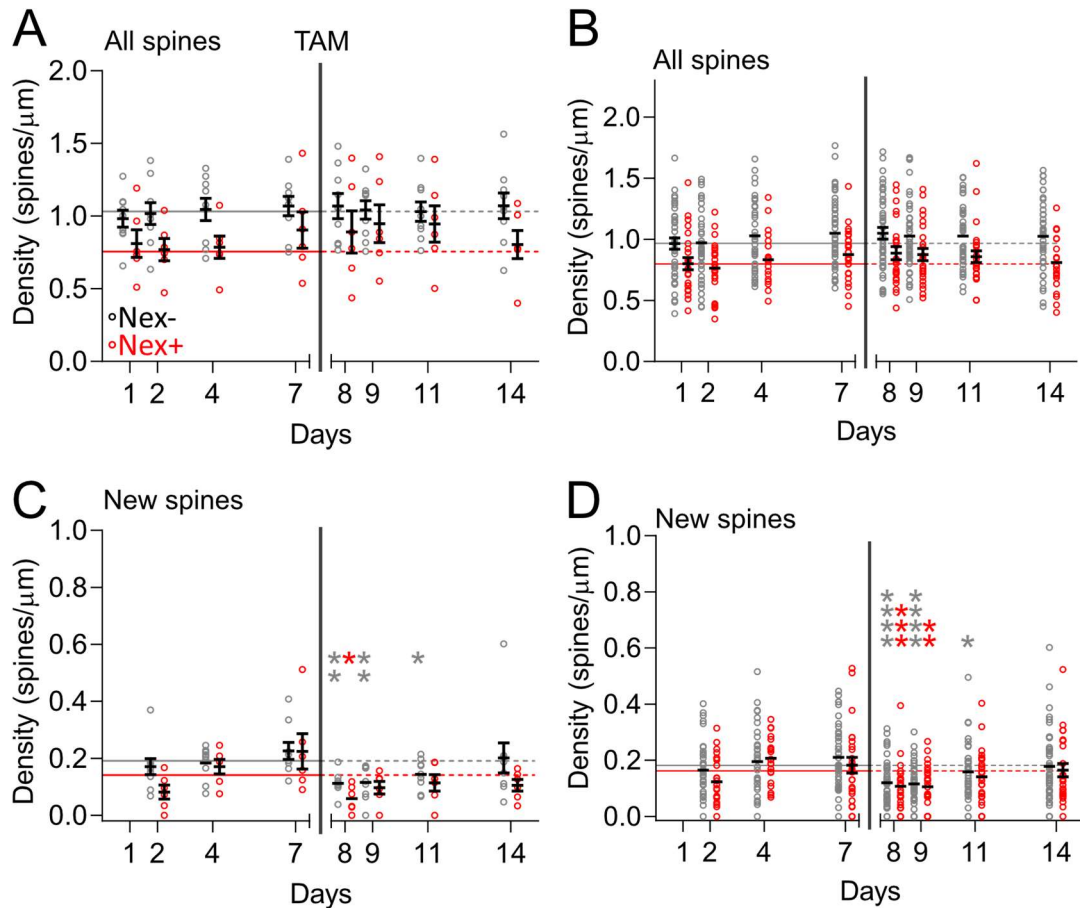

Fig. 5.6.1: Spine densities of all spines and newborn spines plotted as cells (**A** and **C**) and dendrites (**B** and **D**). (**A**) Spine densities of all spines were different between Nex-tdTomato- and Nex-tdTomato+ (Mann-Whitney test, p < 0.0001, n = 9 Nex-tdTomato-, n = 6 Nex-tdTomato+). But they did not change through time (one sample Wilcoxon test each day against respective median baseline densities; Nex-tdTomato- D8 p = 0.8203, D9 p > 0.9999, D11 p = 0.9102, D14 p = 0.7344, Nex-tdTomato+ D8 p = 0.5625, D9 p = 0.3125, D11 p = 0.2188, D14 p = 0.5625). (**B**) Spine densities of all spines were different between Nex-tdTomato- and Nex-tdTomato+ when plotted as dendrites (pairwise Mann-Whitney test, p < 0.0001, n = 42 Nex-tdTomato-, n = 25 Nex-tdTomato+). But they did not change through time (one sample Wilcoxon test each day against respective median baseline densities; Nex-tdTomato- D8 p = 0.1668, D9 p = 0.3785, D11 p = 0.2124, D14 p = 0.2136, Nex-tdTomato+ D8 p = 0.2635, D9 p = 0.3388, D11 p = 0.4418, D14 p = 0.9789). (**C**) Spine densities of newborn spines were different between Nex-tdTomato- and Nex-tdTomato+ (pairwise Mann-Whitney test, p = 0.0005, n = 9 Nex-tdTomato-, n = 6 Nex-tdTomato+). The density of newborn spines of Nex-tdTomato- neurons was reduced compared to its baseline (one sample Wilcoxon test each day against respective median baseline densities; Nex-tdTomato- D8 p = 0.0039, D9 p = 0.0039, D11 p = 0.0391, D14 p = 0.6523, Nex-tdTomato+ D8 p = 0.0313, D9 p = 0.1563, D11 p = 0.5625, D14 p = 0.2188). (**D**) Spine densities of newborn spines from dendrites were not different between Nex-tdTomato- and Nex-tdTomato+ (pairwise Mann-Whitney test, p = 0.0836, n = 42 Nex-tdTomato-, n=25 Nex-tdTomato+). The density of newborn spines of Nex-tdTomato- and Nex-tdTomato+ dendrites was reduced compared to their baseline levels (one sample Wilcoxon test each day against respective median baseline densities; Nex-tdTomato- D8 p < 0.0001, D9 p < 0.0001, D11 p = 0.0392, D14 p = 0.4348, Nex-tdTomato+ D8 p = 0.0006, D9

p = 0.0014, D11 p = 0.1816, D14 p =0.9368). Grey bar indicates time point of 75 mg/kg TAM i.p.. Solid lines medians during baseline, dashed lines median from baseline. * p ≤ 0.05, ** p ≤ 0.01, *** p ≤ 0.001, **** p < 0.0001

We continued analyzing the spine density of newborn spines, and found, when plotting cells, the density of Nex-tdTomato- neurons was significantly higher compared to Nex-tdTomato+ neurons (Mean densities: Nex-tdTomato+: 0.1218 spines/µm, Nex-tdTomato-: 0.1649 spines/µm) (pairwise Mann-Whitney test, p = 0.0005, n = 9 Nex-tdTomato-, n = 6 Nex-tdTomato+). After TAM injection the density of newborn spines of Nex-tdTomato- neurons was reduced compared to its baseline (one sample Wilcoxon test each day against respective median baseline densities; Nex-tdTomato- D8 p = 0.0039, D9 p = 0.0039, D11 p = 0.0391, D14 p = 0.6523, Nex-tdTomato+ D8 p = 0.0313, D9 p = 0.1563, D11 p = 0.5625, D14 p = 0.2188) (**Fig. 5.6.1C**). When plotting dendrites, the density of Nex-tdTomato- dendrites was not different from Nex-tdTomato+ dendrites (Mean densities: Nex-tdTomato+: 0.1473 spines/µm, Nex-tdTomato-: 0.1635 spines/µm) (pairwise Mann-Whitney test, p = 0.0836, n = 42 Nex-tdTomato-, n=25 Nex-tdTomato+). However, after TAM injection the density of newborn spines of Nex-tdTomato- and Nex-tdTomato+ dendrites was reduced compared to their baseline levels (one sample Wilcoxon test each day against respective median baseline densities; Nex-tdTomato- D8 p < 0.0001, D9 p < 0.0001, D11 p = 0.0392, D14 p = 0.4348, Nex-tdTomato+ D8 p = 0.0006, D9 p = 0.0014, D11 p = 0.1816, D14 p =0.9368) (**Fig. 5.6.1D**).

We were wondering whether the dendritic order contributed to the differences in spine density of Nex-tdTomato- and Nex-tdTomato+ dendrites. For that reason I analyzed all dendritic segments and their order of Nex-tdTomato+ and Nex-tdTomato- neurons. The dendritic order was classified as described for the Arc data. I found that I sampled very similar dendritic segments of Nex-tdTomato+ and Nex-tdTomato- neurons (1st: Nex- 14.3%, Nex+ 0%; 2nd: Nex- 33.3%, Nex+ 32%; 3rd: Nex- 38.1%, Nex+ 40.0%; 4th: Nex- 14.3%, Nex+ 28%) (**Fig. 5.6.2**).
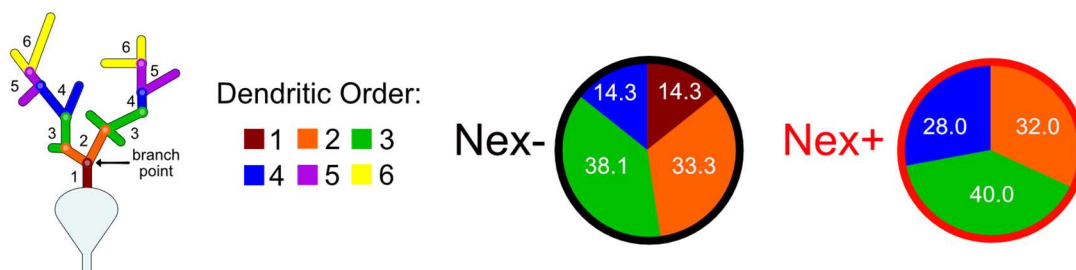

Fig. 5.6.2: Dendritic order of dendritic segments belonging to Nex-tdTomato+ and Nex-tdTomato- neurons. Both groups showed a very similar distribution of dendritic segments. 1st: Nex- 14.3%, Nex+ 0%; 2nd: Nex- 33.3%, Nex+ 32%; 3rd: Nex- 38.1%, Nex+ 40.0%; 4th: Nex- 14.3%, Nex+ 28%.

Next, I analyzed the turnover rate of spines per cell or dendrite. When I analyzed the turnover per day I found that on day 14 Nex-tdTomato+ cells showed a higher turnover rate compared to Nex-tdTomato- (pairwise Mann-Whitney test, d2 p = 0.9546, d4 p = 0.3884, d7 p = 0.9546, d8 p = 0.5287, d9 p = 0.3277, d11 p = 0.1135, d14 p = 0.0176 n = 9 Nex-tdTomato-, n = 6 Nex-tdTomato+) (**Fig. 5.6.3A**). I also pooled time points 2-7 and 9-14 in order to identify major differences between the two groups. I found no difference in turnover rate of Nex-tdTomato- and Nex-tdTomato+ neurons. (Šidák multiple comparisons corrected Mann-Whitney test, baseline Nex-tdTomato- vs. Nex-tdTomato+ p = 0.7051, after TAM Nex-tdTomato- vs. Nex-tdTomato+ p = 0.7526, Nex-tdTomato- baseline vs. after TAM p = 0.1320, Nex-tdTomato+ baseline vs. after TAM p = 0.3888; n = 27 Nex-tdTomato-, n=18 Nex-tdTomato+) (**Fig. 5.3.3B**). Furthermore, I did the same analysis on the dendrite level resulting in identical data as presented in for the cells (pairwise Mann-Whitney test, d2 p = 0.9051, d4 p = 0.1428, d7 p = 0.9308, d8 p = 0.6088, d9 p = 0.8394, d11 p = 0.3753, d14 p = 0.0502 n = 42 Nex-tdTomato-, n = 25 Nex-tdTomato+). I also pooled the data together (Šidák multiple comparisons corrected Mann-Whitney test, baseline Nex-tdTomato- vs. Nex-tdTomato+ p = 0.3780, after TAM Nex-tdTomato- vs. Nex-tdTomato+ p = 0.1013, Nex-tdTomato- baseline vs. after TAM p = 0.0276, Nex-tdTomato+ baseline vs. after TAM p = 0.4088; n = 126 Nex-tdTomato-, n=75 Nex-tdTomato+) (**Fig. 5.6.3C-D**).
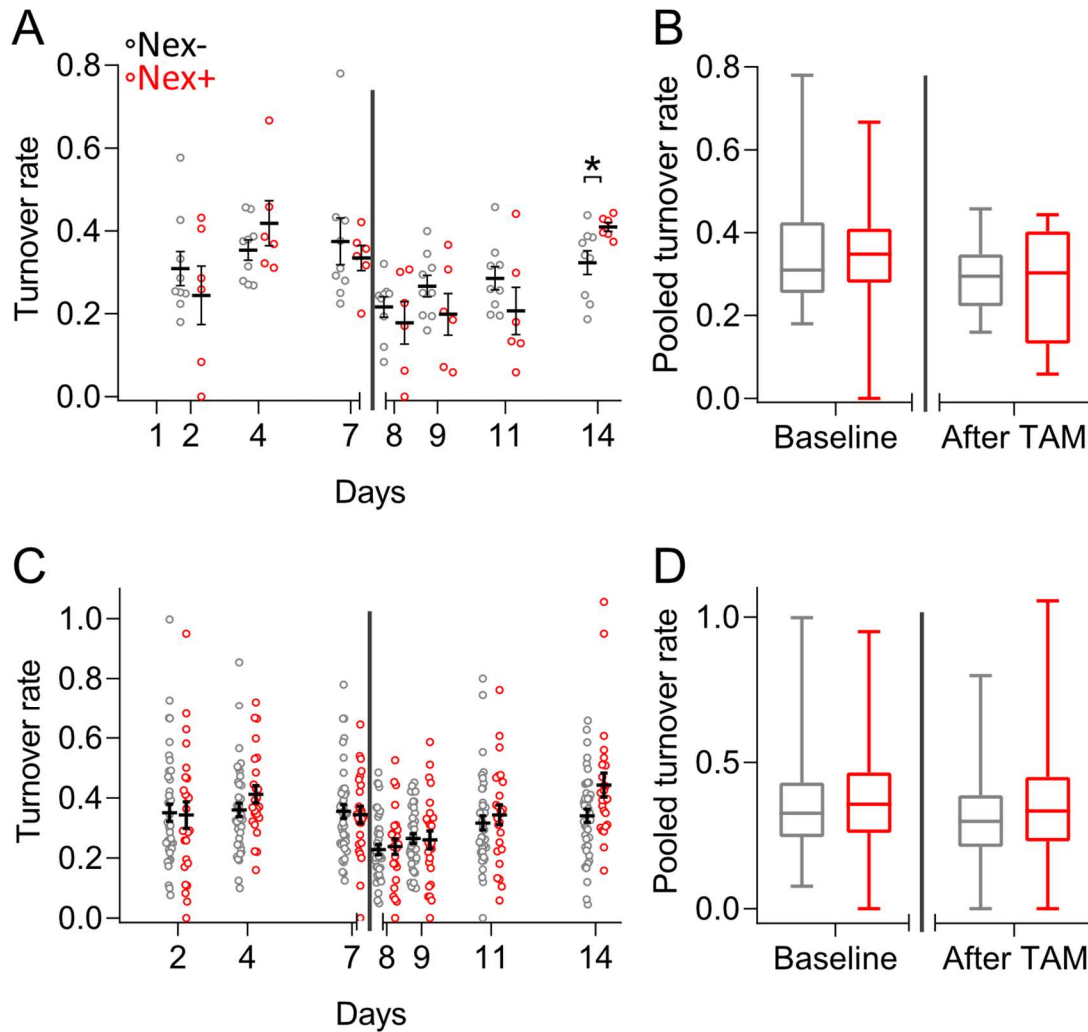
Fig. 5.6.3: (A-B) Data plotted as cells, **(C-D)** Data plotted as dendrites. **(A)** Pairwise comparison of the turnover rate between Nex-tdTomato- and Nex-tdTomato+ pairwise Mann-Whitney test, d2 p = 0.9546, d4 p = 0.3884, d7 p = 0.9546, d8 p = 0.5287, d9 p = 0.3277, d11 p = 0.1135, d14 p = 0.0176 n = 9 Nex-tdTomato-, n = 6 Nex-tdTomato+). **(B)** Pooled data of day 2-7 and day 9-14 (Šidák multiple comparisons corrected Mann-Whitney test, baseline Nex-tdTomato- vs. Nex-tdTomato+ p = 0.7051, after TAM Nex-tdTomato- vs. Nex-tdTomato+ p = 0.7526, Nex-tdTomato- baseline vs. after TAM p = 0.1320, Nex-tdTomato+ baseline vs. after TAM p = 0.3888; n = 27 Nex-tdTomato-, n=18 Nex-tdTomato+). **(C)** Pairwise comparison of the turnover rate between Nex-tdTomato- and Nex-tdTomato+ (pairwise Mann-Whitney test, d2 p = 0.9051, d4 p = 0.1428, d7 p = 0.9308, d8 p = 0.6088, d9 p = 0.8394, d11 p = 0.3753, d14 p = 0.0502 n = 42 Nex-tdTomato-, n = 25 Nex-tdTomato+). **(D)** Pooled data of day 2-7 and day 9-14 (Šidák multiple comparisons corrected Mann-Whitney test, baseline Nex-tdTomato- vs. Nex-tdTomato+ p = 0.3780, after TAM Nex-tdTomato- vs. Nex-tdTomato+ p = 0.1013, Nex-tdTomato- baseline vs. after TAM p = 0.0276, Nex-tdTomato+ baseline vs. after TAM p = 0.4088; n = 126 Nex-tdTomato-, n=75 Nex-tdTomato+). Grey bar indicates time point of 75 mg/kg TAM i.p.. * p ≤ 0.05

Next, I analyzed the fractional gain per day and found no significant difference between Nex-tdTomato- and Nex-tdTomato+ cells (pairwise Mann-Whitney test, d2 p = 0.1906, d4 p = 0.2721, d7 p = 0.8639, d8 p = 0.1810, d9 p = 0.8917, d11 p = 0.5287, d14 p = 0.5083, n = 9 Nex-tdTomato-, n = 6 Nex-tdTomato+) (**Fig. 5.6.4A**). Also the pooled time points 2-7 and 9-14 did not reveal any significance between the two groups (Šidák multiple comparisons

corrected Mann-Whitney test, baseline Nex-tdTomato- vs. Nex-tdTomato+ p = 0.9863, after TAM Nex-tdTomato- vs. Nex-tdTomato+ p = 0.4146, Nex-tdTomato- baseline vs. after TAM p = 0.0583, Nex-tdTomato+ baseline vs. after TAM p = 0.0370; n = 27 Nex-tdTomato-, n = 18 Nex-tdTomato+) (**Fig. 5.6.4B**). Furthermore, I did the same analysis on the dendrite level and found that on day 4 Nex-tdTomato+ cells showed a higher fractional gain compared to Nex-tdTomato- (pairwise Mann-Whitney test, d2 p = 0.9052, d4 p = 0.0347, d7 p = 0.8696, d8 p = 0.6086, d9 p = 0.9461, d11 p = 0.8544, d14 p = 0.5299, n = 42 Nex-tdTomato-, n = 25 Nex-tdTomato+). (**Fig. 5.6.4C**). Pooling timepoints 2-7 and 9-14 for the dendrites resulted in a reduction of fractional gain after the TAM injection for both groups (Šidák multiple comparisons corrected Mann-Whitney test, baseline Nex-tdTomato- vs. Nex-tdTomato+ p = 0.3261, after TAM Nex-tdTomato- vs. Nex-tdTomato+ p = 0.6655, Nex-tdTomato- baseline vs. after TAM p = 0.0021, Nex-tdTomato+ baseline vs. after TAM p = 0.0110; n = 126 Nex-tdTomato-, n = 75 Nex-tdTomato+) (**Fig. 5.6.4D**).
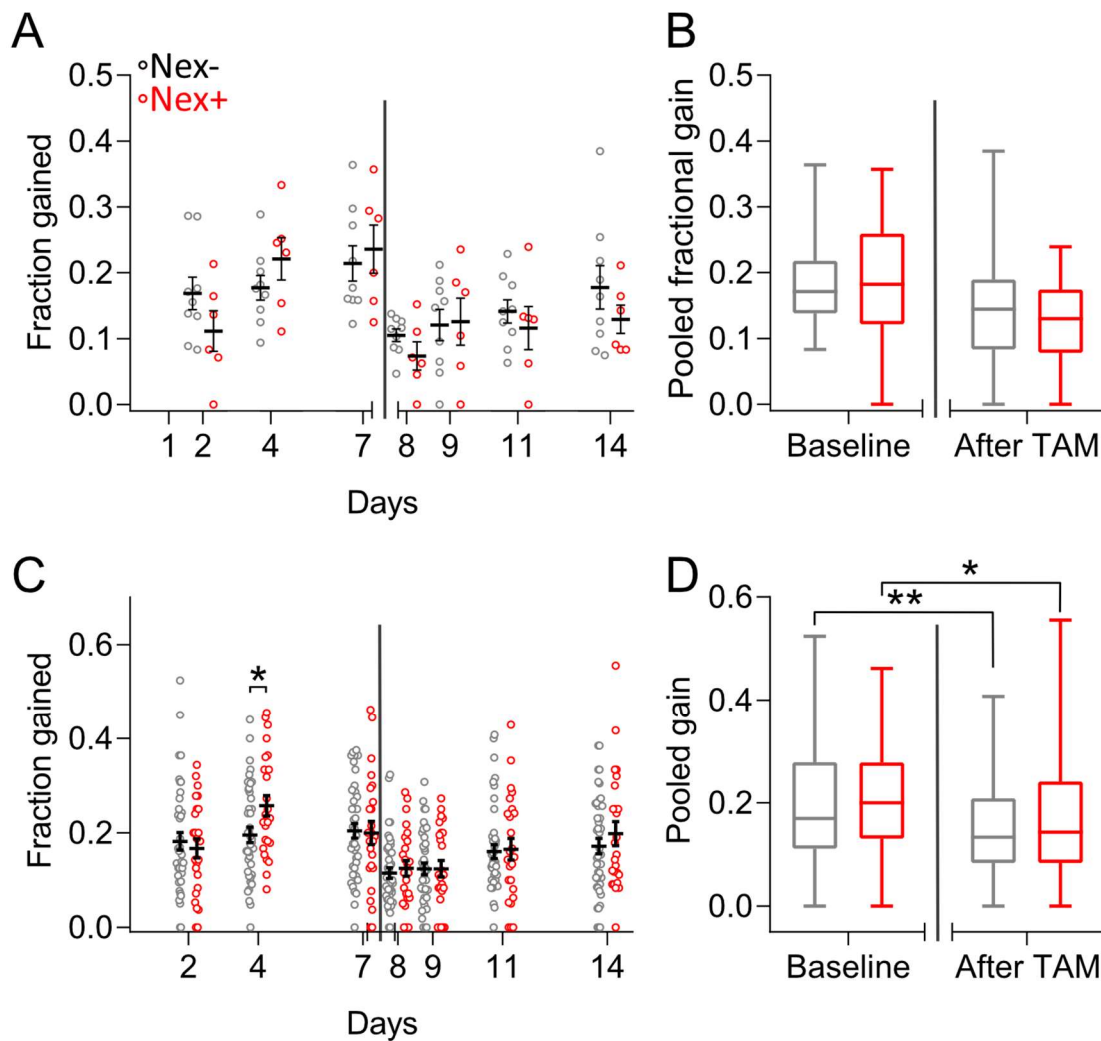
Fig. 5.6.4: (**A-B**) Data plotted as cells, (**C-D**) Data plotted as dendrites. (**A**) Pairwise comparison of the fractional gain between Nex-tdTomato- and Nex-tdTomato+ (pairwise Mann-Whitney test, d2 p = 0.1906, d4 p = 0.2721, d7 p = 0.8639, d8 p = 0.1810, d9 p = 0.8917, d11 p = 0.5287, d14 p = 0.5083, n = 9 Nex-tdTomato-, n = 6 Nex-tdTomato+). (**B**) Pooled data of day 2-7 and day 9-14 (Šidák multiple comparisons corrected Mann-Whitney test, baseline Nex-tdTomato- vs. Nex-tdTomato+ p = 0.9863, after TAM Nex-tdTomato- vs. Nex-tdTomato+ p = 0.4146, Nex-tdTomato- baseline vs. after TAM p = 0.0583, Nex-tdTomato+ baseline vs. after TAM p = 0.0370; n = 27 Nex-tdTomato-, n = 18 Nex-tdTomato+). (**C**) Pairwise comparison of the fractional gain between Nex-tdTomato- and Nex-tdTomato+ dendrites (pairwise Mann-Whitney test, d2 p = 0.9052, d4 p = 0.0347, d7 p = 0.8696, d8 p = 0.6086, d9 p = 0.9461, d11 p = 0.8544, d14 p = 0.5299, n = 42 Nex-tdTomato-, n = 25 Nex-tdTomato+). (**D**) Pooled data of day 2-7 and day 9-14 (Šidák multiple comparisons corrected Mann-Whitney test, baseline Nex-tdTomato- vs. Nex-tdTomato+ p = 0.3261, after TAM Nex-tdTomato- vs. Nex-tdTomato+ p = 0.6655, Nex-tdTomato- baseline vs. after TAM p = 0.0021, Nex-tdTomato+ baseline vs. after TAM p = 0.0110; n = 126 Nex-tdTomato-, n = 75 Nex-tdTomato+). Grey bar indicates time point of 75 mg/kg TAM i.p.. * p ≤ 0.05, ** p ≤ 0.01

At following, I checked the fractional loss per day and found no significant difference between Nex-tdTomato- and Nex-tdTomato+ cells but on day 14 (pairwise Mann-Whitney test, d2 p > 0.9999, d4 p = 0.6070, d7 p = 0.4366, d8 p = 0.9540, d9 p = 0.0815, d11 p = 0.2597, d14 p = 0.0050, n = 9 Nex-tdTomato-, n = 6 Nex-tdTomato+) (**Fig. 5.6.5A**). When I pooled time points 2-7 and 9-14 I did not find any difference in the fractional loss between Arc-tdTomato- and Arc-tdTomato+ neurons neither before nor after the TAM administration (Šidák multiple comparisons corrected Mann-Whitney test, baseline Nex-tdTomato- vs. Nex-tdTomato+ p = 0.8815, after TAM Nex-tdTomato- vs. Nex-tdTomato+ p = 0.9314, Nex-tdTomato- baseline vs. after TAM p = 0.7936, Nex-tdTomato+ baseline vs. after TAM p = 0.9185; n = 27 Nex-tdTomato-, n = 18 Nex-tdTomato+) (**Fig. 5.6.5B**). Furthermore, I did the same analysis on the dendrite level and found the same as for the cells (pairwise Mann-Whitney test, d2 p = 0.5773, d4 p = 0.9974, d7 p = 0.8848, d8 p = 0.9820, d9 p = 0.0815, d11 p = 0.2597, d14 p = 0.0352, n = 9 Nex-tdTomato-, n = 6 Nex-tdTomato+). (**Fig. 5.6.5C**). Pooling time points 2-7 and 9-14 did not reveal a difference in the fractional loss between Nex-tdTomato- and Nex-tdTomato+ dendrites neither before nor after the TAM administration (Šidák multiple comparisons corrected Mann-Whitney test, baseline Nex-tdTomato- vs. Nex-tdTomato+ p = 0.6402, after TAM Nex-tdTomato- vs. Nex-tdTomato+ p = 0.0915, Nex-tdTomato- baseline vs. after TAM p = 0.9511, Nex-tdTomato+ baseline vs. after TAM p = 0.1094; n = 126 Nex-tdTomato-, n = 75 Nex-tdTomato+) (**Fig. 5.6.5D**).
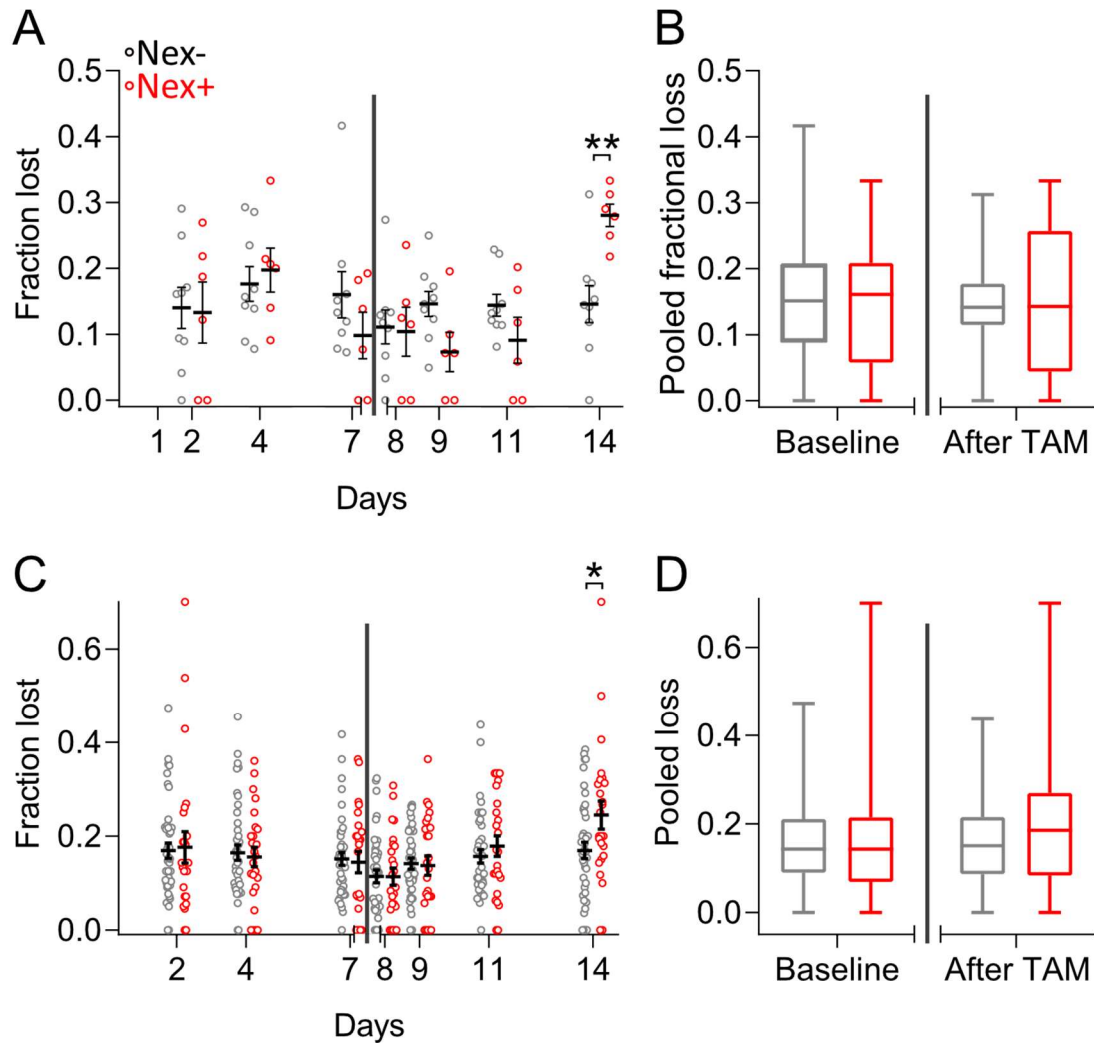
Fig. 5.6.5: (**A-B**) Data plotted as cells, (**C-D**) Data plotted as dendrites. (**A**) Pairwise comparison of the fractional loss between Nex-tdTomato- and Nex-tdTomato+ (pairwise Mann-Whitney test, d2 p > 0.9999, d4 p = 0.6070, d7 p = 0.4366, d8 p = 0.9540, d9 p = 0.0815, d11 p = 0.2597, d14 p = 0.0050, n = 9 Nex-tdTomato-, n = 6 Nex-tdTomato+). (**B**) Pooled data of day 2-7 and day 9-14 (Šidák multiple comparisons corrected Mann-Whitney test, baseline Nex-tdTomato- vs. Nex-tdTomato+ p = 0.8815, after TAM Nex-tdTomato- vs. Nex-tdTomato+ p = 0.9314, Nex-tdTomato- baseline vs. after TAM p = 0.7936, Nex-tdTomato+ baseline vs. after TAM p = 0.9185; n = 27 Nex-tdTomato-, n = 18 Nex-tdTomato+). (**C**) Pairwise comparison of the fractional loss between Nex-tdTomato- and Nex-tdTomato+ dendrites (pairwise Mann-Whitney test, d2 p = 0.5773, d4 p = 0.9974, d7 p = 0.8848, d8 p = 0.9820, d9 p = 0.0815, d11 p = 0.2597, d14 p = 0.0352, n = 9 Nex-tdTomato-, n = 6 Nex-tdTomato+). (**D**) Pooled data of day 2-7 and day 9-14 (Šidák multiple comparisons corrected Mann-Whitney test, baseline Nex-tdTomato- vs. Nex-tdTomato+ p = 0.6402, after TAM Nex-tdTomato- vs. Nex-tdTomato+ p = 0.0915, Nex-tdTomato- baseline vs. after TAM p = 0.9511, Nex-tdTomato+ baseline vs. after TAM p = 0.1094; n = 126 Nex-tdTomato-, n = 75 Nex-tdTomato+). Grey bar indicates time point of 75 mg/kg TAM i.p.. * p ≤ 0.05, ** p ≤ 0.01

Summarizing this data, independent on quantifying the turnover rate, the fractional gain or loss proved that neither TAM injection nor tdTomato expression affected structural synaptic plasticity. Additionally, this data shows that prospective Nex-tdTomato- and Nex-tdTomato+ neurons display the same synaptic dynamics independent on whether they will or will not express tdTomato.

To further strengthen my findings I also measured the surviving fractions as I did for the Arc-data. I started by measuring the surviving fraction of all spines on day 1 and at day 8. This measurement revealed no difference in the surviving fraction from Nex-tdTomato- and Nex-tdTomato+ neurons. This did also not change after the TAM administration (Šidák multiple comparisons corrected shuffled test, d2 p = 0.9114, d4 p = 0.9571, d7 p = 0.9471, d9 p = 0.9275, d11 p = 0.9298, d14 p = 0.1506, Nex-tdTomato- d2 vs. d9 p = 0.6036, d4 vs. d11 p = 0.4851, d7 vs. d14 p = 0.9354, Nex-tdTomato+ d2 vs. d9 p = 0.5301, d4 vs. d11 p = 0.5513, d7 vs. d14 p = 0.0299) (**Fig.5.6.6A**). I further analyzed the numbers as dendrites and also found that the two groups showed the same spine survival (Šidák multiple comparisons corrected Mann-Whitney test, d2 p = 0.5773, d4 p = 0.7450, d7 p = 0.7449, d9 p = 0.7942, d11 p = 0.7500, d14 p = 0.3317, Arc-tdTomato- d2 vs. d9 p = 0.4135, d4 vs. d11 p = 0.3105, d7 vs. d14 p = 0.8326, Arc-tdTomato+ d2 vs. d9 p = 0.7612, d4 vs. d11 p = 0.6967, d7 vs. d14 p = 0.1736) (**Fig.5.6.6B**). Moreover, I focused on pre-existing spines of neurons at day 2 and day 9 I also did not identify any significance between the two groups (Šidák multiple comparisons corrected Mann-Whitney test, d4 p = 0.4745, d7 p = 0.7514, d11 p = 0.1429, d14 p = 0.1532, Nex-tdTomato- d4 vs. d11 p = 0.3865, d7 vs. d14 p = 0.9809, Nex-tdTomato+ d4 vs. d11 p = 0.0628, d7 vs. d14 p = 0.0303) (**Fig.5.6.6C**). However, analyzing pre-existing spines of dendrites at day 2 and day 9 indicated a slight decrease in synaptic stability of Nex-tdTomato dendrites comparing day 7 and day 14 (Šidák multiple comparisons corrected Mann-Whitney test, d4 p = 0.4829, d7 p = 0.2970, d11 p = 0.9461, d14 p = 0.1652, Nex-tdTomato- d4 vs. d11 p = 0.6447, d7 vs. d14 p = 0.2057, Nex-tdTomato+ d4 vs. d11 p = 0.6591, d7 vs. d14 p = 0.0033) (**Fig.5.6.6D**). Also analyzing the surviving fraction of newborn spines showed no difference in the stability of spines from Nex-tdTomato- and Nex-tdTomato+ on the neuron level (Šidák multiple comparisons corrected Mann-Whitney test, d4 p = 0.8272, d7 p > 0.9999, d11 p = 0.7242, d14 p = 0.1173, Nex-tdTomato- d4 vs. d11 p = 0.9840, d7 vs. d14 p = 0.3832, Nex-tdTomato+ d4 vs. d11 p = 0.9683, d7 vs. d14 p = 0.1190) (**Fig.5.6.6E**) and also dendrite level (Šidák multiple comparisons corrected Mann-Whitney test, d4 p = 0.6646, d7 p = 0.6011, d11 p = 0.4845, d14 p = 0.2224, Nex-tdTomato- d4 vs. d11 p = 0.3631, d7 vs. d14 p = 0.1110, Nex-tdTomato+ d4 vs. d11 p = 0.2327, d7 vs. d14 p = 0.0409) (**Fig.5.6.6F).**
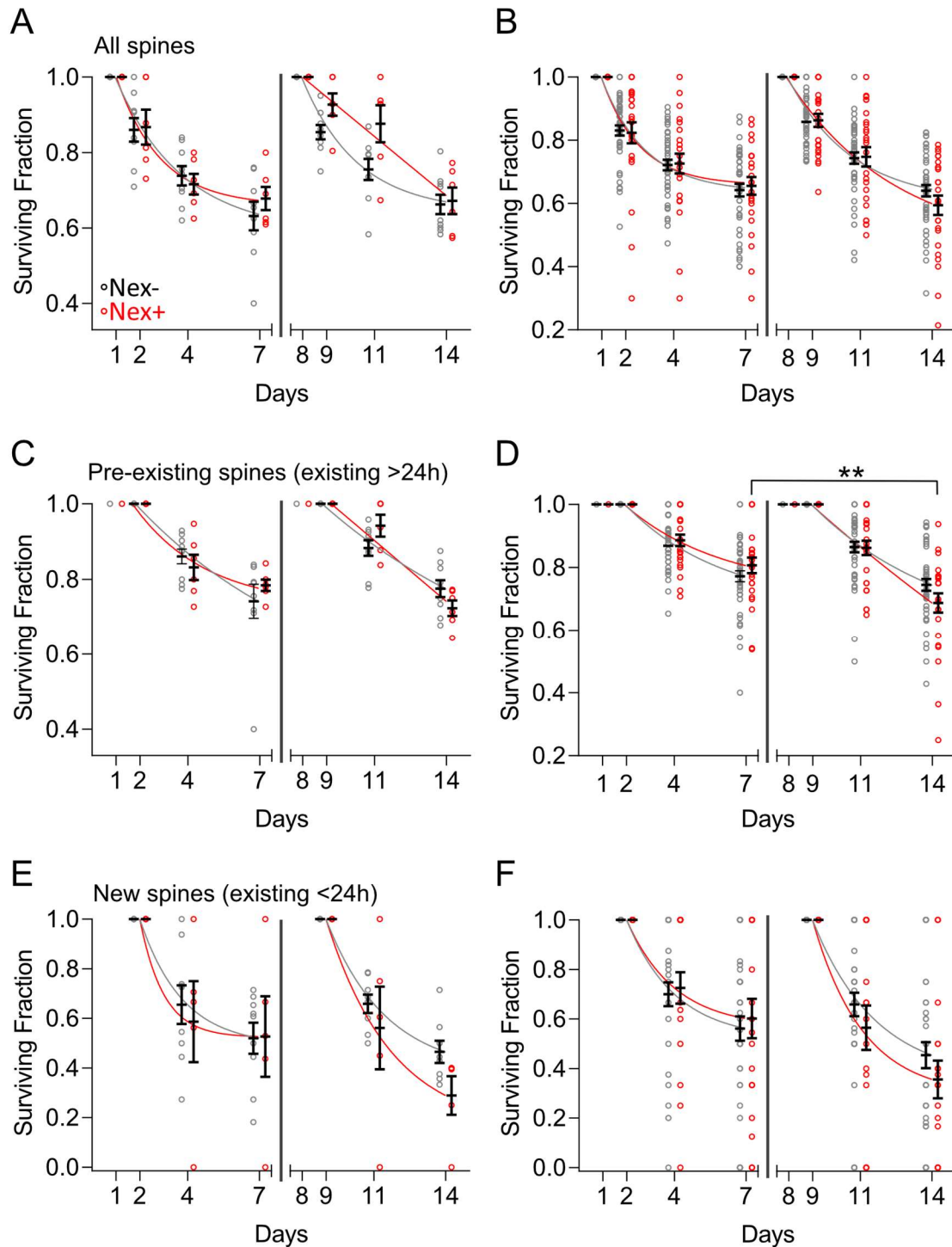
Fig. 5.6.6: Stochastic labeling of CA1 pyramidal neurons does not affect structural synaptic stability before or after expression of tdTomato. (**A**) No difference in the surviving fraction of all spines from Nex-tdTomato- and Nex-tdTomato+ (Šidák multiple comparisons corrected shuffled test, d2 p = 0.9114, d4 p = 0.9571, d7 p = 0.9471, d9 p = 0.9275, d11 p = 0.9298, d14 p = 0.1506, Nex-tdTomato- d2 vs. d9 p = 0.6036, d4 vs. d11 p = 0.4851, d7 vs. d14 p = 0.9354, Nex-tdTomato+ d2 vs. d9 p = 0.5301, d4 vs. d11 p = 0.5513, d7 vs. d14 p = 0.0299). (**B**) No difference in the surviving fraction of all spines from Nex-tdTomato- and Nex-tdTomato+ dendrites (Šidák multiple comparisons corrected Mann-Whitney test, d2 p = 0.5773, d4 p = 0.7450, d7 p = 0.7449, d9 p = 0.7942, d11 p = 0.7500, d14 p = 0.3317, Nex-tdTomato- d2 vs. d9 p = 0.4135, d4 vs. d11 p = 0.3105, d7 vs. d14 p = 0.8326, Nex-tdTomato+ d2 vs. d9 p = 0.7612, d4 vs. d11 p = 0.6967, d7 vs. d14 p = 0.1736). (**C**) No difference in the surviving fraction of pre-existing spines from Nex-tdTomato- and Nex-tdTomato+ neurons (Šidák multiple comparisons corrected Mann-Whitney test, d4 p = 0.4745, d7 p = 0.7514, d11 p = 0.1429, d14 p = 0.1532, Nex-tdTomato- d4 vs. d11 p = 0.3865, d7 vs. d14 p =

0.9809, Nex-tdTomato+ d4 vs. d11 p = 0.0628, d7 vs. d14 p = 0.0303). (**D**) No difference in the surviving fraction of pre-existing spines from Nex-tdTomato- and Nex-tdTomato+ dendrites despite a slight drop in stability of Nex-tdTomato+ dendrites from day 7 to day 14 (Šidák multiple comparisons corrected Mann-Whitney test, d4 p = 0.4829, d7 p = 0.2970, d11 p = 0.9461, d14 p = 0.1652, Nex-tdTomato- d4 vs. d11 p = 0.6447, d7 vs. d14 p = 0.2057, Nex-tdTomato+ d4 vs. d11 p = 0.6591, d7 vs. d14 p = 0.0033). (**E-F**) Newborn spines of neurons and dendrites at day 2 and day 9 did not any significant differences (Neuron: Šidák multiple comparisons corrected Mann-Whitney test, d4 p = 0.8272, d7 p > 0.9999, d11 p = 0.7242, d14 p = 0.1173, Nex-tdTomato- d4 vs. d11 p = 0.9840, d7 vs. d14 p = 0.3832, Nex-tdTomato+ d4 vs. d11 p = 0.9683, d7 vs. d14 p = 0.1190; Dendrite: Šidák multiple comparisons corrected Mann-Whitney test, d4 p = 0.6646, d7 p = 0.6011, d11 p = 0.4845, d14 p = 0.2224, Nex-tdTomato- d4 vs. d11 p = 0.3631, d7 vs. d14 p = 0.1110, Nex-tdTomato+ d4 vs. d11 p = 0.2327, d7 vs. d14 p = 0.0409). Grey bar indicates time point of 75 mg/kg TAM i.p.. Solid lines second order exponential decay fit to data. * $p \leq 0.05$, ** $p \leq 0.01$, *** $p \leq 0.001$, **** $p < 0.0001$

Summarizing this data, before the expression of tdTomato structural synaptic plasticity of prospective Nex-tdTomato- and Nex-tdTomato+ neurons are indistinguishable between the two. This is because they belong to the same class of CA1 pyramidal neurons. In contrast, prospective Arc-tdTomato- and Arc-tdTomato+ neurons have a highly significant difference in the stability of connectivity, and that is the determining factor in becoming Arc-tdTomato+ or Arc-tdTomato-. Additionally, the latest piece of data gives evidence that 75mg/kg TAM i.p. injection; thereby Cre activation and tdTomato expression in a stochastic random population of CA1 pyramidal neurons alone does not change the structural synaptic plasticity. On the other hand, if the marker is activity-dependent and a potent induction of neuronal activity (like the EE) is delivered to the CA1, I see a change in the stability of the network connectivity especially of neurons that displayed less stable connectivity (Arc-tdTomato- neurons) before the neuronal activation.

Summing up, performing the Nex-Cre^ERT2; Thy1-eGFP; Ai9 experiment proved that the changes I observed earlier during the Arc-Cre^ERT2; Thy1-eGFP; Ai9 experiment were exclusively due to the induction of neuronal activity and not due to any potential side effects from longitudinal 2-photon imaging, i.p. TAM injection, Cre activation, and expression of the marker protein tdTomato.

5.7 Identifying Recurrent Synaptic Sites

When I was counting spines over the period of 14 days, I could identify three main classes of dendritic spines. The first class was spines that were stable and apparent throughout the whole period. This class also represented the largest group of the three main classes. Another type, which I already discussed extensively, were newborn spines. Newborn

spines were defined on any day of the experiment despite the day 1. The main criteria to be a newborn spine was that this spine could not be there the previous time point of imaging – independent of whether the last time point was 24, 48, or 72 hours apart. Like this, I could never tell the exact time point of birth of the newborn spine, but I knew that at least it was not present the previous time point of imaging. The third class was the lost spines. To be part of this type, a spine needed to be there from day 1 but then disappeared on any other day during the experiment. Since the time points of imaging were 24, 48, or 72 hours apart, a lost spine could have been lost any time in these time-windows.

However, when I counted the data, I realized that in many cases, newborn spines appeared in locations where previously a lost spine disappeared, having at least one imaging time point no spine in that location. I hesitated in calling the new apparent spine the same spine as the lost spine, but I called it a newborn spine in a <u>recurrent location</u> (a location that was visited multiple times throughout the experiment by several new and lost spines). The reason why I did not want to give the same spine ID to a spine appearing in the same location as the prior lost spine had two bases. The more important was the ignorance of the pre-synaptic partner. In the design of my study, I treated spines as synapses, but as soon as a spine disappeared and a new one appeared in the same location, I was not able to tell if this spine formed precisely the same synapse with the equal pre-synaptic partner as the previous spine did. The other reason was the biological composition of each spine. A new spine born in the same location as a previously lost spine would have for sure a very different molecular composition as the previous one, and for this reason alone it would be a new spine.
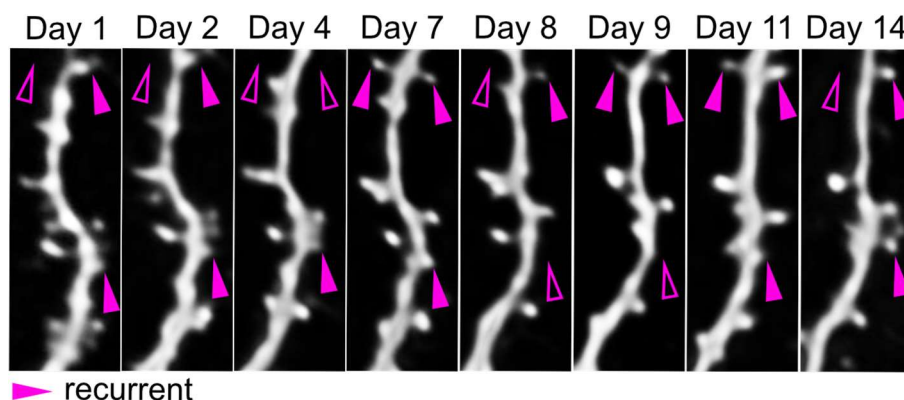

Fig. 5.7.1: Following spine dynamics for 14 days. Focus on recurrent synaptic sites (pink arrowhead). Recurrent sites were occupied by different spines over 14 days.

5.8 The Occupancy and Flips of Recurrent Sites Predicted Arc-tdTomato+ Neurons

I n order to be sure that I was indeed looking at recurrent positions, I needed to define how far away from its original location a recurrent spine could appear to be called "recurrent at the same location". To overcome setting an arbitrary threshold of a couple of micrometers, I instead measured the jitter of stable spines through time and directly compared it to the jitter of recurrent spines. The jitter of recurrent spines peaked around 0 µm and showed the same distribution as the jitter of stable spines (Mann-Whitney test, p = 0.6575, n = 15,176 stable spines, n = 8,444 recurrent spines) (**Fig. 5.8.1A**).
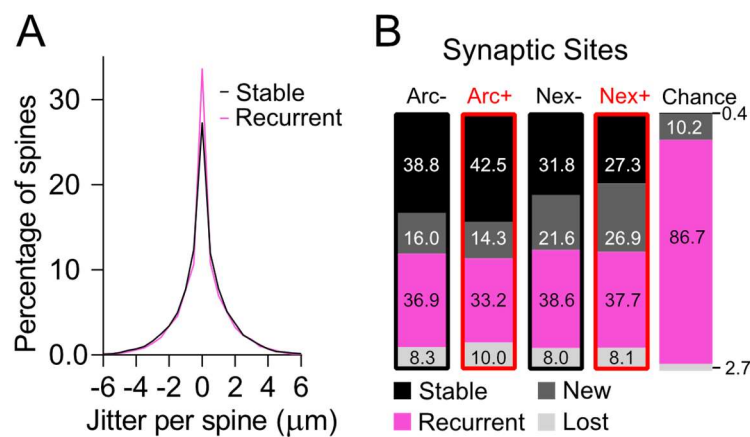
Fig. 5.8.1: (**A**) The distribution of jitter of spines belonging to a recurrent site was similar to the jitter of stable spines. (Mann-Whitney test, p = 0.6575, n = 15,176 stable spines, n = 8,444 recurrent spines). (**B**) Distribution of stable (S), newborn (N), recurrent (R) and lost (L) synaptic sites of Arc-tdTomato- (38.8 S, 16 N, 36.9 R, 8.3 L), Arc-tdTomato+ (42.5 S, 14.3 N, 33.2 R, 10 L), Nex-tdTomato- (31.8 S, 21.6 N, 38.6 R, 8 L), Nex-tdTomato+ (27.3 S, 26.9 N, 37.7 R, 8.1 L) dendrites and also quantified the chance level (0.4 S, 10.2 N, 86.7 R, 2.7 L).

Next, I checked the distribution of the different classes of spines, stable, newborn, lost, and recurrent (**Fig. 5.8.2A-B**) that I observed during my 14-day long imaging experiment. I divided the data into Arc-tdTomato-, Arc-tdTomato+, Nex-tdTomato- and Nex-tdTomato+. All four experimental groups showed similar distributions of the four classes of spines (**Fig. 5.8.1B**). Stable (35.1 ± 5.9 %) and recurrent spines (36.6 ± 2 %) covered the largest part of the distribution while newborn (19.7 ± 4.9 %) and lost spines (8.6 ± 0.8 %) represented a minor part. Interestingly, if I calculated the pure chance of an 8 digit number, where 1 = spine presence and 0 = spine absence, the chance of having a stable spine was 1/256 (possible 1-0 combination of 8 digits) while the possibility of having a recurrent site was the highest at 86.7 % (**Fig. 5.8.1B**).

We were further wondering how the dynamics of recurrent sites would change after neuronal activity. For this, I analyzed recurrent sites of prospective Arc-tdTomato- and Arc-tdTomato+ before the exposure to the EE and also checked for a potential change of their dynamics after the exposure to the EE. I directly compared the results to Nex-tdTomato-, Nex-tdTomato+ recurrent sites, since they were not affected by longitudinal 2-photon in vivo imaging, TAM administration, Cre-activation, and tdTomato expression. I finalized two ways of characterization of the recurrent sites dealing with two different but also similar aspects of the synaptic dynamics. First, I decided to investigate the stability of the synaptic connection formed at a recurrent site. This measure I called "occupancy". The occupancy quantified how many time points the recurrent site contained a spine. For this, I defined a recurrent site over the whole period of 8 imaging time points during 14 days. Then I divided the 8 time points into baseline and after EE or after TAM. Finally, I checked how many times the recurrent site was occupied during each epoch (max. 4 times, min. 0 times) (**Fig. 5.8.2B**). The second measurement that I defined was "flips". Flips rated the dynamic aspect of a recurrent site by counting the transitions from no spine present to one spine present. Like this, the minimum amount of flips that could occur was 0, when the recurrent site was fully occupied or not occupied at all during the analyzed epoch and could range up to 3 flips in 4 imaging time points (**Fig. 5.8.2B**).
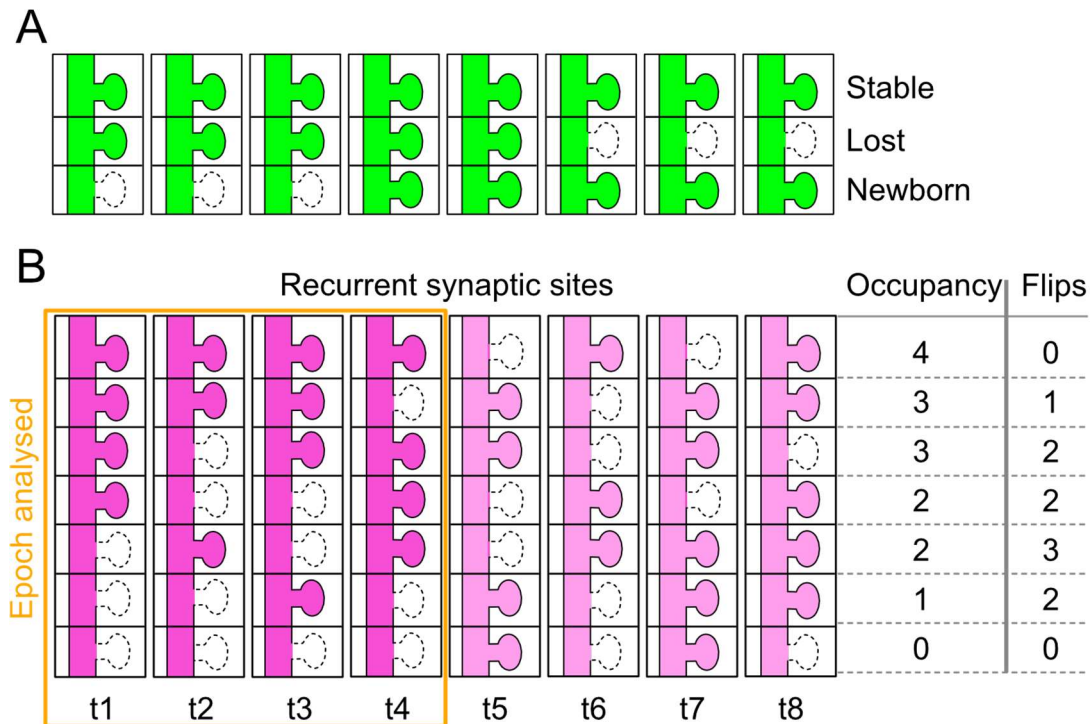

Fig. 5.8.2: Definition of synaptic sites and detailed analysis of recurrent locations. (**A**) Schematic showing, stable, lost, and newborn spines/synaptic sites over 8 time points. (**B**) Recurrent sites are always defined

over 8 time points but then analyzed over epochs of 4 time points. Recurrent sites can be very static and not dynamic, showing an occupancy of 4 and 0 flips. However, if a recurrent site is very dynamic and shows 3 flips, it automatically has an occupancy of 2. Occupancy ranges from 4-0 and flips range from 3-0.

When I started looking at the occupancy, I was surprised how many recurrent sites were occupied on each day. To understand this phenomenon, I asked a simple urn-model question of combinatorics. The question I asked was (at day 1 Arc-tdTomato-): what is the probability that if I have (N) 1173 sites, of which (M) 707 are recurrent and I have (n) 674 potential sites to be occupied that I occupy exactly (k) 515 recurrent sites.

$$Hypergeometric\ function: \quad P(X = k) = \frac{\binom{M}{k}\binom{N-M}{n-k}}{\binom{N}{n}} = \frac{\binom{707}{515}\binom{1173-707}{674-515}}{\binom{1173}{674}} = 6.14 * 10^{-40}$$

This gave me the probability to observe my data by chance. Finally, I performed a probability mass function test to check whether the observed real value was different from chance.

Most of the days recurrent sites of both Arc-tdTomato- and Arc-tdTomato+ dendrites both before and after the EE were stronger occupied from what was expected by chance (probability mass function test, Arc-tdTomato-: d1 p = 3.59E-13, d2 p = 0.0102, d4 p = 0.4362, d7 p = 0.0102, d8 p = 0.0106, d9 p = 0.0129, d11 p = 0.0007, d14 p = 8.91E-13, Arc-tdTomato+: d1 p = 7.76E-13, d2 p = 0.0005, d4 p = 0.9602, d7 p = 0.0230, d8 p = 0.2527, d9 p = 0.4895, d11 p = 9.53E-8, d14 p = 6.87E-13) (**Fig. 5.8.3A**).
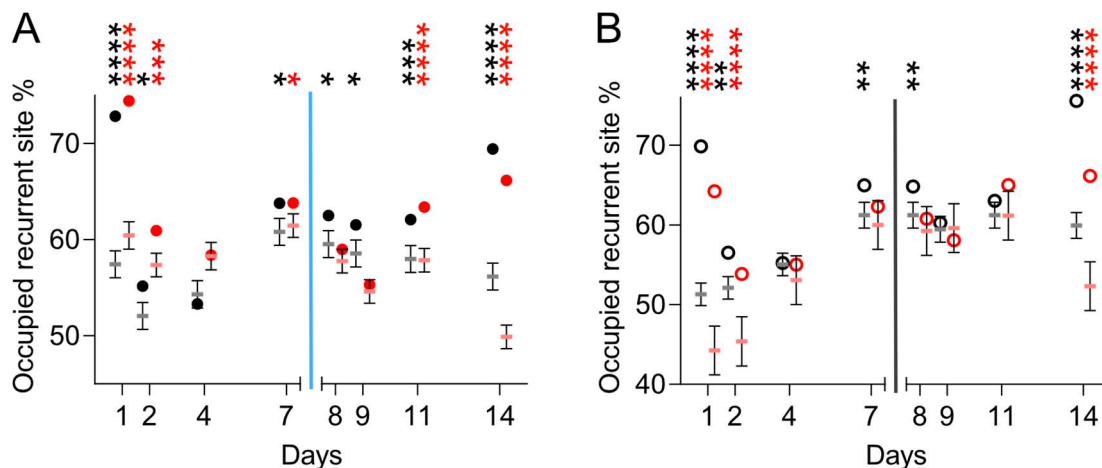

Fig. 5.8.3: Recurrent positions are more frequently occupied from what was expected by chance. (**A**) Recurrent sites of both Arc-tdTomato- and Arc-tdTomato+ dendrites both before and after the EE were stronger occupied than expected by chance (probability mass function test, Arc-tdTomato-: d1 p = 3.59E-13, d2 p = 0.0102, d4 p = 0.4362, d7 p = 0.0102, d8 p = 0.0106, d9 p = 0.0129, d11 p = 0.0007, d14 p = 8.91E-13, Arc-tdTomato+: d1 p = 7.76E-13, d2 p = 0.0005, d4 p = 0.9602, d7 p = 0.0230, d8 p = 0.2527, d9 p = 0.4895, d11 p = 9.53E-8, d14 p = 6.87E-13). (**B**) Recurrent sites of both Nex-tdTomato- and Nex-tdTomato+ dendrites both before and after TAM were generally stronger occupied than expected by chance

(probability mass function test, Arc-tdTomato-: d1 p = 3.22E-13, d2 p = 0.0011, d4 p = 0.9509, d7 p = 0.0046, d8 p = 0.0068, d9 p = 0.5335, d11 p = 0.1669, d14 p = 1.08E-12, Arc-tdTomato+: d1 p = 4.40E-15, d2 p = 7.55E-5, d4 p = 0.4211, d7 p = 0.9566, d8 p = 0.5252, d9 p = 0.2745, d11 p = 0.0815, d14 p = 1.69E-10). Blue bar indicates time point of EE and 75 mg/kg TAM i.p.. Grey bar indicates time point of 75 mg/kg TAM i.p.. * p ≤ 0.05, ** p ≤ 0.01, *** p ≤ 0.001, **** p < 0.0001

Interestingly, this finding also held true for the Nex-tdTomato- and Nex-tdTomato+ dendrites both before and after the TAM even though with a slight weaker result (probability mass function test, Arc-tdTomato-: d1 p = 3.22E-13, d2 p = 0.0011, d4 p = 0.9509, d7 p = 0.0046, d8 p = 0.0068, d9 p = 0.5335, d11 p = 0.1669, d14 p = 1.08E-12, Arc-tdTomato+: d1 p = 4.40E-15, d2 p = 7.55E-5, d4 p = 0.4211, d7 p = 0.9566, d8 p = 0.5252, d9 p = 0.2745, d11 p = 0.0815, d14 p = 1.69E-10)(**Fig. 5.8.3B**).

Independent of the genotype or whether the neuron would be active or inactive recurrent sites seemed to be more occupied than expected by chance. For this reason, I hypothesize that recurrent sites are particular locations to form synapses, and for this reason, I observed a higher occupancy than expected by chance.

Since the findings that the stability of connectivity of neurons predicted if a neuron would become activated and that a potent trigger of neuronal activity, was able to lead to increased stabilization of the network connectivity even of cells that were not directly activated, I wanted to understand if the occupancy as a measure of stability of the synaptic connection formed at a recurrent site would be different in prospective Arc-tdTomato- and Arc-tdTomato+ dendrites and whether the stability would change after the EE.

For this, I plotted the occupancy distributions of prospective Arc-tdTomato- and Arc-tdTomato+ before and after the EE (**Fig. 5.8.4A-B**). The distribution of occupancies showed a longer tail towards higher occupancies for the prospective Arc-tdTomato+ dendrites. This indicated that recurrent sites of prospective Arc-tdTomato+ were more stably connected than prospective Arc-tdTomato- (**Fig. 5.8.4A**). Additionally, this data showed a shift towards higher occupancies after the EE, especially in Arc-tdTomato- dendrites, indicating a network stabilization effect of recurrent sites belonging to inactive neurons (**Fig. 5.8.4B**). Furthermore I directly compared the means of the two distributions also with the means of the distributions form the Nex-data (data in appendix). This revealed, that recurrent sites of prospective Arc-tdTomato+ neurons had a higher occupancy than recurrent sites of Arc-tdTomato- and Nex-tdTomato+ dendrites (Šidák multiple comparisons corrected Mann-Whitney test, Arc-tdTomato- vs. Arc-tdTomato+ p = 0.0110, Nex-tdTomato+ vs. Arc-

tdTomato+ p = 0.0031, Nex-tdTomato- vs Nex-tdTomato+ p = 0.1419, Nex-tdTomato- vs Arc-tdTomato- p = 0.7088; n = 707 Arc-tdTomato-, n = 978 Arc-tdTomato+, n = 614 Nex-tdTomato-, n = 260 Nex-tdTomato+) (**Fig. 5.8.4C**). After the EE and after TAM all groups showed a similar, not significant different occupancy of recurrent sites (Šidák multiple comparisons corrected Mann-Whitney test, Arc-tdTomato- vs. Arc-tdTomato+ p = 0.0295, Nex-tdTomato+ vs. Arc-tdTomato+ p = 0.5945, Nex-tdTomato- vs Nex-tdTomato+ p = 0.0434, Nex-tdTomato- vs Arc-tdTomato- p = 0.2829; n = 707 Arc-tdTomato-, n = 978 Arc-tdTomato+, n = 614 Nex-tdTomato-, n = 260 Nex-tdTomato+) (**Fig. 5.8.4D**).
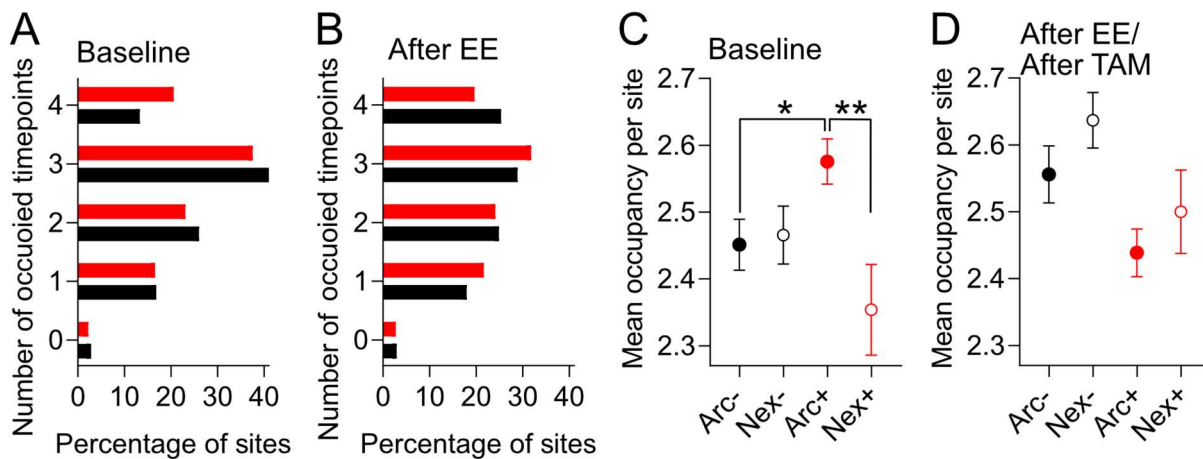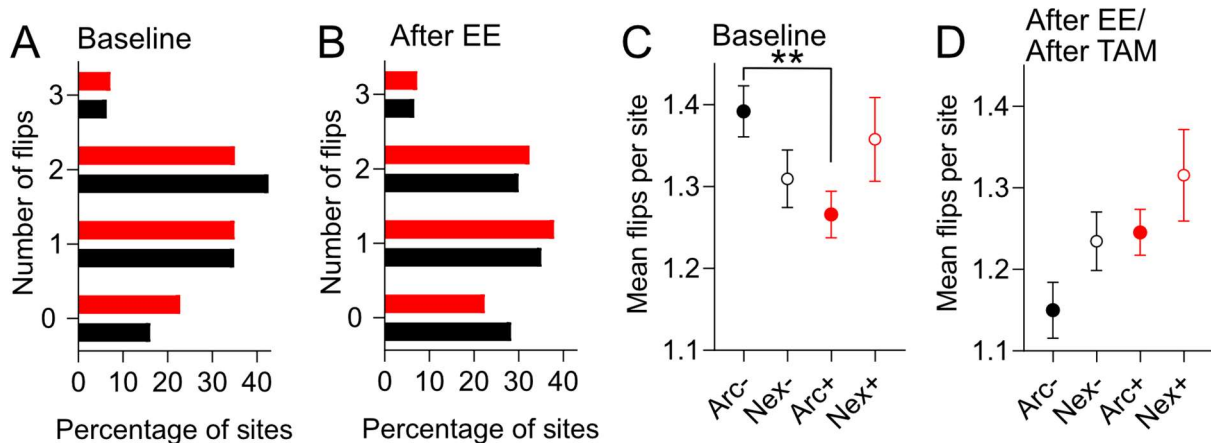

Fig. 5.8.4: Recurrent sites of prospective Arc-tdTomato+ show a higher occupancy before the EE. (A-B) Distributions of occupancies of recurrent sites of Arc-tdTomato- and Arc-tdTomato+ dendrites before and after the EE. (**C**) Recurrent sites of prospective Arc-tdTomato+ show a higher occupancy compared to Arc-tdTomato- and Nex-tdTomato+ before the EE (Šidák multiple comparisons corrected Mann-Whitney test, Arc-tdTomato- vs. Arc-tdTomato+ p = 0.0110, Nex-tdTomato+ vs. Arc-tdTomato+ p = 0.0031, Nex-tdTomato-   vs Nex-tdTomato+ p = 0.1419, Nex-tdTomato- vs Arc-tdTomato- p = 0.7088; n = 707 Arc-tdTomato-, n = 978   Arc-tdTomato+, n = 614 Nex-tdTomato-, n = 260 Nex-tdTomato+). (**D**) After the EE recurrent sites are   equally occupied (Šidák multiple comparisons corrected Mann-Whitney test, Arc-tdTomato- vs. Arc-   tdTomato+ p = 0.0295, Nex-tdTomato+ vs. Arc-tdTomato+ p = 0.5945, Nex-tdTomato- vs Nex-tdTomato+ p   = 0.0434, Nex-tdTomato- vs Arc-tdTomato- p = 0.2829; n = 707 Arc-tdTomato-, n = 978 Arc-tdTomato+, n =   614 Nex-tdTomato-, n = 260 Nex-tdTomato+).* p ≤ 0.05, ** p ≤ 0.01

To further understand the dynamic part of recurrent sites I focused on the flips. For this, I plotted the flips distributions of prospective Arc-tdTomato- and Arc-tdTomato+ dendrites before and after the EE (**Fig. 5.8.5A-B**). The distribution of flips showed a longer tail towards lower amount of flips for the prospective Arc-tdTomato+ dendrites. This indicated that recurrent sites of prospective Arc-tdTomato+ were less dynamic and therefore potentially more stably connected than prospective Arc-tdTomato- (**Fig. 5.8.5A**). Additionally, this data showed a shift towards lower numbers of flips after the EE, especially in Arc-tdTomato- indicating a network stabilization effect of recurrent sited belonging to inactive neurons (**Fig. 5.8.5B**). Furthermore, I directly compared the two distributions also with the distributions

form the Nex-data (data in appendix). This revealed, that recurrent sites of prospective Arc-tdTomato- neurons were more dynamic and had more flips than recurrent sites of Arc-tdTomato+ (Šidák multiple comparisons corrected Mann-Whitney test, Arc-tdTomato- vs. Arc-tdTomato+ p = 0.0023, Nex-tdTomato+ vs. Arc-tdTomato+ p = 0.0958, Nex-tdTomato- vs Nex-tdTomato+ p = 0.4156, Nex-tdTomato- vs Arc-tdTomato- p = 0.0842; n = 707 Arc-tdTomato-, n = 978 Arc-tdTomato+, n = 614 Nex-tdTomato-, n = 260 Nex-tdTomato+) (**Fig. 5.7.5C**). After the EE and after TAM all groups showed a similar, not significant different amount of flips of recurrent sites (Šidák multiple comparisons corrected Mann-Whitney test, Arc-tdTomato- vs. Arc-tdTomato+ p = 0.0285, Nex-tdTomato+ vs. Arc-tdTomato+ p = 0.3559, Nex-tdTomato- vs Nex-tdTomato+ p = 0.3580, Nex-tdTomato- vs Arc-tdTomato- p = 0.0641; n = 707 Arc-tdTomato-, n = 978 Arc-tdTomato+, n = 614 Nex-tdTomato-, n = 260 Nex-tdTomato+) (**Fig. 5.8.5D**).

Fig. 5.8.5: Recurrent sites of prospective Arc-tdTomato+ show lower flips before the EE. (**A-B**) Distributions of flips of recurrent sites of Arc-tdTomato- and Arc-tdTomato+ dendrites before and after the EE. (**C**) Recurrent sites of prospective Arc-tdTomato+ show less flips compared to Arc-tdTomato- before the EE (Šidák's multiple comparisons corrected Mann-Whitney test, Arc-tdTomato- vs. Arc-tdTomato+ p = 0.0023, Nex-tdTomato+ vs. Arc-tdTomato+ p = 0.0958, Nex-tdTomato- vs Nex-tdTomato+ p = 0.4156, Nex-tdTomato- vs Arc-tdTomato- p = 0.0842; n = 707 Arc-tdTomato-, n = 978 Arc-tdTomato+, n = 614 Nex-tdTomato-, n = 260 Nex-tdTomato+). (**D**) After the EE recurrent sites show the same amount of flips (Šidák's multiple comparisons corrected Mann-Whitney test, Arc-tdTomato- vs. Arc-tdTomato+ p = 0.0285, Nex-tdTomato+ vs. Arc-tdTomato+ p = 0.3559, Nex-tdTomato- vs Nex-tdTomato+ p = 0.3580, Nex-tdTomato- vs Arc-tdTomato- p = 0.0641; n = 707 Arc-tdTomato-, n = 978 Arc-tdTomato+, n = 614 Nex-tdTomato-, n = 260 Nex-tdTomato+). * p ≤ 0.05, ** p ≤ 0.01

Summarizing, these results indicated that dendrites contained recurrent synaptic sites that were particular and more frequently occupied compared to other synaptic sites. Since these sites were found throughout all experimental groups, I believe that recurrent synaptic sites are generally important for neuronal function. I could additionally show that the occupancy and the flips of recurrent sites were predictive of whether neurons would become activated.

Both higher occupancies and fewer flips pointed towards the activation of neurons during the EE.

These findings gave further evidence that the stability of connectivity was predictive of neuronal activity. It also strengthened the idea that intense neuronal activity increased the stability of the network connectivity even of inactive neurons.

5.9 Hippocampal Structural Synaptic Plasticity Predicted Hippocampal Memory

After I finished imaging ArcCre^{ERT2}; Thy1-eGFP; Ai9 and NexCre^{ERT2}; Thy1-eGFP; Ai9 mice for two weeks, I trained all mice (independent of genotype and housing) in a hippocampus-dependent trace fear conditioning paradigm (Methods 4.9). The paradigm consisted of one day conditioning and testing for the context- and tone-memory on the second day. During the conditioning in context A, mice had 3 minutes to habituate to the new environment. Afterward, a 20-second tone was played, followed by a 15-second trace, followed by a 1-second electrical shock (0.75 mA) and followed by a 105-second inter-trial interval (ITI). This was repeated 3 times. 24 hours later, mice were exposed to the same context A without presenting neither the tone nor the shock. 30 minutes later, mice were exposed to a new, different context B. They had 3 minutes to habituate to the new environment before a 1-minute tone was presented, followed by a 1 minute trace (**Fig. 5.9.1**). During all time, mice were video-tracked using the commercial software ANY-maze® and freezing as a measure for fear and memory recall was recorded.
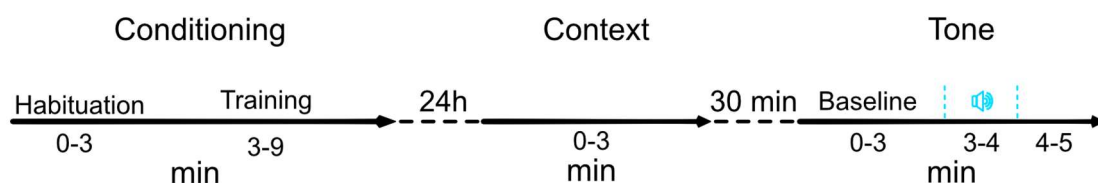

Fig. 5.9.1: Schematic timeline of the hippocampal-dependent trace fear conditioning paradigm. Day 1 conditioning: 3 minutes habituation – 20-second tone – 15-second trace – 1-second electrical shock (0.75mA) – 105-second ITI. Tone, trace, shock, ITI were repeated 3 times. Day 2 Probes: Context: 3-minute exposure to the context A. 30 minutes later, Tone: 3 minutes habituation – 1-minute tone – 1-minute trace.

First, I tested whether all mice were able to learn and to remember the hippocampal-dependent trace fear conditioning paradigm. This was crucial because it could well be, that implantation of the imaging cannula over the dorsal hippocampus, the two-week imaging with 2-photon light of the CA1 and 8 time points of anesthesia, TAM injection and the tdTomato expression could affect the ability to encode hippocampal-dependent memory.

When I tested ArcCre[ERT2]; Thy1-eGFP; Ai9 and NexCre[ERT2]; Thy1-eGFP; Ai9 mice for their memory to the context on day 16, both groups significantly increased freezing compared to freezing during the last minute of habituation on day 15 (Tukey's multiple comparisons test corrected 2-way ANOVA; habituation vs. probe Arc $p < 0.0001$, Nex Arc $p < 0.0001$). This was a clear read-out that the mice remembered the fearful event that happened the day before while they were exploring context A (**Fig. 5.9.2A**). I then tested both experimental groups for their memory to the tone on day 16. Mice significantly increased freezing to the tone compared to freezing during the last minute of habituation to the new context (baseline) (Tukey's multiple comparisons test corrected 2-way ANOVA; habituation vs. probe Arc $p <$ 0.0001, Nex Arc $p < 0.0001$) (**Fig. 5.9.2B**). Additionally, I tested if animals that strongly froze during the context showed a fear generalization and thereby would also show robust freezing to the tone. A fear generalization could be excluded since there was no correlation between freezing to the context and freezing to the tone (Spearman correlation, $r = 0.2657$ and $p = 0.4042$) (**Fig. 5.9.2C**).
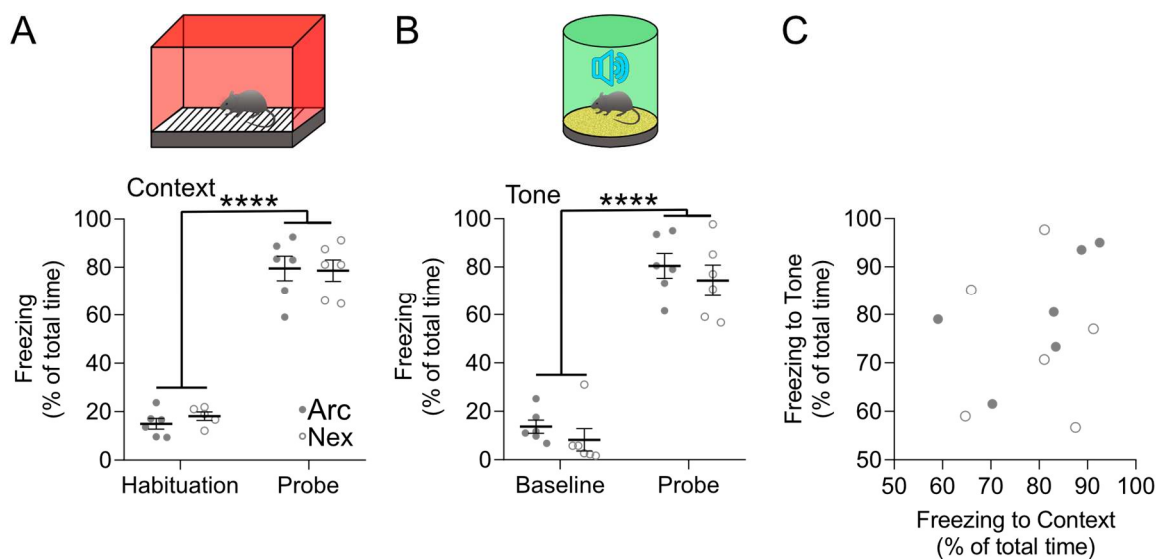

Fig. 5.9.2: Imaging cannula implanted mice show robust learning and memory in a hippocampal-dependent trace fear conditioning. (**A**) ArcCre[ERT2]; Thy1-eGFP; Ai9 and NexCre[ERT2]; Thy1-eGFP; Ai9 mice showed freezing and memory to the context on day 16, both groups significantly increased freezing compared to freezing during the last minute of habituation on day 15 (Tukey's multiple comparisons test corrected 2-way ANOVA; habituation vs. probe Arc $p < 0.0001$, Nex Arc $p < 0.0001$). (**B**) ArcCre[ERT2]; Thy1-eGFP; Ai9 and NexCre[ERT2]; Thy1-eGFP; Ai9 mice showed freezing and memory to the tone on day 16, both groups significantly increased freezing compared to freezing during the last minute of baseline on day 16 (Tukey's multiple comparisons test corrected 2-way ANOVA; habituation vs. probe Arc $p < 0.0001$, Nex Arc $p < 0.0001$). (**C**) There was no correlation between the duration of freezing to the context and to the tone (Spearman correlation, $r = 0.2657$ and $p = 0.4042$). $p \leq 0.05$, ** $p \leq 0.01$, *** $p \leq 0.001$, **** $p < 0.0001$

We were wondering if hippocampal spine dynamics that I observed during baseline were predictive on how well the animal remembered the hippocampal-dependent memory. I

found that the baseline spine density was indicative of how much the mice froze during the recall of the context. It showed that mice having a lower spine density could learn and remember the task better compared to mice with a higher spine density (Spearman correlation, r = -0.6713 and p = 0.0202) (**Fig. 5.9.3A**). Additionally, the data uncovered that mice having a more dynamic hippocampal connectivity could learn and remember the task better compared to mice with more stable connectivity. This was shown by correlating the time constant (τ) of the surviving fractions of all spines of day 1 with the freezing to the context during the probe trial (Spearman correlation, r = -0.2937 and p = 0.0354) (**Fig. 5.9.3C**). Interestingly, there was no correlation of the hippocampal synaptic plasticity to the freezing to the tone in context B (Density: Spearman correlation, r = 0.2238 and p = 0.4851) (Spine survival: Spearman correlation, r = -0.2937 and p = 0.0354) (**Fig. 5.9.3B&D**). This was remarkable because the freezing to the tone is known to be more amygdala and auditory-cortex-dependent (Lavond et al., 1993; Weinberger, 2004) than hippocampus-dependent, which pointed out that the hippocampal structural synaptic dynamics mattered for the hippocampal memory.
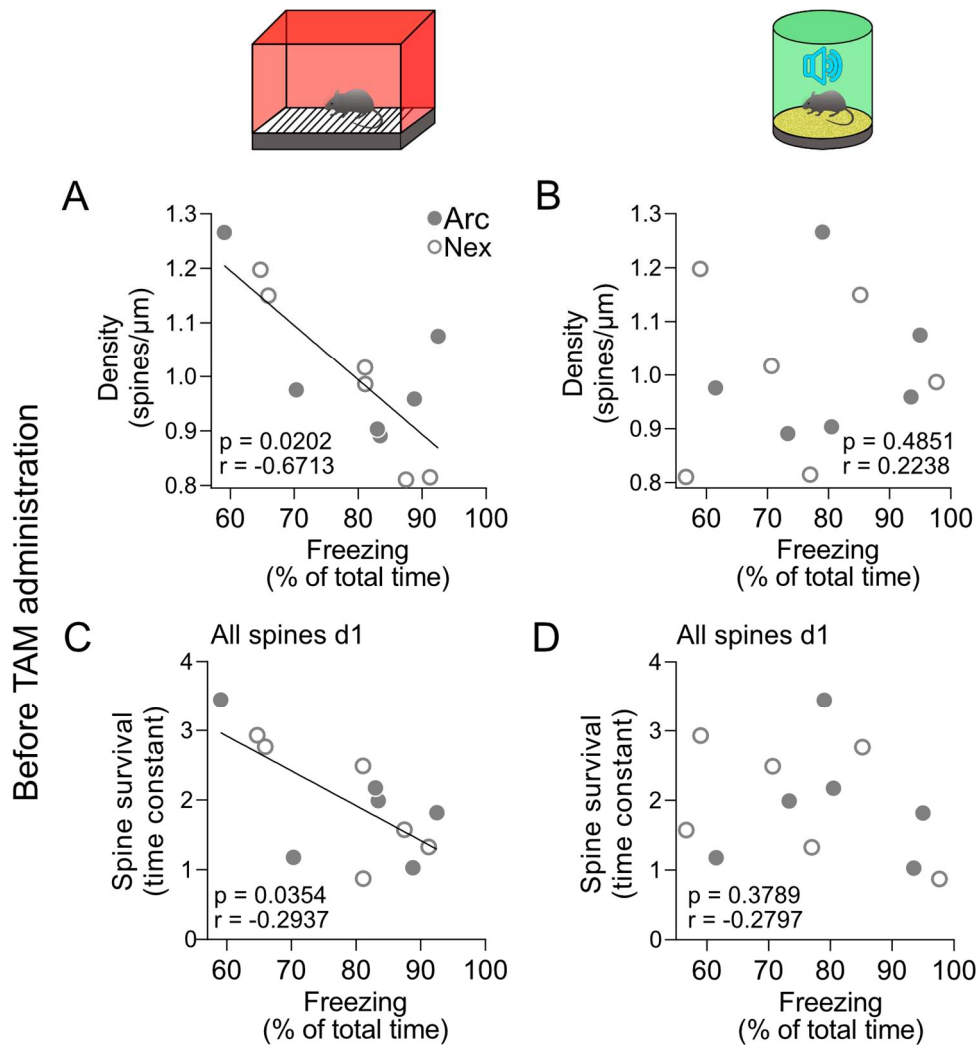
Fig. 5.9.3: Hippocampal spine dynamics predicted hippocampal-dependent learning and memory. (**A**) Significant correlation between freezing to the context and baseline spine density (Spearman correlation, r = -0.6713 and p = 0.0202). (**B**) No correlation between freezing to the tone and baseline spine density (Spearman correlation, r = 0.2238 and p = 0.4851). (**C**) Significant correlation between freezing to the context and baseline spine survival (Spearman correlation, r = -0.2937 and p = 0.0354). (**D**) No correlation between freezing to the tone and baseline spine survival (Spearman correlation, r = -0.2797 and p = 0.3789)

Furthermore, I investigated whether the exposure to the EE would affect hippocampal learning and memory. Since only Arc-Cre[ERT2]; Thy-eGFP; Ai9 animals experienced the EE while Nex-Cre[ERT2]; Thy-eGFP; Ai9 mice received the TAM injection alone, I needed to split the two groups after their treatments. When I checked for an interaction between stable spines after the EE/TAM, I found a positive correlation between stable spines (spines that existed >24h) of animals that were exposed to the EE (Arc-Cre[ERT2]; Thy-eGFP; Ai9) (Spearman correlation, r = 0.9429 and p = 0.0167) (**Fig. 5.9.4A**) but not for animals that received only the TAM (Nex-Cre[ERT2]; Thy-eGFP; Ai9) (Spearman correlation, r = -0.0857 and p = 0.9194) (**Fig. 5.9.4C**). Interestingly this correlation was exclusive to the hippocampal-dependent memory to the context (**Fig. 5.9.4A**) but not to the tone (Arc: Spearman correlation, r =

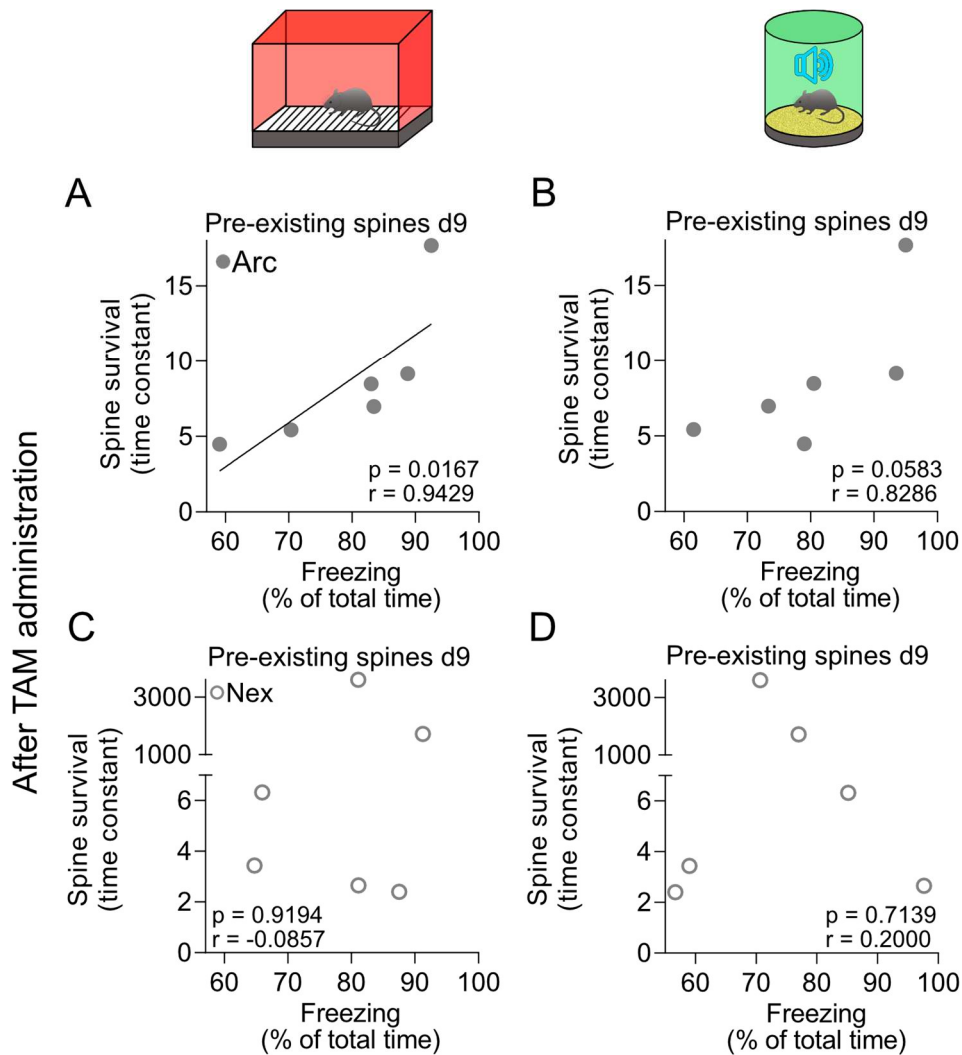0.8286 and p = 0.0583) (Nex: Spearman correlation, r = 0.2000 and p = 0.7139) (**Fig. 5.9.4B&D**).

Fig. 5.9.4: Hippocampal spine dynamics after the EE predicted hippocampal-dependent learning and memory only in animals that were exposed to the EE. (**A**) Significant correlation between freezing to the context and spine survival of stable spines after the EE in Arc-CreERT2; Thy-eGFP; Ai9 animals (Spearman correlation, r = 0.9429 and p = 0.0167). (**B**) No correlation between freezing to the tone and spine survival of stable spines after the EE (Spearman correlation, r = 0.8286 and p = 0.0583). (**C**) No correlation between freezing to the context and spine survival of stable spines after TAM in Nex-CreERT2; Thy-eGFP; Ai9 animals (Spearman correlation, r = -0.0857 and p = 0.9194) (**D**) No correlation between freezing to the tone and spine survival of stable spines after TAM (Spearman correlation, r = 0.2000 and p = 0.7139)

This finding indicates that the EE, but not TAM alone, influenced the stabilization of spines after the EE so that these spines became important for the acquisition of the hippocampal-dependent fear memory.

5.10 Artificial Neuronal Activity to Influence Hippocampal Structural Synaptic Plasticity

To strengthen my findings, I also used artificial neuronal activity induced by ChR2(H134R) expression and stimulation of the dorsal hippocampal pyramidal neurons. The rationale for this was to identify the origin of changed spine dynamics in dCA1 after neuronal activity. I infected the dorsal CA1 of WT C57BL/6 mice using viral infusions (Methods 4.10) of AAV5-CamkII-hChR2(H134R)-eYFP-pA into the dorsal CA1 bilaterally of 3 months old animals. Two weeks after the infection, I unilaterally implanted an optic fiber (400 µm core) just dorsal to the CA1 leaving the *alveus* and the *corpus callosum* intact (Methods 4.12) (**Fig. 5.10.1**).
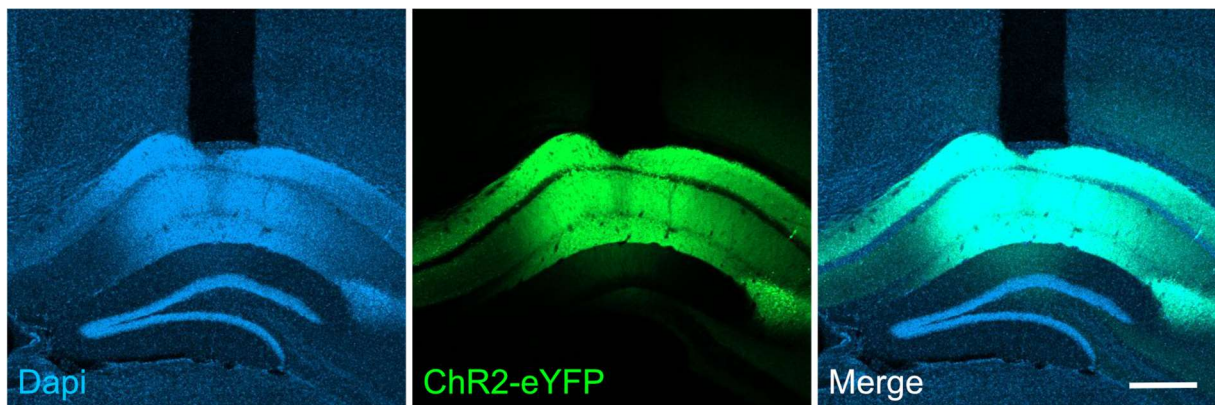
Fig. 5.10.1: Infection of the dorsal CA1 and implantation of an optic fiber just dorsal of CA1. Left DAPI-channel, middle eGFP-channel showing fluorescence of ChR2-eYFP after the infection with AAV5-CamkII-hChR2-eYFP-pA, right merge. Note the implantation site of the optic fiber just dorsal to the CA1 not damaging, but slightly squeezing the tissue. Infection is most concentrated in CA1 but also spreads into the subiculum and CA2 but not the CA3 and the DG. Scale Bar 400 um.

After the implantation, I waited another two weeks before I stimulated the infected CA1 for 30 minutes with blue (460 nm) light. The laser power was adjusted to 5 mW at the tip of the fiber. Then mice were coupled to the optic fiber connected to the laser and put into an empty (home) cage. The stimulation protocol consisted of 30 minutes during which the light was turned on for 5 seconds and off for 10 seconds. During the 5 seconds, light pulses of 5 ms were delivered at 10 Hz (**Fig. 5.10.2**).
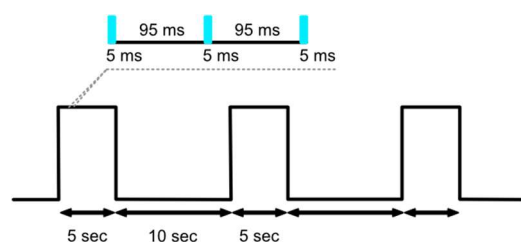
Fig. 5.10.2: Stimulation protocol of ChR2(H134R) expressed in CamKII-positive CA1 pyramidal neurons. The whole protocol lasted for 30 minutes, during which the light was turned on for 5 seconds and off for 10 seconds (lower schematic line). During the 5 seconds of light on, short light pulses of 5 ms were delivered at 10 Hz to the tissue. Laser power was adjusted to reach 5 mW at the tip of the fiber. 460 nm blue light.

75 minutes after the stimulation ended mice were sacrificed and perfused; brain tissue collected, sliced and stained for the IEG cFos as a molecular marker of neuronal activity. I chose 75 minutes because the cFos protein is known to peak at around 90 minutes after the neuronal activity, and I chose 15 minutes into the stimulation protocol to be the climax of neuronal activity. I directly compared cFos expression of the stimulated site - exclusively the area below the optic fiber - to the cFos expression of the contralateral site of the animal. Like this, each mouse was internally controlled for a potential increase of neuronal activity and cFos expression due to ChR2(H134R) activation. Using confocal microscopy, I acquired multiple z-stacks per animal and hemisphere. Because I was interested in the penetration of the virus but also in the number of cFos-positive neurons, I acquired the DAPI-channel in order to normalize the amount of eYFP and cFos-positive neurons over all neurons. I imaged the green-channel to acquire the eYFP signal from the ChR2(H134R)-eYFP to be able to tell how many DAPI cells were ChR2(H134R)-positive. Finally, I recorded the red-channel for the cFos that I stained with a secondary antibody coupled to the fluorophore Alexa594. Since both sites, the ipsilateral stimulated, and contralateral unstimulated, site were infected with ChR2(H134R)-eYFP it was essential to understand whether the expression was similar in both sides. This controlled for the fact if the sheer expression of ChR2(H134R)-eYFP would affect cFos expression alone without light. I confirmed that the ChR2(H134R)-eYFP expression was similar on both ipsi- and contralateral sites and that 97,8% of DAPI-positive cells were also positive for ChR2(H134R)-eYFP (**Fig. 5.10.3**).
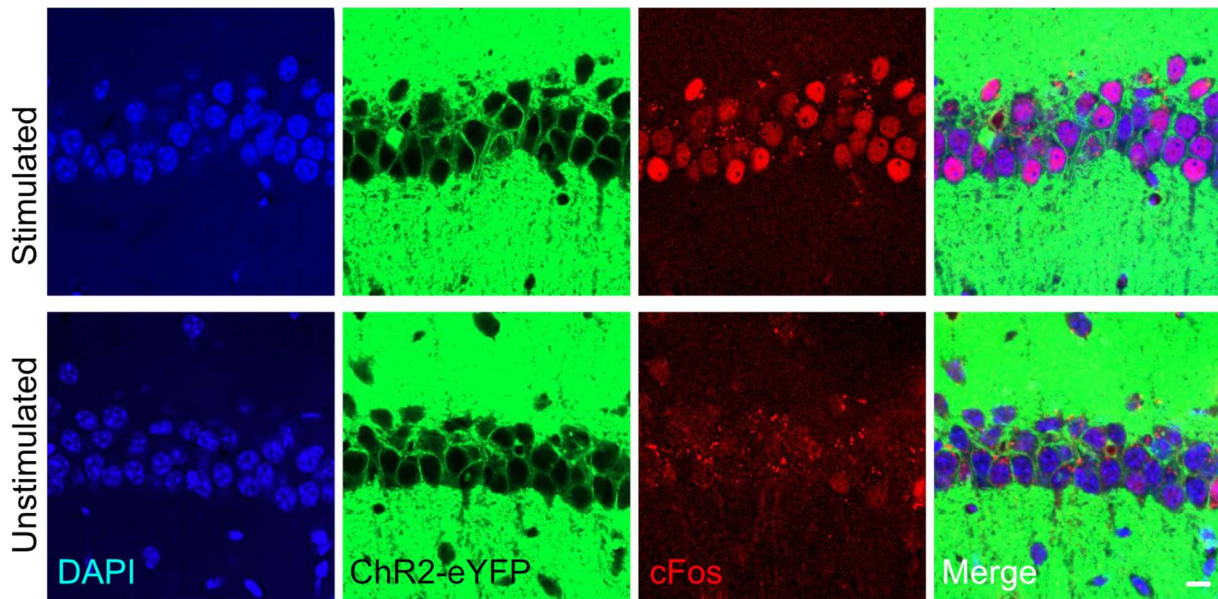
Fig. 5.10.3: Confocal microscopy images from the stimulated hemisphere (upper row) and from the unstimulated site (lower row) from the same animal. From left to right: DAPI-channel in blue, ChR2-eYFP-channel in green, cFos-channel in red and merge. Single z images taken from z-stacks with 5 μm z-steps. 40x magnification. Scale bar 10 μm.

After having acquired the confocal images of 5 mice, I quantified cFos expression (Methods 4.14). I measured the cFos fluorescence of 1099 neurons on the stimulated site and 1077 neurons on the unstimulated site. This revealed a significant increase of fluorescence on the stimulated site compared to the unstimulated site (Mann-Whitney test, $p < 0.0001$) (**Fig. 5.10.4A**). This effect was also present when I analyzed the data as cumulative distributions (Kolmogorov-Smirnov test, $p < 0.0001$) (**Fig. 5.10.4B**). Further, I defined neurons with a brighter fluorescence than one-standard-deviation from the mean as cFos-positive cells. This gave 28.8% cFos-positive neurons on the stimulated and 2.1% cFos-positive neurons on the unstimulated site representing a significant increase of cFos-positive neurons after artificial neuronal activity after ChR2(H134R)-eYFP stimulation (Mann-Whitney test, $p = 0.0079$) (**Fig. 5.10.4C**). Next, I asked if the effect of increased cFos fluorescence on the stimulated site was strong enough to be also visible in individual mice. For this, I split the 1099 stimulated and 1077 unstimulated neurons from five mice into 358, 117, 115, 205, 281 stimulated and 358, 122, 132, 206, 281 unstimulated neurons per mouse. Directly comparing the fluorescence of the stimulated vs. the unstimulated site within each animal resulted in a significant difference between the two sites per mouse (Mann-Whitney test, mouse1; $p < 0.0001$, mouse2; $p < 0.0001$, mouse3; $p < 0.0001$, mouse4; $p < 0.0001$, mouse5; $p < 0.0001$) (**Fig. 5.10.4D**). Last I was wondering if any of the mice showed a more potent activation compared to the other mice. For this, I directly compared the cFos fluorescence of the

stimulated site of all animals. Animal 5 showed a significant higher cFos fluorescence after the stimulation with ChR2(H134R)-eYFP compared to the rest of mice (Dunn's multiple comparison corrected Kruskal-Wallis test, 5 vs 1; $p < 0.0001$, 5 vs 2; $p < 0.0001$, 5 vs 3; $p < 0.0001$, 5 vs 4; $p < 0.0001$) (**Fig. 5.10.4E**).
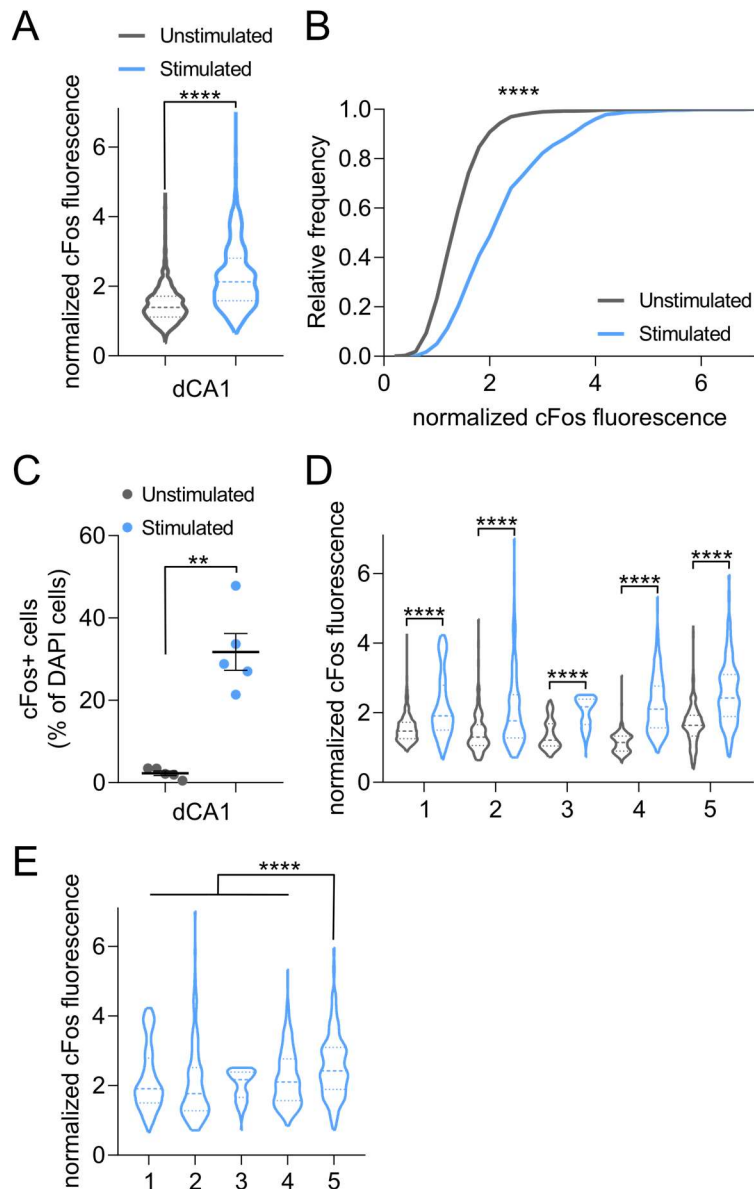

Fig. 5.10.4: Artificial neuronal activation using ChR2 leads to increased cFos expression in the dCA1. (A) Pooling the cFos fluorescence intensities from 5 mice and n = 1099 neurons on the stimulated and n = 1077 on the unstimulated site revealed a significant increase of cFos fluorescence on the stimulated compared to the unstimulated site (Mann-Whitney test, $p < 0.0001$). **(B)** Significant different cumulative distributions of cFos fluorescence on the stimulated compared to the unstimulated site (Kolmogorov-Smirnov test, $p < 0.0001$). **(C)** After light delivery, the stimulated site had more cFos-positive neurons compared to the unstimulated site (Mann-Whitney test, $p = 0.0079$). **(D)** The split data from individual mice also showed (significant differences between the cFos fluorescence on the stimulated compared to the unstimulated site (n- stimulated: 358, 117, 115, 205, 281, n-unstimulated: 358, 122, 132, 206, 281) (Mann-Whitney test, mouse1; $p < 0.0001$, mouse2; $p < 0.0001$, mouse3; $p < 0.0001$, mouse4; $p < 0.0001$, mouse5; $p < 0.0001$). **(E)** Mouse 5 showed the strongest activation and the highest cFos fluorescence after artificial neuronal activity **(**Dunn's multiple comparison corrected Kruskal-Wallis test, 5 vs 1; $p < 0.0001$, 5 vs 2; $p < 0.0001$, 5 vs 3; $p < 0.0001$, 5 vs 4; $p < 0.0001$). $p \leq 0.05$, ** $p \leq 0.01$, *** $p \leq 0.001$, **** $p < 0.0001$

This data gave evidence that ChR2(H134R) was a powerful tool to artificially induce neuronal activity of the dCA1.

Since the idea of this last part of the project was to substitute neuronal activity induced by exposure to EE with artificial neuronal activity using ChR2(H134R) and to image spine dynamics of active and inactive neurons, I needed to have a ChR2 coupled to a red fluorophore to be able to distinguish inactive (eGFP) and active (red fluorophore) neurons from each other. For this reason, I decided to use the transgenic mouse line Ai27, which expresses ChR2(H134R)-tdTomato after activation of the Cre-recombinase. This would be an ideal substitute for my experiment because the tdTomato matched my previous experiments. I crossed Nex-Cre^{ERT2} and Ai27 mice and injected 2 times 100 mg/kg TAM on two consecutive days in order to activate the TAM-dependent Cre-recombinase and to express ChR2(H134R)-tdTomato in Nex-positive CA1 pyramidal neurons. I unilaterally implanted an optic fiber (400 μm core) over the right dorsal hippocampus and performed the same stimulation protocol as described above (**Fig. 5.10.2**). TAM injection resulted in 62.4 % of ChR2(H134R)-tdTomato-positive neurons under the stimulated and unstimulated site (**Fig 5.10.5A**). However, stimulating ChR2(H134R)-tdTomato-positive neurons did not lead to an increase in cFos-fluorescence under the stimulated site compared to the unstimulated site (Mann-Whitney test, $p = 0.9408$) (**Fig 5.10.5B**). This effect was also not present when I analyzed the data as cumulative distributions (Kolmogorov-Smirnov test, $p = 0.0974$) (**Fig. 5.9.4C**). This data indicated that even though ChR2(H134R)-tdTomato was highly expressed in CA1 pyramidal neurons, it did not seem to be functional or at least working as compared to the ChR2(H134R)-eYFP. For this reason, I did not consider continuing working with that transgenic mouse line.
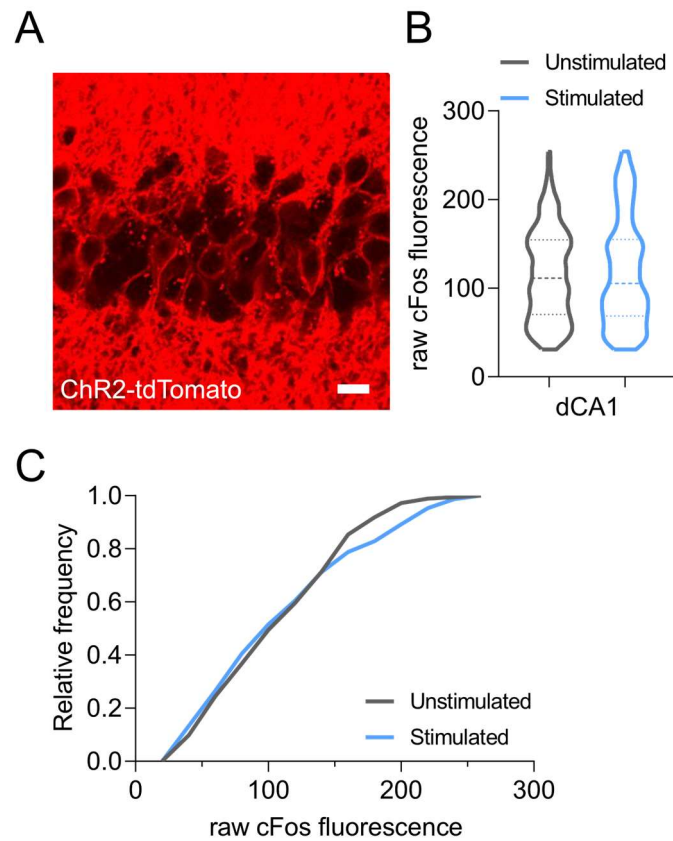
Fig. 5.10.5: ChR2(H134R)-tdTomato activation using blue light did not increase neuronal activity measured by cFos fluorescence. Confocal image, 1 z-plane (**A**) Expression pattern of ChR2(H134R)-tdTomato in the dCA1. (**B**) Activation of ChR2(H134R)-tdTomato-positive neurons did not lead to an increase in cFos-fluorescence on the stimulated site compared to the unstimulated site (Mann-Whitney test, p = 0.9408) (**C**) No different of the cumulative distributions of cFos fluorescence on the stimulated compared to the unstimulated site (Kolmogorov-Smirnov test, p = 0.0974). Scale bar 10 µm

We went on checking alternatives for a red-fluorophore tagged ChR2 and found another possibility using viral overexpression of ChR2(H134R)-mCherry. I infected the dorsal CA1 of Nex-Cre[ERT2] mice bilaterally with an AAV5-EF1a-DIO-hChR2(H134R)-mCherry. Two weeks after the infection, I unilaterally implanted an optic fiber (400 µm core) just dorsal to the CA1 and injected 100 mg/kg i.p. TAM. This concentration was chosen to achieve a sparse label to reproduce the sparse activity of approximately 50 % activity after exposure to an EE. After the implantation and injection, I waited another two weeks before I stimulated the infected CA1 for 30 minutes with blue (460 nm) light. TAM injection of 100 mg/kg resulted in 33.83 % of ChR2(H134R)-mCherry-positive neurons under the stimulated and unstimulated site (**Fig. 5.10.6**).
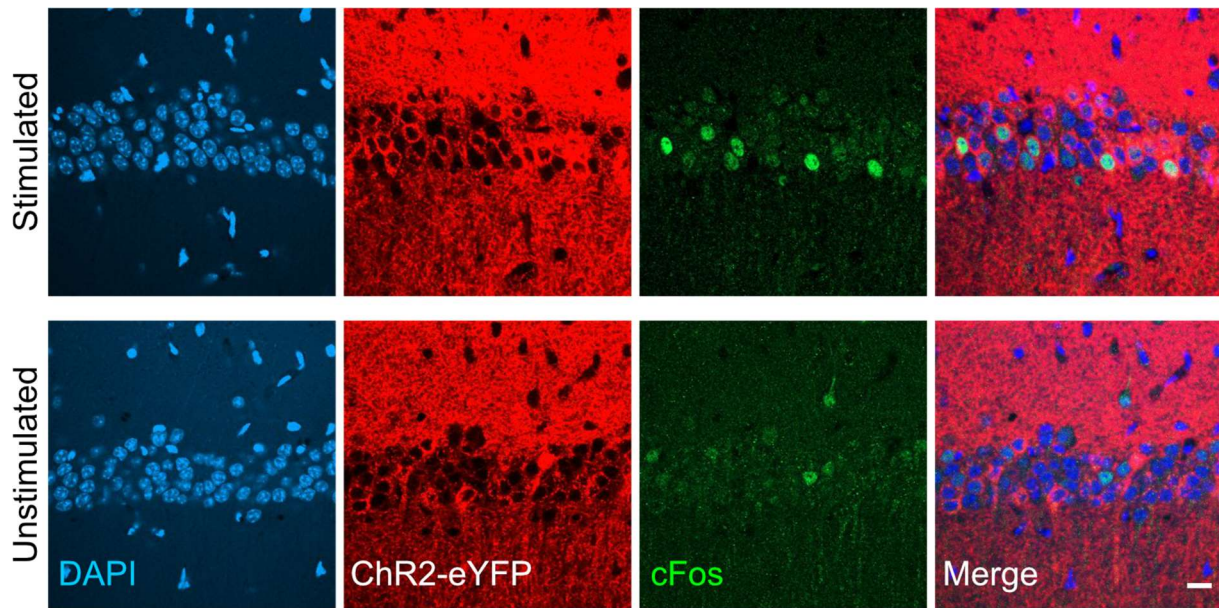
Fig. 5.10.6: Confocal microscopy images from the stimulated hemisphere (upper row) and from the unstimulated site (lower row) from the same animal. From left to right: DAPI-channel in blue, ChR2-mCherry-channel in red, cFos-channel in green and merge. Single z images taken from z-stacks with 5 μm z-steps. 40x magnification. Scale bar 20 μm.

After having acquired the confocal images of 5 mice I quantified cFos expression as explained above. Because of the sparse label I split CA1 pyramidal neurons into four classes: Neurons that were stimulated and ChR2-mCherry-positive (n = 719), neurons that were stimulated and ChR2-mCherry-negative (n = 735), neurons that were unstimulated and ChR2-mCherry-positive (n = 666) and neurons that were unstimulated and ChR2-mCherry-negative (n = 665). This revealed a significant increase of fluorescence on the stimulated site of ChR2-mCherry+ neurons compared to stimulated ChR2-mCherry- and also unstimulated ChR2-mCherry+ and ChR2-mCherry- neurons (Dunn's multiple comparison corrected Kruskal-Wallis test tested against stimulated ChR2-mCherry+, stimulated ChR2-mCherry-; $p < 0.0001$, unstimulated ChR2-mCherry+; $p < 0.0001$, unstimulated ChR2-mCherry-; $p < 0.0001$) (**Fig. 5.10.7A**). This effect was also present when I analyzed the data as cumulative distributions (Šidák's multiple comparisons corrected Kolmogorov-Smirnov test tested against stimulated ChR2-mCherry+, stimulated ChR2-mCherry-; $p < 0.0001$, unstimulated ChR2-mCherry+; $p < 0.0001$, unstimulated ChR2-mCherry-; $p < 0.0001$) (**Fig. 5.10.7B**). Further, I defined neurons with a brighter fluorescence than one standard-deviation from the mean as cFos-positive cells. This gave 15.3% cFos-positive of stimulated ChR2-tmCherry+ neurons, 8.3% cFos-positive of stimulated ChR2-mCherry- neurons, 9.9% cFos-positive of unstimulated ChR2-mCherry+ neurons and 6.3% cFos-positive of unstimulated ChR2-mCherry- neurons (Holm-

Šidák's multiple comparison corrected one-way ANOVA tested against stimulated ChR2-mCherry+, stimulated ChR2-mCherry-; p = 0.0225, unstimulated ChR2-mCherry+; p = 0.0543, unstimulated ChR2-mCherry-; p = 0.0116) (**Fig. 5.10.7C**). Last I was wondering if any of the mice showed a more potent activation compared to the other mice. For this, I directly compared the cFos fluorescence of the stimulated ChR2-mCherry+ cells of all animals. I did not find any significant difference between the four animals (Holm-Šidák's multiple comparison corrected one-way ANOVA tested against animal 91, 99; p = 0.9149, 210; p = 0.9149, 232-; p = 0.9149) (**Fig. 5.10.7D**).
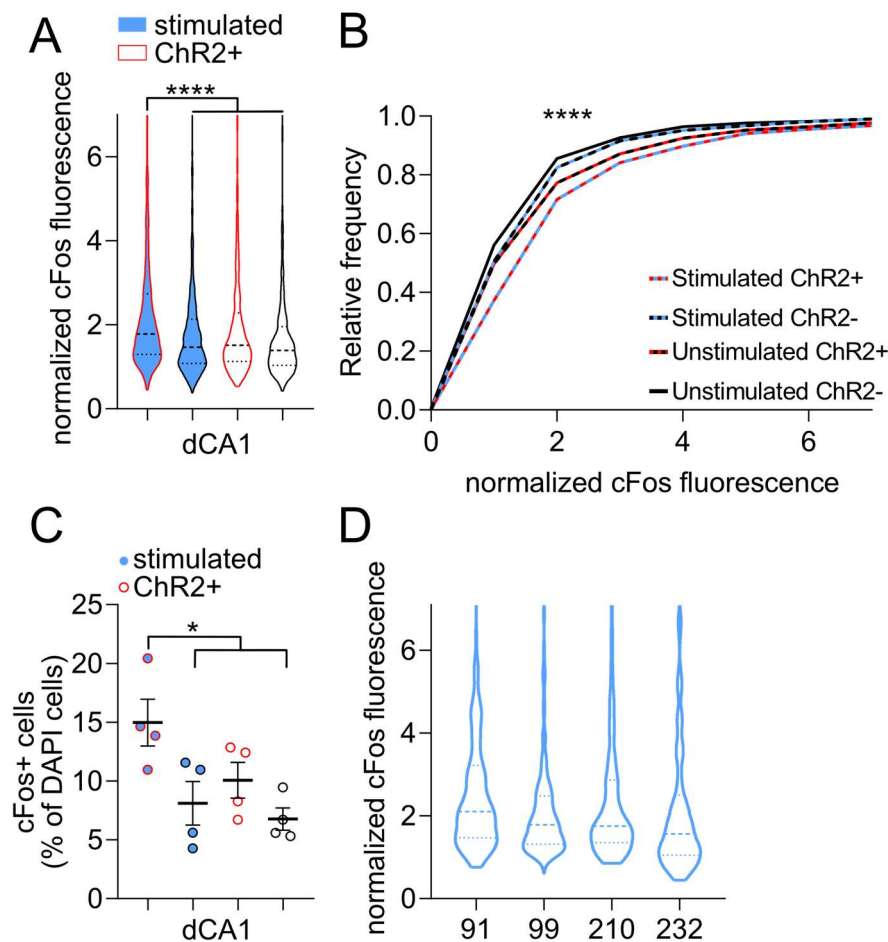
Fig. 5.10.7: ChR2-mCherry+ neurons showed increase neuronal activity measured by cFos expression. (**A**) Significant increase of fluorescence on the stimulated site of ChR2-mCherry+ neurons compared to stimulated ChR2-mCherry- and also unstimulated ChR2-mCherry+ and ChR2-mCherry- neurons (Dunn's multiple comparison corrected Kruskal-Wallis test tested against stimulated ChR2-mCherry+, stimulated ChR2-mCherry-; p < 0.0001, unstimulated ChR2-mCherry+; p < 0.0001, unstimulated ChR2-mCherry-; p < 0.0001) (**B**) Significant cumulative distributions (Šidák's multiple comparisons corrected Kolmogorov-Smirnov test tested against stimulated ChR2-mCherry+, stimulated ChR2-mCherry-; p < 0.0001, unstimulated ChR2-mCherry+; p < 0.0001, unstimulated ChR2-mCherry-; p < 0.0001) (**C**) Significant increase in cFos-positive neurons of stimulated ChR2-mCherry neurons compared to the other neurons (Holm-Šidák's multiple comparison corrected one-way ANOVA tested against stimulated ChR2-mCherry+, stimulated ChR2-mCherry-; p = 0.0225, unstimulated ChR2-mCherry+; p = 0.0543, unstimulated ChR2-mCherry-; p = 0.0116). (**D**) Stimulated ChR2-mCherry neurons from individual mice showed similar cFos

fluorescence (Holm-Šidák's multiple comparison corrected one-way ANOVA tested against animal 91, 99; p = 0.9149, 210; p = 0.9149, 232-; p = 0.9149). p ≤ 0.05, ** p ≤ 0.01, *** p ≤ 0.001, **** p < 0.0001

This data showed that sparse labeling with ChR2 (34%) resulted in a significant increase of cFos fluorescence, specifically in ChR2-mCherry+ neurons under the stimulated site. However, it also gave insight, that a sparse label resulted in an even sparser (15% of 30% = 4.5%) number of cFos – positive pyramidal neurons. For this reason, a sparse labeling of ChR2 seems to be useless to replicate 50% neuronal activity after exposure to an EE.

5.11 A One-day Morris-Water-Maze to Label Active Neurons During a Spatial Navigation Task

In order to further understand how structural synaptic plasticity would support and would be influenced not only by plain neuronal activity induced by exposure to an EE, but by an actual spatial learning paradigm, I sought out developing a shorter variant of the MWM during which I would be able to tag active neurons using the Arc-CreERT2; Thy1-eGFP; Ai9 line.

We first started with training WT C57BL/6 in a regular MWM (Methods 4.15) for 5 days and tested their memory on the 6th day (Morris, 1981). Mice had 4 trials a day, each trail separated by a 30 minutes ITI, starting from four different starting position, to locate a hidden, submerged 12 cm round platform. I measured the latency to find the platform during each trial. When the mouse did not find the platform, it was gently guided towards it until it climbed on it to rest and to orientate itself. Mice learned this task within 5 days indicated by the significant reduction in latency to find the platform (Holm-Šidák's multiple comparison corrected one-way ANOVA tested against d1, d2; p = 0.0262, d3; p = 0.0262, d4; p = 0.0047, d5; p < 0.0001, d6; p < 0.0001). The next day nearly all mice remembered well where the platform was because the latency even further decreased between day 5 and day 6 (**Fig. 5.11.1**).
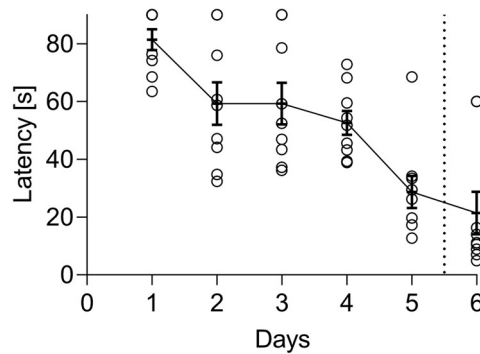
Fig. 5.11.1: 9 WT C57BL/6 animals performing the standard MWM over 5 days. Each day mice had four trials, separated by a 30 min ITI from 4 different starting positions. The latency decreased significantly over time (Holm-Šidák's multiple comparison corrected one-way ANOVA tested against d1, d2; p = 0.0262, d3; p = 0.0262, d4; p = 0.0047, d5; p < 0.0001, d; p < 0.0001). On day 6 the platform is removed, and the latency measured until the mice reach the platform zone for the first time. Open circles are individual mice. Dashed line memory trial on day 6. n=9 mice

To get a more detailed understanding about the memory I removed the platform on day 6 (dashed line) and not only measured the latency until the first entry into the platform zone (**Fig. 5.11.1**) but also quantified the time the animals spent in the target quadrant and the distance they traveled in the target quadrant to find the (removed) platform. To get a very detailed insight into the memory, I further analyzed the number of platform zone crossings. Since the platform was removed from the pool, I could tell how precisely mice checked for the platform in the area where the platform used to be. Mice spent significantly more time in the target quadrant compared to the other quadrants (Holm-Šidák's multiple comparisons corrected one-way ANOVA tested against the target quadrant, SE; p < 0.0001, NE; p < 0.0001, NW; p < 0.0001) (**Fig. 5.11.2A**). Additionally, they also traveled significantly more distance in the target quadrant compared to the other three quadrants (Holm-Šidák's multiple comparisons corrected one-way ANOVA tested against the target quadrant, SE; p < 0.0001, NE; p < 0.0001, NW; p < 0.0001) (**Fig. 5.11.2B**). Further, I analyzed the target platform crossings. Mice showed significant more target platform crossing compared to the platform zone in NE, but not compared to SE and NW (Holm-Šidák's multiple comparisons corrected one-way ANOVA tested against the target quadrant, SE; p = 0.0674, NE; p = 0.0247, NW; p = 0.0674) (**Fig. 5.11.2C**).

This data demonstrates that using this set-up (which I installed) mice were able to acquire this hippocampal-dependent spatial learning and to recall the memory 24 hours later shown by increased time and distance traveled in the target quadrant.
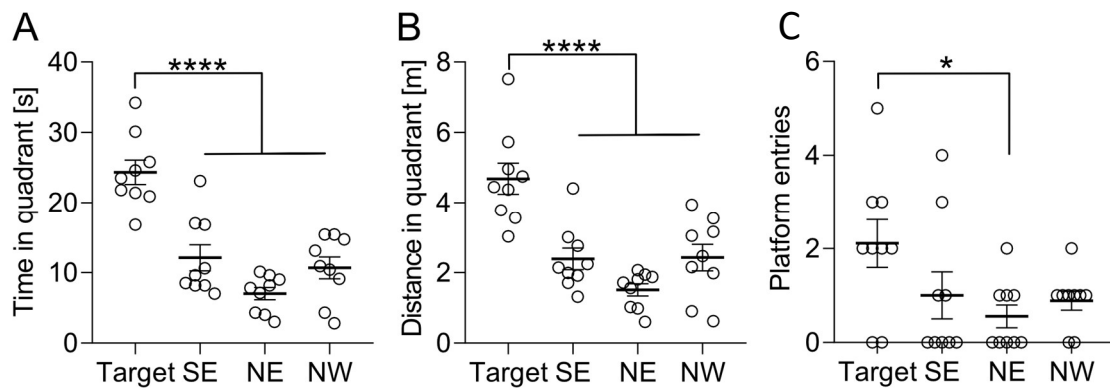
Fig. 5.11.2: MWM memory test 24 hours after the last learning day. (A) Mice spent significantly more time in the target quadrant compared to the other three quadrants (Holm-Šidák's multiple comparison corrected one-way ANOVA tested against the target quadrant, SE; p < 0.0001, NE; p < 0.0001, NW; p < 0.0001). **(B)** Mice traveled significantly more distance in the target quadrant compared to the other three quadrants (Holm-Šidák's multiple comparison corrected one-way ANOVA tested against the target quadrant, SE; p < 0.0001, NE; p < 0.0001, NW; p < 0.0001). **(C)** Mice showed significant more target platform crossing compared to the platform zone in NE, but not compared to SE and NW (Holm-Šidák's multiple comparison corrected one-way ANOVA tested against the target quadrant, SE; p = 0.0674, NE; p = 0.0247, NW; p = 0.0674). Open circles are individual mice. p ≤ 0.05, ** p ≤ 0.01, *** p ≤ 0.001, **** p < 0.0001

Since I aimed for a hippocampal-dependent spatial learning paradigm during which I planned to label active cells using TAM-dependent expression of neuronal activity driven tdTomato using the Arc-CreERT2; Thy1-eGFP; Ai9 I developed a one-day MWM. All mice were trained within 1 day, exposing them to 10 trails (30 min ITI) from four different starting positions. I hypothesized that this was a difficult task for the mice to learn and to remember since for the standard MWM mice had 20 trials distributed over 5 days allowing for consolidation mechanisms to form the memory. For this reason, I was wondering if an exposure to 16 hours EE prior to the 1-d-MWM would increase learning and memory performance of EE exposed animals compared to regularly house mice.

Even though, the data from this 1-d-MWM looked relatively noisy both groups of mice learned to locate the platform indicated by a reduction in latency in later trials of the 1-d-MWM (2-way ANOVA through time; p < 0.0001). However, independent of whether mice were exposed to the EE prior to the water mice or housed in their HC, there was no significant difference between the two groups (2-way ANOVA between groups; p = 0.8286) (**Fig. 5.11.3**).
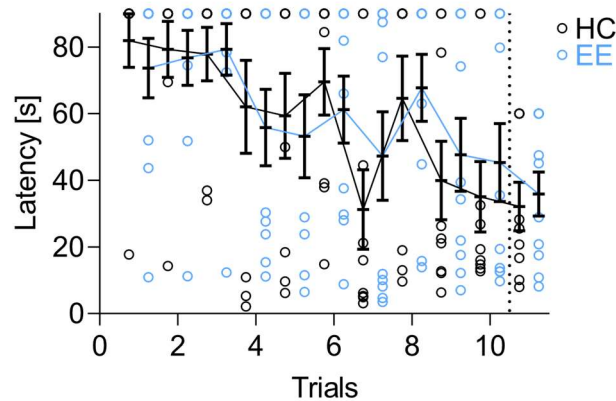
Fig. 5.11.3: One day MWM. Mice had 10 trials within one day to learn and to acquire the memory of a hidden platform. Each trial was separated by a 30 min ITI and mice started from 4 different starting positions. Animals were divided into two groups. Group one was exposed to a 16 hours EE in the night prior to the 1-d-MWM while the other group was housed under standard conditions. Mice learned to locate the platform, indicated by a reduction in latency in later trials of the 1-d-MWM (2-way ANOVA through time; p < 0.0001). However, independent of whether mice were exposed to the EE prior to the water mice or housed in their HC, there was no significant difference between the two groups (2-way ANOVA between groups; p = 0.8286). Black open circles are individual HC mice. Blue open circles are individual EE mice. Dashed line memory trial on day 2.

To get a more detailed understanding about the memory formation I removed the platform on the next day (dashed line) and not only measured the latency until the first entry into the platform zone (**Fig. 5.11.3**) but also quantified the time the animals spent in the target quadrant and the distance they traveled in the target quadrant. HC housed animals did not remember the platform position, since they did not spent more time (Holm-Šidák's multiple comparison corrected one-way ANOVA tested against the target quadrant, SE; p = 0.1639, NE; p = 0.1639, NW; p = 0.0027, All other; p = 0.2231) (**Fig. 5.11.4A**) nor traveled more distance in the target quadrant on the next day (Holm-Šidák's multiple comparison corrected one-way ANOVA tested against the target quadrant, SE; p = 0.3212, NE; p = 0.4124, NW; p = 0.0051, All other; p = 0.4124) (**Fig. 5.11.4C**). Strikingly mice that were exposed to the EE for 16 prior to the 1-d-MWM remembered the location of the platform. This was demonstrated by increased time spent in the target quadrant (Holm-Šidák's multiple comparison corrected one-way ANOVA tested against the target quadrant, SE; p = 0.2929, NE; p = 0.0007, NW; p = 0.0025, All other; p = 0.0111) (**Fig. 5.11.4B**) and also increased distance traveled in the target quadrant (Holm-Šidák's multiple comparison corrected one-way ANOVA tested against the target quadrant, SE; p = 0.3142, NE; p = 0.0068, NW; p = 0.0105, All other; p = 0.0337) (**Fig. 5.11.4D**).
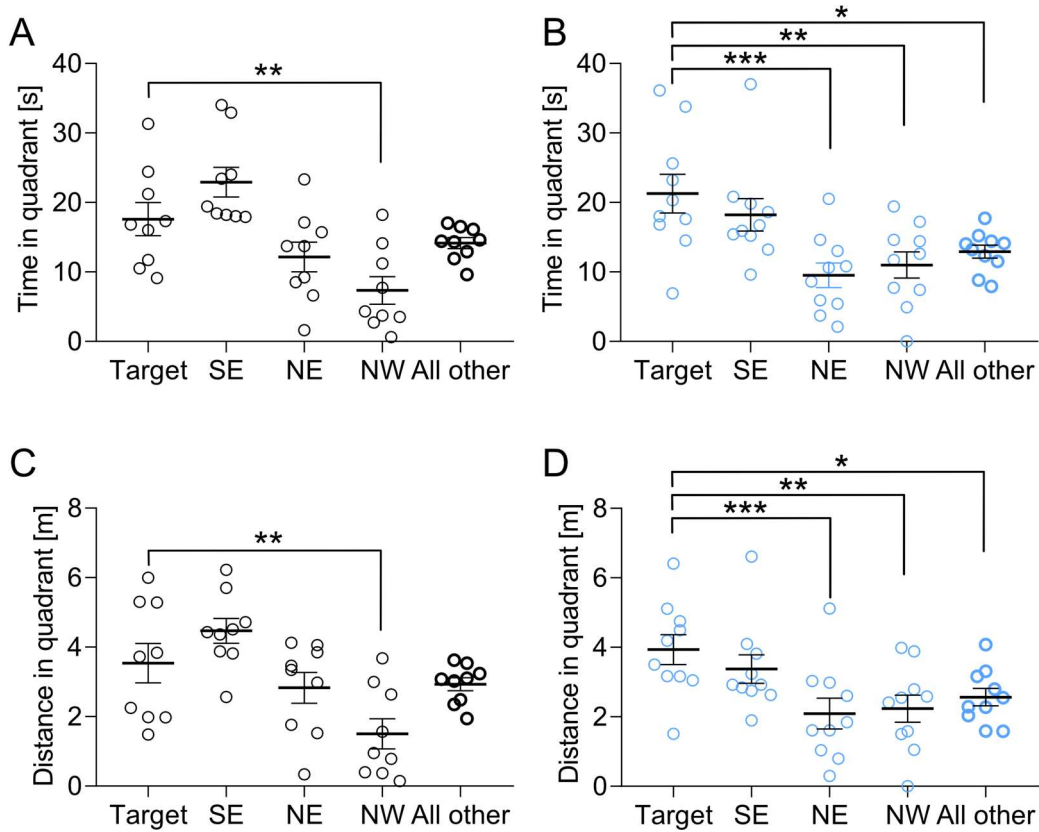
107

Fig. 5.11.4: Mice that were exposed to 16 h of EE prior to the 1-d-MWM formed a spatial memory. (A) Control mice did not spend more time in the target quadrant compared to the other three quadrants and also not compared to the mean of all other quadrants (Holm-Šidák's multiple comparison corrected one-way ANOVA tested against the target quadrant, SE; p = 0.1639, NE; p = 0.1639, NW; p = 0.0027, All other; p = 0.2231). **(B)** Mice exposed to the EE for 16h prior to the 1-d-MWM spent significantly more time in the target quadrant compared to the other three quadrants and also not compared to the mean of all other quadrants (Holm-Šidák's multiple comparison corrected one-way ANOVA tested against the target quadrant, SE; p = 0.2929, NE; p = 0.0007, NW; p = 0.0025, All other; p = 0.0111). **(C)** Control mice did not travel more distance in the target quadrant compared to the other three quadrants and also not compared to the mean of all other quadrants (Holm-Šidák's multiple comparison corrected one-way ANOVA tested against the target quadrant, SE; p = 0.3212, NE; p = 0.4124, NW; p = 0.0051, All other; p = 0.4124). (D) Mice exposed to the EE for 16h prior to the 1-d-MWM traveled significantly more distance in the target quadrant compared to the other three quadrants and also not compared to the mean of all other quadrants (Holm-Šidák's multiple comparison corrected one-way ANOVA tested against the target quadrant, SE; p = 0.3142, NE; p = 0.0068, NW; p = 0.0105, All other; p = 0.0337). Black open circles are individual HC mice. Blue open circles are individual EE mice. p ≤ 0.05, ** p ≤ 0.01, *** p ≤ 0.001

This data gave evidence that exposure to a 16 hours EE prior to the 1-d-MWM significantly improved the memory. Mechanisms as synaptic tagging and capture might play a key role in order to form this more potent memory of mice that experienced the EE (Takeuchi et al., 2016).

CHAPTER

6

CHAPTER 6 – DISCUSSION

6.1 Labeling Active Neurons

For the main experiment in this thesis, I used the so-called TRAP animals to label neurons that were active during a specific period of time. However, when I tried to label active cells using the Fos-Cre[ERT2]; Ai9 mouse line I was not able to increase the tdTomato expression after exposure to an EE to induce neuronal activity even after raising the TAM concentration to a double (300 mg/kg) of the initially published value (Guenthner et al., 2013b). Additionally, to label neurons that were active during a novel environment, the authors used 4-hydroxy-Tamoxifen (4-OHT) which they showed to be more sensitive (they needed a lower concentration) and had a shorter time window of action. Since the TAM injection showed effectiveness onto the tdTomato expression of Arc-Cre[ERT2]; Ai9 mouse line as expected from the literature, I did not doubt that the TAM itself and/or the injections were not working. The recent publication of a second generation Fos-Cre[ERT2] mouse (Allen et al., 2017) gives rise to speculations that there were general problems regarding the activity-dependent expression of reporter genes using the first generation of Fos-Cre[ERT2] mice.

Besides the TRAP technique, I could have also used other well-established techniques to label neurons that were active during a particular period of time. A prominent method is the On/Off Doxycycline (Dox) system, which is usually used in combination with a cFos-tTA mouse line and a TRE-reporter line or AVV (Liu et al., 2012b). For the use of this technique, mice are usually held On Dox (fed with Dox) until the period of interest. The Dox binds to the TRE element preventing tTA from binding and from inducing the expression of the reporter. When the Dox is not present anymore, active and cFos expressing neurons will also express tTA that finally binds to the TRE-element leading to the formation of the reporter gene. Often, an opto- or chemogenetic tool is used as the reporter gene. This enables the manipulation of recently active cells.

This technique can also be combined with a destabilized eGFP* controlled by the same IEG promoter, that leads to tTA expression. This allows labeling active neurons during a specific

time point, re-expose the animal to the same situation and check for overlapping, double positive (tTA-reporter and destabilized eGFP*) populations (Reijmers et al., 2007).

The latter technique could have helped me understanding whether the same population of neurons, that was activated by the exposure the EE was also active during the hippocampal-dependent trace fear conditioning. This correlation could have helped to strengthen my findings further.

Another technique to get longer, but not permanent excess to label active cells could have been the activity-dependent expression H2B-GFP, a fusion protein that takes several weeks to degrade (Tayler et al., 2013). Using this technique, I could have designed longitudinal experiments to assess neuronal re-activation after long-term memory of several weeks.

6.2 Synaptic Stability Predicted Neuronal Activity

We found that the spine density was stable through time. It did not increase after EE. Literature showing increased spine density of the basal dendrites in the rat dCA1 needed to expose their animals for 15 days/ 4 hours per day (Moser et al., 1994). Rampon et al. reported even a daily exposure for 3 hours for 2 months to increase in spine density in the CA1 (Rampon et al., 2000). For that reason, I were not surprised not to see an increase in spine density after 16 hours of EE. On the other hand, I also did not see any decrease in spine density, showing that anesthetizing and imaging of the animal for 8 times in 2 weeks did also not harm the dendritic morphology.

The fact that I found an increased spine density of prospective Arc-tdTomato+ was unexpected. This was the first hint that Arc-tdTomato- and Arc-tdTomato+ neurons could be two distinct neuronal populations. In line with this, Josselyn and colleagues reported that the cAMP response element binding protein (CREB) was able to increase spine density in the lateral amygdala (Sargin et al., 2013) and that neurons with a higher CREB (high CREB) level were more likely to be recruited into a memory trace (Liu et al., 2012a). Strikingly, this was coupled to an increased Arc expression in high CREB neurons after contextual fear conditioning (Han et al., 2009). This could indicate that CREB leads to increased spine density leading to a higher likelihood to become part of a neuronal ensemble and to express Arc due to the neuronal activity.

Further, I observed a decrease in spine density of newborn spines after the EE. This effect was due to the reduction in the turnover rate that I found as a network stabilization effect in inactive neurons. Decreasing the turnover and increasing the synaptic stability does not require the neuron to form new spines constantly. For that reason, the spine density of newborn spines decreased.

We showed that the stability of connectivity increased the likelihood whether a neuron would become active during the EE. This central finding was supported by a difference in turnover rate, fractional gain, fractional loss, and the surviving fraction between prospective Arc-tdTomato+ and Arc-tdTomato- neurons already before the EE. This effect was unexpected and striking because I expected most changes to happen after the EE, specifically in neurons that were activated during the EE. Since Xu et al. reported increased spine formation after the animal had learned a specific motor task and additionally demonstrated that spines that were newly formed during that task were specifically stabilized compared to newborn spines that were born on a different time point (Xu et al., 2009), I also hypothesized to observe the main changes after the EE. However, this was data from the motor-cortex and can, due to different kinetics of spine turnover, hardly be compared to hippocampal data.

On the other hand, I revealed that a potent neuronal activity, as induced by exposure to an EE, leads to a general stabilization of the network connectivity. This was indicated by a decrease in the turnover rate, fractional gain, and fractional loss by Arc-tdTomato- neurons after the EE. This population of neurons also increased their structural synaptic plasticity presented by the increase in surviving fraction after the EE. Also, this finding was unexpected as I expected to observe changes in activated neurons. Attardo et al. reported no change in structural synaptic plasticity in the dCA1 during a prolonged EE of 21 days (Attardo et al., 2015). However, the authors did not distinguish between active and inactive neurons, which made the difference for me. If I would have pooled the two populations of active and inactive neurons, I would not have observed any effect. Additionally, I hypothesize a stronger impact of a short, potent neuronal activation compared to a prolonged repetitive activity that could lead to homeostatic mechanisms (Turrigiano et al., 1998; Murthy et al., 2001; Barnes et al., 2017).

We hypothesized that BDNF released from the active neurons would be able to induce the stabilization of spines of inactive neurons, which would lead to an increase in surviving

fraction and decrease in turnover rate. This hypothesis comes from the observation that 48 hours of BDNF treatment on hippocampal organotypic slice neurons increased spine density compared to BDNF-free medium (Chapleau et al., 2008). Additionally, it was shown that the application of exogenous BDNF onto hippocampal organotypic slices did not lead to increased inward currents showing that BDNF alone was not able to induce neuronal activity. On the other hand, when the authors performed glutamate uncaging in the presence of BDNF, it resulted in spine head enlargement (Tanaka et al., 2008; Harward et al., 2016).

This further supported my hypothesis that BDNF release from active (Arc-tdTomato+) neighboring neurons does not induce the direct neuronal activity of the affected neuron (Arc-tdTomato-), but could lead to a stabilization of structural connectivity by supporting subthreshold activity.

6.3 Growth of Newborn Spines Predicted Neuronal Activity

Additionally, to the difference of structural synaptic stability in prospective Arc-tdTomato+ neurons compared to Arc-tdTomato- neurons, I also found that the growth of newborn spines could be indicative whether a neuron would become activated. Newborn spines of Arc-tdTomato+ neurons increased their size significantly over 5 days before and after the EE. Directly comparing the pooled population of newborn spines with the corresponding pooled population of the stable spines revealed that this effect was specific to newborn spines and not to stable spines of Arc-tdTomato+ neurons. However, measuring the spine size is noisy, especially for 2-photon data with limited resolution in all three dimensions. Even though the effect I observed was relatively small, it was explicitly prominent in newborn spines of the Arc-tdTomato+. So far, only activity-dependent increase in spine size had been reported (Engert and Bonhoeffer 1999). Therefore my finding that a sub-population of neurons generally increases the spine size was novel. However, it is known that the spine size and the PSD-95 surface are highly correlated (Borczyk et al. 2019), making a larger spine also more potent with more AMPA and NMDA receptors. This fundamental change of spine size in Arc-tdTomato+ neurons could lead to increased excitability, which would make an Arc-tdTomato+ neuron more likely to become part of a neuronal representation. A general change of spine size could result in increased excitability, which

would, in turn, could tempt other newborn spines to increase their size, forming a closed loop.

6.4 Stochastic Labeling of Glutamatergic Neurons

For my control experiment, the stochastic labeling of glutamatergic neurons I made use of the previously published mouse line Nex-Cre[ERT2]. This mouse line also contained a TAM dependent Cre-recombinase which was supposed to be, different compared to the Arc-Cre[ERT2], neuronal activity independent and showed most recombination activity in the hippocampus (Agarwal et al., 2012). Also, this mouse line showed dosage-dependent labeling of CA1 pyramidal neurons, which made it possible to titrate the number of neurons containing an active Cre-recombinase (data not shown). I confirmed that the labeling was activity independent. This was proven by the same amount of Nex-tdTomato+ positive neurons after a short EE compared to HC housed animals. This finding suited my requirements for a control mouse line showing stochastic labeling of a random excitatory CA1 pyramidal cell population. The critical feature of this control experiment was that all experimental procedures, imaging time and interval, Thy1-eGFP expression, TAM-dependent Cre-activation, and tdTomato expression, TAM concentration (75 mg/kg), i.p. injection and handling mirrored the Arc-Cre[ERT2] experiment, except for the induction of neuronal activity by the exposure to 16 hours EE.

6.5 No Effect of tdTomato Expression onto Structural Synaptic Plasticity

Quantifying the spine dynamics of Nex-tdTomato+ compared to Nex-tdTomato- neurons, I found a significant difference in the density of all spines. I hypothesized that this disparity in density arose from a sampling of different neuronal populations by chance and was biological irrelevant especially since there was no report available describing a toxic effect of tdTomato expression onto the formation or stability of dendritic spines.

However, I also identified a decrease in spine density of newborn spines after TAM administration. This finding was similar to the observation of the decreased newborn spine density of Arc-Cre[ERT2]- neurons after the EE. I explained this decrease in density by the

increase in structural synaptic stability of Arc-Cre^{ERT2}- neurons after the EE. However, the reduction of newborn spine density of NexCre^{ERT2}- neurons did not fit to the overall result I obtained from further analysis of the spine dynamics of Nex-tdTomato+ compared to Nex-tdTomato neurons. Certainly, comparing each newborn spine density of each day after the TAM administration to the median of the baseline newborn spine density was a strict measure to identify differences from baseline. However, when taking the median over the whole data set (before and after TAM combined) the daily discrepancy from that median was highly reduced and resulted in a more moderate decrease in spine density after TAM only in one day (data not shown).

We further analyzed the differences in turnover rate, fractional gain, and fractional loss as well as the surviving fraction of all, stable and newborn spines. Overall, I found as expected, that tdTomato expression did not influence the structural synaptic dynamics. Nex-tdTomato+ and Nex-tdTomato- neurons showed no significant difference in all of the measurements when I used neurons as the single unit. However, focusing on the pooled gain and the surviving fraction of stable spines, plotting the data as individual dendrites revealed significant differences through time for both Nex-tdTomato+ and Nex-tdTomato- which were absent when using neurons as single units. This illustrated that it was essential to think about the hypothesis before analyzing the data. Since my activity marker could only distinguish between the activity of a whole neuron and not the activity of single dendrites or even individual spines, I decided to focus my quantification and results on the neuron and not dendrite level.

6.6 Identifying Recurrent Synaptic Sites

Previous data had shown that after increased spine loss due to chronic corticosterone treatment, and recovery treatment with ketamine spines significantly re-grew at previously lost positions compared to new locations distributed on that dendritic segment (Moda-Sava et al., 2019). Interestingly I identified 35% of all synaptic sites as recurrent synaptic sites. For that reason, I wanted to dissect the features of these specific sites further.

6.7 The Occupancy and Flips of Recurrent Sites Predicted Arc-tdTomato+ Neurons

To make sure that I was investigating recurrent sites, I compared the jitter of all recurrent positions to the jitter of stable spines. I found that the two distributions were indistinguishable from each other pointing to the fact that even though the recurrent site had no spine for one or more days, as soon as a new spine appeared on the recurrent site, I explicitly identified it as born on a recurrent position. Holtmaat et al. discussed the issue of optical resolution using longitudinal 2-photon microscopy on telling newborn spines apart from stable spines. They defined an arbitrary threshold of 0.5 µm in which the spine had to be present the following imaging time point to be called a stable spine (Holtmaat et al., 2009). This addressed my problem only in part since I demonstrate that spines that were scored as stable showed a mean jitter of 0.0003 µm and only 2.2% had a larger jitter than 2 standard deviations from the mean, while recurrent spines had a mean jitter of 0.0331 µm and only 1.8% had a larger jitter than 2 standard deviations from the mean. However, demonstrating that the two distributions of stable and recurrent jitter were not different from each other proved that I was able to identify recurrent positions.

When I further asked for the likelihood of being born on a recurrent position compared to be born on a new location, I identified a strong bias towards being born at recurrent positions independent of the Arc-Cre^{ERT2} or NexCre^{ERT2} genotype. This showed the biological importance of recurrent sites either influenced by existing pre-synaptic partners (Bloss et al., 2018) releasing glutamate onto the dendritic shaft leading to *de novo* spine formation (Kwon and Sabatini, 2011) or by the molecular postsynaptic composition that could facilitate spine growth at particular locations, like Cofilin-1, CamKIIa, Homer1b (Bosch et al., 2014).

Furthermore, I focused on the occupancy and flips of recurrent sites. As expected from previous findings, the occupancy of prospective Arc-tdTomato+ dendrites was significantly elevated compared to Arc-tdTomato- dendrites and Nex-tdTomato+ dendrites. This result added another layer of information to the fact that prospective Arc-tdTomato+ neurons had more stable connectivity before the neuron became active. Similarly, this was true for the flips that were observed before the EE. A significantly lower number of flips predicted if a neuron would be active during the EE. Also, this finding pointed to the main idea that neurons with more stable connectivity would become activated and part of a neuronal representation.

6.8 Hippocampal Structural Synaptic Plasticity Predicted Hippocampal Memory

A surgical procedure of a chronic preparation enabling visual access to the brain always brings the risk to damage the region that should be exposed. My preparation was no exception, especially since I needed to ablate the overlying cortical tissue to reach the dorsal hippocampus. Mice that were implanted were able to learn the hippocampal-dependent trace fear conditioning paradigm and showed strong memory and freezing behavior to the context on the next day indicating that the hippocampal structure and function was still intact even after the surgery. Mice were also able to learn and to remember the second component of the task displayed by the freezing to the tone which was presented in a new environment. The freezing to the context and to the sound was not correlated, illustrating no generalization of fear.

When I correlated the spine density and the time constants of the surviving fraction of all spines prior to the EE, I found that both a lower spine density and a higher turnover significantly predicted how much the animal froze during the context but not during the tone. This showed that the hippocampal structural synaptic plasticity was correlated with the hippocampal-learning, but it was not related to the amygdala-dependent tone learning (Lavond et al., 1993). Admittedly there is broad discussion whether the encoding of the tone memory and its retrieval is also hippocampus-dependent. There seems to be evidence that the encoding is hippocampus-dependent while the memory retrieval is hippocampus-independent. By measuring the freezing to the tone on the next day, I evaluate the mouse' memory – the hippocampus-independent part of this paradigm – which I demonstrated was not correlated to the hippocampal synaptic plasticity.

Our discovery was supported by recently published data, showing that increased synaptic turnover after CCR5 knock-out was beneficial to improve hippocampal-dependent learning (Frank et al., 2018). I hypothesize that the increased synaptic turnover enables the neuron to respond quickly to changing stimuli and thereby helps to acquire relevant information making a more plastic brain favorable to learning. Modeling the same data of Frank et al. also gave insights into the sparseness of the network, concluding that having a less dense network supported the improvement of memory. This model fits my observed data, that not only the increased turnover but also the lower density correlated with better learning.

Additionally, Sanders et al. showed decreased spine density in active cells (Sanders et al., 2012).

Finally, I investigated whether the structural changes induced after the EE influenced the ability to learn the hippocampal-dependent trace fear conditioning. I found that the time constants of the surviving fractions of stable spines after the EE were positively correlated to the freezing to the context in animals that were exposed to the EE but not in Nex-Cre^{ERT2} animals. I hypothesize that the EE primed synapses, which became stabilized after the EE in a long term synaptic tagging and capture mechanism, making them relevant for acquiring the fear memory (Wang et al., 2010).

6.9 Artificial Neuronal Activity to Influence Hippocampal Structural Synaptic Plasticity

Our next idea was to substitute neuronal activity, which I induced by exposure to EE, with the artificial firing of the CA1 using optogenetic tools. Initially, I needed to establish this tool. For that reason, I injected AAV5-CamkIIa-hChR2(H134R)-eYFP-pA into the dorsal CA1 bilaterally of 3 months old WT animals. I continued with implanting an optic fiber to the dorsal hippocampus to deliver blue light to the CA1 pyramidal layer. For the stimulation, I designed a more physiological (1-5 Hz) (Hirase et al., 2001) 30-minute protocol where 5 ms light pulses were delivered at 10 Hz for 5 seconds. After 5 seconds, the light was turned off for 10 seconds before it was turned on again. This is in contrast to an un-physiological protocol widely used, exposing the neurons to 20 Hz 15 ms light pulses for 3 minutes (Ramirez et al., 2013).

Next, I quantified the cFos expression under the stimulation area of the dCA1 and the corresponding contralateral site. I realized that the CA1 did not display a clear distinction between a cFos positive or cFos negative neuron. Instead, it showed a continuum from no fluorescence through slight fluorescence to bright fluorescence. For that, I decided not to quantify the amount of cFos positive neurons but to quantify cFos fluorescence over blindly chosen DAPI ROIs. This yielded, as expected, a significant cFos fluorescence on the stimulated site compared to the unstimulated site. This effect was potent enough to be also visible per individual animal and coherent with literature (Ramirez et al., 2013).

Further, I tested the transgenic mouse line Ai27 that expressed a Cre-dependent ChR2-tdTomato. However, even though the expression of tdTomato was prominent in the dorsal CA1 using my stimulation protocol, I was not able to induce cFos expression. I believe this was due to the nature of the ChR2-tdTomato construct itself. Reports from the original publication comparing the Ai27 (ChR2-tdTomato) with the Ai32 (ChR2-eYFP) line already pointed out a 4-times weaker photo-stimulation effect (Madisen et al., 2012).

We went on with tailoring the experiment to my needs in order to be able to combine artificial neuronal activation by ChR2 with the *in vivo* 2-photon imaging. I chose to have a sparse label of ChR2-mCherry (30%) to achieve two populations of neurons in the dCA1. The first one would be ChR2-positive and activated by ChR2 stimulation and would correspond to the Arc-tdTomato neurons after the EE, while the second would be ChR2-negative, inactive, and would mirror the Arc-tdTomato- population. Choosing the Nex-Cre[ERT2] line in combination with the AAV5-EF1a-DIO-hChR2(H134R)-mCherry injection and 100mg/kg TAM i.p. administration resulted in 30% ChR2-positive neurons. Because of the sparseness of ChR2 expression, I needed to divide the neurons in ChR2-positive or negative for quantification of cFos expression. This resulted in a significant increase in cFos expression in ChR2+ neurons under the stimulated area. However, when I checked for the number of cFos+ neurons out of the total amount of ChR2+ neurons under the stimulated area, I realized that only 15% were cFos+ (clearly activated). That finding made it impossible for me to transfer the system *in vivo* directly. I aimed for a system in which I could tell by the fluorescent marker which cell was active. However, 15% out of 30% labeled cells resulted in only 4.5% active neurons. For this reason, I further decided to take a hybrid approach, continuing using the Arc-Cre[ERT2]; Thy1-eGFP; Ai9 line, as a reporter for neuronal activity in combination with an AAV-CamKIIa-driven ChR2 without any fluorophore. I had shown that AAV-CamKIIa-driven ChR2 was expressed in close to 100% of cells, and that stimulation resulted in robust (30-50% cFos+) neurons. Combing these two approaches with a 75 mg/kg TAM injection would label active/Arc+ neurons with tdTomato after artificial induction of neuronal activity using ChR2.

6.10 A One-day Morris-Water-Maze to Label Active Neurons During a Spatial Navigation Task

Richard Morris developed a water maze task to train rats to find a hidden, submerged platform in a circular pool to assess hippocampal-dependent spatial learning (Morris, 1981). This paradigm became widely used and also adapted in other species such as mice. A regular training protocol for mice consisted of 5-7 days of training with 4 training trials per day (Vorhees and Williams, 2006). I established the task aiming for a one-day variant of the task. WT mice learned to locate the platform within 5 days of training and also showed increased memory measured 24h after the last day of training. Shortening the procedure to half the trials in one day made the acquisition more complicated but still resulting in significant learning through time. However, only mice that were exposed to an EE for 16 hours immediately before the onset of learning showed a memory 24 hours after the training, whereas HC housed mice showed evidence of learning by significantly decreased escape latencies but no significant sign of memory. I hypothesize that the EE-induced enhancement of memory resulted from a synaptic tagging during the EE which was captured during the 1-d-MWM, finally producing the enhanced memory. My assumption was supported by the finding that mice trained in a complicated place learning paradigm only remembered the rewarded location 24 hours after the initial visit if they experienced a novel environment 30 minutes after or 23 hours before the initial visit (Takeuchi et al., 2016).

Following this finding, I had two main ideas to translate this into an *in vivo* 2-photon imaging experiment. Both include the usage of activity-dependent labeling of neurons using the Arc-Cre[ERT2]; Thy1-eGFP; Ai9 mouse line. The first idea was to label active neurons during the period of the 1-d-MWM of EE exposed, and HC housed animals. This investigation could tell whether EE (invisible) tagged neurons contributed to the 1-d-MWM learning and if this influenced structural synaptic plasticity of neurons that were active during the water maze. The second possibility would be to label active neurons during the EE and during HC exploration. I know that activated neurons did not change their spine dynamics after the EE, but if they changed their dynamics, I would be able to dissect their contribution onto the 1-d-MWM. This would contribute to the idea of synaptic tagging during the EE and capturing during the water maze.

CHAPTER 7 – CONCLUSION AND OUTLOOK

In summary, I found, that dCA1 pyramidal neurons showed differences in their stability of connectivity. The degree of stability was predictive of whether a neuron would become active and part of the neuronal representation of an enriched environment or not. Neurons displaying more stable connectivity and less synaptic turnover were more likely to become part of the neuronal ensemble. This finding was striking because it was not expected but biologically meaningful. Additionally, my data showed a stabilization of the network connectivity after the exposure to the EE of inactive neurons. Neurons which were not active during the EE decreased their synaptic turnover and increased the stability of spines. I did not expect to observe changes in the inactive population of neurons after the EE. I hypothesized that the EE, as a potent neuronal activity trigger, affected the overall stability of dCA1 connectivity. Furthermore, I tested if stochastic labeling of random CA1 pyramidal neurons would result in a similar finding. However, the differences in stability were only present when related to neuronal activity and were not randomly distributed. I continued to analyze my data more profoundly and identified that prospective active neurons were not only different in their synaptic stability but also showed differences in the spine growth of newborn spines compared to prospective inactive neurons. Neurons that became part of the ensemble showed an increase in their newborn spine size. Continuing my thorough analysis, I identified recurrent synaptic sites as hotspots for newborn spines. Additionally, the static measurement of the occupancy and the dynamic measure of the flips of recurrent sites were both predictive of whether a neuron became part of the neuronal representation or not. Displaying higher occupancy and less flips made neurons more likely to become active compared to neurons with low occupancy and high dynamic flips. Finally, I discovered that hippocampal spine dynamics and hippocampal-dependent learning were correlated. Animals with a high synaptic density learned and remembered the fear conditioning task worse, reflected by decreased freezing to the context, compared to animals with a low spine density. Interestingly also the stability of connectivity was negatively correlated to the freezing. Animals with less stable connectivity learned and remembered the task better. This

finding goes into the same direction as previously published data (Frank et al., 2018). Overall I provided new, detailed, and surprising insights into activity-dependent spine dynamics in the dorsal hippocampus.

For future experiments, I plan to take the introduced and established optogenetic stimulation to substitute the exposure to an EE to induce neuronal activity. I could show, that ChR2 expression in nearly 100% of CA1 pyramidal neurons yielded in 30% of cFos+ neurons. Combining the Arc-Cre^{ERT2}; Thy1-eGFP; Ai9 mouse line to label active neurons with an AAV-CamkII-ChR2 infection would label active neurons after artificial neuronal activation using ChR2 stimulation. This experiment would be helpful to understand activity-dependent structural synaptic plasticity further. Active, Arc-tdTomato+ neurons should not display more stable connectivity compared to inactive neurons prior to the ChR2 activation. The changes of spine dynamics after neuronal activity by ChR2 activation are entire speculation. At the moment I am running further pilot experiments to identify if I should directly infect and stimulate the dorsal CA1 or whether I should infect the contralateral CA3 and stimulate the afferents over the dCA1.

An additional perspective *in vivo* imaging experiment would be in combination with the established 1-d-MWM. This experiment would consist of two sub-experiments. Using the Arc-Cre^{ERT2}; Thy1-eGFP; Ai9 mouse line I plan label active neurons during the 1-d-MWM after the animals were exposed to a 16 hours EE or HC. Observing spine dynamics only in EE exposed mice compared to HC housed mice, would give direct evidence that these changes in spine dynamics are responsible for the animal to learn and to remember. The second experiment would label active neurons either during the 16 hours of EE or during HC prior to the 1-d-MWM. My preliminary data showed that exposure to the EE improved memory of the 1-d-MWM. If I could observe changes in spine dynamics in neurons that were active during the EE after the water maze, I could directly assign the contribution of these changes to the water maze. This is because, in my current data, I did not see changes in spine dynamics after the EE in activated neurons. This experiment could be highly interesting to understand whether neurons which become active during a difficult learning task change their spine dynamics because of the learning itself or whether neurons that were primed and active during the EE become re-involved into the water maze learning and therefore change their spine dynamics.

The last experiment that I propose would be the manipulation of synaptic stability by the knockdown of CCR5 (Frank et al., 2018). Knocking down this gene had been shown to result in increased spine turnover, less synaptic stability, and improved learning and memory in the hippocampus. I would create a sparse knockdown of CA1 pyramidal neurons in the Arc-Cre^{ERT2}; Thy1-eGFP; Ai9. I would then expose the mice to an EE and label active neurons during the EE. I hypothesize that CCR5 knockdown cells would be less likely to become part of the neuronal representation due to their increased synaptic turnover and reduced stability of synaptic connectivity.

Overall, coming back to my aim and motivation to pursue the experiments presented in this thesis, the future experiments would lead to the strengthening of my understanding on how synaptic stability, neuronal activity and the ability to learn and remember are interconnected together.

Abbreviations

AAV	Adeno Associated Virus
AMPA	α-amino-3-hydroxy-5-methyl-4-isoxazolepropionic acid
AMPAR	AMPA-Receptor
Arc	Activity-regulated cytoskeleton-associated protein
BDNF	Brain-derived-neuronal-growth-factor
CA1	cornus ammonis 1
CamKII	calmodulin dependent kinase II
C. elegans	Caenorhabditis elegans
ChR2	Channelrhodopsin-2
cm	centimeter
cm^2	square centimeter
CREB	cAMP response element-binding protein

d	day
DAPI	4′, 6-Diamidin-2-phenylindol
dCA1	dorsal CA1
ddH2O	double distilled water
DG	Dentate Gyrus
DNA	deoxyribonucleic acid
Dox	Doxycycline
eArch	enhanced Archaerhodopsin
EE	enriched environment
e.g.	for example
eGFP	enhanced GFP
eGFP*	destabilized eGFP
eNpHR	enhanced Halorhodopsin
eYFP	enhanced YFP
Fig	figure
fs	femto second
g	gram
GABA	gamma-aminobutyric acid
GFP	green fluorescent protein
GUI	graphical user interface
h	hour
HC	home cage
Hz	Hertz
IEG	immediate early gene
ITI	inter trial interval
l	liter
LA	lateral amygdala

LSM	laser scanning microscope
LTP	long-term-potentiation
m	meter
m	milli
M	molar
MHz	mega Herz
min	minute
MIP	maximum intensity projection
mm	milli meter
ms	milli second
mRNA	messenger RNA
MWM	Morris water maze
n	nano
NA	numerical apature
NE	north-east
NMDA	N-methyl-D-aspartate
NMDAR	N-methyl-D-aspartate receptor
n.s.	not significant
NW	north-west
PBS	phosphate buffered saline
PDGF	Platelet-derived growth factor
PFA	paraformaldehyde
PMT	photon multiplier tube
PSD-95	post-synaptic-density-protein
PV	parvalbumin
RNA	Ribonucleic acid
ROI	region of interest
RT	room temperature

Sec   seconds

SE   south-east

SOM   somatostatin

SW   south-west

TAM   Tamoxifen

TRE   tetracycline response element

tTA   tetracycline trans activator

WT   wild type

°   degree

°C   degree Celsius

μ   micro

μm   micrometer

4-OHT   4-hydroxy-Tamoxifen

List of Figures

List of Tables

References

Agarwal, A., Dibaj, P., Kassmann, C.M., Goebbels, S., Nave, K.-A., and Schwab, M.H. (2012). In vivo imaging and noninvasive ablation of pyramidal neurons in adult NEX-CreERT2 mice. Cerebral cortex (New York, N.Y. : 1991) *22*, 1473–1486.

Allen, W.E., DeNardo, L.A., Chen, M.Z., Liu, C.D., Loh, K.M., Fenno, L.E., Ramakrishnan, C., Deisseroth, K., and Luo, L. (2017). Thirst-associated preoptic neurons encode an aversive motivational drive. Science *357*, 1149–1155.

Arellano, J.I., Espinosa, A., Fairén, A., Yuste, R., and DeFelipe, J. (2007). Non-synaptic dendritic spines in neocortex. Neuroscience *145*, 464–469.

Asrican, B., Lisman, J., and Otmakhov, N. (2007). Synaptic strength of individual spines correlates with bound Ca2+-calmodulin-dependent kinase II. The Journal of neuroscience : the official journal of the Society for Neuroscience *27*, 14007–14011.

Attardo, A., Fitzgerald, J.E., and Schnitzer, M.J. (2015). Impermanence of dendritic spines in live adult CA1 hippocampus. Nature *523*, 592.

Attardo, A., Lu, J., Kawashima, T., Okuno, H., Fitzgerald, J.E., Bito, H., and Schnitzer, M.J. (2018). Long-Term Consolidation of Ensemble Neural Plasticity Patterns in Hippocampal Area CA1. Cell reports *25*, 640-650.e2.

Baddeley, A.D. (1966). The influence of acoustic and semantic similarity on long-term memory for word sequences. The Quarterly journal of experimental psychology *18*, 302–309.

Bamann, C., Kirsch, T., Nagel, G., and Bamberg, E. (2008). Spectral characteristics of the photocycle of channelrhodopsin-2 and its implication for channel function. Journal of molecular biology *375*, 686–694.

Bannerman, D.M., Sprengel, R., Sanderson, D.J., McHugh, S.B., Rawlins, J.N.P., Monyer, H., and Seeburg, P.H. (2014). Hippocampal synaptic plasticity, spatial memory and anxiety. Nature reviews. Neuroscience *15*, 181–192.

Barnes, S.J., Franzoni, E., Jacobsen, R.I., Erdelyi, F., Szabo, G., Clopath, C., Keller, G.B., and Keck, T. (2017). Deprivation-Induced Homeostatic Spine Scaling In Vivo Is Localized to Dendritic Branches that Have Undergone Recent Spine Loss. Neuron *96*, 871-882.e5.

Béïque, J.-C., Lin, D.-T., Kang, M.-G., Aizawa, H., Takamiya, K., and Huganir, R.L. (2006). Synapse-specific regulation of AMPA receptor function by PSD-95. Proceedings of the National Academy of Sciences of the United States of America *103*, 19535–19540.

Berry KP & Nedivi E (2017). Spine Dynamics. Are They All the Same? Neuron *96*, 43–55.

Bliss, T.V., and Gardner-Medwin, A.R. (1973). Long-lasting potentiation of synaptic transmission in the dentate area of the unanaestetized rabbit following stimulation of the perforant path. The Journal of physiology *232*, 357–374.

Bliss, T.V., and Lomo, T. (1973). Long-lasting potentiation of synaptic transmission in the dentate area of the anaesthetized rabbit following stimulation of the perforant path. The Journal of physiology *232*, 331–356.

Bloss, E.B., Cembrowski, M.S., Karsh, B., Colonell, J., Fetter, R.D., and Spruston, N. (2018). Single excitatory axons form clustered synapses onto CA1 pyramidal cell dendrites. Nature Neuroscience *21*, 353.

Bonnevie, T., Dunn, B., Fyhn, M., Hafting, T., Derdikman, D., Kubie, J.L., Roudi, Y., Moser, E.I., and Moser, M.-B. (2013). Grid cells require excitatory drive from the hippocampus. Nature Neuroscience *16*, 309.

Bosch, M., Castro, J., Saneyoshi, T., Matsuno, H., Sur, M., and Hayashi, Y. (2014). Structural and molecular remodeling of dendritic spine substructures during long-term potentiation. Neuron *82*, 444–459.

Bottai, D., Guzowski, J.F., Schwarz, M.K., Kang, S.H., Xiao, B., Lanahan, A., Worley, P.F., and Seeburg, P.H. (2002). Synaptic activity-induced conversion of intronic to exonic sequence in Homer 1 immediate early gene expression. The Journal of neuroscience : the official journal of the Society for Neuroscience *22*, 167–175.

Bouet, V., Frereta, T., Dutarb, P., Billardb, J.M., and Boulouarda M (2011). Continuous enriched environment improves learning and memory in adult NMRI mice through theta burst-related-LTP independent mechanisms but is not efficient in advanced aged animals. Mechanisms of Ageing and Development *132*, 240–248.

Bourne, J., and Harris, K.M. (2007). Do thin spines learn to be mushroom spines that remember? Current opinion in neurobiology *17*, 381–386.

Boyden, E.S., Zhang, F., Bamberg, E., Nagel, G., and Deisseroth, K. (2005). Millisecond-timescale, genetically targeted optical control of neural activity. Nature Neuroscience *8*, 1263–1268.

Brun, V.H., Leutgeb, S., Wu, H.-Q., Schwarcz, R., Witter, M.P., Moser, E.I., and Moser, M.-B. (2008). Impaired spatial representation in CA1 after lesion of direct input from entorhinal cortex. Neuron *57*, 290–302.

Buzsáki, G., and Moser, E.I. (2013). Memory, navigation and theta rhythm in the hippocampal-entorhinal system. Nature Neuroscience *16*, 130–138.

Cane, M., Maco, B., Knott, G., and Holtmaat, A. (2014). The relationship between PSD-95 clustering and spine stability in vivo. The Journal of neuroscience : the official journal of the Society for Neuroscience *34*, 2075–2086.

Chalfie, M., Tu, Y., Euskirchen, G., Ward, W.W., and Prasher, D.C. (1994). Green fluorescent protein as a marker for gene expression. Science (New York, N.Y.) *263*, 802–805.

Chapleau, C.A., Carlo, M.E., Larimore, J.L., and Pozzo-Miller, L. (2008). The actions of BDNF on dendritic spine density and morphology in organotypic slice cultures depend on the presence of serum in culture media. Journal of neuroscience methods *169*, 182–190.

Chen, B.E., Lendvai, B., Nimchinsky, E.A., Burbach, B., Fox, K., and Svoboda, K. (2000). Imaging high-resolution structure of GFP-expressing neurons in neocortex in vivo. Learning & memory (Cold Spring Harbor, N.Y.) *7*, 433–441.

Ciocchi, S., Passecker, J., Malagon-Vina, H., Mikus, N., and Klausberger, T. (2015). Brain computation. Selective information routing by ventral hippocampal CA1 projection neurons. Science (New York, N.Y.) *348*, 560–563.

Clayton, N.S., Griffiths, D.P., Emery, N.J., and Dickinson, A. (2001). Elements of episodic-like memory in animals. Philosophical transactions of the Royal Society of London. Series B, Biological sciences *356*, 1483–1491.

Conrad, C.D. (2010). A critical review of chronic stress effects on spatial learning and memory. Progress in neuro-psychopharmacology & biological psychiatry *34*, 742–755.

Costa-Mattioli, M., Gobert, D., Harding, H., Herdy, B., Azzi, M., Bruno, M., Bidinosti, M., Mamou, C.B., Marcinkiewicz, E., Yoshida, M., Imataka, H., Cuello, A.C., Seidah, N., Sossin, W., Lacaille, J.-C., Ron, D., Nader, K., and Sonenberg, N. (2005). Translational control of hippocampal synaptic plasticity and memory by the eIF2α kinase GCN2. Nature *436*, 1166.

D.O. Hebb (1949). The Organization of Behavior,. Wiley *50*, 437.

Danielson, N.B., Kaifosh, P., Zaremba, J.D., Lovett-Barron, M., Tsai, J., Denny, C.A., Balough, E.M., Goldberg, A.R., Drew, L.J., Hen, R., Losonczy, A., and Kheirbek, M.A. (2016). Distinct Contribution of Adult-Born Hippocampal Granule Cells to Context Encoding. Neuron *90*, 101–112.

Deng, W., Mayford, M., and Gage, F.H. (2013). Selection of distinct populations of dentate granule cells in response to inputs as a mechanism for pattern separation in mice. eLife *2*, e00312.

Denk, W., Delaney, K.R., Gelperin, A., Kleinfeld, D., Strowbridge, B.W., Tank, D.W., and Yuste, R. (1994). Anatomical and functional imaging of neurons using 2-photon laser scanning microscopy. Journal of neuroscience methods *54*, 151–162.

Denk, W., Piston, D.W., and Webb, W.W. (1995). Two-Photon Molecular Excitation in Laser-Scanning Microscopy. In HANDBOOK OF BIOLOGICAL CONFOCAL MICROSCOPY (1), J.B. Pawley, ed. (SPRINGER: CHAM), pp. 445–458.

Denk, W., Strickler, J.H., and Webb, W.W. (1990). Two-photon laser scanning fluorescence microscopy. Science (New York, N.Y.) *248*, 73–76.

Denk, W., and Svoboda, K. (1997). Photon upmanship. Why multiphoton imaging is more than a gimmick. Neuron *18*, 351–357.

Denny, C.A., Kheirbek, M.A., Alba, E.L., Tanaka, K.F., Brachman, R.A., Laughman, K.B., Tomm, N.K., Turi, G.F., Losonczy, A., and Hen, R. (2014). Hippocampal memory traces are differentially modulated by experience, time, and adult neurogenesis. Neuron *83*, 189–201.

Dudai, Y., and Morris, R.G.M. (2000). To consolidate or not to consolidate. What are the questions? In Brain, perception, memory. Advances in cognitive neuroscience / editor, Johan J. Bolhuis, J.J. Bolhuis, ed. (Oxford University Press: Oxford), pp. 149–162.

Ehrlich, I., Klein, M., Rumpel, S., and Malinow, R. (2007). PSD-95 is required for activity-driven synapse stabilization. Proceedings of the National Academy of Sciences of the United States of America *104*, 4176–4181.

Eichenbaum, H. (2000). A cortical-hippocampal system for declarative memory. Nature reviews. Neuroscience *1*, 41–50.

Eichenbaum, H. (2001). The hippocampus and declarative memory. Cognitive mechanisms and neural codes. Behavioural Brain Research *127*, 199–207.

Engelmann, M., Hädicke, J., and Noack, J. (2011). Testing declarative memory in laboratory rats and mice using the nonconditioned social discrimination procedure. Nature Protocols *6*, 1152.

Engert, F., and Bonhoeffer, T. (1999). Dendritic spine changes associated with hippocampal long-term synaptic plasticity. Nature *399*, 66–70.

Fanselow, M.S., and Dong, H.-W. (2010). Are the dorsal and ventral hippocampus functionally distinct structures? Neuron *65*, 7–19.

Feng G, Mellor R, Bernstein M, Keller-Peck C, Nguyen Q, Wallace M, Nerbonne J, Lichtman J, and Sanes J (2000). Imaging Neuronal Subsets in Transgenic Mice Expressing Multiple Spectral Variants of GFP. Neuron *28*, 41–51.

Fischer, M., Kaech, S., Knutti, D., and Matus, A. (1998). Rapid actin-based plasticity in dendritic spines. Neuron *20*, 847–854.

Flexner JB (1963). Memory in mice as affected by intracerebral puromycin. Science (New York, N.Y.) *141*, 57–59.

Frank, A.C., Huang, S., Zhou, M., Gdalyahu, A., Kastellakis, G., Silva, T.K., Lu, E., Wen, X., Poirazi, P., Trachtenberg, J.T., and Silva, A.J. (2018). Hotspots of dendritic spine turnover facilitate clustered spine addition and learning and memory. Nature Communications *9*, 422.

Fyhn, M., Molden, S., Witter, M.P., Moser, E.I., and Moser, M.-B. (2004). Spatial representation in the entorhinal cortex. Science (New York, N.Y.) *305*, 1258–1264.

Gage, G.J., Kipke, D.R., and Shain, W. (2012). Whole Animal Perfusion Fixation for Rodents. JoVE, e3564.

Gray EG (1959). Electron microscopy of synaptic contacts on dendrite spines of the cerebral cortex. Nature *183*, 1592–1593.

Greenberg, M.E., and Ziff, E.B. (1984). Stimulation of 3T3 cells induces transcription of the c-fos proto-oncogene. Nature *311*, 433–438.

Greenberg, M.E., Ziff, E.B., and Greene, L.A. (1986). Stimulation of neuronal acetylcholine receptors induces rapid gene transcription. Science (New York, N.Y.) *234*, 80–83.

Grutzendler, J., Kasthuri, N., and Gan, W.-B. (2002). Long-term dendritic spine stability in the adult cortex. Nature *420*, 812–816.

Guenthner, C.J., Miyamichi, K., Yang, H.H., Heller, H.C., and Luo, L. (2013a). Permanent genetic access to transiently active neurons via TRAP. Targeted recombination in active populations. Neuron *78*, 773–784.

Guenthner, C.J., Miyamichi, K., Yang, H.H., Heller, H.C., and Luo, L. (2013b). Permanent Genetic Access to Transiently Active Neurons via TRAP. Targeted Recombination in Active Populations. Neuron *78*, 773–784.

Hafting, T., Fyhn, M., Molden, S., Moser, M.-B., and Moser, E.I. (2005). Microstructure of a spatial map in the entorhinal cortex. Nature *436*, 801–806.

Han, J.-H., Kushner, S.A., Yiu, A.P., Cole, C.J., Matynia, A., Brown, R.A., Neve, R.L., Guzowski, J.F., Silva, A.J., and Josselyn, S.A. (2007). Neuronal competition and selection during memory formation. Science (New York, N.Y.) *316*, 457–460.

Han, J.-H., Kushner, S.A., Yiu, A.P., Hsiang, H.-L.L., Buch, T., Waisman, A., Bontempi, B., Neve, R.L., Frankland, P.W., and Josselyn, S.A. (2009). Selective erasure of a fear memory. Science (New York, N.Y.) *323*, 1492–1496.

Harris, K.M., Jensen, F.E., and Tsao, B. (1992). Three-dimensional structure of dendritic spines and synapses in rat hippocampus (CA1) at postnatal day 15 and adult ages. Implications for the maturation of synaptic physiology and long-term potentiation [published erratum appears in J Neurosci 1992 Aug;12(8):following table of contents]. J. Neurosci. *12*, 2685–2705.

Harward, S.C., Hedrick, N.G., Hall, C.E., Parra-Bueno, P., Milner, T.A., Pan, E., Laviv, T., Hempstead, B.L., Yasuda, R., and McNamara, J.O. (2016). Autocrine BDNF–TrkB signalling within a single dendritic spine. Nature *538*, 99.

Hill, T.C., and Zito, K. (2013). LTP-induced long-term stabilization of individual nascent dendritic spines. The Journal of neuroscience : the official journal of the Society for Neuroscience *33*, 678–686.

Hirase, H., Leinekugel, X., Czurkó, A., Csicsvari, J., and Buzsáki, G. (2001). Firing rates of hippocampal neurons are preserved during subsequent sleep episodes and modified by novel awake experience. Proceedings of the National Academy of Sciences of the United States of America *98*, 9386–9390.

Hofer, S.B., Mrsic-Flogel, T.D., Bonhoeffer, T., and Hübener, M. (2009). Experience leaves a lasting structural trace in cortical circuits. Nature *457*, 313.

Holtmaat, A., Bonhoeffer, T., Chow, D.K., Chuckowree, J., Paola, V.D., Hofer, S.B., Hübener, M., Keck, T., Knott, G., Lee, W.-C.A., Mostany, R., Mrsic-Flogel, T.D., Nedivi, E., Portera-Cailliau, C., Svoboda, K., Trachtenberg, J.T., and Wilbrecht, L. (2009). Long-term, high-resolution imaging in the mouse neocortex through a chronic cranial window. Nature Protocols *4*, 1128.

Holtmaat, A., Wilbrecht, L., Knott, G.W., Welker, E., and Svoboda, K. (2006). Experience-dependent and cell-type-specific spine growth in the neocortex. Nature *441*, 979–983.

Holtmaat, A.J.G.D., Trachtenberg, J.T., Wilbrecht, L., Shepherd, G.M., Zhang, X., Knott, G.W., and Svoboda, K. (2005). Transient and persistent dendritic spines in the neocortex in vivo. Neuron *45*, 279–291.

Hu, E., Mueller, E., Oliviero, S., Papaioannou, V.E., Johnson, R., and Spiegelman, B.M. (1994). Targeted disruption of the c-fos gene demonstrates c-fos-dependent and -independent pathways for gene expression stimulated by growth factors or oncogenes. The EMBO Journal *13*, 3094–3103.

Joëls, M., Karst, H., Alfarez, D., Heine, V.M., Qin, Y., van Riel, E., Verkuyl, M., Lucassen, P.J., and Krugers, H.J. (2004). Effects of chronic stress on structure and cell function in rat hippocampus and hypothalamus. Stress (Amsterdam, Netherlands) *7*, 221–231.

Jones, B.J., and Roberts, D.J. (1968). The quantiative measurement of motor inco-ordination in naive mice using an acelerating rotarod. The Journal of pharmacy and pharmacology *20*, 302–304.

Jung, C.K.E., and Herms, J. (2014). Structural dynamics of dendritic spines are influenced by an environmental enrichment. An in vivo imaging study. Cerebral cortex (New York, N.Y. : 1991) *24*, 377–384.

Juraska, J.M., Fitch, J.M., and Washburne, D.L. (1989). The dendritic morphology of pyramidal neurons in the rat hippocampal CA3 area. II. Effects of gender and the environment. Brain Research *479*, 115–119.

Keck, T., Mrsic-Flogel, T.D., Vaz Afonso, M., Eysel, U.T., Bonhoeffer, T., and Hübener, M. (2008). Massive restructuring of neuronal circuits during functional reorganization of adult visual cortex. Nature Neuroscience *11*, 1162–1167.

Kempermann, G., Kuhn, H.G., and Gage, F.H. (1997). More hippocampal neurons in adult mice living in an enriched environment. Nature *386*, 493–495.

Kwon, H.-B., and Sabatini, B.L. (2011). Glutamate induces de novo growth of functional spines in developing cortex. Nature *474*, 100–104.

Lang, C., Barco, A., Zablow, L., Kandel, E.R., Siegelbaum, S.A., and Zakharenko, S.S. (2004). Transient expansion of synaptically connected dendritic spines upon induction of hippocampal long-term potentiation. Proceedings of the National Academy of Sciences of the United States of America *101*, 16665–16670.

Lavond, D.G., Kim, J.J., and Thompson, R.F. (1993). Mammalian brain substrates of aversive classical conditioning. Annual review of psychology *44*, 317–342.

Lendvai, B., Stern, E.A., Chen, B., and Svoboda, K. (2000). Experience-dependent plasticity of dendritic spines in the developing rat barrel cortex in vivo. Nature *404*, 876–881.

Link, W., Konietzko, U., Kauselmann, G., Krug, M., Schwanke, B., Frey, U., and Kuhl, D. (1995). Somatodendritic expression of an immediate early gene is regulated by synaptic activity. Proceedings of the National Academy of Sciences of the United States of America *92*, 5734–5738.

Liu, N., He, S., and Yu, X. (2012a). Early natural stimulation through environmental enrichment accelerates neuronal development in the mouse dentate gyrus. PloS one *7*, e30803.

Liu, X., Ramirez, S., Pang, P.T., Puryear, C.B., Govindarajan, A., Deisseroth, K., and Tonegawa, S. (2012b). Optogenetic stimulation of a hippocampal engram activates fear memory recall. Nature *484*, 381–385.

Liu, X., Ramirez, S., and Tonegawa, S. (2014). Inception of a false memory by optogenetic manipulation of a hippocampal memory engram. Philosophical Transactions of the Royal Society B: Biological Sciences *369*.

Lugo, J.N., Smith, G.D., and Holley, A.J. (2014). Trace fear conditioning in mice. Journal of visualized experiments : JoVE.

Lyford, G.L., Yamagata, K., Kaufmann, W.E., Barnes, C.A., Sanders, L.K., Copeland, N.G., Gilbert, D.J., Jenkins, N.A., Lanahan, A.A., and Worley, P.F. (1995). Arc, a growth factor and activity-regulated gene, encodes a novel cytoskeleton-associated protein that is enriched in neuronal dendrites. Neuron *14*, 433–445.

Madisen, L., Mao, T., Koch, H., Zhuo, J.-m., Berenyi, A., Fujisawa, S., Hsu, Y.-W.A., Garcia, A.J., Gu, X., Zanella, S., Kidney, J., Gu, H., Mao, Y., Hooks, B.M., Boyden, E.S., Buzsáki, G., Ramirez, J.M., Jones, A.R., Svoboda, K., Han, X., Turner, E.E., and Zeng, H. (2012). A toolbox of Cre-dependent optogenetic transgenic mice for light-induced activation and silencing. Nature Neuroscience *15*, 793–802.

Madisen, L., Zwingman, T.A., Sunkin, S.M., Oh, S.W., Zariwala, H.A., Gu, H., Ng, L.L., Palmiter, R.D., Hawrylycz, M.J., Jones, A.R., Lein, E.S., and Zeng, H. (2010). A robust and high-throughput Cre reporting and characterization system for the whole mouse brain. Nature Neuroscience *13*, 133–140.

Majewska, A.K., Newton, J.R., and Sur, M. (2006). Remodeling of synaptic structure in sensory cortical areas in vivo. The Journal of neuroscience : the official journal of the Society for Neuroscience *26*, 3021–3029.

Malenka, R.C. (1991). Postsynaptic factors control the duration of synaptic enhancement in area CA1 of the hippocampus. Neuron *6*, 53–60.

Maletic-Savatic, M., Malinow, R., and Svoboda, K. (1999). Rapid dendritic morphogenesis in CA1 hippocampal dendrites induced by synaptic activity. Science (New York, N.Y.) *283*, 1923–1927.

Martin, S.J., and Clark, R.E. (2007). The rodent hippocampus and spatial memory. From synapses to systems. Cellular and molecular life sciences : CMLS *64*, 401–431.

Martin, S.J., Grimwood, P.D., and Morris, R.G. (2000). Synaptic plasticity and memory. An evaluation of the hypothesis. Annual review of neuroscience *23*, 649–711.

Matsuzaki, M., Ellis-Davies, G.C., Nemoto, T., Miyashita, Y., Iino, M., and Kasai, H. (2001). Dendritic spine geometry is critical for AMPA receptor expression in hippocampal CA1 pyramidal neurons. Nature Neuroscience *4*, 1086–1092.

Matsuzaki, M., Honkura, N., Ellis-Davies, G.C.R., and Kasai, H. (2004). Structural basis of long-term potentiation in single dendritic spines. Nature *429*, 761–766.

McClelland, J.L., McNaughton, B.L., and O'Reilly, R.C. (1995). Why there are complementary learning systems in the hippocampus and neocortex. Insights from the successes and failures of connectionist models of learning and memory. Psychological Review *102*, 419–457.

Migaud, M., Charlesworth, P., Dempster, M., Webster, L.C., Watabe, A.M., Makhinson, M., He, Y., Ramsay, M.F., Morris, R.G., Morrison, J.H., O'Dell, T.J., and Grant, S.G. (1998). Enhanced long-term potentiation and impaired learning in mice with mutant postsynaptic density-95 protein. Nature *396*, 433–439.

Miller, G., Galanter, E., and and Pribram K (1960). Plans and the structure of behavior. J. Comp. Neurol. *115*, 217.

Miller, G.A. (1956). The magical number seven, plus or minus two. Some limits on our capacity for processing information. Psychological Review *63*, 81–97.

Milner B, Squire LR, and Kandel ER (1998). Cognitive Neuroscience and the Study of Memory. Neuron *20*, 445–468.

Miyake, A. & Shah, P. (1999). Models of Working Memory: Mechanisms of Active Maintenance and Executive Control. Cambridge Univ. Press, 28–61.

Moda-Sava, R.N., Murdock, M.H., Parekh, P.K., Fetcho, R.N., Huang, B.S., Huynh, T.N., Witztum, J., Shaver, D.C., Rosenthal, D.L., Alway, E.J., Lopez, K., Meng, Y., Nellissen, L., Grosenick, L., Milner, T.A., Deisseroth, K., Bito, H., Kasai, H., and Liston, C. (2019). Sustained rescue of prefrontal circuit dysfunction by antidepressant-induced spine formation. Science (New York, N.Y.) *364*.

Monné, L. (1948). Functioning of the cytoplasm. Adv. Enzymol, 1–69.

Morris, R.G. (2001). Episodic-like memory in animals. Psychological criteria, neural mechanisms and the value of episodic-like tasks to investigate animal models of neurodegenerative disease. Philosophical transactions of the Royal Society of London. Series B, Biological sciences *356*, 1453–1465.

Morris, R.G., Anderson, E., Lynch, G.S., and Baudry, M. (1986). Selective impairment of learning and blockade of long-term potentiation by an N-methyl-D-aspartate receptor antagonist, AP5. Nature *319*, 774–776.

Morris, R.G., Garrud, P., Rawlins, J.N., and O'Keefe, J. (1982). Place navigation impaired in rats with hippocampal lesions. Nature *297*, 681–683.

Morris, R.G.M. (1981). Spatial localization does not require the presence of local cues. Learning and Motivation *12*, 239–260.

Moser, M.B., Trommald, M., and Andersen, P. (1994). An increase in dendritic spine density on hippocampal CA1 pyramidal cells following spatial learning in adult rats suggests the formation of new synapses. Proceedings of the National Academy of Sciences of the United States of America *91*, 12673–12675.

Murthy, V.N., Schikorski, T., Stevens, C.F., and Zhu, Y. (2001). Inactivity produces increases in neurotransmitter release and synapse size. Neuron *32*, 673–682.

Nader, K., Schafe, G.E., and Le Doux, J.E. (2000). Fear memories require protein synthesis in the amygdala for reconsolidation after retrieval. Nature *406*, 722–726.

Nagel, G., Brauner, M., Liewald, J.F., Adeishvili, N., Bamberg, E., and Gottschalk, A. (2005). Light activation of channelrhodopsin-2 in excitable cells of Caenorhabditis elegans triggers rapid behavioral responses. Current biology : CB *15*, 2279–2284.

Nagel, G., Ollig, D., Fuhrmann, M., Kateriya, S., Musti, A.M., Bamberg, E., and Hegemann, P. (2002). Channelrhodopsin-1. A light-gated proton channel in green algae. Science (New York, N.Y.) *296*, 2395–2398.

Nagel, G., Szellas, T., Huhn, W., Kateriya, S., Adeishvili, N., Berthold, P., Ollig, D., Hegemann, P., and Bamberg, E. (2003). Channelrhodopsin-2, a directly light-gated cation-selective membrane channel. Proceedings of the National Academy of Sciences of the United States of America *100*, 13940–13945.

Nägerl, U.V., Eberhorn, N., Cambridge, S.B., and Bonhoeffer, T. (2004). Bidirectional activity-dependent morphological plasticity in hippocampal neurons. Neuron *44*, 759–767.

Nedivi, E., Hevroni, D., Naot, D., Israeli, D., and Citri, Y. (1993). Numerous candidate plasticity-related genes revealed by differential cDNA cloning. Nature *363*, 718.

Nedivi, E., Wu, G.Y., and Cline, H.T. (1998). Promotion of dendritic growth by CPG15, an activity-induced signaling molecule. Science (New York, N.Y.) *281*, 1863–1866.

O'Keefe, J., and Dostrovsky, J. (1971). The hippocampus as a spatial map. Preliminary evidence from unit activity in the freely-moving rat. Brain Research *34*, 171–175.

Olton DS, Becker JT, and Handelman G. E. (1979). Hippocampus, space, and memory. Behav. Brain Sci., 313–365.

Pak, D.T.S., and Sheng, M. (2003). Targeted protein degradation and synapse remodeling by an inducible protein kinase. Science (New York, N.Y.) *302*, 1368–1373.

Park, E., Dvorak, D., and Fenton, A.A. (2011). Ensemble place codes in hippocampus. CA1, CA3, and dentate gyrus place cells have multiple place fields in large environments. PloS one *6*, e22349.

Pavlov, I.P. (1927). Conditioned Reflexes: An Investigation of the Physiological Activity of the Cerebral Cortex. Oxford University Press.

Pelkey, K.A., Chittajallu, R., Craig, M.T., Tricoire, L., Wester, J.C., and McBain, C.J. (2017). Hippocampal GABAergic Inhibitory Interneurons. Physiological reviews *97*, 1619–1747.

Peters, A., and Kaiserman-Abramof, I.R. (1970). The small pyramidal neuron of the rat cerebral cortex. The perikaryon, dendrites and spines. The American journal of anatomy *127*, 321–355.

Rajasethupathy, P., Sankaran, S., Marshel, J.H., Kim, C.K., Ferenczi, E., Lee, S.Y., Berndt, A., Ramakrishnan, C., Jaffe, A., Lo, M., Liston, C., and Deisseroth, K. (2015). Projections from neocortex mediate top-down control of memory retrieval. Nature *526*, 653–659.

Ramirez, S., Liu, X., Lin, P.-A., Suh, J., Pignatelli, M., Redondo, R.L., Ryan, T.J., and Tonegawa, S. (2013). Creating a false memory in the hippocampus. Science (New York, N.Y.) *341*, 387–391.

Ramon y Cajal (1893). Neue Darstellung vom hiostorischen Bau des Zentralnervensystems. Arch Anat Entwick, 319–428.

Rampon, C., Tang, Y.-P., Goodhouse, J., Shimizu, E., Kyin, M., and Tsien, J.Z. (2000). Enrichment induces structural changes and recovery from nonspatial memory deficits in CA1 NMDAR1-knockout mice. Nature Neuroscience *3*, 238.

Reijmers, L.G., Perkins, B.L., Matsuo, N., and Mayford, M. (2007). Localization of a stable neural correlate of associative memory. Science (New York, N.Y.) *317*, 1230–1233.

Rubin, A., Geva, N., Sheintuch, L., and Ziv, Y. (2015). Hippocampal ensemble dynamics timestamp events in long-term memory. eLife *4*.

Sanders, J., Cowansage, K., Baumgärtel, K., and Mayford, M. (2012). Elimination of Dendritic Spines with Long-Term Memory Is Specific to Active Circuits. J. Neurosci. *32*, 12570–12578.

Sargin, D., Mercaldo, V., Yiu, A.P., Higgs, G., Han, J.-H., Frankland, P.W., and Josselyn, S.A. (2013). CREB regulates spine density of lateral amygdala neurons. Implications for memory allocation. Frontiers in behavioral neuroscience *7*, 209.

Schacter, D.L. (1987). Implicit memory. History and current status. Journal of Experimental Psychology: Learning, Memory, and Cognition *13*, 501–518.

Scharf, M.T., Woo, N.H., Lattal, K.M., Young, J.Z., Nguyen, P.V., and Abel, T. (2002). Protein synthesis is required for the enhancement of long-term potentiation and long-term memory by spaced training. Journal of neurophysiology *87*, 2770–2777.

Scoville & Milner, B. (1957). Loss of recent memory after bilateral hippocampal lesions. Journal of neurology, neurosurgery, and psychiatry *20*, 11–21.

Semon R (1904). Die Mneme. Wilhelm Engelmann.

Sineshchekov, O.A., Jung, K.-H., and Spudich, J.L. (2002). Two rhodopsins mediate phototaxis to low- and high-intensity light in Chlamydomonas reinhardtii. Proceedings of the National Academy of Sciences of the United States of America *99*, 8689–8694.

Sparta, D.R., Stamatakis, A.M., Phillips, J.L., Hovelsø, N., van Zessen, R., and Stuber, G.D. (2011). Construction of implantable optical fibers for long-term optogenetic manipulation of neural circuits. Nature Protocols *7*, 12–23.

Spellman, T., Rigotti, M., Ahmari, S.E., Fusi, S., Gogos, J.A., and Gordon, J.A. (2015). Hippocampal-prefrontal input supports spatial encoding in working memory. Nature *522*, 309–314.

Squire, L.R., and Zola-Morgan, S. (1991). The medial temporal lobe memory system. Science (New York, N.Y.) *253*, 1380–1386.

Squirrell, J.M., Wokosin, D.L., White, J.G., and Bavister, B.D. (1999). Long-term two-photon fluorescence imaging of mammalian embryos without compromising viability. Nature biotechnology *17*, 763–767.

Steward, O., Wallace, C.S., Lyford, G.L., and Worley, P.F. (1998). Synaptic activation causes the mRNA for the IEG Arc to localize selectively near activated postsynaptic sites on dendrites. Neuron *21*, 741–751.

Suh, J., Rivest, A.J., Nakashiba, T., Tominaga, T., and Tonegawa, S. (2011). Entorhinal cortex layer III input to the hippocampus is crucial for temporal association memory. Science (New York, N.Y.) *334*, 1415–1420.

Sutherland, R.J., Whishaw, I.Q., and Kolb, B. (1983). A behavioural analysis of spatial localization following electrolytic, kainate- or colchicine-induced damage to the hippocampal formation in the rat. Behavioural Brain Research *7*, 133–153.

Takeuchi, T., Duszkiewicz, A.J., Sonneborn, A., Spooner, P.A., Yamasaki, M., Watanabe, M., Smith, C.C., Fernández, G., Deisseroth, K., Greene, R.W., and Morris, R.G.M. (2016). Locus coeruleus and dopaminergic consolidation of everyday memory. Nature *537*, 357.

Tanaka, J.-I., Horiike, Y., Matsuzaki, M., Miyazaki, T., Ellis-Davies, G.C.R., and Kasai, H. (2008). Protein synthesis and neurotrophin-dependent structural plasticity of single dendritic spines. Science (New York, N.Y.) *319*, 1683–1687.

Tanaka, K.Z., Pevzner, A., Hamidi, A.B., Nakazawa, Y., Graham, J., and Wiltgen, B.J. (2014). Cortical representations are reinstated by the hippocampus during memory retrieval. Neuron *84*, 347–354.

Tavazoie, M., van der Veken, L., Silva-Vargas, V., Louissaint, M., Colonna, L., Zaidi, B., Garcia-Verdugo, J.M., and Doetsch, F. (2008). A specialized vascular niche for adult neural stem cells. Cell stem cell *3*, 279–288.

Tayler, K.K., Tanaka, K.Z., Reijmers, L.G., and Wiltgen, B.J. (2013). Reactivation of neural ensembles during the retrieval of recent and remote memory. Current biology : CB *23*, 99–106.

Theer, P., Hasan, M.T., and Denk, W. (2003). Two-photon imaging to a depth of 1000 microm in living brains by use of a Ti:Al2O3 regenerative amplifier. Optics letters *28*, 1022–1024.

Trachtenberg, J.T., Chen, B.E., Knott, G.W., Feng, G., Sanes, J.R., Welker, E., and Svoboda, K. (2002). Long-term in vivo imaging of experience-dependent synaptic plasticity in adult cortex. Nature *420*, 788–794.

Tsien, J.Z., Huerta, P.T., and Tonegawa, S. (1996). The essential role of hippocampal CA1 NMDA receptor-dependent synaptic plasticity in spatial memory. Cell *87*, 1327–1338.

Tulvig & Donaldson (1972). Episodic and semantic memory. Organization if memory, 381–403.

Tulving, E., and Markowitsch, H.J. (1998). Episodic and declarative memory. Role of the hippocampus. Hippocampus *8*, 198–204.

Turrigiano, G.G., Leslie, K.R., Desai, N.S., Rutherford, L.C., and Nelson, S.B. (1998). Activity-dependent scaling of quantal amplitude in neocortical neurons. Nature *391*, 892–896.

Ulivi A., Castello-Waldow, T.P., Weston, G., Yan, L., Yasuda, R., Chen, A., and Attardo, A. (2019). Longitudinal Two-Photon Imaging of Dorsal Hippocampal CA1 in Live Mice. JoVE.

Vorhees, C.V., and Williams, M.T. (2006). Morris water maze. Procedures for assessing spatial and related forms of learning and memory. Nature Protocols *1*, 848–858.

Wang, S.-H., Redondo, R.L., and Morris, R.G.M. (2010). Relevance of synaptic tagging and capture to the persistence of long-term potentiation and everyday spatial memory. Proceedings of the National Academy of Sciences of the United States of America *107*, 19537–19542.

Weinberger, N.M. (2004). Specific long-term memory traces in primary auditory cortex. Nature reviews. Neuroscience *5*, 279–290.

Wong-Riley, M.T. (1989). Cytochrome oxidase. An endogenous metabolic marker for neuronal activity. Trends in neurosciences *12*, 94–101.

Xie, H., Liu, Y., Zhu, Y., Ding, X., Yang, Y., and Guan, J.-S. (2014). In vivo imaging of immediate early gene expression reveals layer-specific memory traces in the mammalian brain. Proceedings of the National Academy of Sciences of the United States of America *111*, 2788–2793.

Xu, T., Yu, X., Perlik, A.J., Tobin, W.F., Zweig, J.A., Tennant, K., Jones, T., and Zuo, Y. (2009). Rapid formation and selective stabilization of synapses for enduring motor memories. Nature *462*, 915.

Yang, G., Lai, C.S.W., Cichon, J., Ma, L., Li, W., and Gan, W.-B. (2014). Sleep promotes branch-specific formation of dendritic spines after learning. Science (New York, N.Y.) *344*, 1173–1178.

Yang, G., Pan, F., and Gan, W.-B. (2009). Stably maintained dendritic spines are associated with lifelong memories. Nature *462*, 920–924.

Zelikowsky, M., Hersman, S., Chawla, M.K., Barnes, C.A., and Fanselow, M.S. (2014). Neuronal ensembles in amygdala, hippocampus, and prefrontal cortex track differential components of contextual fear. The Journal of neuroscience : the official journal of the Society for Neuroscience *34*, 8462–8466.

Zemla R & Basu J (2017). Hippocampal function in rodents. Current opinion in neurobiology *43*, 187–197.

Zhang, F., Wang, L.-P., Boyden, E.S., and Deisseroth, K. (2006). Channelrhodopsin-2 and optical control of excitable cells. Nature methods *3*, 785–792.

Zhou, Y., Won, J., Karlsson, M.G., Zhou, M., Rogerson, T., Balaji, J., Neve, R., Poirazi, P., and Silva, A.J. (2009). CREB regulates excitability and the allocation of memory to subsets of neurons in the amygdala. Nature Neuroscience *12*, 1438–1443.

Ziv NE & Smith SJ (1996). Evidence for a Role of Dendritic Filopodia in Synaptogenesis and Spine Formation. Neuron *17*, 91–102.

Zuo, Y., Lin, A., Chang, P., and Gan, W.-B. (2005). Development of long-term dendritic spine stability in diverse regions of cerebral cortex. Neuron *46*, 181–189.

Appendices

Complementary Data

So far I only showed the means of the distributions of the occupancy and flips of Nex-tdTomato- and Nex-tdTomato+ dendrites. Both groups showed similar occupancies before the administration of TAM (Nex-: 2.46; Nex+: 2.35) (**Fig. A1A**) and after the TAM injection (Nex-: 2.63; Nex+: 2.50) (**Fig. A1B**). The same was true for the flips, which was measurement of the dynamic characteristic of the recurrent sites. Both groups showed similar numbers of flips before the administration of TAM (Nex-: 131; Nex+: 1.35) (**Fig. A1C**) and after the TAM injection (Nex-: 1.24; Nex+: 1.31) (**Fig. A1D**).
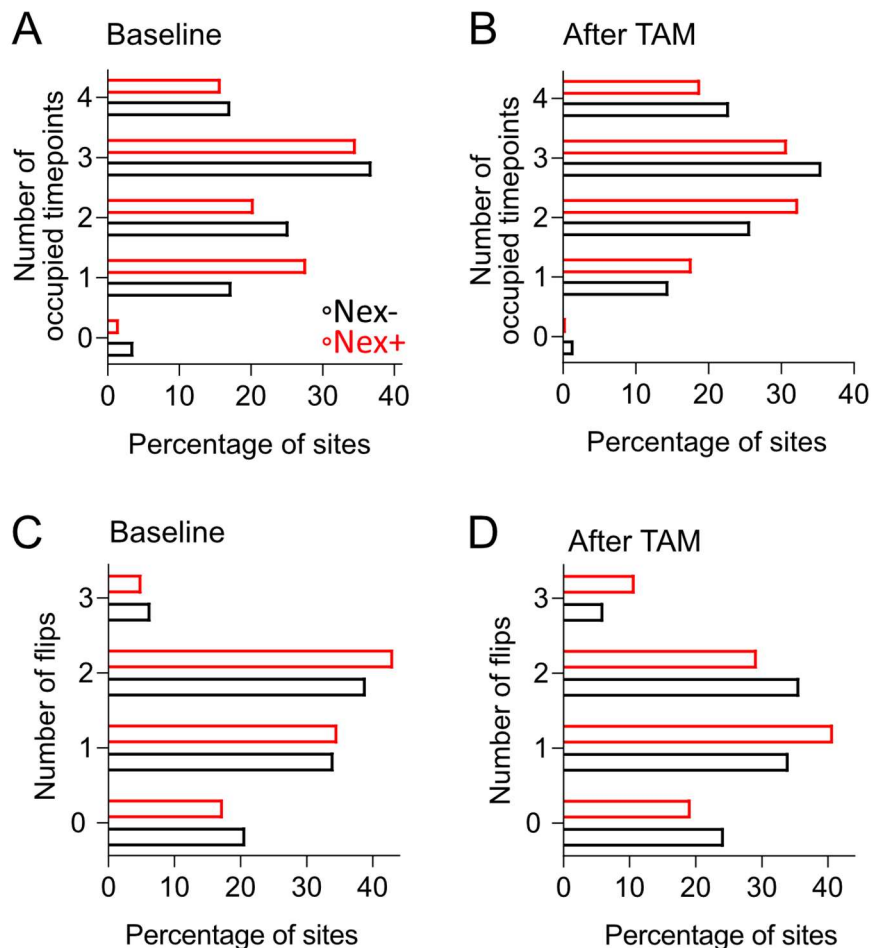

Fig. A1: (**A**) Before the administration of TAM Nex-tdTomato- and Nex-tdTomato+ dendrites showed a similar amount of occupied sites (Nex-: 2.46; Nex+: 2.35). (**B**) After the administration of TAM Nex-tdTomato- and Nex-tdTomato+ dendrites showed a similar amount of occupied sites (Nex-: 2.63; Nex+: 2.50). (**C**) Before the administration of TAM Nex-tdTomato- and Nex-tdTomato+ dendrites showed a similar amount of flips (Nex-: 131; Nex+: 1.35). (**D**) After the administration of TAM Nex-tdTomato- and Nex-tdTomato+ dendrites showed a similar amount of flips (Nex-: 1.24; Nex+: 1.31).

Contributions

The author contributed to the design, the execution, and analysis of all studies. He carried out all surgical procedures, both in vivo imaging experiments, the counting of spines, and the further analysis and interpretation of the data. All experiments shown in this study, including the behavioral studies, the optogenetic stimulations, and the immunostainings were exclusively done by the author.

Dr. Alessio Attardo supervised all experiments and contributed to the design and the interpretation of all data. He often guided the author in the correct direction and always had constructive feedback.

Ghabiba Weston contributed by automating the post-processing of the 2-photon images. Furthermore, she scripted the imaging flow at the microscope. Moreover, she took care of de-bugging the counting code.

Prof. Dr. Yonatan Loewenstein contributed to the interpretation of data and assisted with the shuffled-test statistics

Dr. Alireza Chenani helped with the conceptualization and execution of the hypergeometric probability tests

Acknowledgments

First of all, I want to thank Alessio Attardo, my direct supervisor, for giving me the excellent opportunity to pursue my Ph.D. together with him. Thank you for putting your confidence in me and for giving me free rein to be able to develop my own ideas and projects. You did not treat me as being my boss but as being my colleague. You always had great ideas pushing my work and my results towards what I have achieved now. I am pretty sure that my experience during the last four years helped me in becoming a real scientist (someday ☺). You were a fantastic supervisor with constructive criticism and vivid discussions. I am not regretting at all that I chose you and your young group for my Ph.D. We had great times together, even outside of work.

I would also like to thank my TAC-members Carsten Wotjak and Anton Sirota. I was lucky when I picked you as my TAC-members because you had constructive feedback and

refreshing ideas for my work. You always had an open ear, and I enjoyed our yearly Intermezzos.

Especially I would like to thank Ghabi, my dense, brave colleague. I was so happy to have you as my first colleague in the A-Lab. You were simply great! Thanks for debugging code, helping with the post-processing and helping me in pushing my analysis. I really appreciated our rare but honest conversations from time to time. I had great fun with you exploiting the 2P-system and writing our thesis until late at night. I will miss you.

Of course, I need to thank the whole A-Lab. We were a great team, always helping each other finding constructive criticism, going hiking, out for lunch or for a drink. I could always rely on you guys!

I also want to thank my friends, supporting me during the time of my Ph.D. I can be lucky that I found such open and tolerant friends. Special thanks to Maxi. You cannot imagine how I enjoyed going climbing with you after a working day full of experiments that didn't work. You pushed my physical but also mental borders a couple of times. I am pretty sure that helped me to stay focused during my Ph.D.

Of course, I want to thank my family! You were always my backbone! No matter what happened, I could always rely on you, and you will always be there for me. I could always complain about work, and you always listened without judging. I guess everybody says this, but I was pretty lucky getting you as my family. Kris, I will never forget our yearly wild nights in Arnhem. They are already now legendary! Mama, Papa, Rine, Kris Ihr seid die Besten!! Schade, dass ihr alle so weit weg seid und wir so wenig Zeit miteinander haben!

In the end, I need to thank my wife, Alisa. I cannot put in words what you mean to me and how you helped me during my Ph.D. You are the one who suffered the most from long working days, imaging on the weekends, or just coming in "quickly" to check my mice. You needed to take it all, and you took it with minor complains. The way you welcomed me when I came home always made me smile because I felt true love. You were always so warm and loving, and even though you hated the working hours of my job; you always supported me in pushing even harder. Alisa, ich liebe dich so sehr und ich bin so glücklich, dich an meiner Seite zu haben.